DISSERTATION

Computation of Torques in Magnetic Tunnel Junctions

ausgeführt zum Zwecke der Erlangung des akademischen Grades
eines Doktors der technischen Wissenschaften

unter der Betreuung von

Privatdoz. MSc PhD Viktor Sverdlov
O.Univ.Prof. Dipl.-Ing. Dr.techn. Dr.h.c. Siegfried Selberherr

eingereicht an der Technischen Universität Wien
Fakultät für Elektrotechnik und Informationstechnik
von

Simone Fiorentini, MSc.
Matrikelnummer: 11839446

Wien, im Februar 2023 ______________________________

Die approbierte gedruckte Originalversion dieser Dissertation ist an der TU Wien Bibliothek verfügbar.
The approved original version of this doctoral thesis is available in print at TU Wien Bibliothek.
TU WIEN Bibliothek Your knowledge hub

Die approbierte gedruckte Originalversion dieser Dissertation ist an der TU Wien Bibliothek verfügbar.
The approved original version of this doctoral thesis is available in print at TU Wien Bibliothek.
TU WIEN Bibliothek Your knowledge hub

Abstract

Non-volatility is an emerging solution to stand-by power leakages caused by the down-scaling of traditional semiconductor components. Spin-transfer torque magnetoresistive random access memory (STT-MRAM) is a viable nonvolatile candidate, thanks to its simple structure and compatibility with CMOS technology. It possesses high speed and excellent endurance, being thus promising for applications ranging from IoT and automotive uses to embedded DRAM and last level caches. Accurate simulation tools offer valuable insight in the design of STT-MRAM devices. The description of the temporal evolution of the magnetization is given by solving the Landau-Lifshitz-Gilbert (LLG) equation. The LLG equation can be enriched with terms describing the torque generated by an electric current flowing through the device, responsible for STT-MRAM operation. The present work focuses on the development and calibration of simulation approaches for dealing with the sources of torque acting in STT-MRAM devices.

First, an in-house solver based on the finite difference method, with the STT included using the Slonczewski expression, is generalized for performing switching simulations of an MRAM cell. The solver is updated to allow running switching simulations with three different approaches: with uniform and constant current density, with more realistic non-uniform current density and constant total current, and with constant voltage. The validity of the description with the fixed current density for predicting the switching time is tested by comparing its results with the ones of the other two approaches, and the switching time dependence on several system parameters is evaluated. The obtained results show that a correction on the value of the applied current allows for all the approaches to deliver compatible results.

To accurately evaluate torques beyond the interface Slonczewski approximation in composite layered structures, consisting of several ferromagnetic parts separated by nonmagnetic metal spacers and tunnel barriers, an approach based on the solution of coupled spin and charge transport equations to determine the non-equilibrium spin accumulation is adopted and implemented in a finite element-based framework. The formalism is extended to describe transport through magnetic tunnel junctions. The tunneling magnetoresistance (TMR) effect is included by modeling the tunnel barrier as a poor conductor, whose conductivity is locally dependent on the relative magnetization orientation of the ferromagnetic layers. The tunneling spin current polarization is included via appropriate boundary conditions at the interface between oxide and

Die approbierte gedruckte Originalversion dieser Dissertation ist an der TU Wien Bibliothek verfügbar.
The approved original version of this doctoral thesis is available in print at TU Wien Bibliothek.
TU WIEN Bibliothek Your knowledge hub

ferromagnetic layers. The proposed approach successfully reproduces angular and voltage dependencies of the torque exerted in MTJs, and allows to evaluate the interplay between the interface and bulk sources of torque. The approach is successfully applied to switching simulations and design of ultra-scaled STT-MRAM cells.

Die approbierte gedruckte Originalversion dieser Dissertation ist an der TU Wien Bibliothek verfügbar.
The approved original version of this doctoral thesis is available in print at TU Wien Bibliothek.
TU WIEN Bibliothek Your knowledge hub

Kurzfassung

Nichtflüchtigkeit ist eine aufkommende Lösung für Standby-Leistungsverluste, die durch das Herunterskalieren herkömmlicher Halbleiterkomponenten verursacht werden. Magnetoresistiver Spin-Transfer-Torque-Direktzugriffsspeicher (STT-MRAM) ist dank seiner einfachen Struktur und Kompatibilität mit der CMOS-Technologie ein geeigneter nichtflüchtiger Kandidat. Er verfügt über eine hohe Geschwindigkeit und eine hervorragende Lebensdauer und ist daher vielversprechend für die Verwendung in IoT- und Automobilanwendungen bis hin zu eingebettetem DRAM und Last-Level-Caches. Präzise Simulationswerkzeuge bieten wertvolle Einblicke in das Design von STT-MRAM-Bauelementen. Die Beschreibung der zeitlichen Entwicklung der Magnetisierung erfolgt durch Lösung der Landau-Lifshitz-Gilbert (LLG)-Gleichung. Die LLG-Gleichung kann mit Termen erweitert werden, die das Drehmoment beschreiben, das durch einen fließenden elektrischen Strom erzeugt wird, und für das Funktionieren des STT-MRAM verantwortlich ist. Die vorliegende Arbeit konzentriert sich auf die Entwicklung und Kalibrierung von Simulationsansätzen zum Umgang mit den Drehmomentquellen, die in STT-MRAM-Bauelementen wirken.

Im ersten Teil der Arbeit werden die Ergebnisse von Schaltsimulationen von MRAM-Zellen beschrieben, welche mit einem hauseigenen Solver durchgeführt wurden, der auf der Finite-Differenzen Methode basiert und der das STT unter Verwendung des Slonczewski-Ausdrucks berücksichtigt. Der Solver wird erweitert, um das Ausführen von Schaltsimulationen mit drei verschiedenen Ansätzen zu ermöglichen: mit gleichmäßig verteilter und konstanter Stromdichte, mit realistischer ungleichmäßig verteilter Stromdichte und konstantem Gesamtstrom und mit konstanter Spannung. Die Gültigkeit der Beschreibung mit der festen Stromdichte zur Abschätzung der Schaltzeit wird durch Vergleich der Ergebnisse mit denen der anderen zwei Ansätze getestet. Die Abhängigkeit der Schaltzeit von mehreren Systemparametern wird analysiert, was zeigte, dass eine Korrektur des Werts des angelegten Stroms es ermöglicht, dass alle Ansätze vergleichbare Ergebnisse liefern.

Um Drehmomente jenseits der Slonczewski-Näherung der Grenzfläche in zusammengesetzten Schichtstrukturen genau zu bewerten, die aus mehreren ferromagnetischen Teilen bestehen und die durch nichtmagnetische Metallabstandshalter und Tunnelbarrieren getrennt sind, wird ein Ansatz in einem Finite-Elemente-basierten Rahmenwerk übernommen und implementiert, der auf der Lösung gekoppelter Spin- und Ladungstransportgleichungen zur Bestimmung der Nichtgleichgewichtsspinakku-

Die approbierte gedruckte Originalversion dieser Dissertation ist an der TU Wien Bibliothek verfügbar.
The approved original version of this doctoral thesis is available in print at TU Wien Bibliothek.
TU WIEN Bibliothek Your knowledge hub

mulation basiert ist. Der Formalismus wird erweitert, um den Transport durch magnetische Tunnelkontakte zu beschreiben. Der magnetoresistive Tunneleffekt (TMR) wird miteinbezogen, indem die Tunnelbarriere als schlechter Leiter modelliert wird, deren Leitfähigkeit lokal abhängig von der relativen Magnetisierungsorientierung der ferromagnetischen Schichten ist. Die Polarisation des Tunnelspinstroms wird über geeignete Randbedingungen an der Grenzfläche zwischen Oxid und ferromagnetischer Schicht berücksichtigt. Der vorgeschlagene Ansatz reproduziert Winkel- und Spannungsabhängigkeiten des in MTJs ausgeübten Drehmoments erfolgreich und ermöglicht die Bewertung des Zusammenspiels zwischen die Drehmomentquellen der Grenzfläche und des Bulks. Der Ansatz wird auf Schaltsimulationen und das Design ultraskalierter STT-MRAM-Zellen erfolgreich angewendet.

Die approbierte gedruckte Originalversion dieser Dissertation ist an der TU Wien Bibliothek verfügbar.
The approved original version of this doctoral thesis is available in print at TU Wien Bibliothek.
TU WIEN Bibliothek Your knowledge hub

Sommario

La non volatilità è una soluzione emergente per le perdite di potenza in stand-by causate dal ridimensionamento dei tradizionali componenti a semiconduttore. La memoria ad accesso casuale magnetoresistiva a torsione da trasferimento di spin (STT-MRAM) è un valido candidato non volatile, grazie alla sua struttura semplice e alla compatibilità con la tecnologia CMOS. Possiede alta velocità ed eccellente durabilità, risultando quindi promettente per applicazioni che vanno dall'IoT e dagli usi automobilistici alla DRAM incorporata e alle cache di ultimo livello. Strumenti di simulazione accurati offrono informazioni preziose nella progettazione di dispositivi STT-MRAM. La descrizione dell'evoluzione temporale della magnetizzazione è fornita dall'equazione di Landau-Lifshitz-Gilbert (LLG). L'equazione LLG può essere arricchita con termini che descrivono la torsione generata da una corrente elettrica che scorre attraverso il dispositivo, responsabile delle operazioni di STT-MRAM. Questa tesi si concentra sullo sviluppo e la calibrazione di approcci di simulazione per descrivere le fonti di torsione che agiscono nei dispositivi STT-MRAM.

In primo luogo, un risolutore ad uso interno basato sul metodo delle differenze finite, con il contributo di STT incluso utilizzando l'espressione di Slonczewski, è generalizzato per eseguire simulazioni di switching di una cella MRAM. Il risolutore è aggiornato per consentire l'esecuzione di simulazioni di switching con tre diversi approcci: con densità di corrente uniforme e costante, con una più realistica densità di corrente non uniforme e corrente totale costante, e con tensione costante. La validità della descrizione con la densità di corrente fissa per la stima del tempo di switching è verificata confrontando i suoi risultati con gli altri due approcci. È inoltre valutata la dipendenza del tempo di switching da diversi parametri del sistema, dimostrando che una correzione sul valore della corrente applicata permette di ottenere risultati compatibili con tutti e tre gli approcci.

Per valutare con precisione la torsione, andando oltre l'approssimazione di Slonczewski all'interfaccia, in strutture stratificate composite costituite da diverse sezioni ferromagnetiche separate da distanziatori metallici non magnetici e barriere a effeto tunnel, è utilizzato un approccio basato sulla soluzione delle equazioni di trasporto di spin e carica per determinare l'accumulo di spin, implementato in un framework basato sul metodo agli elementi finiti. Il formalismo è esteso per descrivere il trasporto attraverso giunzioni a effetto tunnel magnetiche. L'effetto della tunnel magnetoresistance (TMR) è incluso modellando la barriera ad effetto tunnel come un

Die approbierte gedruckte Originalversion dieser Dissertation ist an der TU Wien Bibliothek verfügbar.
The approved original version of this doctoral thesis is available in print at TU Wien Bibliothek.
TU Bibliothek WIEN Your knowledge hub

cattivo conduttore, la cui conduttività dipende localmente dall'orientazione relativa della magnetizzazione negli strati ferromagnetici. La polarizzazione della corrente di spin trasmessa per effetto tunnel è inclusa tramite opportune condizioni al contorno all'interfaccia tra ossido e strati ferromagnetici. L'approccio proposto riproduce con successo la dipendenza, sia angolare che dalla tensione applicata, della torsione presente nelle MTJ, e consente di valutare l'interazione tra le sorgenti di torsione all'interfaccia e nel bulk. L'approccio è applicatio con successo a simulazioni di switching e design di celle STT-MRAM ultra ridimensionate.

Die approbierte gedruckte Originalversion dieser Dissertation ist an der TU Wien Bibliothek verfügbar.
The approved original version of this doctoral thesis is available in print at TU Wien Bibliothek.
TU WIEN Bibliothek Your knowledge hub

Acknowledgement

I would like to thank Dr. Viktor Sverdlov for the great opportunity to pursue a doctorate under his supervision, for his patience, guidance and support throughout my stay at the Institute of Microelectronics, and for his very successful approach to unite the demands of industry and research in the Christian Doppler Laboratory for Nonvolatile Magnetoresistive Memory and Logic.

I would like to express my gratitude to Prof. Siegfried Selberherr, who founded the Institute more than 30 years ago, for providing his full support and guidance on all my efforts and for always maintaining an excellent working environment.

I thank my colleagues of the Christian Doppler Laboratory for Nonvolatile Magnetoresistive Memory and Logic Roberto, Johannes, Tomáš, Nils, Mario and Wilton for their friendship, help, and for the always interesting discussions. Furthermore, I would like to also thank Wolfgang Goes for the successful collaboration with our Laboratory.

I thank all the staff of the Institute for Microelectronics for making the years together a very enjoyable experience. In particular, I would like to thank Diana for the constant support on all bureaucratic matters, and Cerv for the help on fixing issues with my computer.

I would like to thank my family, for their unfaltering support during all my studies which allowed me to be where I am now, and all my friends, for always being there for me.

Finally, I would like to give a special thanks to Valeria, my beloved wife, for her constant support and encouragement, especially during the long pandemic months. Without her, everything would have been much harder.

Die approbierte gedruckte Originalversion dieser Dissertation ist an der TU Wien Bibliothek verfügbar.
The approved original version of this doctoral thesis is available in print at TU Wien Bibliothek.
TU WIEN Bibliothek Your knowledge hub

Die approbierte gedruckte Originalversion dieser Dissertation ist an der TU Wien Bibliothek verfügbar.
The approved original version of this doctoral thesis is available in print at TU Wien Bibliothek.
TU WIEN Bibliothek Your knowledge hub

Contents

Abstract iii

Kurzfassung v

Sommario vii

Acknowledgement ix

List of Abbreviations xv

List of Symbols xvii

List of Figures xix

List of Tables xxiii

1 Motivation and Goals 1
1.1 Outline of the Thesis 3
1.2 Research Setting 4

2 Spin-Transfer Torque MRAM 5
2.1 Magnetoresistive RAM Working Principle 6
2.2 Magnetoresistance 7
2.3 Spin-Transfer Torque Writing 9

3 Micromagnetics Modeling 13
3.1 Landau Lifshitz Gilbert Equation 13
3.2 Effective Field 16
3.2.1 Exchange Field 17
3.2.2 Anisotropy Field 17
3.2.3 External Field 21
3.2.4 Demagnetizing Field 21
3.2.5 Ampere Field 22
3.2.6 Thermal Field 23
3.3 LLG Constraints 24
3.4 Spin Transfer Torque 24

TU WIEN Bibliothek Your knowledge hub
Die approbierte gedruckte Originalversion dieser Dissertation ist an der TU Wien Bibliothek verfügbar.
The approved original version of this doctoral thesis is available in print at TU Wien Bibliothek.

4 Charge Current Redistribution and Finite Difference Implementation of the LLG Equation 29
4.1 Nonuniform Current Density Distribution 30
4.2 Finite Difference Implementation of the LLG Equation 35
4.2.1 External Field Discretization 36
4.2.2 Exchange Field Discretization 36
4.2.3 Magnetocrystalline Anisotropy Field 36
4.2.4 Demagnetizing Field 37
4.2.5 Ampere Field Discretization 38
4.2.6 Thermal Field Discretization 38
4.2.7 Current Density Approaches 38
4.2.8 Time Discretization 39

5 Switching Simulations of Perpendicular STT-MRAM Under Fixed Voltage and Fixed Current Approaches 41
5.1 Switching Realizations 42
5.2 Switching Time Comparison 45
5.3 Study of the Current Correction Dependencies 47
5.3.1 Dependence on the TMR at Room Temperature 47
5.3.2 Dependence on the TMR at Zero Temperature 48
5.3.3 Macrospin Approximation 49
5.3.4 Dependence on the Surface and Resistance Area 51

6 Spin and Charge Drift-Diffusion for the Computation of Spin Torques and Finite Element Implementation 55
6.1 Spin and Charge Drift-Diffusion 56
6.1.1 Spin Dephasing Term 58
6.2 Finite Element Implementation 65
6.2.1 The Finite Element Method 65
6.2.2 Weak Formulation of the Micromagnetic Equations 69

7 Charge Current Redistribution and MTJ Torque Magnitude in the Finite Element Drift-Diffusion Formalism 73
7.1 Reproduction of the TMR Effect 73
7.2 Finite Element Solution for the Spin Accumulation 76
7.3 Torque Evaluation in Spin-Valve Structures 80
7.4 Parameters Investigation for Reproducing the Torque in MTJs 82
7.4.1 Limitations of the Effective Parameters' Approach 91

8 Tunneling Spin Current in the Drift-Diffusion Formalism and Applications to Ultra-Scaled MRAM Switching Simulations 93
8.1 Spin Drift-Diffusion Extension to Include MTJ Properties 93
8.1.1 Spin Accumulation and Spin Torque Solutions 96
8.1.2 Voltage Dependence of the Spin Torques and TMR 98
8.2 GMR Effect in Spin-Valves 99

Die approbierte gedruckte Originalversion dieser Dissertation ist an der TU Wien Bibliothek verfügbar.
The approved original version of this doctoral thesis is available in print at TU Wien Bibliothek.
TU WIEN Bibliothek Your knowledge hub

8.3 Torques in Elongated Ultra-Scaled Devices 102
8.4 Switching Simulations of Ultra-Scaled MRAM Devices 108
8.5 Ballistic Spin Current Terms 112

9 Summary and Outlook 115

A Analytical Solution 119
A.1 Five Layers N1|F1|C|F2|N2 120
A.1.1 Interface N1|F1 120
A.1.2 Interface F1|C 121
A.1.3 Interface C|F2 122
A.1.4 Interface F2|N2 123
A.2 Tunneling Spin Current 123
A.2.1 Interface F1|C 124
A.2.2 Interface C|F2 124
A.3 Ballistic Spin Current 125
A.3.1 Interface N1|F1 125
A.3.2 Interface F1|C 126
A.3.3 Interface C|F2 126
A.3.4 Interface F2|N2 127

Die approbierte gedruckte Originalversion dieser Dissertation ist an der TU Wien Bibliothek verfügbar.
The approved original version of this doctoral thesis is available in print at TU Wien Bibliothek.
TU WIEN Bibliothek Your knowledge hub

Die approbierte gedruckte Originalversion dieser Dissertation ist an der TU Wien Bibliothek verfügbar.
The approved original version of this doctoral thesis is available in print at TU Wien Bibliothek.
TU WIEN Bibliothek Your knowledge hub

List of Abbreviations

RAM	Random-access memory
SRAM	Static random-access memory
DRAM	Dynamic random-access memory
MRAM	Magnetoresistive random-access memory
STT	Spin-transfer torque
MTJ	Magnetic tunnel junction
FM	Ferromagnetic
NM	Nonmagnetic
AFM	Antiferromagnetic
TB	Tunnel barrier
RL	Reference layer
FL	Free layer
P	Parallel
AP	Anti-parallel
LLG	Landau-Lifshitz-Gilbert
GMR	Giant magnetoresistance
TMR	Tunnel magnetoresistance
FE	Finite element
FD	Finite difference
PL	Pinning layer
NMS	Nonmagnetic and conductive spacer
AMR	Anisotropic magnetoresistance
DOS	Density of states
pMTJ	Perpendicular magnetic tunnel junction
DD	Drift-Diffusion
PDE	Partial differential equation
DL	Damping-like
FL	Field-like
ZL	Zhang-Li

Die approbierte gedruckte Originalversion dieser Dissertation ist an der TU Wien Bibliothek verfügbar.
The approved original version of this doctoral thesis is available in print at TU Wien Bibliothek.
TU Bibliothek WIEN Your knowledge hub

Die approbierte gedruckte Originalversion dieser Dissertation ist an der TU Wien Bibliothek verfügbar.
The approved original version of this doctoral thesis is available in print at TU Wien Bibliothek.
TU WIEN Bibliothek Your knowledge hub

List of Symbols

$_{\mathrm{S}}$ (A/m)	Saturation magnetization
(N/A)	Vacuum permeability
(rad/(T s))	Gyromagnetic ratio
(C)	Elementary charge
(J s)	Planck constant
$\hbar$ (J s)	Reduced Planck constant
$_{B}$ (J/T)	Bohr magneton
	Electron g-factor
	Gilbert damping constant
	Spin-transfer torque efficiency
	Unit magnetization vector
= (m/(A s))	Rescaled gyromagnetic ratio
(J/m)	Exchange coefficient
(J/m)	Anisotropy coefficient
$_{\mathrm{int}}$ (J/m)	Interface anisotropy coefficient
$_{\mathrm{eff}}$ (A/m)	Effective magnetic field vector
$_{\mathrm{C}}$ (A/m)	Charge current vector
$_{\mathrm{C}}$ (A)	Total charge current
$_{\mathrm{S}}$ (A/(m s))	Spin torque vector
	Slonczewski polarization factor
(V/m)	Electric field vector
(S/m)	Electrical conductivity
(S)	Elctrical conductance
( )	Electrical resistance
(V)	Electrical potential
(A/m)	Spin accumulation vector
$_{\mathrm{e}}$ (m /s)	Electron diffusion coefficient
$_{\mathrm{J}}$ (m)	Exchange length
$_{\varphi}$ (m)	Dephasing length
$_{\sigma}$	Conductivity polarization
$_{\mathrm{D}}$	Diffusion polarization
$_{\mathrm{S}}$ (A/s)	Spin current polarization density tensor
$_{\mathrm{sf}}$ (m)	Spin-flip length
(m)	Momentum relaxation length
$_{\mathrm{S}}$ (m /s)	Diffusion coefficient in the TB

Die approbierte gedruckte Originalversion dieser Dissertation ist an der TU Wien Bibliothek verfügbar.
The approved original version of this doctoral thesis is available in print at TU Wien Bibliothek.
TU WIEN Bibliothek Your knowledge hub

	In-plane torque reduction
η	Out-of-plane polarization

Die approbierte gedruckte Originalversion dieser Dissertation ist an der TU Wien Bibliothek verfügbar.
The approved original version of this doctoral thesis is available in print at TU Wien Bibliothek.
TU WIEN Bibliothek Your knowledge hub

List of Figures

1.1 MTJ structure. . . . 2
1.2 Model examples of elongated ultra-scaled MRAM cells. . . . 3

2.1 Schematization of the GMR effect in spin valves. . . . 7
2.2 Schematization of the TMR effect in MTJs. . . . 8
2.3 MRAM structures for field-assisted and STT switching. . . . 10

3.1 Magnetization precession around the effective field, without damping. 14
3.2 Magnetization trajectory prescribed by the LLG equation. . . . 15
3.3 Projection on the unit sphere of the uniaxial anisotropy function. . . 18
3.4 Projection on the unit sphere of the planar anisotropy function. . . . 19
3.5 Projection on the unit sphere of the cubic anisotropy function. . . . 20
3.6 Magnetization trajectory in the presence of spin-transfer torque. . . 25
3.7 Schematic representation of an STT-MRAM cell. . . . 26
3.8 Angular dependence of the Slonczewski damping-like torque. . . . 27

4.1 MTJ structure with nonuniform magnetization distribution in the FL. 31
4.2 Current density in a two-dimensional MTJ with nonuniform magnetization. . . . 33
4.3 Current density in a three-dimensional MTJ with nonuniform magnetization. . . . 35
4.4 Flowchart of the FD solver. . . . 39

5.1 Schemtic representation of the simulated pMTJ stack. . . . 42
5.2 Time evolution of the magnetization during switching. . . . 43
5.3 Snapshots of the free layer magnetization vectors during the switching process. . . . 44
5.4 Thermal field effect on ten switching realizations. . . . 45
5.5 Switching realizations for the three different current density approaches. . . . 46
5.6 Comparison between AP to P and P to AP switching times at T=300 K. . . . 47
5.7 Comparison of switching times for the tuned values of input currents at T=300 K. . . . 47
5.8 Dependence of the current correction on the TMR at T=300 K 48
5.9 Dependence of the current correction on the TMR at T=0 K 48

Die approbierte gedruckte Originalversion dieser Dissertation ist an der TU Wien Bibliothek verfügbar.
The approved original version of this doctoral thesis is available in print at TU Wien Bibliothek.
TU WIEN Bibliothek Your knowledge hub

5.10 Comaprison between swicthing realizations at T=0 K and T=300 K. 49
5.11 Switching time as a function of the TMR at T=0 K and T=300 K. . 49
5.12 Macrospin switching realizations at fixed voltage and fixed current, for several values of the correction. 50
5.13 Dependence of the correction on the switching time in the macrospin scenario. 50
5.14 Comparison between switching realizations at different surface areas. 52
5.15 Dependence of the current correction on the surface area. 52
5.16 Dependence of the current correction on the resistance area of the structure. 52

6.1 Representation of the finite element approxiamtion in a one-dimensional setting. 68
6.2 Flowchart of the FE solver. 70

7.1 Results obtained through the FE solver for the charge current. . . . 75
7.2 Current density distribution through a cylindrical MTJ stack. 76
7.3 Comparison of FE and analytical spin accumulation solutions in a single FM layer. 77
7.4 Spin current and spin torque computed from the spin accumulation in a single FM layer. 78
7.5 Spin accumulation and spin torque solutions in a spin-valve. 79
7.6 Comparison of the drift-diffusion torque in a spin-valve to the Slonczewski expression. 80
7.7 Damping-like torque in a structure including a PL. 81
7.8 Spin accumulation solution with different values of the diffusion coefficient in the TB. 83
7.9 Spin accumulation in the presence of long NM contacts. 84
7.10 Dependence of the average torques acting on the FL on various system parameters. 85
7.11 Dependence of the average damping-like torques acting on the FL on various combinations of system parameters. 87
7.12 Dependence of the torque on the FL and RL polarization parameters. 88
7.13 Results for spin accumulation and torques with an updated set of parameters. 89
7.14 Spin accumulation computed with non-uniform magnetization configuration. 90
7.15 Torque obtained combining multiple analytical solutions compared to the one obtained by the FE solver. 90
7.16 Angular dependence of the DL torque acting on a semi-infinite FL based on the drift-diffusion approach and on the Slonczewski expression. 91

8.1 Spin accumulation and torque computed with the inclusion of the tunneling spin current. 96

Die approbierte gedruckte Originalversion dieser Dissertation ist an der TU Wien Bibliothek verfügbar.
The approved original version of this doctoral thesis is available in print at TU Wien Bibliothek.
TU WIEN Bibliothek Your knowledge hub

8.2 Angular dependence of the torque with the spin-current boundary conditions. . . . 96
8.3 Spin accumulation and torque in a symmetric MTJ structure including NM contacts. . . . 97
8.4 Bias dependence of resistance and torque compared with experimental results. . . . 98
8.5 Comparison of the spin accumulation obtained through the direct and iterative approaches. . . . 101
8.6 Angular dependence of the charge current in a spin-valve and in an MTJ. . . . 101
8.7 Comparison of the spin torque to the Zhang-Li one for long magnetization texture. . . . 103
8.8 Comparison of the spin torque to the Zhang-Li one for short magnetization texture and different dephasing lengths. . . . 103
8.9 Torque computed for a structure with elongated FL presenting a magnetization texture. . . . 105
8.10 Torque computed in a single FM layer in the presence of a domain wall. 106
8.11 Spin currents and torques generated for the magnetization in the FL going from the +x- to the -x-direction over a domain wall. . . . 107
8.12 Spin currents and torques generated for the magnetization in the FL going from the -x- to the +x-direction over a domain wall. . . . 107
8.13 Switching results for structures with elongated and composite FLs. . 109
8.14 Switching stages of an ultra-scaled STT-MRAM cell with composite FL. . . . 110
8.15 Visual representation of the torques acting during switching of an MRAM cell with composite FL. . . . 110
8.16 Switching results for a structure with three FL segments. . . . 112
8.17 Torque computed with the inclusion of ballistic corrections to the spin current. . . . 113

Die approbierte gedruckte Originalversion dieser Dissertation ist an der TU Wien Bibliothek verfügbar.
The approved original version of this doctoral thesis is available in print at TU Wien Bibliothek.
TU Bibliothek Your knowledge hub WIEN

Die approbierte gedruckte Originalversion dieser Dissertation ist an der TU Wien Bibliothek verfügbar.
The approved original version of this doctoral thesis is available in print at TU Wien Bibliothek.
TU Bibliothek Your knowledge hub WIEN

List of Tables

5.1 Parameters employed for the FD switching simulations. 42

7.1 Parameters used in the drift-diffusion simulations. 77
7.2 Modified parameters used to reproduce the Slonczewski torque magnitude. 89

8.1 Parameters used in the DD simulations with the TB boundary terms. 95
8.2 Parameters employed for reproducing the experimental bias depenndence. 98
8.3 Parameters used for the structure with elongated FL. 105

Die approbierte gedruckte Originalversion dieser Dissertation ist an der TU Wien Bibliothek verfügbar.
The approved original version of this doctoral thesis is available in print at TU Wien Bibliothek.
TU WIEN Bibliothek Your knowledge hub

Die approbierte gedruckte Originalversion dieser Dissertation ist an der TU Wien Bibliothek verfügbar.
The approved original version of this doctoral thesis is available in print at TU Wien Bibliothek.
TU WIEN Bibliothek Your knowledge hub

Chapter 1

Motivation and Goals

Die approbierte gedruckte Originalversion dieser Dissertation ist an der TU Wien Bibliothek verfügbar.
The approved original version of this doctoral thesis is available in print at TU Wien Bibliothek.
TU Bibliothek Your knowledge hub WIEN

Recent outstanding improvements in the development of computer memories have been possible thanks to the down-scaling of semiconductor devices. This, however, has increased the stand-by power consumption of traditional volatile components, such as static and dynamic random-access memory (SRAM and DRAM, respectively), especially due to the presence of leakage currents [1]. By introducing nonvolatile memory components, stand-by power consumption can be mitigated, as they do not require refreshing of the memory bits. While being a valuable candidate, nonvolatile flash memories have poor endurance and are also becoming increasingly complex and expensive to downscale for embedded application [2]. Moreover, the price for a gigabit of traditional flash memories does not follow the down-scaling of the technology node, as it ceased to decrease. These factors prompt emerging memories entering the market to replace NOR flash, SRAM, and DRAM for stand-alone and embedded applications. Spin-transfer torque magnetoresistive random-access memory (STT-MRAM) is a nonvolatile memory which possesses a simple structure and whose fabrication is compatible with CMOS processing. Instead of relying on charge for storing information, MRAM is based on the electron's spin. In contrast to traditional flash memory, STT-MRAM presents good speed and high endurance. This makes it particularly attractive for both, stand-alone as well as embedded applications, for example, in Systems-on-Chip, where STT-MRAM is poised to replace SRAM and flash memory [2–11].

The core of modern STT-MRAM cells consists of a magnetic tunnel junction (MTJ), a sandwich of two ferromagnetic (FM) layers separated by a tunnel barrier (TB), see Fig. 1.1. The FM layers are referred to as reference layer (RL) and free layer (FL). The RL is fixed either by proper choice of materials, or by antiferromagnetic coupling to an additional ferromagnetic pinning layer, while the magnetization of the FL can be reversed. The use of MTJs with perpendicular magnetic anisotropy (PMA) permits to obtain better thermal stability, better scalability, and a lower switching current [12].

When the magnetization vectors are in the parallel (P) state, the electrical resistance is lower than in the anti-parallel (AP) state, providing a way to store binary information. Switching between these two stable configurations can be achieved by letting an electric current flow through the structure. Electrons tunneling from the

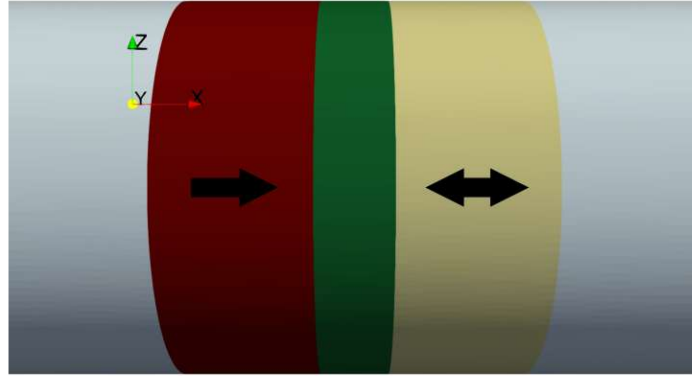

Figure 1.1: MTJ structure with the inclusion of NM contacts (light blue). The structure is composed of a reference layer (red), a tunnel barrier (green) and a free layer (yellow). The RL magnetization is fixed, while the magnetization in the FL is free to move. The figure is adapted from [13].

fixed RL become spin-polarized, generating a spin current. When entering the FL, the non-equilibrium spin accumulation acts on the magnetization via the exchange interaction. When the magnetization vectors are not aligned, the transverse spin current components are quickly absorbed, generating the spin-transfer torque through conservation of angular momentum [14, 15]. If the current is sufficiently strong, the magnetization of the free layer can be switched between the two stable P and AP configurations, relative to the RL.

The development of accurate simulation tools is essential in helping the design of efficient devices. Modeling of STT switching, which allows to describe the writing process of an STT-MRAM cell, requires a solution of the time-dependent Landau-Lifshitz-Gilbert (LLG) equation with the inclusion of a term describing the torque acting on the magnetization. Such a task can be performed by assuming a Slonczewski-like torque approach [16]. In micromagnetic modeling of STT switching, the typical simplified approach is to assume that the current density is position- and time-independent [17]. In circuits, however, it is often the voltage, rather than the current density, that remains fixed during switching. The resistance of the tunnel junction depends on the relative magnetization alignment of the free and the reference layer, so the current through the structure is not constant during the process. Moreover, as the magnetization of the FL is not uniform at switching, but depends on the position, so does the local tunneling conductance. The assumption of a constant current density is violated, especially in advanced MTJs with a tunnel magnetoresistance (TMR) ratio, characterizing the difference between P and AP resistance, of about 200% and higher [18]. It is thus important to investigate the switching behavior under fixed bias voltage and the effects of non-uniform currents, which is the focus of the first part of this thesis.

Moreover, the implementation of a Slonczewski-like torque allows to approximately simulate the magnetization dynamics of a thin FL only. Recent STT-MRAM devices rely however on structures which are increasingly complex. In order to boost

Die approbierte gedruckte Originalversion dieser Dissertation ist an der TU Wien Bibliothek verfügbar.
The approved original version of this doctoral thesis is available in print at TU Wien Bibliothek.
TU WIEN Bibliothek Your knowledge hub

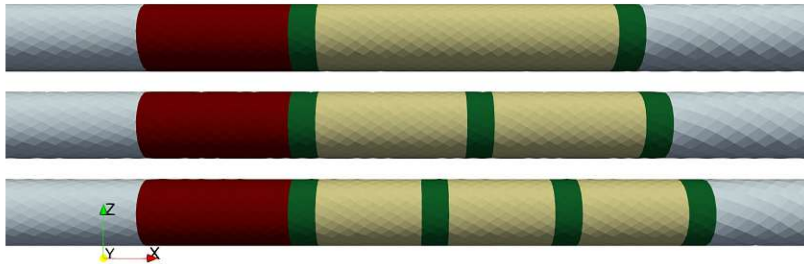

Figure 1.2: Model examples of elongated ultra-scaled MRAM cells. The NM contacts are in light blue, the RL is in red, the TBs are in green, and the FL segments are in yellow. The figure was published in [13].

the PMA provided by the interface between CoFeB and crystalline MgO, the FL is often capped with a second MgO layer [19]. Recently, more advanced structures were proposed to boost the PMA even further, either by introducing more MgO layers in the FL or using the shape anisotropy of elongated FLs [20–22], while also improving scalability thanks to a reduced diameter. Accurate simulation tools can provide valuable support in the design of these ultra-scaled MRAM cells, exemplified in Fig. 1.2. In order to model such devices, it is paramount to generalize the traditional Slonczewski approach to incorporate normal metal buffers or MgO barriers between multiple CoFeB FL segments, as well as the barrier between RL and FL, and the torques coming from magnetization textures or domain walls that can be generated in elongated FLs. A more complete description of the process can be achieved by computing the non-equilibrium spin accumulation across the whole structure. In a spin-valve structure with a non-magnetic spacer layer, this successfully accomplished by solving the spin and charge drift-diffusion equations, both in a finite element (FE) [23, 24] and finite difference (FD) setting [25]. Inclusion of the MTJ properties is needed in order to describe modern MRAM devices in the drift-diffusion formalism, and to be able to apply it to switching simulations of ultra-scaled MRAM cells. The second part of this thesis focuses on extending the drift-diffusion formalism, implemented in a FE solver based on open-source software, to account for transport properties of MTJs.

1.1 Outline of the Thesis

This thesis is devoted to the employment and development of simulation tools capable of handling the different sources of torques acting in STT-MRAM devices, in order to be able to predict their switching behavior. The software used to produce the results reported in this work is based on C++ libraries.

Chapter 2 gives a brief overview of the development and state of the art of modern STT-MRAM cells.

Die approbierte gedruckte Originalversion dieser Dissertation ist an der TU Wien Bibliothek verfügbar.
The approved original version of this doctoral thesis is available in print at TU Wien Bibliothek.
TU WIEN Bibliothek Your knowledge hub

In Chapter 3, a summary of the derivation of the LLG equation for simulating the magnetization dynamics is reported, together with a description of the most prominent contributions to the effective field therein. Moreover, simplified expressions for the spin-transfer torque acting in both spin-valves and MTJs are provided.

Chapter 4 focuses first on the computation of the current density redistribution in an MTJ with non-uniform magnetization. Then, the FD implementation of the LLG equation, employed by an in-house solver, is described, and is updated with fixed current density, fixed total current, and fixed voltage approaches to the torque term.

Chapter 5 reports the results obtained by comparing switching simulations performed with the three different approaches to the torque term, showing how a correction to the current value in the fixed current approaches is able to generate compatible results in all three models.

In Chapter 6, a brief description of the spin and charge drift-diffusion formalism, providing a more general expression for the torque, is reported. Moreover, an FE implementation of the coupled LLG and drift-diffusion equations is described.

In Chapter 7, a way to deal with the TMR effect in the scope of the drift-diffusion formalism is derived. The implemented software is employed to study the torque dependence on the system parameters, in order to reproduce the torque magnitude expected in MTJs.

In Chapter 8, an extension of the drift-diffusion formalism to account for the polarized tunneling spin-current is derived. The approach is shown to be capable of reproducing the torque properties expected in MTJs. The updated equations, capable of predicting interactions between different sources of torque, are then applied to perform switching simulations in recently proposed ultra-scaled MRAM cells. Moreover, by computing a solution to the drift-diffusion equations based on analytical expressions in the presence of ballistic corrections to the spin current, it is shown how a more complex oscillatory behavior of the torque can be reproduced.

Finally, Chapter 9 reports a summary of the main results of the thesis.

The equations employed to derive a solution for the spin accumulation with analytical expressions are reported in Appendix A.

1.2 Research Setting

The research presented in this dissertation was conducted within the scope of the Christian Doppler Laboratory for Nonvolatile Magnetoresistive Memory and Logic (NOVOMEMLOG). The Christian Doppler Association promotes the cooperation between research institutions and companies pursuing application-orientated basic research. For this laboratory, the cooperation was established between the Institute for Microelectronics at the TU Wien and Silvaco Inc., a company developing and providing electronic device automation and software tools for Technology Computer-Aided Design (TCAD) .

Die approbierte gedruckte Originalversion dieser Dissertation ist an der TU Wien Bibliothek verfügbar.
The approved original version of this doctoral thesis is available in print at TU Wien Bibliothek.
TU WIEN Bibliothek Your knowledge hub

Chapter 2

Spin-Transfer Torque MRAM

Die approbierte gedruckte Originalversion dieser Dissertation ist an der TU Wien Bibliothek verfügbar.
The approved original version of this doctoral thesis is available in print at TU Wien Bibliothek.
TU WIEN Bibliothek Your knowledge hub

The following chapter gives a brief overview of the development and working principles of MRAM, with particular focus on STT-MRAM. The contents are mostly based on the review papers [26], [27], and [28].

The history of random access memory began in the middle of the 20th century, when Williams Kilburn developed a system to store bits as electrically charged spots on the face of a cathode-ray tube [29]. In the 1950s, this early memory technology was replaced by magnetic core memories, where the data was stored in the rotation sense of an array of magnetic rings [30]. Magnetic core memories were largely employed for about two decades, until they were replaced by dynamic random access memory, based on newly developed semiconductor technology. The new memory provided increased scalability, could be easily mass-manufactured and could be employed in the then-emerging integrated chips [31].

Interest in a magnetic approach to RAM grew again with the discovery of the giant magnetoresistance (GMR) effect in 1988 [32, 33]. The effect arises in a cell composed of two ferromagnetic layers with a nonmagnetic conductive metal between them. It describes the difference in the resistance when the magnetic moments of the two layers are parallel or anti-parallel to each other, with the parallel orientation having lower resistance. The higher the resistance ratio, the better the signal, enabling an easier detection of the written bits. The invention of magnetic tunnel junctions, where the effect is labeled tunnel magnetoresistance due to the underlying tunneling process, boosted research efforts in MRAM devices even further [34–39], thanks especially to the high TMR granted by using crystalline magnesium oxide as the tunneling layer [40–45]. First applications involving the GMR or TMR effect, however, relied on an external field to achieve switching of the magnetization direction, which prevents the scalability of the technology to small sizes and its application to high-density devices.

Such issue was overcome by the discovery of spin-transfer torque assisted switching. Magnetization reversal in STT-MRAM is achieved through purely electrical means, making it CMOS compatible and allowing a potentially faster switching capability, reliability, and scalability for future applications [14, 15, 46–50]. Thanks to

these properties, research aimed at improving STT-MRAM to broaden its application range has been growing steadily and is still ongoing [2–8, 51].

2.1 Magnetoresistive RAM Working Principle

Magnetoresistive random access memory is a nonvolatile memory based on the magnetoresistance principle. The resistance dependence on the magnetization state is used as a way to retrieve the bit information, while the magnetic anisotropy energy is employed to retain the information. MRAM based devices have recently been released for niche applications, and researchers believe that MRAM could possibly replace SRAM and DRAM as technology progresses [1, 52].

The first storage element used in MRAM was based on the GMR effect in a spin valve structure, which mainly consists of two ferromagnetic layers sandwiching a nonmagnetic conductive layer. The two FM layers are called the free layer and the reference layer, respectively. An antiferromagnetic (AFM) layer can be employed in proximity of or in contact with the RL in order to pin its magnetization direction, which should not be reversed during the operation of the memory device. For better functionality, a pinning layer (PL), antiferromagnetically coupled to the RL, can be employed to reduce the stray field, which may affect the FL stability.

More recent developments focus on the TMR effect in magnetic tunnel junctions, because of their superior reading signals. An MTJ cell consists of a thin layer of an insulating material, sandwiched by two ferromagnetic layers. Similar to a spin valve, the resistance states can be high (anti-parallel configuration) or low (parallel configuration), based on the relative orientation of the magnetizations in the RL and FL. MTJs have been the predominant storage element in MRAMs for the past decade, as they provide a difference between the resistance states significant enough to be suitable for RAM applications.

In an MRAM cell, the magnetization direction of the RL is fixed and only the one of the FL varies to store '0' and '1' bit states. Since the direction of the RL needs to be fixed during the switching process, it is made of materials and shapes which ensure a higher energy barrier than the one of the FL. The FL magnetic anisotropy, albeit lower than the one of the RL, still needs to guarantee retention of the magnetization state for a given amount of years (typically 10 at room temperature). Given an energy barrier $_{\mathrm{B}}$ separating the '0' and '1' states, the thermal stability factor can be expressed as [53]

$$= \frac{_{\mathrm{B}}}{_{\mathrm{B}}} \tag{2.1}$$

where $_{B}$ is the Boltzmann constant and the temperature. The energy barrier that separates the two magnetization directions can be expressed as

$$_{\mathrm{B}} = \frac{\mu \quad _{\mathrm{S}} \ _{\mathrm{K}}}{2} \tag{2.2}$$

where μ is the vacuum permeability, $_{\mathrm{S}}$ is the saturation magnetization, is the volume of the FL, and $_{\mathrm{K}}$ is the anisotropy field. For a 10 year retention on a bit

Die approbierte gedruckte Originalversion dieser Dissertation ist an der TU Wien Bibliothek verfügbar.
The approved original version of this doctoral thesis is available in print at TU Wien Bibliothek.
TU WIEN Bibliothek Your knowledge hub

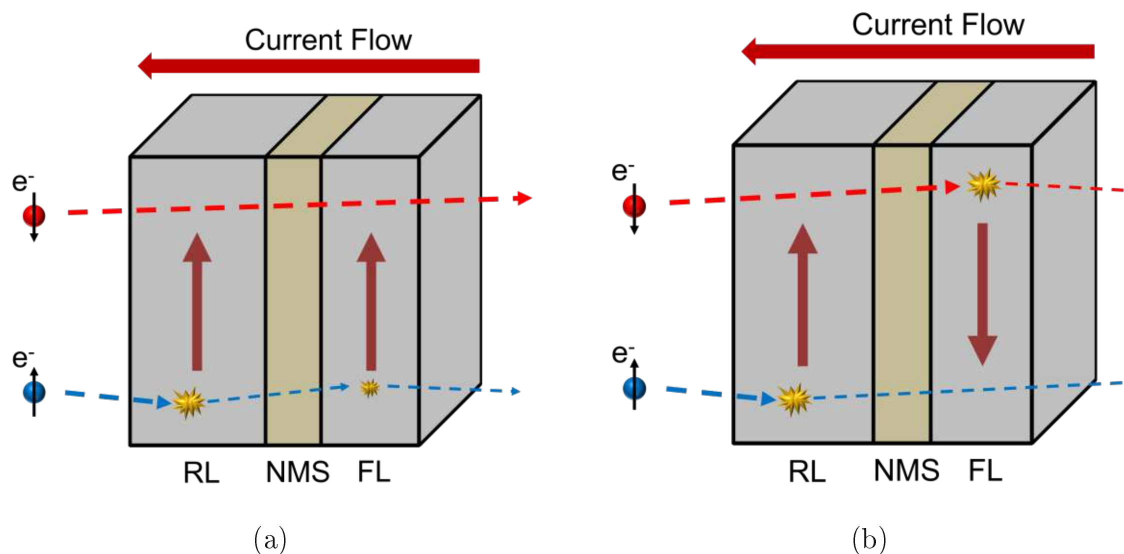

Figure 2.1: Schematization of the GMR effect in spin valves. The magnetization state of the RL and FL is indicated by the bold red arrows. NMS indicates a nonmagnetic and conductive spacer. Electrons scatter less in the parallel state (b) as compared to the anti-parallel one (a), so that the resistance of the latter is higher.

level, needs to have values of 40 or above [54], and the required value increases with the memory capacity [55].

2.2 Magnetoresistance

Being able to read information is one of the most important criteria for new memory devices. The reading process of MRAM cells is based on the magnetoresistance effect, which relates the electrical resistance of certain materials or structures on their magnetization configuration. It is essential to achieve a high magnetoresistance ratio to make the MRAM more reliable, as a higher resistance difference between different magnetization configurations allows to more easily read the state of the memory.

The discovery of the GMR effect and its application in the reading heads of hard disk drives was an important advancement, as high GMR values lead to improved reading signals compared to the ones given by the anisotropic magnetoresistance (AMR) effect [56]. The GMR effect is a consequence of spin dependent electron scattering. When the magnetic moments of two neighboring magnetic layers are aligned in an anti-parallel orientation, both the minority (spin parallel to the magnetization) and majority (spin anti-parallel to the magnetization) electrons are equally scattered when transiting through the structure. When the magnetization vectors are parallel, however, the majority electrons scatter less in comparison to the minority ones, so that a drop in the overall resistivity of the structure is observed. The process is schematized in Fig. 2.1. Spin-valve based devices relying on the GMR effect were suitable for hard disk applications. However, as the GMR ratio in these devices has

Die approbierte gedruckte Originalversion dieser Dissertation ist an der TU Wien Bibliothek verfügbar.
The approved original version of this doctoral thesis is available in print at TU Wien Bibliothek.
TU WIEN Bibliothek Your knowledge hub

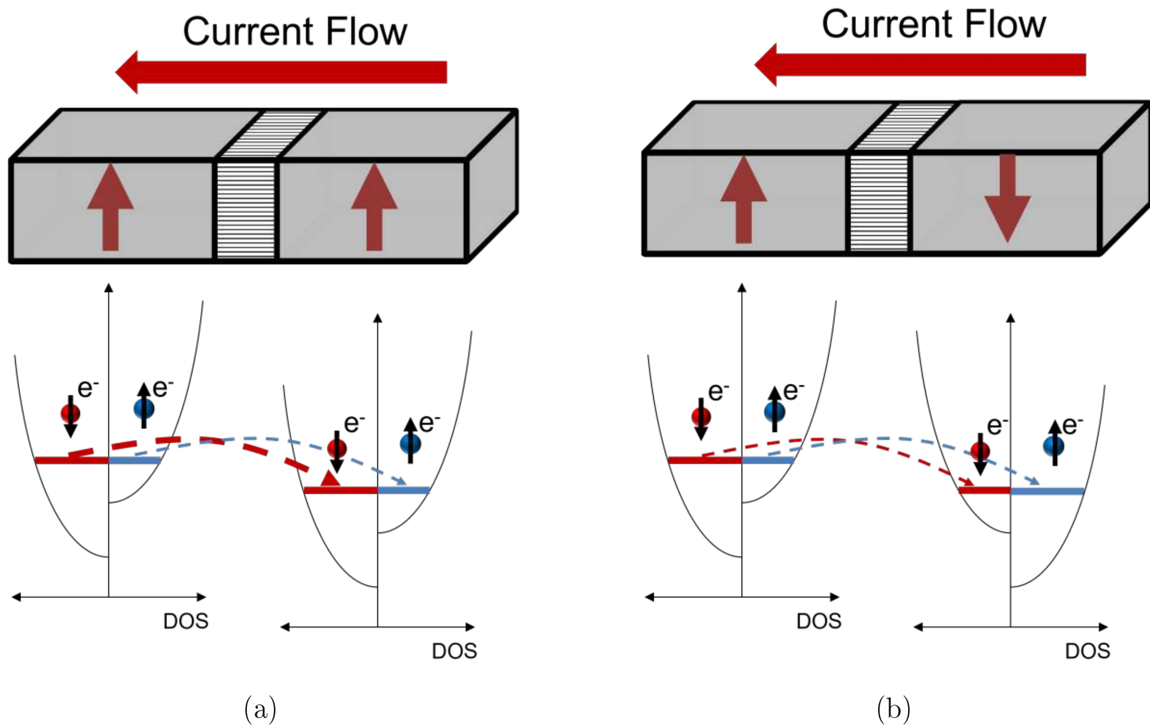

Figure 2.2: Schematization of the TMR effect in MTJs. The magnetization state of the RL and FL is indicated by the bold red arrows. Due to matching of the majority and minority bands, tunneling of the electrons is easier in the parallel state (b) as compared to the anti-parallel one (a), so that the resistance of the latter is higher.

never exceeded values of about 10–20% [57, 58], the difference between the high and low resistance states was not sufficient for MRAM applications.

The TMR effect, first reported at room temperature by Miyazaki *et al.* and Moodera *et al.* in 1995, was a major boost for MRAM applications [36, 37], with TMR values of about 20% using an amorphous Al O barrier. In the presence of such an amorphous barrier, the tunneling depends mainly on the electronic band structure of the ferromagnetic materials, and a maximum TMR value of 70% was obtained by employing Al O [59]. When using crystalline barriers, such as the ones composed of MgO, the tunneling mainly depends on electronic band matching at the interfaces between the oxide an the ferromagnetic layers. This effect was theoretically predicted in 2001 [40, 41], with experimental confirmations coming in the middle of the 2000s and showing how MgO based MTJs exhibit a higher TMR than Al O barriers [60–62]. The TMR achieved using MgO gradually increased to record high values of more than 600% in laboratory conditions at room temperature [63]. TMR values of 100–200% are readily achieved in modern devices [18], providing a sufficient resistance difference for MRAM applications.

The main component of an MRAM cell based on the TMR effect is an MTJ, where two ferromagnetic layers sandwich a very thin insulating barrier, so that electrons can tunnel through it depending on the available free electron states of the ferromagnetic

Die approbierte gedruckte Originalversion dieser Dissertation ist an der TU Wien Bibliothek verfügbar.
The approved original version of this doctoral thesis is available in print at TU Wien Bibliothek.
TU Bibliothek WIEN Your knowledge hub

layers. The resistance difference in an MTJ is caused by spin-dependent tunneling, and arises from the difference in the electronic density of states (DOS) at the Fermi level $_{\mathrm{F}}$ between spin-up and spin-down electrons. Since electrons preserve their spin orientation during the tunneling process, they can only tunnel into the band of the same spin orientation (see Fig. 2.2). A change from the parallel magnetization configuration (Fig. 2.2(a)) to the antiparallel configuration (Fig. 2.2(b)) of the two electrodes will result in a swap between the two spin bands in one of the electrodes. Consequently, a corresponding change in the conductance will be observed, as electrons will have a lower probability of tunneling when the DOS for majority and minority electrons in the two layers are not matching. The corresponding TMR ratio is defined as [26, 27]

$$= \frac{_{\mathrm{AP}} \quad _{\mathrm{P}}}{_{\mathrm{P}}} = \frac{_{\mathrm{P}} \quad _{\mathrm{AP}}}{_{\mathrm{AP}}} \tag{2.3}$$

where $_{\mathrm{AP}}$ and $_{\mathrm{P}}$ ($_{\mathrm{AP}}$ and $_{\mathrm{P}}$) are the resistances (conductances) in the AP and P state, respectively. When the relative magnetization orientations are at an angle , the conductance becomes proportional to cos as [27, 64, 65]

$$(\ ) = \frac{_P + \ _{AP}}{2} + \frac{_P \quad _{AP}}{2} \cos \quad = \frac{_P + \ _{AP}}{2}\left(1 + \frac{}{2 +} \cos \right) \tag{2.4}$$

2.3 Spin-Transfer Torque Writing

The second requirement of a memory device is that there must be a method to write data in the memory cells. The most straight-forward writing mechanism, and one of the first ones to be employed, is based on applying a magnetic field, which needs to be generated by an electric current flowing close to the MTJ. As the current density required to achieve the switching field increases when the cross-section of the line decreases [66], scaling of the memory cells towards smaller dimensions becomes troublesome. This limits the scalability of field-assisted MRAM devices (also referred to as toggle MRAM) to a size of about 90 nm [66, 67].

The predictions of STT, independently proposed by Berger and Slonczewski in 1996, paved the way for a purely electrical switching mechanism [14, 15]. The first demonstration of magnetization reversal induced by STT was presented by Katine *et al.* using a fully metallic spin valve device in 2000 [46]. The first STT-switching demonstration in MTJ-based devices was carried out by Huai, *et al.* in 2004 on tunneling junctions employing an Al O oxide layer [68], and in 2005 several demonstrations of MgO-based MRAM cells were reported [69–71]. Such devices do not need an external field, simplifying the fabrication process (see Fig. 2.3), and possess good scalability [54]. In STT-MRAM, the switching from the anti-parallel to the parallel orientation is achieved by passing an electrical current through the MTJ, with electrons going from the RL to the FL (positive current flowing from the FL to the RL). The majority electrons are able to transit through the RL and pass to the FL, generating a polarized spin current. The spin of the polarized electrons aligns almost immediately with the magnetization in the FL and, due to conservation of the angular

Die approbierte gedruckte Originalversion dieser Dissertation ist an der TU Wien Bibliothek verfügbar.
The approved original version of this doctoral thesis is available in print at TU Wien Bibliothek.
TU WIEN Bibliothek Your knowledge hub

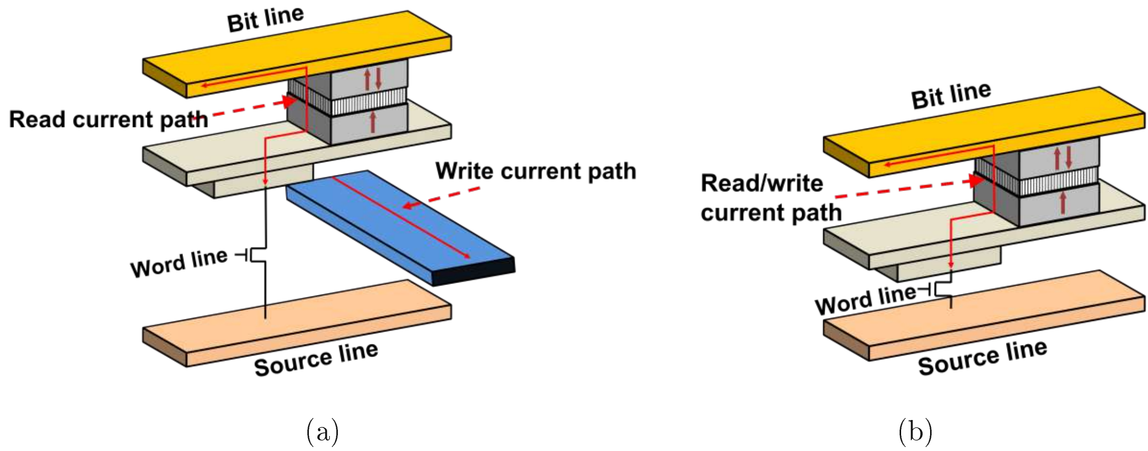

(a) (b)

Figure 2.3: Structure of MRAMs for (a) field-assisted switching and (b) STT switching. The STT mechanism allows to employ the same line for reading and writing currents, reducing the complexity of the overall architecture.

momentum, the spin current polarization change is transferred to the magnetization via the exchange interaction, providing the torque. In parallel to anti-parallel switching, electrons flow from the FL to the RL (positive current from the RL to the FL). In this case, it is the minority electrons, reflected back into the FL, that transfer their angular momentum to the magnetization and provide the torque. If the current is sufficiently strong, the magnetization of the FL can be switched between the two stable configurations, parallel or anti-parallel, relative to the reference layer. The critical current $_{\mathrm{C,0}}$ required to reverse the magnetization state of the FL at zero temperature is given by [53]

$$_{C,} = 2 \frac{}{\mu_B \; (\;)} \quad _{\mathrm{B}} = \frac{}{\mu_B} \quad _{\mathrm{S}} \quad _{\mathrm{K}} \tag{2.5}$$

where equation (2.2) was applied, and the critical current density by

$$_{\mathrm{C,0}} = \frac{_{\mathrm{C,0}}}{} = \frac{}{\mu_B \; (\;)} \quad _{\mathrm{S}} \quad _{\mathrm{K}} \quad _{\mathrm{FL}} \tag{2.6}$$

is the gyromagnetic ratio, is the elementary charge, μ_{B} is the Bohr magneton, $_{\mathrm{FL}}$ is the thickness of the FL, is the surface area of the FL, and is the Gilbert damping constant, which represents the rate at which the magnetization relaxes to its equilibrium position. ( ) is the STT efficiency parameter [14,16], which is related to the spin polarization of the injected current and the angle between the magnetization vectors in the two FM layers (see equations (3.48) and (3.49)).

Based on the storage mechanism, MRAM cells may be classified into two types; (i) in-plane MRAM, which has the magnetization of the ferromagnetic layers in the FL plane and (ii) perpendicular MRAM having the magnetization perpendicular to the FL plane [66].

In-plane MRAM was largely employed in the first generations of MRAM devices, as the magnetic fields generated in toggle MRAM lie in the plane of the films. In-plane MRAM cells are also easier to manufacture, as using an elliptic storage layer

Die approbierte gedruckte Originalversion dieser Dissertation ist an der TU Wien Bibliothek verfügbar.
The approved original version of this doctoral thesis is available in print at TU Wien Bibliothek.
TU WIEN Bibliothek Your knowledge hub

is sufficient to have a preferred orientation along the long axis, due to the shape anisotropy. The thermal stability of the FL can be enhanced by employing materials with uniaxial magnetocrystalline anisotropy. In order to keep the RL fixed, exchange bias is employed to pin the direction of the magnetization [72]. The RL is antiferromagnetically coupled to an additional magnetic PL, forming a so-called synthetic antiferromagnet (SAF). The magnetization of the PL in the SAF is pinned by direct contact with a layer of antiferromagnetic material. Such configuration allows to both boost significantly the stability of the RL, and to reduce the stray field acting on the FL [73].

In recent years, however, research interest has shifted to materials and structures possessing a perpendicular magnetic anisotropy (PMA) which enables the magnetization to have a stable configuration in the direction perpendicular to the plane of the magnetic film. Devices based on PMA present a better thermal stability and scalability, as well as a lower switching current, due to the fact that the path for electric switching and thermally-induced switching is the same in structures with magnetization perpendicular to the plane [12]. Several multilayered thin films have been studied in order to improve the properties of FLs with perpendicular magnetization [74–77]. It turned out that CoFeB which was predominantly employed for in-plane MRAM cells, possesses properties suitable for the fabrication of perpendicular MRAM cells as well. Results presented by Ikeda *et al.* in 2010 evidenced how PMA is present in MTJs based on thin films of CoFeB interfaced by MgO [53]. Perpendicular anisotropy in these systems is achieved due to interface effects between the CoFeB and MgO layer, and the annealing process is an important step to achieve both good PMA and high TMR [78]. As in the case of in-plane devices, the RL of perpendicular MTJs (pMTJs) is usually kept stable by antiferromagnetic coupling to an additional FM layer, forming a SAF. Due to the extremely high anisotropies achievable with materials exhibiting PMA, the pinning AFM layer is not necessary. Such SAF structures have been successfully and extensively developed and integrated into MgO-based pMTJ applications [79–81].

Further research has focused on improving the thermal stability as well as the switching properties, both by adding additional MgO layers to the structure [19, 82], and later employing elongated FLs to have a contribution from the shape anisotropy in the perpendicular direction [22]. This has led to practical pMTJ devices with the desired low switching current and high energy barrier needed for nonvolatile memory.

Die approbierte gedruckte Originalversion dieser Dissertation ist an der TU Wien Bibliothek verfügbar.
The approved original version of this doctoral thesis is available in print at TU Wien Bibliothek.
TU WIEN Bibliothek Your knowledge hub

TU WIEN Bibliothek Your knowledge hub
Die approbierte gedruckte Originalversion dieser Dissertation ist an der TU Wien Bibliothek verfügbar.
The approved original version of this doctoral thesis is available in print at TU Wien Bibliothek.

Chapter 3

Micromagnetics Modeling

Simulation tools are a powerful help in the design of modern STT-MRAM devices. Micromagnetics modeling allows to have a description of the evolution in time of the magnetization, described as a continuous quantity. The following chapter gives a brief overview of the magnetization dynamics's modeling via the Landau-Lifschitz Gilbert equation. The contents are mostly based on references [17], [83], and [84].

3.1 Landau Lifshitz Gilbert Equation

The explanation of ferromagnetism on the basis of exchange interactions, developed by Heisenberg and Dirac in 1928, created the possibility of developing a mesoscopic theory of magnetism which combined Maxwell's equations and quantum theory. The first description of time dependent motion of magnetic moments presenting no exchange coupling and without energy dissipation, thus in the absence of damping, was reported by Bloch in 1932 [85]. Landau and Lifshitz proposed a continuous equation for the description of the damped motion of the magnetization in a ferromagnet in 1935 [86]. Such a description was strictly valid only for small damping. A formulation which could be employed to describe strong damping in thin films was then developed by Gilbert in 1955 [87]. Following the work by Gilbert, a derivation of the equation of motion for the magnetization dynamics from considerations of the magnetic moment of electrons is hereby presented.

The magnetic moment represents the strength and orientation of the magnetic dipole of an object. It can be defined as the vector describing the relation of an external magnetic field to the torque it exerts on the object generating the moment itself. Such relationship is given by

$$\boldsymbol{\tau} = \boldsymbol{\mu} \tag{3.1}$$

where $\boldsymbol{\tau}$ is the torque, $\boldsymbol{\mu}$ is the magnetic moment, and is the magnetic induction. Given the presence of a torque acting on an object, the equation describing its rotational motion is

$$\frac{}{} = \boldsymbol{\tau} \tag{3.2}$$

Die approbierte gedruckte Originalversion dieser Dissertation ist an der TU Wien Bibliothek verfügbar.
The approved original version of this doctoral thesis is available in print at TU Wien Bibliothek.
TU WIEN Bibliothek Your knowledge hub

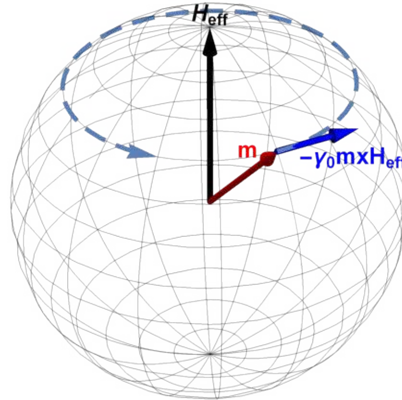

Figure 3.1: Magnetization precession around the effective field, in the absence of dissipative processes.

where is the angular momentum of the particle. The relation of the magnetic moment of an electron and its angular momentum is described by

$$\boldsymbol{\mu} = \tag{3.3}$$

where is the gyromagnetic ratio of the electron. By putting equations (3.1) and (3.3) into (3.2), one obtains the following equation of motion:

$$\frac{\boldsymbol{\mu}}{} = \boldsymbol{\mu} \tag{3.4}$$

Equation (3.4) is satisfied by a single magnetic moment. In micromagnetism, the magnetization is considered a continuous vector quantity, which takes the place of the single magnetic moment in the equation of motion previously described. Moreover, in the case of constant temperature and uniform density of spins, which is often considered for micromagnetic simulations, the continuous magnetization has a constant value and can thus be written in terms of a unit vector as

$$= {}_{\mathrm{S}} \quad \text{with} \quad = 1 \tag{3.5}$$

where the saturation magnetization $_{\mathrm{S}}$ is a material parameter. The quantity will be referred to as magnetization throughout this thesis. In order to derive a general equation of motion, the magnetic induction is replaced with an effective field $_{\mathrm{eff}}$, which describes not only the effects of an externally induced magnetic field, but also of contributions intrinsic to the ferromagnet, as will be clarified in Section 3.2. By taking the rescaled value of the gyromagnetic ratio $=$, the equation of motion for the magnetization takes the following form:

$$\frac{}{} = {}_{\mathrm{eff}} \tag{3.6}$$

Die approbierte gedruckte Originalversion dieser Dissertation ist an der TU Wien Bibliothek verfügbar.
The approved original version of this doctoral thesis is available in print at TU Wien Bibliothek.
TU WIEN Bibliothek Your knowledge hub

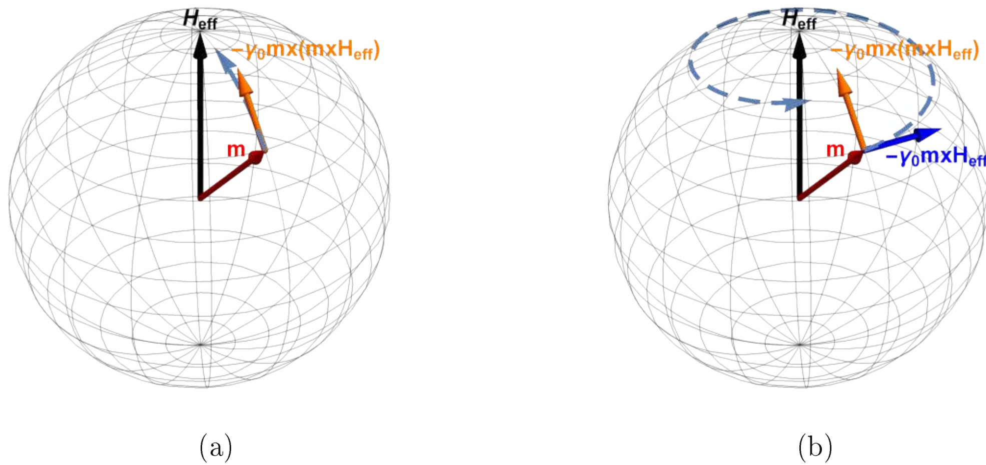

(a) (b)

Figure 3.2: (a) Magnetization trajectory under the action of the damping term only. The magnetization moves towards the effective field. (b) Magnetization trajectory prescribed by the complete LLG equation. The magnetization precesses around the effective field while relaxing towards it.

The equation derived until now describes a precessional motion of the magnetization around the magnetic field, see Fig. 3.1. From experiments, however, the magnetization dynamics is dissipative. The effect of an energy loss mechanism can be introduced in the equation in a phenomenological way, taking into consideration two main aspects: the damping process should lead the magnetization relaxing parallel to the effective field, as to minimize the energy, and it should not affect the magnetization magnitude (see Fig. 3.2(a)). This was first done in 1935 by L. D. Landau and E. M. Lifshitz, resulting in the so called Landau-Lifshitz equation [86]:

$$\frac{}{} = \qquad {}_{\text{eff}} \qquad (\qquad {}_{\text{eff}}) \tag{3.7}$$

> 0 is a dimensionless phenomenological damping parameter, which can be determined experimentally and is material dependent. The proposed equation describes a magnetization rotating around the effective magnetic field and being slowly quenched towards it (see Fig. 3.2(b)). The speed of the damping process is determined by the magnitude of . In order to deal with situations in which a strong damping is present, in 1955 T. L. Gilbert proposed a modified equation with a different form of the damping term, to be taken directly proportional to the time derivative of the magnetization [88]. The modified equation reads as

$$\frac{}{} = \qquad \left(\quad {}_{\text{eff}} \qquad \frac{}{} \right) \tag{3.8}$$

where is a viscosity parameter. By separating the two vector products, the equation takes the form

$$\frac{}{} = \qquad {}_{\text{eff}} + \qquad \frac{}{} \tag{3.9}$$

Die approbierte gedruckte Originalversion dieser Dissertation ist an der TU Wien Bibliothek verfügbar.
The approved original version of this doctoral thesis is available in print at TU Wien Bibliothek.
TU WIEN Bibliothek Your knowledge hub

where = is a dimensionless parameter referred to as Gilbert damping constant. In this formulation, the equation is known as Gilbert equation. It can be noted that equations (3.7) and (3.9) are equivalent, up to the rescaling of the constants. By cross-multiplying both sides of equation (3.7) by , by employing the triple product expansion formula and by taking into consideration the constraint = 1, it can be rewritten as

$$\frac{}{} = (1+) \quad _{\text{eff}} + \quad \frac{}{} \tag{3.10}$$

Using the same procedure on equation (3.9), it can be expressed as

$$\frac{}{} = \frac{}{1+} \quad _{\text{eff}} \quad \frac{}{1+} \quad (\quad _{\text{eff}}) \tag{3.11}$$

Equation (3.11) is commonly referred to as the Landau–Lifshitz–Gilbert (LLG) equation. Throughout the thesis, the Gilbert form of the damping will be employed.

3.2 Effective Field

In order to derive an expression for the various contributions to the effective field the magnetic Gibbs free energy of a ferromagnetic body must first be defined. Such quantity, indicated as $\mathcal{E}$, includes various contributions, such as the exchange energy, the anisotropy energy, the energy from an applied external field, and the magnetostatic energy. Such contributions will be described more in detail in the following sections. Once an expression for the Gibbs energy is known, a stable configuration of the magnetization is one that minimizes it, leading to the minimization problem

$$\min_{|\mathbf{m}|} \mathcal{E}(\quad) \tag{3.12}$$

A stable magnetization configuration constitutes a balancing point between the energy contributions. The effective field acting on the magnetization in the LLG equation stems directly from this minimization problem, and is defined as the functional derivative of the magnetic Gibbs free energy with respect to the magnetization [89]:

$$_{\text{S}} \quad _{\text{eff}} = \frac{\mathcal{E}(\quad)}{} \tag{3.13}$$

In fact, from the Euler-Lagrange equations associated to (3.12), it stems that any solution to it is also a solution to the boundary value problem

$$_{\text{eff}} = 0 \tag{3.14a}$$

$$\frac{\mathcal{E}(\quad)}{_i} = 0 \quad \text{for} \quad 1 \quad\quad 3 \tag{3.14b}$$

is the unit vector normal to the external boundary of the ferromagnetic domain under investigation. It can be noted that a configuration minimizing the energy requires the magnetization vector to be parallel to the local effective field. It is then

Die approbierte gedruckte Originalversion dieser Dissertation ist an der TU Wien Bibliothek verfügbar.
The approved original version of this doctoral thesis is available in print at TU Wien Bibliothek.
TU WIEN Bibliothek Your knowledge hub

clear that the process described by the LLG equation is a relaxation towards a state with minimal energy. The effective field contributions considered throughout this thesis are the following:

$$ {}_{\mathrm{eff}} = {}_{\mathrm{exc}} + {}_{\mathrm{ani}} + {}_{\mathrm{ext}} + {}_{\mathrm{demag}} + {}_{\mathrm{th}} \tag{3.15}$$

${}_{\mathrm{exc}}$ is the exchange field, ${}_{\mathrm{ani}}$ is the anisotropy field, ${}_{\mathrm{ext}}$ is the external field, ${}_{\mathrm{demag}}$ is the demagnetizing field, also called magnetostatic field, and ${}_{\mathrm{th}}$ is the thermal field. Each contribution will be described more in detail in the following sections.

3.2.1 Exchange Field

In ferromagnetic materials, it is energetically favorable for magnetic moments of neighboring atoms to be parallel to each other, due to the exchange interaction between them. Such interaction is of quantum mechanical origin, and was first predicted by W. K. Heisenberg in 1926. In micromagnetism which takes into consideration a continuous magnetization vector, this interaction is reflected in an energy contribution which penalizes magnetization variations throughout the magnetic domain, and can be expressed as [89]

$$\mathcal{E}_{\mathrm{exc}}(\quad) = \int_{\omega} \quad \mathrm{d} \tag{3.16}$$

where refers to the volume of the ferromagnetic domain, and is the exchange coefficient, which is a material dependent parameter expressed in units of J/m. Equation (3.16) exactly represents the lowest order phenomenological energy expression that penalizes inhomogeneous magnetization configurations. By employing the relation (3.13), the exchange field contribution to ${}_{\mathrm{eff}}$ can be derived as

$$ {}_{\mathrm{exc}} = \frac{2}{\quad {}_{\mathrm{S}}} \tag{3.17}$$

3.2.2 Anisotropy Field

In the presence of magnetic anisotropy, the magnetic free energy is minimized by the magnetization lying in one or more preferred orientations, referred to as easy axes. One of the main sources of magnetic anisotropy is given by the properties of the crystalline structure of the material, and is referred to as magnetocrystalline anisotropy. The three most important cases of magnetocrystalline anisotropy are the uniaxial, planar and cubic anisotropy. Each of them is characterized by a different contribution to the magnetic free energy, and so to the effective field [89]. Other sources of magnetic anisotropy include interface effects between different materials (interface anisotropy) and the particular shape of the magnetic domain under consideration (shape anisotropy).

Interface anisotropy is particularly important when discussing magnetic layers with the magnetization perpendicular to the main plane of the structure, and is usually taken into account as a uniaxial anisotropy contribution. The contribution of the shape anisotropy is accounted for by the demagnetizing field, which will be described

Die approbierte gedruckte Originalversion dieser Dissertation ist an der TU Wien Bibliothek verfügbar.
The approved original version of this doctoral thesis is available in print at TU Wien Bibliothek.
TU WIEN Bibliothek Your knowledge hub

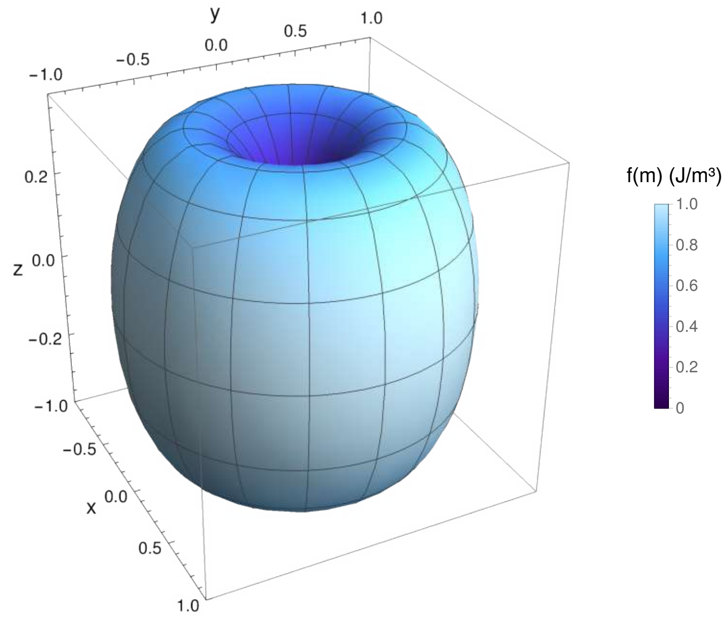

Figure 3.3: Projection on the unit sphere of the function ( ) = (1) representing the uniaxial anisotropy energy, for = 1 J/m and the unit vector pointing along the z-axis. The energy has is minimum value along the z-direction.

in section 3.2.4. The origin of the magnetocrystalline and interface anisotropy energy contributions lies in the spin-orbit coupling either due to an anisotropic crystal structure or due to lattice deformation at material interfaces, respectively.

Uniaxial Anisotropy

In the case of uniaxial anisotropy, there is only one preferred direction. In this case, the anisotropy energy, which can be taken as the work necessary to rotate the magnetization away from the easy axis, can be written as

$$\mathcal{E}_{\mathrm{ani}}(\quad) = \int_{\omega} (1 \qquad) \, \mathrm{d} \tag{3.18}$$

where 0 is the material anisotropy coefficient and is the unit vector identifying the easy axis. A visual representation of the energy distribution described by (3.18) is provided in Fig. 3.3. From (3.13), the anisotropy contribution to the effective field in this case is

$$_{\mathrm{ani}} = \frac{2}{_{\mathrm{S}}} (\qquad) \tag{3.19}$$

As previously mentioned, an uniaxial anisotropy contribution can be employed to take the interfacial anisotropy, and in particular the PMA acting in pMTJs, into account. The anisotropy coefficient takes in this case the form $= {}_{\mathrm{int}} \; {}_{\mathrm{FM}}$, where ${}_{\mathrm{int}}$ is the interface anisotropy, in units of J/m , and ${}_{\mathrm{FM}}$ is the thickness of the

Die approbierte gedruckte Originalversion dieser Dissertation ist an der TU Wien Bibliothek verfügbar.
The approved original version of this doctoral thesis is available in print at TU Wien Bibliothek.
TU WIEN Bibliothek Your knowledge hub

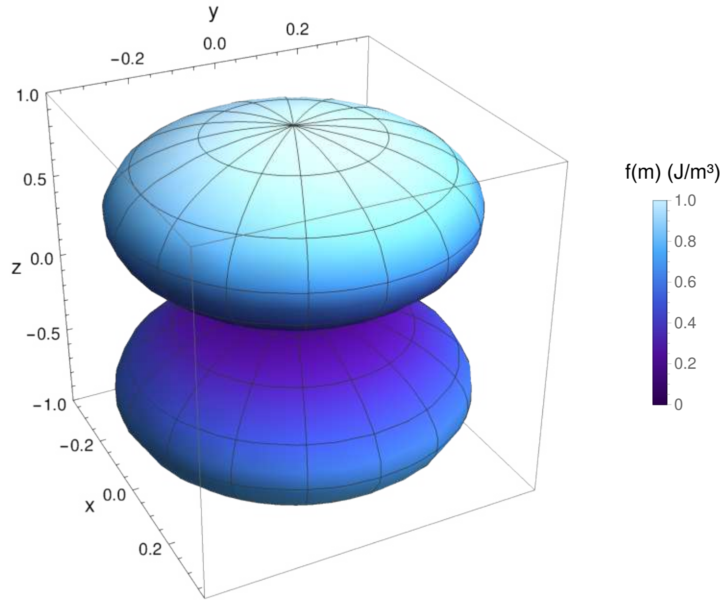

Figure 3.4: Projection on the unit sphere of the function ( ) = ( ) representing the planar anisotropy energy, for = 1 J/m and the unit vector pointing along the z-axis. The energy has is minimum value in the plane perpendicular to the z-direction.

FM layer under consideration. The relation between and the anisotropy field ${}_{\mathrm{K}}$ entering (2.2) is given by

$$ {}_{\mathrm{K}} = \frac{2\ {}_{\mathrm{eff}}}{\ {}_{\mathrm{S}}} \tag{3.20a}$$

$$ {}_{\mathrm{eff}} = \qquad \frac{\ {}_{\mathrm{S}}}{2} \tag{3.20b}$$

The second term on the right hand side of (3.20b) stems from the shape anisotropy. is the difference between the longitudinal and transverse demagnetizing factors in cylindrical layers, taking positive values for thin layers and negative values for elongated layers [22].

Planar Anisotropy

In the case of planar anisotropy, the magnetization prefers to lie in a plane normal to the axis described by the unit vector . The anisotropy energy in this case is

$$\mathcal{E}_{\mathrm{ani}}(\ ) = \int_{\omega} (\qquad)\ \mathrm{d} \tag{3.21}$$

A visual representation of the energy distribution described by (3.21) is provided in Fig. 3.4. The anisotropy, derived From (3.13), can be expressed as

$$ {}_{\mathrm{ani}} = \frac{2}{\ {}_{\mathrm{S}}} (\qquad) \tag{3.22}$$

Die approbierte gedruckte Originalversion dieser Dissertation ist an der TU Wien Bibliothek verfügbar.
The approved original version of this doctoral thesis is available in print at TU Wien Bibliothek.
TU WIEN Bibliothek Your knowledge hub

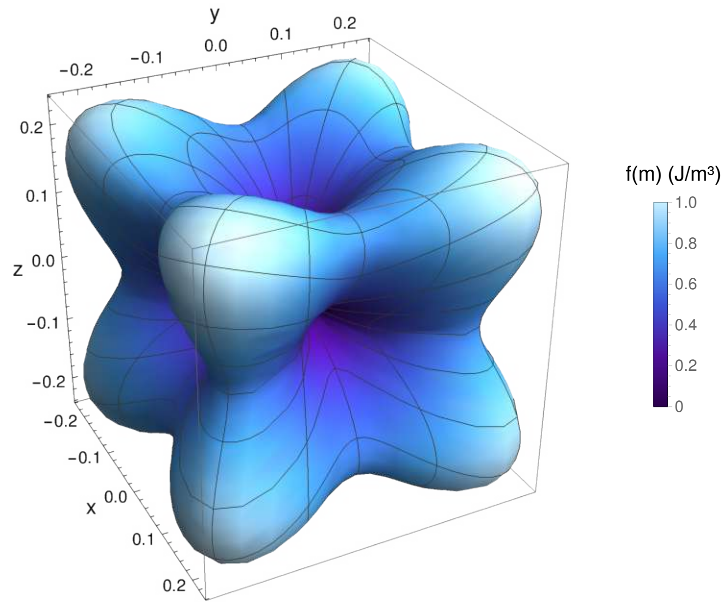

Figure 3.5: Projection on the unit sphere of the function ( ) = [( ) ( ) + ( ) ( ) + ( ) ( )] + ( ) ( ) ( ) representing the cubic anisotropy energy, for $_{1,2} = 1$ J/m and the unit vectors , and pointing along the x-, y- and z-axis, respectively. The energy has is minimum value along the x-, y- and z-direction.

Cubic Anisotropy

In the case of cubic anisotropy, there are three orthogonal preferred orientations for the magnetization, defining three easy axes. These are indicated by the unit vectors , and . The anisotropy energy can be described by the following expression:

$$\mathcal{E}_{\text{ani}}(\ ) = \int_{\omega} \{\ [(\ )\ (\ ) + (\ )\ (\ ) + (\ )\ (\ )] + (\ )\ (\ )\ (\ )\}\,\mathrm{d} \tag{3.23}$$

and are anisotropy coefficients specific to the material, which can be positive or negative. A visual representation of the energy distribution described by (3.18) is provided in Fig. 3.5. The cubic anisotropy field in this case is calculated from (3.13) as

$$\begin{aligned} _{\text{ani}} = \frac{2}{_{S}} & (\ )(\ )[(\ ) + (\ )] + \\ & (\ )(\ )[(\ ) + (\ )] + \\ & (\ )(\ )[(\ ) + (\ )] + \\ & (\ )(\ )(\ )[(\ )(\ ) + \\ & (\ )(\ ) + (\ )(\ )] \end{aligned} \tag{3.24}$$

Die approbierte gedruckte Originalversion dieser Dissertation ist an der TU Wien Bibliothek verfügbar.
The approved original version of this doctoral thesis is available in print at TU Wien Bibliothek.
TU WIEN Bibliothek Your knowledge hub

3.2.3 External Field

An external field acts on the magnetization as to have it aligned to itself. The contribution of the external field to the free energy, referred to as Zeeman energy, penalizes deviations of the magnetization from this field throughout the magnetic domain, and can be written as

$$\mathcal{E}_{\text{ext}}(\quad) = \quad {}_{\text{S}} \int_{\omega} \quad {}_{\text{ext}} \quad \text{d} \tag{3.25}$$

$_{\text{ext}}$ denotes the external field expressed in A/m, which can be directly added to the effective field (3.15).

3.2.4 Demagnetizing Field

In a ferromagnetic material, the magnetization itself generates a field contribution to be considered in the effective field, referred to as demagnetizing field, as it acts on the magnetization to reduce its total moment. The related energy contribution, called demagnetization energy, accounts for the dipole-dipole interaction of a magnetic system. Unlike the previously described contributions, the demagnetizing field depends both on the shape of the magnetic domain and on the orientation of the magnetization, acting differently in different structures and geometries, and giving rise to the formation of magnetic domains. Such contribution can be described resorting to the magnetostatic Maxwell equations

$$= \quad (\quad + \quad {}_{\text{S}} \quad) \tag{3.26a}$$
$$= 0 \tag{3.26b}$$
$$= \quad {}_{\text{C}} \tag{3.26c}$$

where $_{\text{C}}$ is the charge current density. The demagnetizing field generated by the magnetization, noted as $_{\text{demag}}$, is only the portion of independent from electric currents in the system. By putting equations (3.26a) and (3.26b) together, it follows that the demagnetizing field satisfies

$$_{\text{demag}} = \quad {}_{\text{S}} \tag{3.27a}$$
$$_{\text{demag}} = 0 \tag{3.27b}$$

It follows from (3.27b) that $_{\text{demag}}$, being a conservative field, can be derived as $_{\text{demag}} =$, where is a scalar potential referred to as magnetostatic potential. From (3.27), continuity considerations at the boundary of the magnetic domain and an open boundary condition, it follows that the magnetostatic potential inside the

Die approbierte gedruckte Originalversion dieser Dissertation ist an der TU Wien Bibliothek verfügbar.
The approved original version of this doctoral thesis is available in print at TU Wien Bibliothek.
TU WIEN Bibliothek Your knowledge hub

magnetic domain ($_{\mathrm{in}}$) and outside of it ($_{\mathrm{out}}$) satisfy the following set of equations:

$$_{\mathrm{in}} = \quad _{\mathrm{S}} \qquad \text{in} \tag{3.28a}$$

$$_{\mathrm{out}} = 0 \qquad \text{outside} \tag{3.28b}$$

$$(\ _{\mathrm{in}} \quad _{\mathrm{out}}) = 0 \qquad \text{at} \tag{3.28c}$$

$$(\quad _{\mathrm{in}} \quad _{\mathrm{out}}) = \quad _{\mathrm{S}} \qquad \text{at} \tag{3.28d}$$

$$_{\mathrm{out}}(\ ) = \mathcal{O}(1 \quad) \qquad \text{as} \tag{3.28e}$$

indicates the external boundary of the magnetic domain, and is the unit vector normal to the boundary. By referring to the quantities $_{\mathrm{S}}$ and $_{S}$ as the volume magnetic charge and surface magnetic charge , respectively, the magnetostatic potential can be expressed as [89, 90]

$$(\ ) = \frac{1}{4}\left(\int_{\omega} \frac{(\ ')}{\ '} \mathrm{d} \ ' + \int_{\partial\omega} \frac{(\ ')}{\ '} \mathrm{d} \ '\right) \tag{3.29}$$

From (3.27a), the demagnetizing field can then be computed as

$$_{\mathrm{demag}}(\ ) = \frac{1}{4}\left(\int_{\omega} \frac{(\quad ') \ (\ ')}{\ '} \mathrm{d} \ ' + \int_{\partial\omega} \frac{(\quad ') \ (\ ')}{\ '} \mathrm{d} \ '\right) \tag{3.30}$$

An alternative expression, more convenient for the discretization of the equation using the FD method, can be obtained as the convolution of the magnetization and a kernel representing the dipole interaction [91]:

$$_{\mathrm{i}}^{\mathrm{demag}}(\ ) = \frac{\ _{\mathrm{S}}}{4} \sum_{\mathrm{j}} \int_{\omega} \frac{1}{\ '} \left(\frac{\ _{\mathrm{i}} \quad _{\mathrm{i'}}}{\ '} \frac{\ _{\mathrm{j}} \quad _{\mathrm{j'}}}{\ '} \quad _{\mathrm{ij}} \right) \ _{\mathrm{j}}(\ ') \, \mathrm{d} \ ' \tag{3.31}$$

i,j $= 1 \ 2 \ 3$ are the vector components.

The magnetic energy associated with $_{\mathrm{demag}}$, usually referred to as magnetostatic energy, can be understood as the energy of the magnetization's interaction with its own demagnetizing field, and is expressed as

$$\mathcal{E}_{\mathrm{demag}}(\ ) = \frac{\ _{\mathrm{S}}}{2} \int_{\omega} \ _{\mathrm{demag}} \quad \mathrm{d} \tag{3.32}$$

3.2.5 Ampere Field

When a current is flowing through the magnetic domain, it generates a contribution to the effective field referred to as Ampere field. Looking back at equation (3.26), it can be observed that this field, noted $_{\mathrm{curr}}$, is the component of that satisfies

$$_{\mathrm{curr}} = 0 \tag{3.33a}$$

$$_{\mathrm{curr}} = \quad _{\mathrm{C}} \tag{3.33b}$$

Die approbierte gedruckte Originalversion dieser Dissertation ist an der TU Wien Bibliothek verfügbar.
The approved original version of this doctoral thesis is available in print at TU Wien Bibliothek.
TU WIEN Bibliothek Your knowledge hub

Equation (3.33) can be combined with the vector identity

$$(\qquad {}_{\mathrm{curr}}) = \quad (\qquad {}_{\mathrm{curr}}) \qquad {}_{\mathrm{curr}} \tag{3.34}$$

in order to obtain

$$ {}_{\mathrm{C}} = \qquad\qquad {}_{\mathrm{curr}} = \qquad {}_{\mathrm{curr}} \tag{3.35}$$

With suitable continuity conditions at the boundary of the magnetic domain and the same open boundary condition considered for the demagnetizing potential, the Ampere field satisfies the following set of equations:

$$ {}^{\mathrm{in}}_{\mathrm{curr}} = \qquad {}_{\mathrm{e}} \quad \text{in} \tag{3.36a}$$

$$ {}^{\mathrm{out}}_{\mathrm{curr}} = 0 \quad \text{outside} \tag{3.36b}$$

$$ {}^{\mathrm{in}}_{\mathrm{curr}} \qquad {}^{\mathrm{out}}_{\mathrm{curr}} = 0 \quad \text{at} \tag{3.36c}$$

$$(\qquad {}^{\mathrm{in}}_{\mathrm{curr}} \qquad {}^{\mathrm{out}}_{\mathrm{curr}}) = \qquad {}_{\mathrm{C}} \quad \text{at} \tag{3.36d}$$

$$ {}^{\mathrm{out}}_{\mathrm{curr}}(\quad) = \mathcal{O}(1 \qquad) \quad \text{as} \tag{3.36e}$$

denotes the vector gradient, with components $(\qquad)_{\mathrm{ij}} = \quad {}_{\mathrm{i}}/ \quad {}_{\mathrm{j}}$. A solution for $\quad {}_{\mathrm{curr}}$ consistent with (3.36) is given by Bio-Savart's law [89]

$$ {}_{\mathrm{curr}} = \frac{1}{4} \int_{\omega} \quad {}_{\mathrm{C}} \qquad \frac{(\qquad ')}{\qquad '} \, \mathrm{d} \quad ' \tag{3.37}$$

The contribution of the Ampere field to the Gibbs free energy is given by

$$\mathcal{E}_{\mathrm{curr}}(\quad) = \qquad {}_{\mathrm{S}} \int_{\omega} \quad {}_{\mathrm{curr}} \qquad \mathrm{d} \tag{3.38}$$

3.2.6 Thermal Field

In the presence of a non-zero temperature, the magnetization in a ferromagnet undergoes thermal fluctuations due to heating. The effect of such thermal fluctuations can be described in the LLG formalism by the introduction of an auxiliary random contribution to the effective field, referred to as thermal field. This field must fulfill the following statistical properties [92, 93]:

$$\langle \quad {}^{\mathrm{th}}_{\mathrm{i}}(\quad) \rangle = 0 \tag{3.39a}$$

$$\langle \quad {}^{\mathrm{th}}_{\mathrm{i}}(\quad) \qquad {}^{\mathrm{th}}_{\mathrm{j}}(\quad ') \rangle = \qquad {}_{\mathrm{ij}} \quad (\qquad ') \tag{3.39b}$$

i,j = 1 2 3 are the spacial coordinates, the constant measures the strength of the thermal fluctuations, and denotes the average taken over different realizations of the stochastic field. Such equations describe a field whose components are uncorrelated in both time and space, and are obtained as random Gaussian distributed numbers with zero mean value. The value of is obtained from the Fokker-Planck equation [94]. Given $\quad {}_{\mathrm{th}}$, its contribution to the total Gibbs free energy is given by

$$\mathcal{E}_{\mathrm{th}}(\quad) = \qquad {}_{\mathrm{S}} \int_{\omega} \quad {}_{\mathrm{th}} \qquad \mathrm{d} \tag{3.40}$$

Die approbierte gedruckte Originalversion dieser Dissertation ist an der TU Wien Bibliothek verfügbar.
The approved original version of this doctoral thesis is available in print at TU Wien Bibliothek.
TU WIEN Bibliothek Your knowledge hub

3.3 LLG Constraints

As already stated, the LLG equation describes the motion of the magnetization towards a state of minimal energy, described by (3.14). In particular, equation (3.14b) enforces boundary conditions which depend on energy contributions involving spacial derivatives of . The only such term considered throughout this dissertation is the exchange energy, described by (3.16). This term gives rise to the homogeneous Neumann boundary conditions

$$(\quad) = \qquad (3.41)$$

Even though these boundary conditions were derived for the stationary relaxed state, it can be shown that they remain physically valid also in the dynamic case [95], and so they are usually employed when describing the magnetization dynamics through the LLG equation.

Additionally, the modulus constraint $= 1$ introduced in (3.5) must be satisfied. It turns out that, as long as the constraint is satisfied by the initial magnetization, it remains satisfied at any subsequent point in time. To show that, first the scalar product of with either (3.9), (3.10) or (3.11) is taken, obtaining

$$\frac{}{} = 0 \qquad (3.42)$$

Then, by taking the time derivative of the modulus of squared, the following expression is derived:

$$\frac{}{} = 2 \quad \frac{}{} = 0 \qquad (3.43)$$

It follows that the modulus constraint is always satisfied, provided that it is satisfied by the vector describing the initial magnetization.

3.4 Spin Transfer Torque

The equations discussed up until now allow to describe the magnetization dynamics in the presence of an external field and of contributions internal to the magnetized system. In order to the describe the switching process of an STT-MRAM cell, equation (3.8) must be supplemented with terms describing the spin-transfer torque coming from polarized electrons flowing through the structure. The LLG equation with the addition of this torque contribution takes the form [96, 97]

$$\frac{}{} = \quad {}_{\mathrm{eff}} + \quad \frac{}{} + \frac{1}{{}_{\mathrm{S}}} \; {}_{\mathrm{S}} \qquad (3.44)$$

where ${}_{\mathrm{S}}$ is the torque contribution related to the angular momentum transfer between the magnetization and the spin of polarized electrons flowing through the ferromagnetic layers.

Die approbierte gedruckte Originalversion dieser Dissertation ist an der TU Wien Bibliothek verfügbar.
The approved original version of this doctoral thesis is available in print at TU Wien Bibliothek.
TU WIEN Bibliothek Your knowledge hub

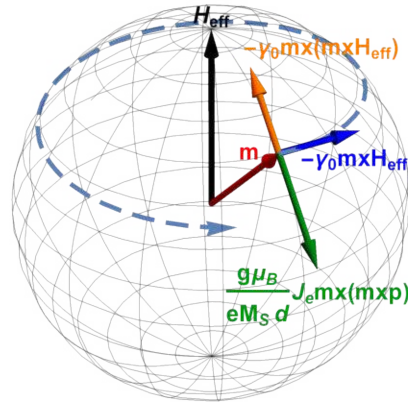

Figure 3.6: Magnetization trajectory in the presence of spin-transfer torque. If the magnetization of the reference layer is positive along the z-axis and the current $_{e}$ is also positive, the damping-like torque will work against the effective field and allow the magnetization of the free layer to switch from the parallel to the anti-parallel configuration.

When considering only the torque acting on the free layer of an STT-MRAM cell, schematized in Fig. 3.7, $_{S}$ can be written in terms of the free layer magnetization and the fixed reference layer magnetization , and is comprised of two contributions, referred to as damping-like and field-like torque [98, 99]:

$$_{S} = \quad (\quad) + \quad (\quad) \tag{3.45}$$

and are parameters depending on the current density flowing through the cell for the damping-like and field-like components, respectively. The damping-like component is the one causing the magnetization of the FL to move towards the direction of the magnetization of the RL, for AP to P switching, or away from it, for P to AP switching. The field-like component causes a precession of the FL magnetization around the direction of the magnetization of the RL.

Similarly to (3.11), equation (3.44) can be written in a more numerically tractable form:

$$\frac{\quad}{\quad} = \frac{1}{1+\quad}\Bigg\{ \quad _{\mathrm{eff}} \quad (\quad _{\mathbf{eff}}) + \frac{\hbar \quad _{\mathrm{C}}}{\quad _{\mathrm{S}} \quad _{\mathrm{FL}}} (\;) [\quad (\quad) \quad (\quad)] \Bigg\} \tag{3.46}$$

$_{\mathrm{FL}}$ is the thickness of the free layer, and $_{\mathrm{C}}$ is the modulus of the current density, flowing perpendicular to the structure. ( ) is the expression describing the torque efficiency, depending on the relative angle between the magnetization vectors of the

Die approbierte gedruckte Originalversion dieser Dissertation ist an der TU Wien Bibliothek verfügbar.
The approved original version of this doctoral thesis is available in print at TU Wien Bibliothek.
TU WIEN Bibliothek Your knowledge hub

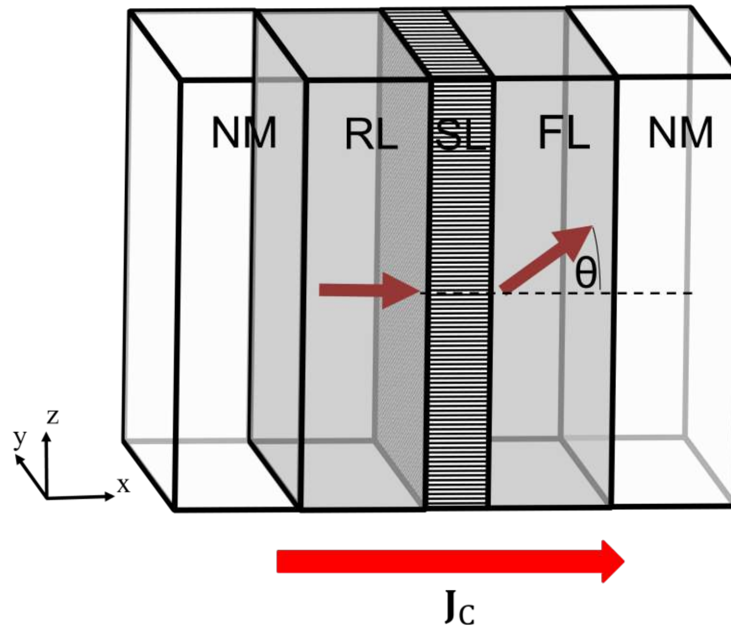

Figure 3.7: Schematic representation of an STT-MRAM cell. The RL is fixed during the switching process, and serves as a polarizer, while the FL is the one where the spin-transfer torque is able to act and reverse the magnetization direction. The spacer layer (SL) can be either a nonmagnetic conducting material (in spin valves, based on the GMR effect) or an insulating tunnel barrier (in MTJs, based on the TMR effect). The current density is positive when going from the RL to the FL. As electrons travel in the opposite direction of the current, a negative current density provides the torque for AP to P switching, while a positive current provides the torque for P to AP switching.

free and reference layer $=$. is a coefficient describing the intensity of the field-like torque. When the field-like contribution is not considered, $=$. Equation (3.46) is often written by taking the substitution $= \quad _{\mathrm{B}} \; \hbar$, in the form [92, 93, 100–104]

$$— = \frac{1}{1+} \Big\{ \qquad _{\mathrm{eff}} \qquad (\qquad _{\mathbf{eff}}) + $$

$$+ \frac{_{\mathrm{B}} \quad _{\mathrm{C}}}{_{\mathrm{S}} \quad _{\mathrm{FL}}} \; (\;) \, [\qquad (\qquad) \qquad (\qquad)] \Big\} \tag{3.47}$$

where is the electron g-factor.

The torque efficiency factor ( ) takes different forms for conducting spin-valve structures and MTJs. In the presence of a non-magnetic conducting spacer layer in a symmetric spin-valve, the expression, derived by Slonczewski, is [14]

$$(\;) = \left[\quad 4 + (1 + \quad) \frac{3 + \cos}{4 \qquad /} \right]^{-} \tag{3.48}$$

Die approbierte gedruckte Originalversion dieser Dissertation ist an der TU Wien Bibliothek verfügbar.
The approved original version of this doctoral thesis is available in print at TU Wien Bibliothek.
TU WIEN Bibliothek Your knowledge hub

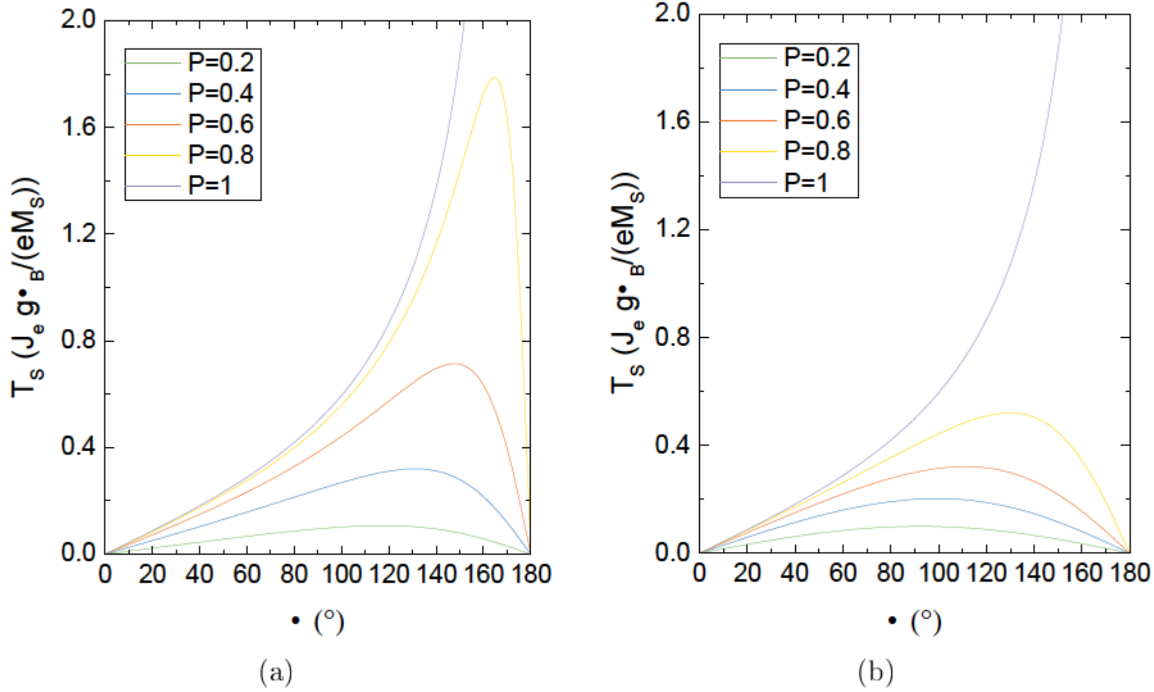

Figure 3.8: Dependence of the damping-like torque acting on the FL on the relative angle between the magnetization vectors in the FL and RL. In (a) the dependence in the presence of a nonmagnetic conducting spacer layer, where the torque efficiency is described by (3.48), is reported. In (b) the dependence in the presence of an insulating spacer layer, where the efficiency is described by (3.49), is reported.

P is the polarization factor, taken to be equal in the RL and FL. In the presence of a thin insulating spacer layer in an MTJ, the expression, also derived by Slonczewski, takes the form [16]

$$\eta(\theta) = \frac{P}{2(1 + P^2 \cos\theta)} . \tag{3.49}$$

A comparison of the resulting damping-like torque dependence on the angle θ between the spin-valve and the MTJ expression, for several values of the polarization parameter P, is reported in Fig. 3.8.

In an MTJ where the RL and the FL have different polarization factors, equation (3.49) for the torque efficiency of the FL can be expressed as

$$\eta(\theta) = \frac{P_{\mathrm{RL}}}{2(1 + P_{\mathrm{RL}}\, P_{\mathrm{FL}} \cos\theta)} , \tag{3.50}$$

where $P_{\mathrm{FL(RL)}}$ is the polarization of the FL(RL). The torque acting from electrons back-scattering to the RL can be expressed by changing P_{FL} to P_{RL} and vice-versa in the previous expression. The relation between the polarization factors and the TMR can be expressed using Julliere's formula [16,99,105,106]

$$\mathrm{TMR} = \frac{2\, P_{\mathrm{RL}}\, P_{\mathrm{FL}}}{1 - P_{\mathrm{RL}}\, P_{\mathrm{FL}}} . \tag{3.51}$$

Die approbierte gedruckte Originalversion dieser Dissertation ist an der TU Wien Bibliothek verfügbar.
The approved original version of this doctoral thesis is available in print at TU Wien Bibliothek.
TU WIEN Bibliothek Your knowledge hub

As previously stated, equations (3.48) and (3.49) are best employed when simulating the magnetization dynamics of a single, thin FL, with a single RL acting as the polarizer. A more general expression for the torque, which allows to deal with an arbitrary number of ferromagnetic and nonmagnetic layers, can be obtained by computing the non-equilibrium spin accumulation in the structure under study, and will be discussed in Chapter 6.

Die approbierte gedruckte Originalversion dieser Dissertation ist an der TU Wien Bibliothek verfügbar.
The approved original version of this doctoral thesis is available in print at TU Wien Bibliothek.
TU WIEN Bibliothek Your knowledge hub

Chapter 4

Charge Current Redistribution and Finite Difference Implementation of the LLG Equation

When dealing with switching simulations of STT-MRAM devices, there can be multiple ways to approach both the evaluation of torques and the evaluation of the current density giving rise to them. This chapter first describes the effects of a high TMR value on the current density distribution in an MRAM cell during switching. This is achieved by deriving an analytical solution for the current density in an MTJ. Then, the FD discretization of the LLG equation employed to perform switching simulations is presented, and is extended with three different approaches to describe the current and its distribution during the switching process.

The magnetization dynamics described by equation (3.47) address the current polarization, giving rise to the STT, via the efficiency terms described by equations (3.48) and (3.49). These terms are based on the theoretical predictions of J. C. Slonczewski, and were derived by considering a macrospin approach to the ferromagnetic leads, where the magnetization in the whole layer can be represented by a single vector. In realistic structures with diameters in the range of tens of nanometers, however, non-uniform switching of the magnetization is expected [107].

In micromagnetic modeling of STT switching, the typical simplified approach is to still rely on the efficiency terms derived by Slonczewski, by using a position dependent angle ( ) between the magnetization in the RL and FL [17]. Such approach also assumes a position- and time-independent current density $_{\mathrm{C}}$. In circuits, however, the voltage, rather than the current density, remains fixed during switching. The resistance of the tunnel junction depends on the relative magnetization alignment of the FL and the RL, according to (2.4), so the current through the structure is not constant during the process. Moreover, as the magnetization of the FL is not uniform at switching, but depends on the position, so does the local tunneling conductance. The assumption of a constant current density adopted in the description of STT-MRAM switching needs thus to be tested, especially in advanced MTJs with a TMR

Die approbierte gedruckte Originalversion dieser Dissertation ist an der TU Wien Bibliothek verfügbar.
The approved original version of this doctoral thesis is available in print at TU Wien Bibliothek.
TU WIEN Bibliothek Your knowledge hub

ratio of about 200% and higher [18].

4.1 Nonuniform Current Density Distribution

The main effect of a non-uniform magnetization distribution in the FL is to make the resistance of the barrier dependent on the lateral position. The magnitude of the relative resistance variation will be proportional to the TMR of the MTJ. Obtaining a solution for the current density in such a scenario can help evaluate its non-uniformity, and if it needs to be taken into account when performing switching simulations. The MTJ structure in which the current is computed is reported in Fig. 4.1. The considered MTJ has magnetization perpendicular to the plane of the thin ferromagnetic films (p-MTJ), as such structures present better thermal stability and scalability, and lower switching currents (see Chapter 2). The ferromagnetic leads are here contacted directly. The equation for the charge current density in the metallic leads, where the distribution of charges is uniform, is

$$_{\mathrm{C}} = \qquad (4.1)$$

where is the conductivity, and is the electric field. In the absence of transient magnetic fields, Maxwell's equations describe as an irrotational field, so that in can be written in terms of the electric potential as

$$= \qquad (4.2)$$

Moreover, the FM layers do not contain sources of electric current, so that

$$_{\mathrm{C}} = 0 \qquad (4.3)$$

As any displacement of the charge density relax almost instantly in metals, terms involving its time derivative / are hereby not considered. By taking the divergence of both sides of (4.1) and taking (4.2) and (4.3) into consideration, the following Laplace equation for can be derived:

$$= 0 \qquad (4.4)$$

By putting together equations (4.1) and (4.2), the current density can be expressed in terms of the potential as

$$_{\mathrm{C}} = \qquad (4.5)$$

To obtain a unique solution for the potential and the current in the FM layers, the boundary conditions need to be defined. Considering the RL, the left side is contacted directly, so that a Dirichlet condition on the voltage, prescribing its value, is applied. The right side of the layer presents the interface with the TB. Here, the tunneling current going to the FL is proportional to the local resistance, which depends on the relative angle between magnetization vectors in the FL and RL, due to the polarized tunneling process in an MTJ, and can be described through equation (2.4). The local resistance of the TB can be modeled through the following Neumann boundary

TU Bibliothek Your knowledge hub WIEN
Die approbierte gedruckte Originalversion dieser Dissertation ist an der TU Wien Bibliothek verfügbar.
The approved original version of this doctoral thesis is available in print at TU Wien Bibliothek.

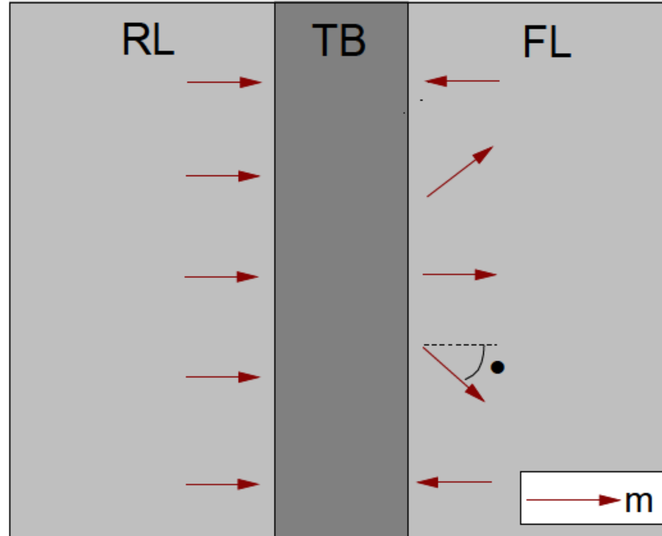

Figure 4.1: MTJ structure with directly contacted FM leads and nonuniform magnetization distribution in the FL.

condition, assuming a coordinate system where the x-axis is the one perpendicular to the TB interface:

$$-\sigma_{\mathrm{RL}}\boldsymbol{\nabla}V\cdot\mathbf{n}=-\sigma_{\mathrm{RL}}\frac{\mathrm{d}V}{\mathrm{d}x}\bigg|_{x=t_{\mathrm{RL}}}=J_{\mathrm{C,TB}}(\theta)\approx\frac{G_{\mathrm{MTJ}}(\theta)}{S}\Delta V_{\mathrm{TB}} \tag{4.6}$$

σ_{RL} is the conductivity of the RL, $\mathbf{n}$ is the unit vector normal to the boundary, t_{RL} is the RL thickness, $J_{\mathrm{C,TB}}$ is the tunneling spin current density, S is the TB surface area, and ΔV_{TB} is the average potential drop across the barrier, computed as the potential on the RL side minus the one on the FL side. The approximate expression for the tunneling current density is justified when the majority of the potential drop across the structure happens at the barrier, so when the resistance of the TB is much higher than the one of the metal contacts. The resistivity of thin films of CoFeB, the most common material for both RL and FL in modern MTJs, is of the order of $10^{-6}\,\Omega m$ [108, 109]. The typical resistance of an MTJ of 40 nm diameter is of the order of $10\,k\Omega$ [53], giving a resistivity value of about $10^{-1}\,\Omega m$. Such a resistivity is several orders of magnitude greater then the one of the metal leads, so that the expression for $J_{\mathrm{C,TB}}$ is justified.

The solution is first computed for the 2D section of the structure presented in Fig. 4.1, with the x-axis perpendicular to the barrier interface and the y-axis pointing along it. If the angle θ entering (4.6) can be described as a function of the position along the TB interface y, then the set of equations describing the potential in the RL

Die approbierte gedruckte Originalversion dieser Dissertation ist an der TU Wien Bibliothek verfügbar.
The approved original version of this doctoral thesis is available in print at TU Wien Bibliothek.
TU Bibliothek WIEN Your knowledge hub

layer is

$$\left(\frac{}{} + \frac{}{} \right) = 0 \quad (4.7a)$$

$$(0 \quad) = \quad (4.7b)$$

$$\frac{d}{d}(\quad _{RL} \quad) = \quad (\ ) \quad (4.7c)$$

$$\frac{d}{d}(\quad 0) = \frac{d}{d}(\quad) = 0 \quad (4.7d)$$

$_{RL}$ and are the thickness of the RL and width of the structure, respectively, and the sides of the structure are treated with homogeneous Neumann boundary conditions $_{C} \quad = 0$. In order to solve this set of equations, an explicit expression for the function ( ), describing a highly nonuniform magnetization distribution, is first provided. The approximate expression for the average voltage drop $_{TB}$ in equation (4.6) is obtained by considering the three layers as resistors in series:

$$_{TB} = \frac{_{MTJ}}{_{RL} + \quad _{FL} + \quad _{TB}} \quad (4.8)$$

$_{RL(FL)} = \quad _{RL(FL)} \left(\quad _{RL(FL)} \quad \right)$ is the resistance of the RL(FL), and the resistance of the TB is taken as $_{TB} = \quad \int_S \quad _{MTJ}(\ ) d \quad$. With this expression, boundary condition (4.6) can be rewritten as

$$(\ ) = \frac{1}{_{RL}} \frac{_{RL}}{_{RL} + \quad _{FL} + \quad _{TB}} \quad \left(1 + \frac{\mathrm{TMR}}{2 + \mathrm{TMR}} \cos \quad \right) \quad (4.9)$$

If the unit vector of the RL magnetization is pointing along x, then cos , being equal to $_{RL} \quad _{FL}$, is equivalent to $_{x,FL}$. This component of the magnetization is taken to be going from anti-parallel on the sides to parallel in the center of the structure, as $_{x,FL}(\ ) = (\quad 1 + 2\sin(\quad))$. By taking a TMR value of 200%, the boundary condition (4.7c) can thus finally be written as

$$(\ ) = \frac{_{R}}{_{RL}} \quad (\ ) \quad (4.10a)$$

$$(\ ) = \left(\frac{1}{2} + \sin\left(\frac{}{} \right) \right) \quad (4.10b)$$

$$_{R} = \frac{_{RL}}{_{RL} + \quad _{FL} + \quad _{TB}} \quad (4.10c)$$

A solution satisfying (4.7), with the boundary condition (4.10), takes the form

$$(\quad) = \quad \frac{_{R}}{_{RL}} \quad \left(\frac{}{2} \quad + \sum_{n}^{\infty} \frac{_{n}}{\cosh\left(\frac{n\pi d_{RL}}{w}\right)} \sinh\left(\frac{}{} \right) \cos\left(\frac{}{} \right) \right) \quad (4.11)$$

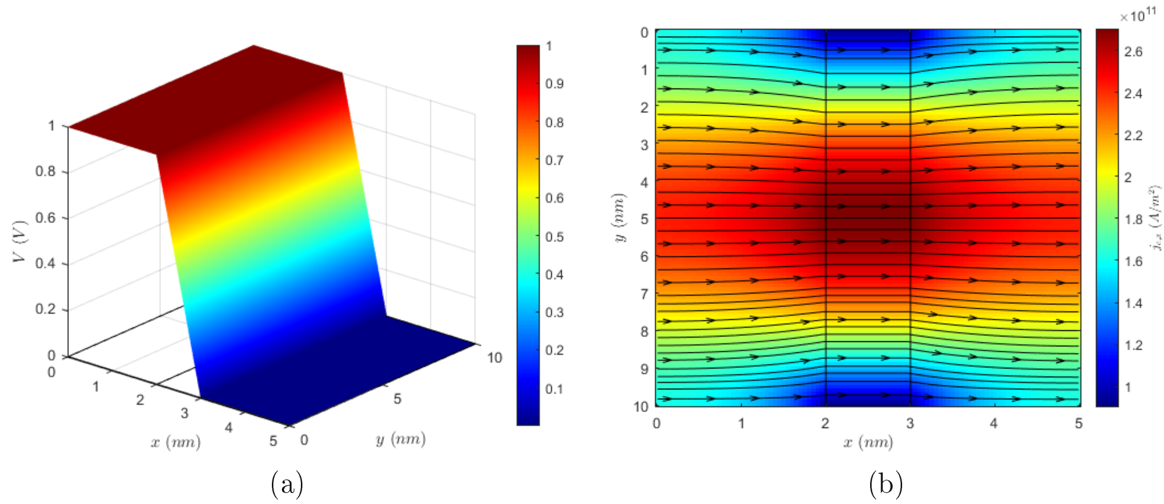

Figure 4.2: (a) Two dimensional solution for the electric potential, described by (4.7). The main drop happens across the TB. (b) Two dimensional solution for the current density. The field lines are evidenced in black, the color bar is based on the magnitude of the x-component. The current is redistributed to accommodate the varying conductance in the middle layer.

where the coefficients $_n$ are given by the Fourier cosine series of $(\ )$:

$$(\ ) = \frac{}{2} + \sum_{n}^{\infty} {}_n \cos\left(\frac{}{}\right) \qquad {}_n = \frac{2}{} \int^{w} (\ ) \cos\left(\frac{}{}\right) \mathrm{d} \tag{4.12}$$

A similar solution can be obtained for the FL, with the Neumann boundary condition applied on its left side instead of the right one, and Dirichlet conditions fixing the potential to 0 on the right side. In the middle layer, a linear decay of the potential from the RL to the FL interface is assumed. The complete solution for both the potential and the current density is reported in Fig. 4.2, for $_{\mathrm{RL}} = {}_{\mathrm{FL}} = 10$ S/m, $= 4\ 76 \quad 10^{-}$ S, and $= 1$ V. The dimensions of the structure are taken as $_{\mathrm{RL}} = {}_{\mathrm{FL}} = 2$ nm and $= 10$ nm, and the thickness of the TB is 1 nm. A voltage drop localized at the TB can be clearly observed in Fig 4.2(a), while the voltage in the two FM contacts is basically constant. The current density profile is reported in Fig. 4.2(b), where the black lines follow the current density vector field. The color bar is based on the magnitude of the x-component of the current. The current density is redistributed to accommodate the conductance variation in the TB, with the percentage difference between the lowest and highest value of the x-component being dictated by the TMR value.

The presented solution can be extended to a three dimensional structure with rectangular cross section. In this case, the partial differential equation to solve for

Die approbierte gedruckte Originalversion dieser Dissertation ist an der TU Wien Bibliothek verfügbar.
The approved original version of this doctoral thesis is available in print at TU Wien Bibliothek.
TU WIEN Bibliothek Your knowledge hub

the potential in the RL is

$$\left(\frac{}{} + \frac{}{} + \frac{}{} \right) = 0 \tag{4.13a}$$

$$(0 \quad) = \tag{4.13b}$$

$$\frac{\mathrm{d}}{\mathrm{d}}(\ {}_{\mathrm{RL}} \quad) = (\quad) \tag{4.13c}$$

$$\frac{\mathrm{d}}{\mathrm{d}}(\ 0 \ ) = \frac{\mathrm{d}}{\mathrm{d}}(\quad) = 0 \tag{4.13d}$$

$$\frac{\mathrm{d}}{\mathrm{d}}(\quad 0) = \frac{\mathrm{d}}{\mathrm{d}}(\quad) = 0 \tag{4.13e}$$

is the height of the structure in the z-direction. Using the same reasoning as before, the boundary condition (4.13c) ca be written as

$$\frac{\mathrm{d}}{\mathrm{d}}(\ {}_{\mathrm{RL}} \quad) = \frac{{}_{\mathrm{R}}}{{}_{\mathrm{RL}}} \quad (\quad) \tag{4.14a}$$

$$(\quad) = \left(\frac{1}{2} + \sin\left(\frac{}{}\right) \sin\left(\frac{}{}\right) \right) \tag{4.14b}$$

$$\tag{4.14c}$$

A solution satisfying this set of equations takes the form

$$\begin{aligned} (\quad) = \frac{{}_{\mathrm{R}}}{{}_{\mathrm{RL}}} \Bigg(\frac{}{4} &+ \sum_{n}^{\infty} \frac{{}_{n}}{2 \quad \cosh\left(\frac{n\pi d_{\mathrm{RL}}}{w}\right)} \sinh\left(\frac{}{}\right) \cos\left(\frac{}{}\right) + \\ &+ \sum_{m}^{\infty} \frac{{}_{m}}{2 \quad \cosh\left(\frac{n\pi d_{\mathrm{RL}}}{h}\right)} \sinh\left(\frac{}{}\right) \cos\left(\frac{}{}\right) + \\ &+ \sum_{n,m}^{\infty} \frac{{}_{nm}}{{}_{nm} \ \cosh(\ {}_{nm} \quad {}_{\mathrm{RL}})} \sinh(\ {}_{nm} \quad) \cos\left(\frac{}{}\right) \cos\left(\frac{}{}\right) \Bigg) \end{aligned} \tag{4.15a}$$

$$ {}_{nm} = \sqrt{\left(\frac{}{}\right) + \left(\frac{}{}\right)} \tag{4.15b}$$

where the coefficients ${}_{n,m}$ are again given by the Fourier cosine series for $(\quad)$:

$$\begin{aligned} (\quad) = \frac{}{4} + \sum_{n}^{\infty} \frac{{}_{n}}{2} \cos\left(\frac{}{}\right) + \sum_{m}^{\infty} \frac{{}_{m}}{2} \cos\left(\frac{}{}\right) + \\ + \sum_{n,m}^{\infty} \ {}_{nm} \cos\left(\frac{}{}\right) \cos\left(\frac{}{}\right) \end{aligned} \tag{4.16a}$$

$$ {}_{nm} = \frac{4}{} \int^{w} \mathrm{d} \int^{h} \mathrm{d} \quad (\quad) \cos\left(\frac{}{}\right) \cos\left(\frac{}{}\right) \tag{4.16b}$$

Results for the three-dimensional solution are reported in Fig. 4.3. The distribution of the x-component of the current density is reported for planes located at

Die approbierte gedruckte Originalversion dieser Dissertation ist an der TU Wien Bibliothek verfügbar.
The approved original version of this doctoral thesis is available in print at TU Wien Bibliothek.
TU WIEN Bibliothek Your knowledge hub

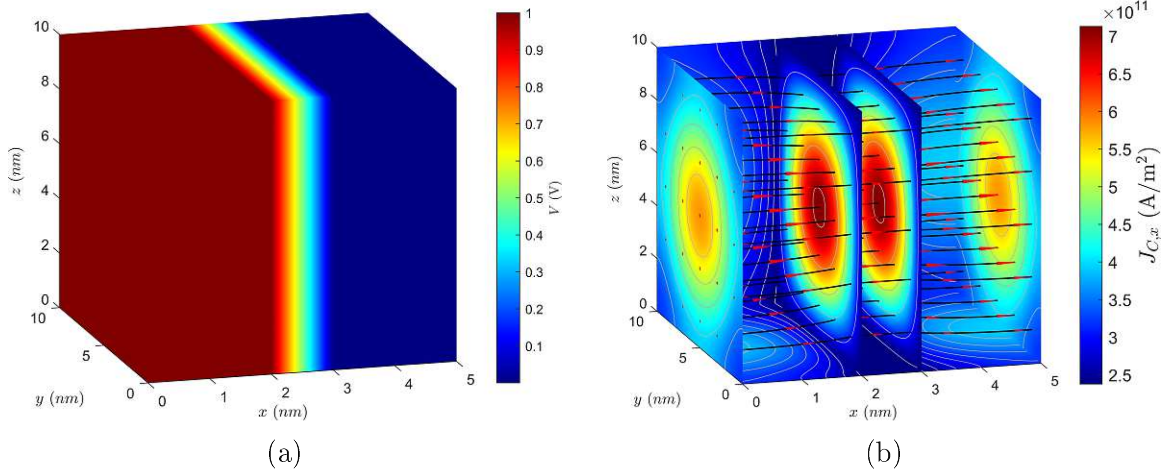

Figure 4.3: (a) Three dimensional solution for the electric potential, described by (4.13). The main drop happens across the TB. (b) Three dimensional solution for the current density. The black lines with red arrows represent the field lines of the current. The color bar is based on the magnitude of the x-component. The current is redistributed to accommodate the higher conductance at the center of the layer, due to parallel magnetization vectors. (b) was adapted from [110].

the contacts and at the TB interfaces. Both the potential and the current density showcase the same behavior reported for the two-dimensional case.

These results underline how the current density component perpendicular to the MTJ plane can be strongly nonuniform when dealing with inhomogeneous magnetization configurations during switching. The validity of the description with the fixed current density for the switching process' simulation needs thus to be evaluated against models which include the possibility of current density redistribution.

4.2 Finite Difference Implementation of the LLG Equation

The software employed to this end is an in-house solver based on the FD method [17], applied to a pMTJ. The effective magnetic field is calculated directly from the discretized magnetization [91]. Only the dynamics of the FL are computed, while the influence of the RL stray field is added as an external contribution to the effective field. The simulation domain is divided in parallelepiped cells, with volume = , where , and represent the discretization along the three Cartesian directions. The number of cells in each direction is labeled x, y and z, respectively. A unit magnetization vector = (x y z)^T is associated with the center of the cell. The software is extended to include the possibility of having several approaches for the local current density computation:

- an approach where the voltage across the structure is fixed, with the current redistribution exemplified by the results of the previous section;

Die approbierte gedruckte Originalversion dieser Dissertation ist an der TU Wien Bibliothek verfügbar.
The approved original version of this doctoral thesis is available in print at TU Wien Bibliothek.
TU Bibliothek WIEN Your knowledge hub

- the typical fixed current density approach;
- an approach with a fixed total current, redistributed according to the local resistance value, extending the reference model described in [111] to pMTJs.

This section provides a brief description of the FD implementation of the terms entering the effective field and torque computation described in chapter 3, as well as the equations employed to address the proposed approaches to the current density redistribution. All the simulations take into account the presence of a single layer of cells along the FL thickness. The labels indicate cells in the three Cartesian directions.

4.2.1 External Field Discretization

A uniform and constant external field vector can be provided as an input parameter to the simulation. Its value is directly added to the effective field vector.

$$ _{\text{ext}}(\quad) = \quad _{\text{ext,input}} \tag{4.17}$$

4.2.2 Exchange Field Discretization

The exchange field contribution, being proportional to the Laplacian of the magnetization, as seen in (3.17), requires knowledge of its value in both the computational cell and its nearest neighbor cells. In the most general case, there are 6 neighbors, two for every Cartesian direction. A first order discretized expression for this contribution takes the form [89]

$$ _{\text{exc}}(\quad) = \frac{2}{\quad _{\text{S}}} \sum_{i',j',k'} \frac{(\ ' \ ' \ ') \qquad (\qquad)}{\quad _{i',j',k'}} \tag{4.18}$$

In this expression, the triplet $(\ ' \ ' \ ')$ describes the nearest neighbors, and can take the forms $(\quad 1 \quad)$, $(\quad 1 \quad)$, and $(\quad 1)$. $_{i',j',k'}$ is the distance between the two magnetization vectors, taking the values , and for the different nearest neighbor cells.

The behavior of expression (4.18) at the boundary, where some of the nearest neighbor locations are not part of the simulation domain, needs to be consistent with the boundary condition described by (3.41). The most common way to enforce the given boundary condition is to introduce a 'ghost' magnetization vector at the missing location, with the same value as the nearest magnetic moment inside the boundary [89]. In the solver, this is achieved by having $(\ ' \ ' \ ') = (\quad)$ for missing neighboring cells.

4.2.3 Magnetocrystalline Anisotropy Field

The computation of the discretized anisotropy field contribution only needs to take into account the magnetization vector in the computational cell. Equations (3.19),

Die approbierte gedruckte Originalversion dieser Dissertation ist an der TU Wien Bibliothek verfügbar.
The approved original version of this doctoral thesis is available in print at TU Wien Bibliothek.
TU WIEN Bibliothek Your knowledge hub

(3.22) and (3.24) can be directly employed for the calculation of the field. In the present work, the interface-induced perpendicular anisotropy, typical of pMTJ devices, is modeled as a uniaxial anisotropy contribution. The related discretized expression for the anisotropy field is given by

$$_{\mathrm{ani}}(\quad) = \frac{2}{\quad_S} (\; (\quad) \;) \tag{4.19}$$

where is the easy axis for the magnetization, taken to be perpendicular to the plane of the structure.

4.2.4 Demagnetizing Field

The demagnetizing field is the most computationally expensive contribution to the effective field. As its origin stems from the dipole interaction, it is a strongly non-local quantity, and its value at a particular location depends on the magnetization vectors in the whole structure. This means that the demagnetizing field calculation in a particular cell requires an iteration over the magnetic moments of all other cells.

For the computation of the demagnetizing field of the FL, a discretization of equation (3.31) is employed. The field for each computational cell is calculated as the sum of the individual demagnetization contributions coming from the magnetic moments of all the cells in the computational domain:

$$_{\mathrm{demag}}(\quad) = \frac{\quad_{\mathrm{S}}}{4} \sum_{i'}^{N_{\mathrm{x}}} \sum_{j'}^{N_{\mathrm{y}}} \sum_{k'}^{N_{\mathrm{z}}} \Big(\; (\quad ' \; ' \; ') \; (' \; ' \; ') \Big) \tag{4.20}$$

is a space-dependent matrix describing the dipole-dipole interaction kernel. A detailed derivation of this matrix based on fast calculations of the integrals involved is described in [91]. As the matrix is symmetric, only 6 of its 9 components need to be evaluated. The matrix is also time-independent, so that it can be computed only once at the beginning of the simulation.

The field describing the magnetostatic coupling between RL and FL has the same physical origin of the FL demagnetizing field, but since the magnetization of the RL does not change with time, it can be computed only once at the beginning of the simulation and treated as an external field contribution. In order to compute it, the RL is divided into parallelepiped elementary cells with unit vector magnetization $= \quad_{\mathrm{RL}} \quad_{\mathrm{S,RL}}$, where $_{\mathrm{RL}}$ is the local magnetization of the RL and $_{\mathrm{S,RL}}$ is its saturation magnetization. An equation similar to (4.20) can be employed for the computation of the magnetostatic contribution:

$$_{\mathrm{ms}}(\quad) = \frac{\quad_{\mathrm{S}}}{4} \sum_{i'}^{N_{\mathrm{x,RL}}} \sum_{j'}^{N_{\mathrm{y,RL}}} \sum_{k'}^{N_{\mathrm{z,RL}}} \Big(\; (\quad ' \; ' \; ') \; (' \; ' \; ') \Big) \tag{4.21}$$

$_{\mathrm{x,RL}}$, $_{\mathrm{y,RL}}$ and $_{\mathrm{x,RL}}$ are the number of RL cells in the x-,y-, and z-direction, respectively.

Die approbierte gedruckte Originalversion dieser Dissertation ist an der TU Wien Bibliothek verfügbar.
The approved original version of this doctoral thesis is available in print at TU Wien Bibliothek.
TU Bibliothek WIEN Your knowledge hub

4.2.5 Ampere Field Discretization

A discretized version of equation (3.33) is employed for the computation of the Ampere field. The field acting in each computational cell is obtained by summing the contributions generated by the current density flowing through all the other cells in the simulated domain as

$$_{\mathrm{curr}} = \frac{1}{4} \sum_{i'}^{N_x} \sum_{j'}^{N_y} \sum_{k'}^{N_z} (\;_{\mathrm{C}}(' \; ' \; ') \quad '(\quad ' \; ' \; ')) \tag{4.22}$$

where $' =$, $' =$, and $' =$. $_{\mathrm{C}}$ is the current density vector, and $'$ is a space-dependent vector containing the interaction coefficients between different cells. A detailed description of the derivation of $'$ based on the fast computation of the integrals involved can be found in [112]. The value of the Ampere field is approximately computed at the beginning of the simulation by assuming a constant current density, and is added to $_{\mathrm{eff}}$ as an external field contribution.

4.2.6 Thermal Field Discretization

The implementation of the thermal field must be consistent with (3.39). This can be achieved by computing the thermal field as [113]

$$_{\mathrm{th,l}}(\quad) = \; (\quad) \sqrt{\frac{2 \; _B}{1 + \quad \quad _{\mathrm{S}}}} \tag{4.23}$$

where $=$ is a subscript indicating each thermal field component, is the time-step employed for the simulation and is the volume of a single computational cell. is a value generated from a Gaussian distribution uncorrelated in space and time, with standard deviation equal to 1.

4.2.7 Current Density Approaches

The spin-transfer torque term presented in (3.47) can be computed directly from the discretized FL magnetization ( ) and the RL magnetization , which remains constant during the switching process. The current density $_C$ entering the equation, representing the value of the component orthogonal to the TB interface, is given by different expressions, depending on the chosen simulation approach. Noting $_{\mathrm{C}}$ the total current density flowing in the FL, in the fixed voltage approach the expressions for the currents are

$$= \mathrm{const} \qquad _{\mathrm{C}}(\quad) = \; (\; (\quad)) - \qquad _{\mathrm{C}}(\,) = \int_S \; _{\mathrm{C}}(\quad) \, \mathrm{d} \tag{4.24}$$

In the fixed current density approach, they are

$$_{\mathrm{C}} = \mathrm{const} \qquad _{\mathrm{C}} = \; _{\mathrm{C}} \tag{4.25}$$

Die approbierte gedruckte Originalversion dieser Dissertation ist an der TU Wien Bibliothek verfügbar.
The approved original version of this doctoral thesis is available in print at TU Wien Bibliothek.
TU WIEN Bibliothek Your knowledge hub

Finally, in the fixed total current approach they are

$$_{\mathrm{C}} = \mathrm{const} \qquad _{\mathrm{C}}(\quad) = \frac{(\;(\quad))\;_{\mathrm{C}}}{\int_S \;(\;(\quad))\,\mathrm{d}} \tag{4.26}$$

Here, is the surface area of the FL, and is the applied bias. ( ) is described by equation (2.4) and ( ) = ( ) . From these equations, the following discretized expressions for $_{\mathrm{C}}$ in the fixed voltage and fixed current density approaches can be derived:

$$\text{Fixed Voltage:} \qquad _{\mathrm{C}}(\quad) = \;(\;(\quad 1)) - \tag{4.27a}$$

$$\text{Fixed Current:} \qquad _{\mathrm{C}}(\quad) = \frac{(\;(\quad 1))\;_{\mathrm{C}}}{\sum_{i,j,} \;(\;(\quad 1))} \tag{4.27b}$$

The conductance only depends on the angle (1) = (1) between the RL magnetization and the FL magnetization in the first layer of cells, closest to the TB, and is the surface area of a single cell.

4.2.8 Time Discretization

In order to obtain the magnetization dynamics, the LLG equation needs to be integrated over time. The solver employed for this work is based on the fourth-order

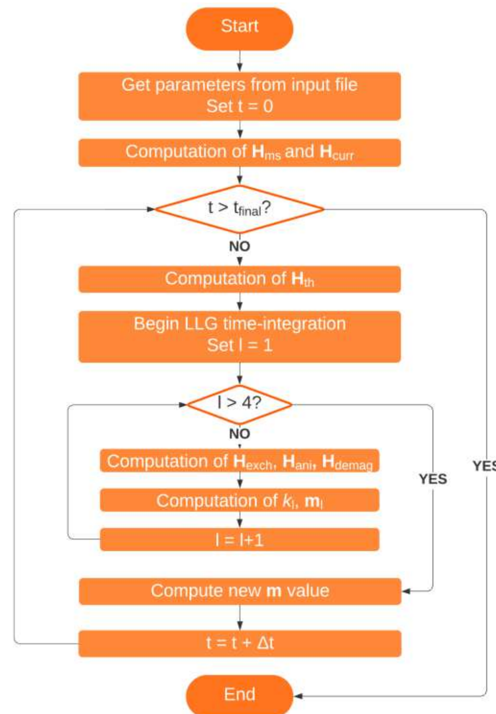

Figure 4.4: Flowchart of the FD solver employed for the switching simulations. The integer number l, going from 1 to 4, is used to loop through the LLG solver and compute the four coefficients of the fourth-order Runge-Kutta method (4.28).

Die approbierte gedruckte Originalversion dieser Dissertation ist an der TU Wien Bibliothek verfügbar.
The approved original version of this doctoral thesis is available in print at TU Wien Bibliothek.
TU Bibliothek WIEN Your knowledge hub

Runge-Kutta method, with a constant time-step . The new value of the magnetization of each cell $_{\mathrm{n+1}} = (_{\mathrm{n+1}})$, where n is an integer indicating the current time-step and $_{\mathrm{n+1}} = _{\mathrm{n}} +$, is given by obtaining a weighted average of four increments, where each increment is the product of and an estimated slope specified by the LLG equation at different points of the time-step:

$$_{\mathrm{n+1}} = \; _{\mathrm{n}} + \frac{}{6}(\; + 2 \; + 2 \; + \;) \tag{4.28a}$$

$$= \mathrm{LLG}(_{\mathrm{n}} \;\; _{\mathrm{n}}) \tag{4.28b}$$

$$= \mathrm{LLG}\left(_{\mathrm{n}} + \frac{}{2} \;\; _{\mathrm{n}} + \frac{}{2} \right) \tag{4.28c}$$

$$= \mathrm{LLG}\left(_{\mathrm{n}} + \frac{}{2} \;\; _{\mathrm{n}} + \frac{}{2} \right) \tag{4.28d}$$

$$= \mathrm{LLG}(_{\mathrm{n+1}} \;\; _{\mathrm{n}} + \;\;) \tag{4.28e}$$

The solver implementation and the simulation process are summarized by the flowchart shown in Fig. 4.4.

Die approbierte gedruckte Originalversion dieser Dissertation ist an der TU Wien Bibliothek verfügbar.
The approved original version of this doctoral thesis is available in print at TU Wien Bibliothek.
TU WIEN Bibliothek Your knowledge hub

Chapter 5

Switching Simulations of Perpendicular STT-MRAM Under Fixed Voltage and Fixed Current Approaches

This chapter compares switching simulations of the FL of an STT-MRAM cell obtained by computing the torques under the fixed current and fixed voltage approaches previously introduced. The results hereby presented were published by the author in references [110], [114], [115], and [116].

The simulations are carried out in the FL of a cylindrical pMTJ stack, with the system's parameters set to match experimental structures [19, 53, 117]. The diameter of the stack is 40 nm, the equivalent thickness of the CoFeB FL and RL are 1 7 nm and 1 nm, respectively, and the thickness of the MgO TB is 1 nm. The cell size employed for the FD discretization is 2 2 1 7 nm . A representation of the MTJ stack employed for these simulations is reported in Fig. 5.1. The perpendicular anisotropy provided by the interface between the CoFeB and MgO layers is reproduced using an uniaxial anisotropy contribution to the effective field. The interfecial anisotropy strength $_{\text{int}}$ = 1 53 10^{-} J/m is employed, giving an uniaxial anisotropy coefficient = $_{\text{int}}$ $_{\text{FL}}$ = 0 9 J/m . The other contributions to the effective magnetic field $_{\text{eff}}$ considered in this work are the external field, the exchange interaction, the demagnetizing field, the thermal field, and the stray field coming from the reference layer/magnetic stack. The simulations are carried out for the case were the TB polarization factor is the same for the FL and RL. In order to account for the differences between the models, the value of the current employed for the fixed current approaches is set to $_{\text{P}}$ = $_{\text{P}}$ for simulations going from the AP to P configuration, and to $_{\text{AP}}$ = $_{\text{AP}}$ for switching from the P to AP configuration. $_{\text{P(AP)}}$ is the resistance of the MTJ in the P(AP) configuration, is the voltage applied in the fixed voltage approach. The values of the parameters entering the LLG equation are reported in Table 5.1.

Die approbierte gedruckte Originalversion dieser Dissertation ist an der TU Wien Bibliothek verfügbar.
The approved original version of this doctoral thesis is available in print at TU Wien Bibliothek.
TU WIEN Bibliothek Your knowledge hub

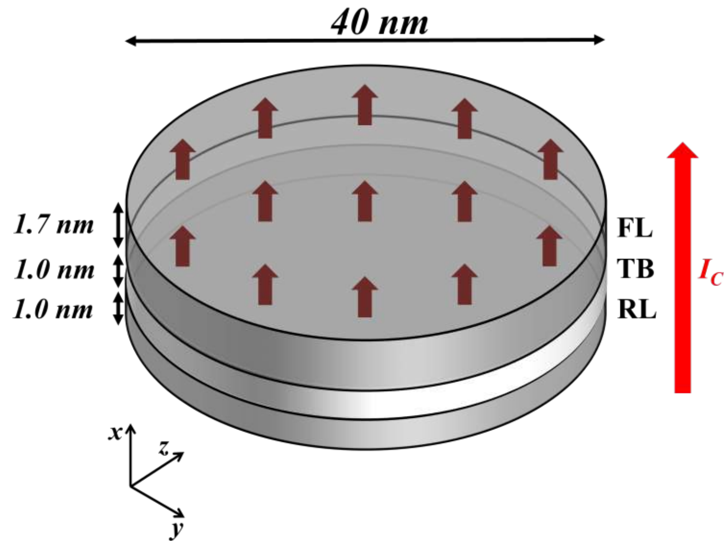

Figure 5.1: Schematic representation of the pMTJ stack employed to obtain the results reported in this chapter. The current and current density have a positive sign when flowing from the RL to the FL, and they flow in the x-direction, perpendicular to the stack. The FL and RL are also magnetized along the x-direction.

Table 5.1: Parameters employed for the FD switching simulations.

Parameter	Value
Gilbert damping factor,	0 02
Saturation magnetization, $_{S}$	1 2 10 A/m
Exchange constant,	10^{-} J/m
Perpendicular anisotropy coefficient,	0 9 10 J/m
Thermal stability,	67
Voltage,	2 V
Resistance Area,	18 m
Parallel resistance, $_{P}$	1.4 k
Antiparallel resistance, $_{AP}$	4.2 k
Tunneling magnetoresistance ratio,	200 %
Free layer surface area,	1257 nm

5.1 Switching Realizations

With the setup described in the previous section, switching simulations are carried out employing the three proposed approaches to the current density computation. The time evolution of all three components of the magnetization in a realization of the fixed voltage AP to P switching is reported in Fig. 5.2. After an incubation period of around 5 ns, during which the perpendicular component of the magnetization

Die approbierte gedruckte Originalversion dieser Dissertation ist an der TU Wien Bibliothek verfügbar.
The approved original version of this doctoral thesis is available in print at TU Wien Bibliothek.
TU WIEN Bibliothek Your knowledge hub

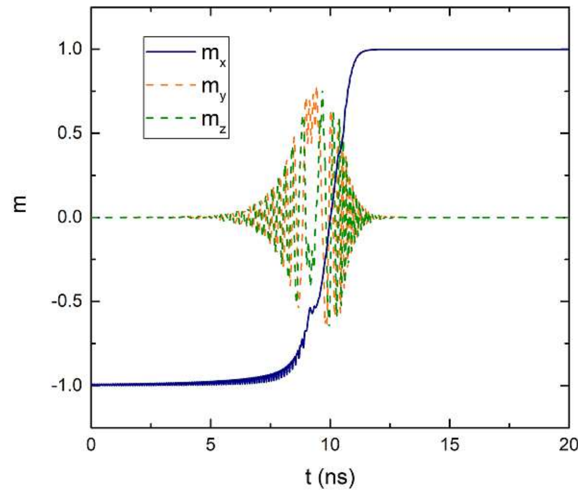

Figure 5.2: Time evolution of the three components of the magnetization, averaged across the free layer, during AP to P switching under fixed voltage. After an incubation period, the magnetization undergoes switching with a precessional motion.

stays close to the starting value of -1, the oscillations of the planar components of the magnetization increase and the switching process starts. The magnetization reversal takes about 5 ns, and then the perpendicular component stabilizes at the end value of +1, parallel to the RL magnetization.

Fig. 5.3 showcases snapshots of the magnetization in the FL at different stages of the switching process. The magnetization reversal starts from the border of the FL, where the action of the demagnetizing field, pushing the magnetization towards the plane, is the strongest. When the torque becomes strong enough to move the magnetization away from the -x orientation, the magnetic moments on the external boundary start to oscillate, until a first seed of moments pointing to the +x orientation is generated. At this point, this region quickly expands to encompass the whole of the FL, completing the switching. From these snapshots, it is clear how the magnetization is extremely non-uniform during the process, so that an investigation of the effects of the current redistribution is called for.

The simulation is carried out at the room temperature of 300 K. Due to the fluctuations of the magnetization under non-zero temperature, reproduced in the simulations by the thermal field contribution, every switching realization takes a slightly different path. A set of 10 realizations using the fixed voltage approach is showcased in Fig. 5.4. The different realizations present a similar behavior, but the start of the magnetization reversal happens at a slightly different time-step for each of them. It can be noted that the switching time required to go from P to AP is higher than that from AP to P. This is due to the uncompensated stray field of the RL, which tends to keep the magnetization of the two ferromagnetic layers aligned, helping the switching to the parallel configuration and opposing the switching to the antiparallel one. Due to this, during the P to AP process, even after the formation

Die approbierte gedruckte Originalversion dieser Dissertation ist an der TU Wien Bibliothek verfügbar.
The approved original version of this doctoral thesis is available in print at TU Wien Bibliothek.
TU Bibliothek WIEN Your knowledge hub

Die approbierte gedruckte Originalversion dieser Dissertation ist an der TU Wien Bibliothek verfügbar.
The approved original version of this doctoral thesis is available in print at TU Wien Bibliothek.
TU Bibliothek WIEN Your knowledge hub

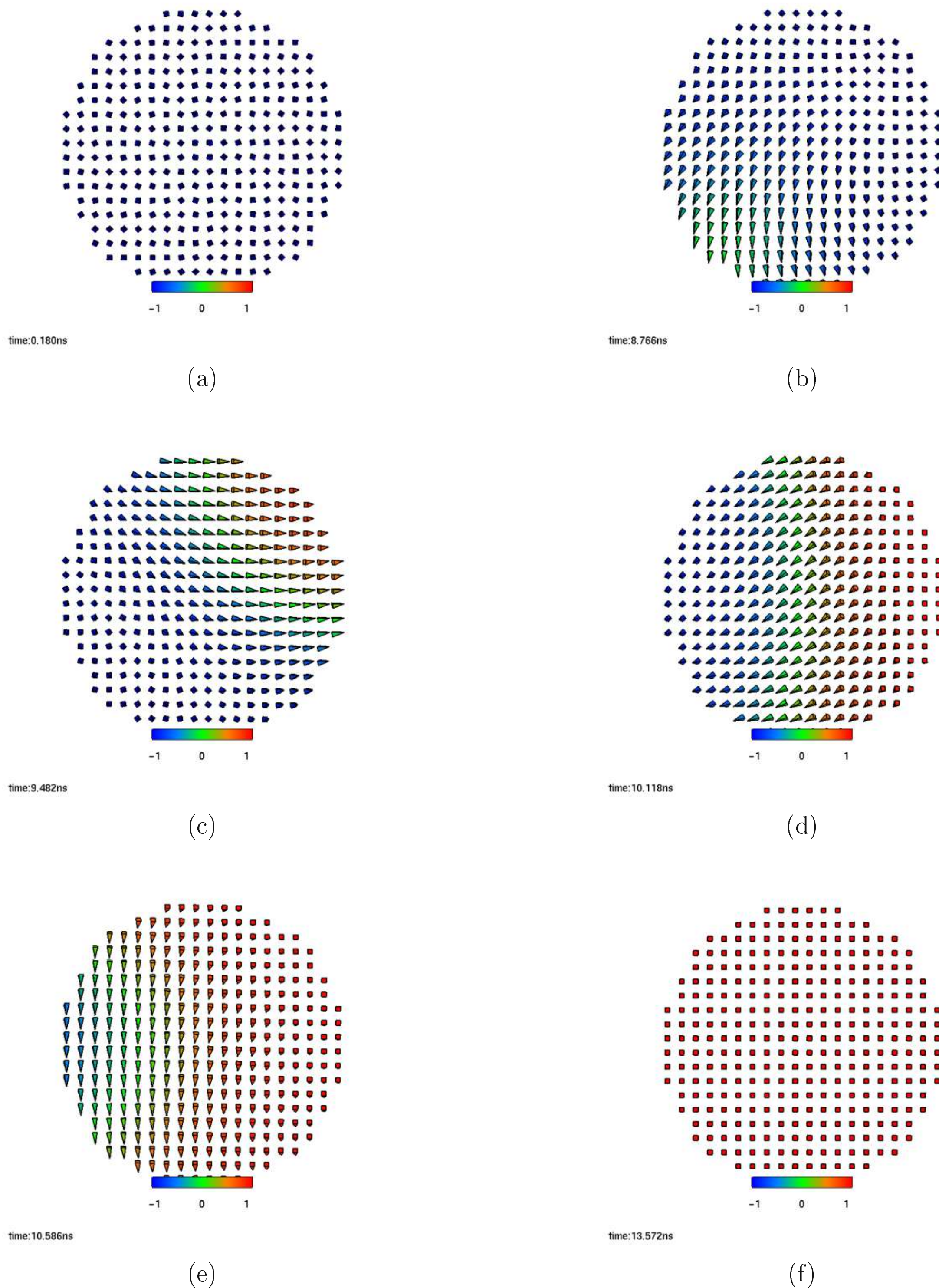

Figure 5.3: Snapshots of the free layer magnetization vectors during the AP to P switching process, under fixed voltage. The color bar describes the x-component. After the incubation period, the vectors on the side of the structure start to move away from the initial -x orientation. Once a seed of vectors pointing towards +x is established, it quickly propagates through the FL, completing the switching.

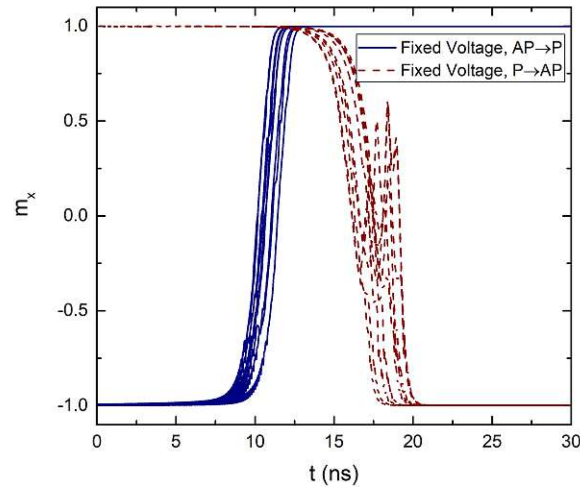

Figure 5.4: Time evolution of the x-component of the magnetization, perpendicular to the plane of the structure, during ten switching realizations. The simulations are carried out in the presence of the stochastic thermal field, for the constant voltage approach and for both AP to P and P to AP switching. Each simulation follows a different path due to the random value of the thermal field contribution. In the P to AP switching attempts, the stray field from the fixed layer is opposing the magnetization reversal, creating the observable oscillations.

of the first region of reversed moments the magnetization can still undergo large oscillations before stabilizing along the antiparallel orientation. This can be observed in some realizations of the P to AP switching process, which present peaks in the trajectory of the perpendicular magnetization component.

5.2 Switching Time Comparison

Examples of switching realizations for the three current approaches are shown in Fig. 5.5, for both AP to P and P to AP processes. A clear difference between the results can not be easily understood from looking at the magnetization trajectories of single realizations, due to the influence of the thermal field. The time required to complete the magnetization reversal, labeled switching time, can be a good indicator of the different performance of the models. As already discussed, the switching time difference between the AP to P and P to AP processes is due to the influence of the RL. By using a pinned layer antiferromagnetically coupled to the RL, the total stray field acting on the FL can be compensated, enabling a more symmetric switching process in the two magnetization configurations. The presence of the pinning layer is introduced in the simulations by modulating the total saturation magnetization of the antiferromagnetically coupled layers. The value of the combined saturation magnetization of the two layers is labeled $_{\mathrm{S,pin}}$.

Die approbierte gedruckte Originalversion dieser Dissertation ist an der TU Wien Bibliothek verfügbar.
The approved original version of this doctoral thesis is available in print at TU Wien Bibliothek.
TU WIEN Bibliothek Your knowledge hub

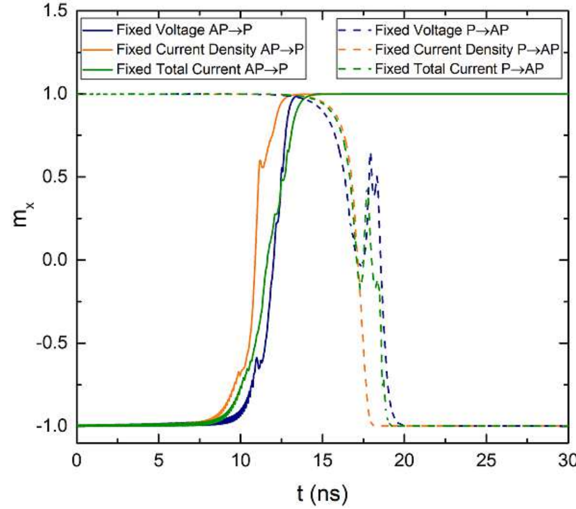

Figure 5.5: x-component of the magnetization during the AP to P and P to AP switching, for the three different approaches to the current density described in the text. In the P to AP switching attempts, the stray field from the fixed layer is opposing the magnetization reversal, creating the observable oscillations.

Fig. 5.6(a) reports the switching times as a function of uncompensated stray field. The switching time is taken at the end of the process, when the difference between the value of $_x$ and the maximum value of 1 is less than 5%. The results are averaged over 20 realizations, in order to take into account the effects of the thermal field. The error is taken as half the difference between the highest and lowest obtained values. As expected, compensating the stray field results in a higher switching time for the AP to P configuration and a lower one for P to AP. As shown in the figure, the average switching times assuming a fixed total current or a fixed current density are remarkably similar for both P to AP and AP to P switching. However, the switching for the fixed constant voltage looks quite different. The switching times are 15% higher for AP to P and 10% lower for P to AP for the fixed current approaches, as compared to the model with fixed voltage. This discrepancy is attributed to the fact that, when the voltage is fixed, the total current is allowed to vary according to the MTJ resistance, while the other two approaches have the same total current flowing through the structure during the whole reversal process. In order to compensate the effect of varying resistance, the total current value under the assumption of a fixed current must be increased by 9% for AP to P and decreased by 4% for P to AP switching. The resulting switching times are shown in Fig. 5.7: with this tuned choice of currents, all the models produce compatible results within the thermal spread.

The proposed current adjustment, albeit providing a feasible way of producing results compatible with a fixed voltage approach even in the more commonly implemented fixed current assumption, could depend on various system parameters, especially the TMR ratio and the dimensions of the stack. Further analysis and simulations are required in order to gather a better understanding of these dependencies. The analysis is performed in the next section.

Die approbierte gedruckte Originalversion dieser Dissertation ist an der TU Wien Bibliothek verfügbar.
The approved original version of this doctoral thesis is available in print at TU Wien Bibliothek.
TU WIEN Bibliothek Your knowledge hub

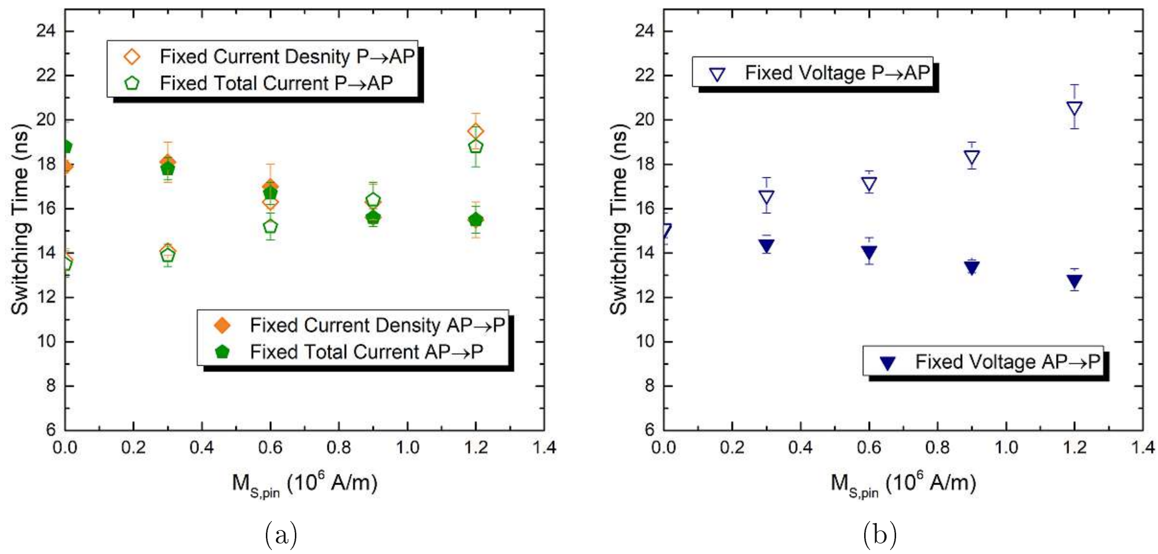

(a) (b)

Figure 5.6: Comparison between AP to P and P to AP switching times for various levels of the uncompensated stray field at T=300 K. Filled symbols represent AP to P switching, empty ones P to AP. (a) reports the switching times for the fixed current models, (b) the ones for the fixed voltage approach. The error bars show switching time variations due to thermal fluctuations. The figures were published in [116].

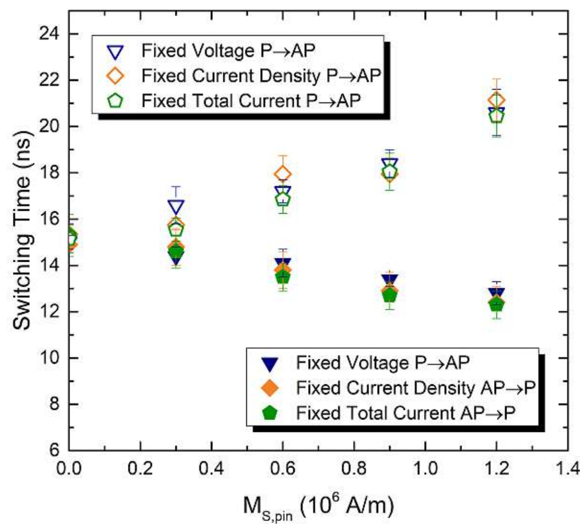

Figure 5.7: Comparison of switching times for the tuned values of input currents at T=300 K. The switching times of all three approaches are compatible within the thermal variation. The figure was published in [116].

5.3 Study of the Current Correction Dependencies

5.3.1 Dependence on the TMR at Room Temperature

The TMR is arguably the most important characteristic of an MRAM device, as its value determines both the read performance and the torque magnitude through the

Die approbierte gedruckte Originalversion dieser Dissertation ist an der TU Wien Bibliothek verfügbar.
The approved original version of this doctoral thesis is available in print at TU Wien Bibliothek.
TU WIEN Bibliothek Your knowledge hub

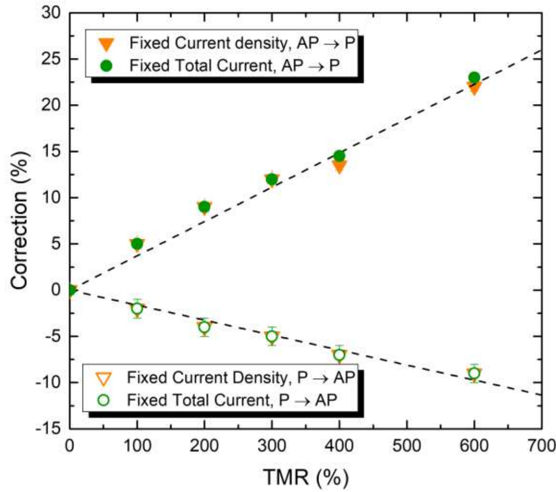

Figure 5.8: The correction to the current, which must be given in order for all three models to give consistent results, as a function of TMR at T=300 K, for both P to AP and AP to P switching. The dashed lines represent a linear fit. The figure was published in [116].

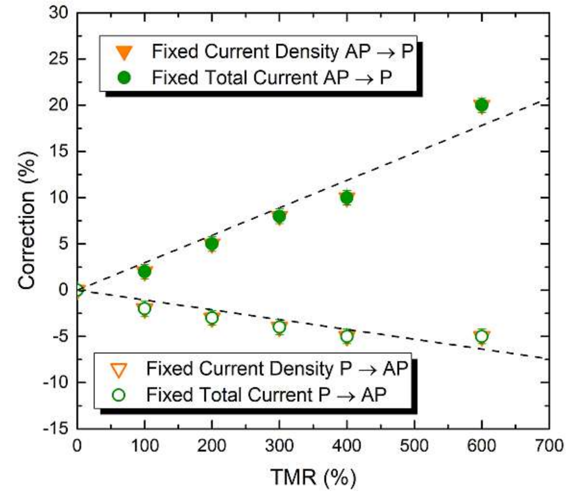

Figure 5.9: Correction to the current as a function of TMR at T=0 K, for both P to AP and AP to P switching. The dashed lines represent a linear fit. The figure was published in [116].

Julliere formula (3.51). The dependence of the current correction on this parameter is thus investigated. The TMR is varied, while the others parameters are kept at the values shown in Table 5.1. The correction to the current value necessary to obtain a switching time comparable to the one at fixed voltage is evaluated for both fixed current approaches. The dependence of the correction on the TMR is shown in Fig. 5.8. The results imply that the constant current density assumption can be employed in the realistic case of switching at a constant voltage at room temperature, provided that the current is appropriately corrected for the P to AP and the AP to P scenario, and that the correction must be adapted to the TMR value. The obtained dependence can be well reproduced by a linear fit, as showcased by the dashed lines.

5.3.2 Dependence on the TMR at Zero Temperature

In order to further elaborate on the origin and magnitude of the current correction, the TMR dependence is computed again for the case of zero temperature, where the thermal field is not active and switching is deterministic. Like in the case of room temperature, the results for the switching time under the assumption of a fixed voltage differ from those with the fixed current. However, with the appropriate current correction, all three models provide similar results. The dependence of the correction on the TMR at zero temperature is reported in Fig. 5.9. The dependence still follows a linear trend, with the dashed lines reporting a linear fitting of the results. The current correction required is smaller than the one obtained at room temperature for all tested values of the TMR. It can be also noted that the switching process is

TU Bibliothek WIEN Your knowledge hub
Die approbierte gedruckte Originalversion dieser Dissertation ist an der TU Wien Bibliothek verfügbar.
The approved original version of this doctoral thesis is available in print at TU Wien Bibliothek.

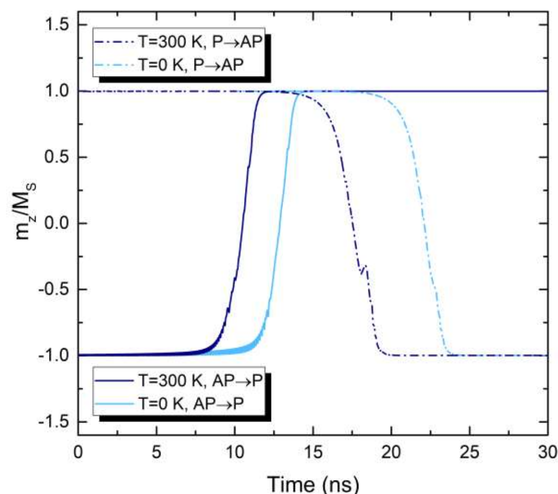

Figure 5.10: Comparison between switching realizations for the fixed voltage model, with TMR=200%, at T=0 K and T=300 K. The switching is slower at low temperature. The figure was published in [116].

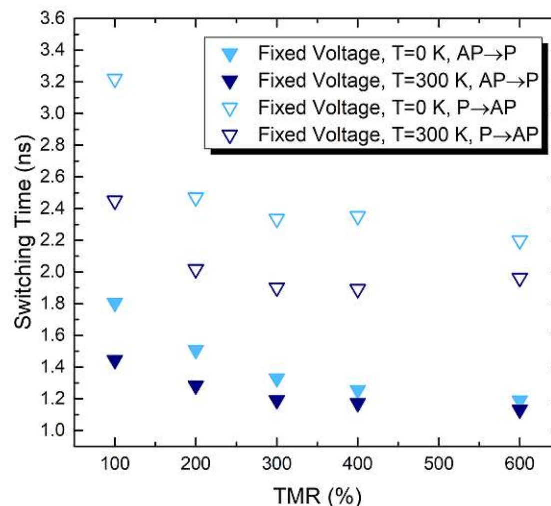

Figure 5.11: Switching time as a function of the TMR in the fixed voltage approach, for both AP to P and P to AP switching, at T=0 K and T=300 K. The switching time at zero temperature is always higher than the one at room temperature. The figure was published in [116].

faster at room temperature for both AP to P and P to AP processes, as depicted in Fig. 5.10. This happens because the stochastic thermal field helps to give the initial push to move the magnetization away from the parallel or antiparallel configuration, giving way for the torque to act on it and shortening the incubation period. Next, the switching time difference between room and zero temperature is investigated, at various values of the TMR. Results for both AP to P and P to AP switching are reported in Fig. 5.11. It can be observed that the switching time is always longer at zero temperature than at room temperature, as expected. Notably, the switching time shows also a clear dependence on the TMR, decreasing with higher TMR values. This dependence of the switching time on the TMR can be explained with the help of (3.50) and (3.51). The torque intensity increases with the polarizing factor due to the relation expressed in (3.50), while the polarizing factor increases with the TMR as described by (3.51). Thus, higher TMR values create a stronger torque, making the switching happen faster.

5.3.3 Macrospin Approximation

To have a deeper understanding of the possible reasons for the dependence of the current correction on the TMR and temperature, switching simulations are performed in the macrospin approximation, where the magnetization of the whole FL is represented by a single vector. In the FD implementation, this is achieved by representing the FL as a single cell with dimensions 40 40 1 7 nm . The simulations are carried out at

Die approbierte gedruckte Originalversion dieser Dissertation ist an der TU Wien Bibliothek verfügbar.
The approved original version of this doctoral thesis is available in print at TU Wien Bibliothek.
TU WIEN Bibliothek Your knowledge hub

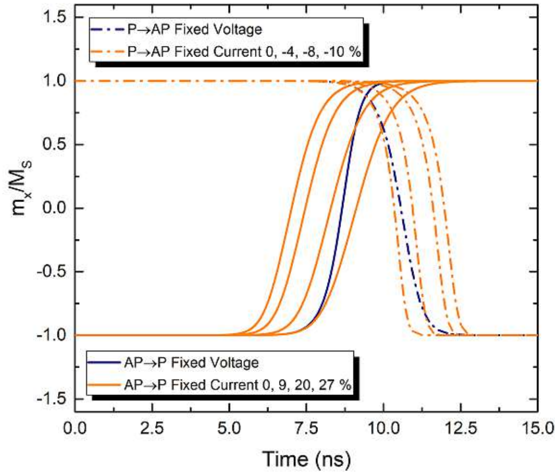

Figure 5.12: Switching realizations in the macrospin scenario for the fixed voltage and fixed current density models, with different values of the correction. A higher amount of correction in the fixed current density approach produces faster (slower) switching for AP to P (P to AP). The two approaches present a different slope during switching. The figure was published in [116].

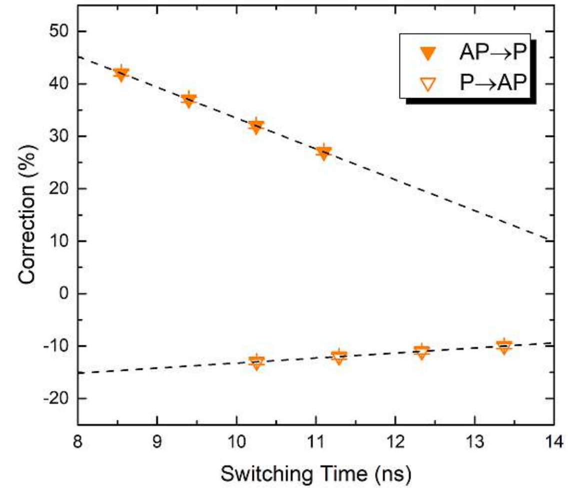

Figure 5.13: Dependence of the correction on the switching time in the macrospin scenario. When the switching becomes faster, a higher amount of correction is required for the fixed current approach to reproduce the switching time of the fixed voltage one. The figure was published in [116].

zero temperature. In the macrospin approximation, the nucleation process portrayed in Fig. 5.3 is not possible. Moreover, at zero temperature, the thermal field is not acting, so that there is no contribution which can remove the magnetization from its initial parallel or antiparallel orientation. For this reason, the starting magnetization direction is slightly tilted, so that the STT torque can act and achieve magnetization reversal.

Fig. 5.12 presents results obtained from the fixed voltage and fixed current density approaches, for several values of the current correction and for both AP to P and P to AP realizations. As only one magnetization vector is present, there is no possibility for current density redistribution in the fixed total current approach, and expressions (4.25) and (4.26) produce exactly the same torque. The macrospin simulations demonstrate clearly that the switching process with a fixed voltage is steeper for AP to P switching than that with a fixed current. In order to compensate for the more gradual slope at fixed current and obtain similar switching time, the switching process must start earlier, which is achieved by increasing the current value. For the switching from P to AP, with the fixed current model providing a steeper magnetization trajectory, the switching is slower in the fixed voltage approach. Therefore, the current needs to be lowered to make the switching start later and compensate for the difference in slope, achieving similar switching time.

Die approbierte gedruckte Originalversion dieser Dissertation ist an der TU Wien Bibliothek verfügbar.
The approved original version of this doctoral thesis is available in print at TU Wien Bibliothek.
TU WIEN Bibliothek Your knowledge hub

The difference in the switching trajectory between the two approaches can be explained by looking at equations (2.4), (3.50) and (3.51), describing the conductance, the torque and the relation between polarization and TMR in an MTJ. In the model with fixed voltage the dependence of the current on the magnetization configuration, coming from (2.4), completely compensates the angular dependence in the denominator of (3.50), so that the torque magnitude only depends on the sine of the angle between magnetization vectors, coming from the vector product term [16, 99, 118]. Under the fixed current assumption, the denominator is not compensated, and it is minimal at the beginning of AP to P switching. At this point, the torque is the same as under the fixed voltage assumption, due to the choice of having the same current at the beginning of switching in the two approaches. The denominator then grows larger as the configuration proceeds towards P, reducing the torque. This trend must be compensated by a current correction to increase the initial value of the torque. The scenario is opposite for the case of P to AP switching, with the torque becoming larger as the magnetization proceeds towards the antiparallel orientation, in agreement with the switching results of Fig. 5.12. The denominator is maximal at the beginning and becomes weaker during magnetization reversal, and the trend can be compensated by employing a weaker current.

By gradually increasing the initial tilting angle, the switching process can be made faster without changing the system parameters. The dependence of the current correction on the switching time can thus be evaluated, as reported in Fig. 5.13. The data show that a faster switching requires a higher correction to the current value. As the average switching time is shorter at room temperature, it explains a slightly larger current correction required to match the results for switching times from all three models at T=300 K as compared to the simulations at T=0 K. It also explains the dependence of the correction on the TMR, as higher TMR values give a stronger torque and decrease the switching time for both AP to P and P to AP switching, so that the current correction required becomes higher.

5.3.4 Dependence on the Surface and Resistance Area

In order to corroborate these findings, switching simulations with different diameters of the stack, providing different surface areas, are performed at room temperature. As the resistance of a structure is inversely proportional to the surface area , the total current, given by $_{\mathrm{C}} =$, is directly proportional to it. The current density is approximately given by $_{\mathrm{C}} = {}_{\mathrm{C}}$, so its value does not depend on the lateral size of the MTJ. By keeping the same voltage employed for the previous simulations, the same current density is also maintained. Fig. 5.14 reports a comparison between switching simulations performed at diameter values of 40 nm and 50 nm, providing a surface area value of 1257 nm and 1963 nm , respectively. The results show how the magnetization reversal happens faster in the wider stack, for both AP to P and P to AP realizations. when the lateral size of the junction is bigger, the resistance is lower, and the total current flowing through the structure is higher. Moreover, the

TU Bibliothek Your knowledge hub WIEN
Die approbierte gedruckte Originalversion dieser Dissertation ist an der TU Wien Bibliothek verfügbar.
The approved original version of this doctoral thesis is available in print at TU Wien Bibliothek.

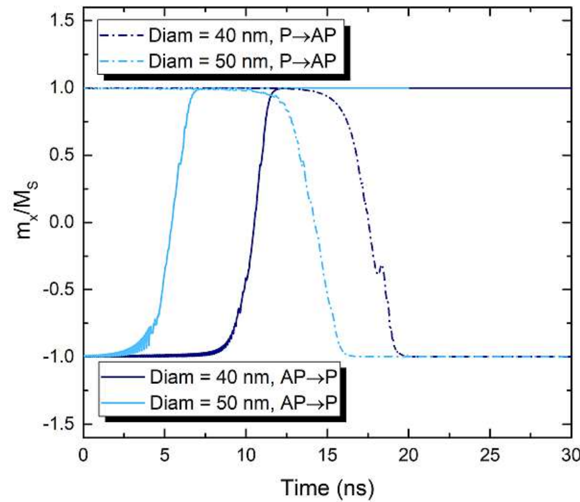

Figure 5.14: Comparison between switching realizations for the fixed voltage model, with TMR=200% and T=300 K, at diameters of 40 nm and 50 nm. The switching is slower for the smaller structure size. The figure was published in [116].

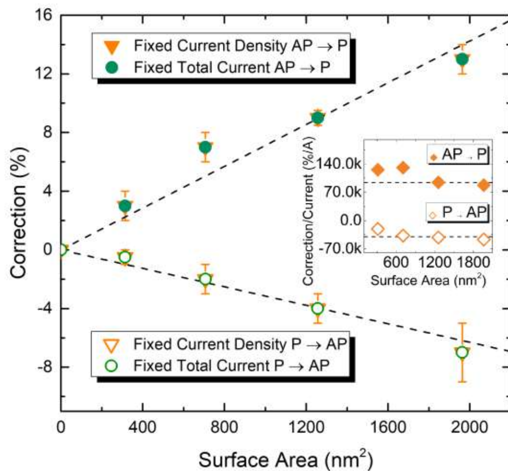

Figure 5.15: Dependence of the current correction on the surface area of the structure at T=300 K, for both P to AP and AP to P switching. The dashed lines represent a linear fit. In the inset, the ratio of correction over total current is shown for every surface area. The figure was published in [116].

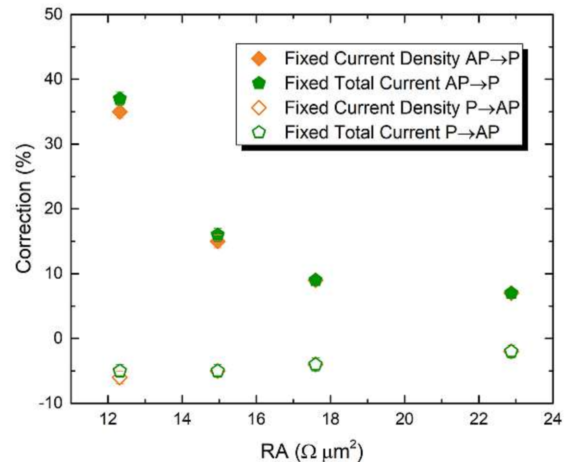

Figure 5.16: Dependence of the current correction on the resistance area of the structure at T=300 K, for both P to AP and AP to P switching. The figure was published in [116].

nucleation of domains with tilted magnetizations is easier for bigger diameters, as it is more difficult for the exchange interaction to keep the magnetization vectors in the whole layer aligned. This reduces the incubation time and creates an overall faster

Die approbierte gedruckte Originalversion dieser Dissertation ist an der TU Wien Bibliothek verfügbar.
The approved original version of this doctoral thesis is available in print at TU Wien Bibliothek.
TU WIEN Bibliothek Your knowledge hub

switching process. The dependence of the correction on the size of the structure is reported in Fig. 5.15, showing how the required correction is higher for larger surface areas. The inset shows that the ratio of the correction on the current value does not depend on the area, underlining how the correction increases with the total current.

Finally, Fig. 5.16 shows the dependence of the correction on the resistance area (RA) of the structure, achieved by changing the values of both $_{\mathrm{P}}$ and $_{\mathrm{AP}}$, so as to keep the same TMR. At lower RA values, both the current and the current density increase, leading to much faster switching, which in turn lead to higher values of the current correction required to reproduce the switching times of the fixed voltage approach. In this case, the dependence of the correction cannot be successfully fitted by a linear regression. The dependence of the correction on both the surface area and the resistance area agrees well with the previous discussion, as in both cases, when the switching time becomes shorter (for higher surface area and lower RA), the required correction increases.

With an understanding of the behavior of the current correction, it can be applied to allow for the simple constant current density approach to correctly reproduce the switching time distribution, so that it can be employed in place of more complex and time consuming approaches. The development of a compact model for the correction will thus allow to obtain fast simulation tools for aiding and guiding the design of future devices.

Die approbierte gedruckte Originalversion dieser Dissertation ist an der TU Wien Bibliothek verfügbar.
The approved original version of this doctoral thesis is available in print at TU Wien Bibliothek.
TU WIEN Bibliothek Your knowledge hub

TU Bibliothek Your knowledge hub WIEN
Die approbierte gedruckte Originalversion dieser Dissertation ist an der TU Wien Bibliothek verfügbar.
The approved original version of this doctoral thesis is available in print at TU Wien Bibliothek.

Chapter 6

Spin and Charge Drift-Diffusion for the Computation of Spin Torques and Finite Element Implementation

The driving factor of the writing process in modern MRAM cells is the torque generated by the polarization process of electrons transiting through the ferromagnetic layers in an MTJ stack. The simulation of the switching process can be achieved by solving the LLG equation for magnetization dynamics, with the inclusion of a term describing the torque acting on the magnetization. As seen in the previous chapters, such term can be defined by employing a Slonczewski-like torque approach [16]. This, however, allows to approximately simulate the magnetization dynamics of a thin free layer only. A more complete description of the process can be obtained by computing the non-equilibrium spin accumulation across the whole structure. The following sections demonstrate that a more general expression for the torque term $_{\mathrm{S}}$ entering (3.44) can be given as [25, 119, 120]

$$_{\mathrm{S}} = \quad _{\mathrm{e}}\frac{\quad}{_J} \quad _{\mathrm{e}}\frac{(\quad)}{_\varphi} \tag{6.1}$$

where $_{\mathrm{e}}$ is the electron diffusion coefficient. The first term describes precession around the exchange field and is characterized by the exchange length $_J$, and the second term describes the dephasing process of the spins of the transiting electrons, and is characterized by the dephasing length $_\varphi$.

The spin accumulation describes the deviation of the polarization of the conducting electrons from the equilibrium configuration created by a charge current density $_{\mathrm{C}}$, in units of the transported magnetic moment (A/m). Thus, by definition is non-zero only when an electric current is flowing through the system [83]. A solution for in all nonmagnetic and ferromagnetic layers of an MRAM cell can be obtained by means of the spin and charge drift-diffusion formalism.

Die approbierte gedruckte Originalversion dieser Dissertation ist an der TU Wien Bibliothek verfügbar.
The approved original version of this doctoral thesis is available in print at TU Wien Bibliothek.
TU Bibliothek WIEN Your knowledge hub

6.1 Spin and Charge Drift-Diffusion

Spin and charge drift-diffusion equations in the presence of a spin-valve structure where the ferromagnetic layers have co-linear (parallel or anti-parallel) magnetization were first derived by T. Valet and A. Fert [121]. A formulation of the equations for the computation of in the presence of arbitrary magnetization orientation was later reported by S. Zhang, P. Levy and A. Fert [98], and will be hereby summarized. In a magnetic multilayer with the current perpendicular to the plane of the layer, along the x-direction, the linear response of the current to the electric field can be written in spinor form as

$$= \quad (\ ) \quad — \tag{6.2}$$

where is the electric field, which can be expressed in terms of the electric potential as $=$ / , and , , , and are the 2 2 spinor matrices representing the current density, the conductivity, the diffusion coefficient, and the accumulation at a given position. For a metal, the diffusion constant and the conductivity are connected via the Einstein relation $=$ $_{\mathrm{F}}$, with $_{\mathrm{F}}$ the spin-dependent density of states at the Fermi level. These matrices can in general be expressed in terms of the Pauli matrix vector $\boldsymbol{\sigma}$:

$$= \quad + \quad \boldsymbol{\sigma} \tag{6.3}$$

$$= \quad + \quad \boldsymbol{\sigma} \tag{6.4}$$

$$= \quad + \quad \boldsymbol{\sigma} \tag{6.5}$$

2 is the charge accumulation, is related to the conductivity by $= 2$, and is related to the electron diffusion coefficient by $_{\mathrm{e}} = 2$. The two vectors and are related to the different conductivity and diffusion constant for the majority and minority electrons, labeled $^{\uparrow}$, $^{\uparrow}_{\mathrm{e}}$ and $^{\downarrow}$, $^{\downarrow}_{\mathrm{e}}$, respectively. This difference is characterized by the conductivity polarization parameter $_{\sigma} = (^{\uparrow} \quad ^{\downarrow}) \ (^{\uparrow} + ^{\downarrow})$ and the diffusion polarization parameter $_{\mathrm{D}} = (^{\uparrow}_{\mathrm{e}} \quad ^{\downarrow}_{\mathrm{e}}) \ (^{\uparrow}_{\mathrm{e}} + ^{\downarrow}_{\mathrm{e}})$. For a transition ferromagnet, is then defined as $= _{\sigma}$ and $= _{\mathrm{D}}$. The two polarization parameters are different when the density of states for majority and minority electrons is not the same. By inserting (6.3)-(6.5) into (6.2), one obtains the following expressions for the charge current density $_{\mathrm{C}}$ and spin polarization current density $_{\mathrm{S}}$ along the x-direction:

$$_{\mathrm{C}} \quad \mathrm{Re}\Big(\mathrm{Tr}\Big[\ \Big]\Big) = \quad + \frac{}{_{\mathrm{B}}} \ _{\mathrm{D}} \ _{\mathrm{e}} — \tag{6.6a}$$

$$_{\mathrm{S}} \quad \mathrm{Re}\Big(\mathrm{Tr}\Big[\boldsymbol{\sigma} \ \Big]\Big) = \frac{_{\mathrm{B}}}{} \ _{\sigma} \qquad _{\mathrm{e}} — \tag{6.6b}$$

Terms involving the spatial derivative of the charge accumulation have been ignored, as in metals the distribution of charges can be considered uniform. The factor $_{\mathrm{B}}$ converts from the units of electric charge, , to the ones of the spin polarization current density, . The latter can be converted to the typical units of spin current

Die approbierte gedruckte Originalversion dieser Dissertation ist an der TU Wien Bibliothek verfügbar.
The approved original version of this doctoral thesis is available in print at TU Wien Bibliothek.
TU WIEN Bibliothek Your knowledge hub

density by multiplication with the factor $\hbar\ (2\ _{\mathrm{B}})$. The spin current polarization density will be referred to as spin current for brevity from now on.

Equation (6.6) only describes the spin and charge currents on the axis perpendicular to a multilayer structure. The generalization to a three-dimensional formulation leads to the following expressions:

$$_{\mathrm{C}} = \quad + \frac{}{\mathrm{B}}\ _{\mathrm{D}}\ _{\mathrm{e}}(\quad)^{\mathrm{T}} \tag{6.7a}$$

$$_{\mathrm{S}} = \ -\frac{\mathrm{B}}{}\ _{\sigma} \quad (\quad) \quad _{\mathrm{e}} \tag{6.7b}$$

is the outer product, $_{\mathrm{C}}$ is the charge current density vector, $_{\mathrm{S}}$ is the spin current tensor, where the components $_{\mathrm{S,ij}}$ indicate the flow of the i-th component of spin polarization in the j-th direction, and is the vector gradient of , with components $(\quad)_{\mathrm{ij}} = \ _{\mathrm{i}}/\ _{\mathrm{j}}$. The term $(\quad)^{\mathrm{T}}$ is a vector with components $\left((\quad)^{\mathrm{T}}\right)_{\mathrm{i}} = \sum_{\mathrm{j}} (\ _{\mathrm{j}}/\ _{\mathrm{i}})\ _{j}$. In case the current density distribution is known, the spin current can be expressed in terms of the charge current by inserting (6.7a) into (6.7b):

$$_{\mathrm{S}} = \ -\frac{B}{}\ _{\sigma} \quad \left(\ _{\mathrm{C}} \quad \frac{}{B}\ _{D}\ _{e}(\quad)^{\mathrm{T}}\right) \quad _{e} \tag{6.8}$$

The equation of motion for the spin accumulation in a ferromagnet is determined by the interaction of the local magnetization moment and the spin of the itinerant electrons. This interaction can be described by the Hamiltonian term

$$_{\mathrm{int}} = \tag{6.9}$$

where is the coupling strength between local moments and itinerant electrons. The following equation of motion for the spin accumulation can thus be derived:

$$\frac{\mathrm{d}}{\mathrm{d}} \quad \frac{}{\hbar} \quad = \ \frac{}{_{\mathrm{sf}}} \tag{6.10}$$

$_{\mathrm{sf}}$ is the spin-flip relaxation time of the conduction electrons. The second term on the left hand side describes the processional motion of the accumulation due to the exchange interaction. It plays a role when the non-equilibrium spin accumulation and the local magnetization moment are not parallel. The rate of change of can be expressed in terms of its partial derivative in time and the divergence of the spin current as $\mathrm{d}\ /\mathrm{d}\ = \ /\ + \ _{\mathrm{S}}$. By replacing this expression in (6.10), the equation for the spin accumulation becomes

$$\frac{}{} = \quad _{\mathrm{S}} \quad _{\mathrm{e}}\frac{}{_{sf}} + \ _{\mathrm{e}}\frac{}{_{J}} \tag{6.11}$$

where the two length parameters $_{\mathrm{sf}}$ and $_{\mathrm{J}}$ are defined as $_{\mathrm{sf}} = \sqrt{\ _{\mathrm{e}}\ _{\mathrm{sf}}}$ and $_{\mathrm{J}} = \sqrt{\ _{\mathrm{e}}\hbar\ }$. $_{\mathrm{S}}$ is the divergence of $_{\mathrm{S}}$ with components $\left(\quad _{\mathrm{S}}\right)_{\mathrm{i}} = \sum_{\mathrm{j}}\ _{\mathrm{S,ij}}/\ _{\mathrm{j}}$.

Die approbierte gedruckte Originalversion dieser Dissertation ist an der TU Wien Bibliothek verfügbar.
The approved original version of this doctoral thesis is available in print at TU Wien Bibliothek.
TU WIEN Bibliothek Your knowledge hub

Equation (6.11) can be further simplified by taking into consideration the fact that the typical time-scales for the spin accumulation and the magnetization are very different. While the former is of the order of picoseconds, the latter is of the order of nanoseconds [98]. For the computation of the spin torque, to be added to the LLG equation (3.44), it is thus sufficient to consider a steady-state expression for the spin accumulation. This assumption was numerically verified in [122]. With $/ = 0$, the equation describing the spin accumulation becomes

$$\mathrm{S} \qquad \mathrm{e}\frac{}{sf} + \mathrm{e}\frac{}{J} = 0 \tag{6.12}$$

An expression for the torque can be extracted from (6.12) by considering a conservation argument [123]. In the original work of Slonczewski [14], it was argued that the spin current lost by the conducting electrons, described by the divergence term, must have been gained by the magnetization, due to conservation of the total angular momentum. This is always valid in the absence of additional relaxation mechanisms for the spin accumulation [99]. However, in the presence of spin-orbit coupling, part of the angular momentum is transferred to the lattice. This process is responsible for the spin-flip relaxation, described by the $_{\mathrm{sf}}$ term. Spin current lost due to this mechanism does not contribute to the torque acting on the magnetization. The torque can then be obtained as

$$\mathrm{S} = \qquad \mathrm{S} \qquad \mathrm{e}\frac{}{\mathrm{sf}} = \qquad \mathrm{e}\frac{}{J} \tag{6.13}$$

6.1.1 Spin Dephasing Term

The previous section showed the derivation of a spin torque expression where both the absorption and decay of the transverse spin accumulation components are governed by the exchange length $_{\mathrm{J}}$. Another possible mechanism for the absorption of the transverse components is the dephasing process. Dephasing occurs when, after traveling for a certain distance, different spins have precessed different amounts, so that their transverse components tend to cancel out [120]. In the context of spin transfer torques, this can occur from the variation of electron velocities over the Fermi surface [124] or from spins precessing at the same rate but arriving at different times due to scattering [125]. The behavior of the spin accumulation with both precessional and dephasing terms was described in terms of the Continuous Random Matrix Theory (CRMT) in [125], and the equivalence of CMRT and the spin and charge drift-diffusion formalism was shown. This section gives a brief overview of the derivation thereby presented.

The Landauer-Büttiker formalism, or scattering formalism, is the base for CRMT, and is expressed through a scattering matrix relating the initial state and the final state of a physical system undergoing a scattering process [126]. The form of the matrix is derived by considering a system where two leads are connected to a central scattering region. The leads are quasi-one-dimensional waveguides. By assuming the

Die approbierte gedruckte Originalversion dieser Dissertation ist an der TU Wien Bibliothek verfügbar.
The approved original version of this doctoral thesis is available in print at TU Wien Bibliothek.
TU WIEN Bibliothek Your knowledge hub

solutions to the Schrödinger equation $^{\pm}_{n} = (\ )\exp(\ _{n}\ )$ are known outside of the scattering region, the wave functions $^{\pm}(\ )_{L/R}$ on the left (L) and right (R) side can be expressed as a linear combination of them:

$$^{\pm}(\ )_{L/R} = \sum_{n} {}^{\pm}_{n,L/R}\ (\ )\exp(\ _{n}\ ) \tag{6.14}$$

$(\ )_{L}$ and $^{-}(\ )_{R}$ are the incoming wave functions, while $^{-}(\ )_{L}$ and $(\ )_{R}$ are the outgoing wave functions. By expressing the vectors containing the expansion coefficients $^{\pm}_{n,L/R}$ as $^{\pm}_{L/R}$, the incoming and outgoing vectors can be related by a matrix composed of reflection ($'$) and transmission ($'$) submatrices:

$$\begin{pmatrix} ^{-}_{L} \\ _{R} \end{pmatrix} = \begin{pmatrix} & ' \\ ' & \end{pmatrix} \begin{pmatrix} _{L} \\ ^{-}_{R} \end{pmatrix} \qquad \begin{pmatrix} & ' \\ ' & \end{pmatrix} = \tag{6.15}$$

If two conductors A and B described by this scattering formalism are in series, the transmission and reflection of the whole system can be written as

$$_{AB} = \ _{B}\frac{1}{1 \quad _{A}\ '_{B}}\ _{A} \tag{6.16a}$$

$$_{AB} = \ _{B} + \ _{B}\frac{1}{1 \quad _{A}\ '_{B}}\ _{A}\ '_{B} \tag{6.16b}$$

The conductance of a system can be expressed in terms of its transmission matrix as

$$= -T \qquad T = \mathrm{Tr}[\ ^{\dagger}] \tag{6.17}$$

The value T corresponds to the sum over the probabilities of being transmitted from one side of the system to the other, and is the Planck constant. The same expression holds true for the reflection probabilities, represented by the quantity $R = \mathrm{Tr}[\ ^{\dagger}]$. By taking a semi-classical limit and assuming that successive reflections mix together different channels, it can be assumed that each electron traveling through the system picks up a certain phase. The transmission through the whole system takes then the form

$$_{AB} = \ _{B}\frac{1}{1 \quad _{A}\ '_{B}}\ _{A} \tag{6.18}$$

where $= \exp(\ )$ describes the phase acquired by the traveling electrons. An expression for the conductance is obtained by taking the average over all values of :

$$_{AB} = - \ T_{AB} \tag{6.19}$$

The average value can be computed through the residual theorem by integrating over the phase in the complex space. This leads to the expression

$$T_{AB} = T_{B}\frac{1}{1 \quad R_{A}R'_{B}}T_{A} \tag{6.20}$$

Die approbierte gedruckte Originalversion dieser Dissertation ist an der TU Wien Bibliothek verfügbar.
The approved original version of this doctoral thesis is available in print at TU Wien Bibliothek.
TU Bibliothek WIEN Your knowledge hub

which has the same form of (6.16a), but it relates probabilities instead of amplitudes. The same is also true for the quantity R_{AB} . This means that, within the semi-classical limit, transport can be described by a scattering-like formalism concerning only probabilities.

The same theoretical description, employed until now only in the presence of multiple channels, can also be applied in the presence of the additional spin degree of freedom. In this case, the transmission and reflection matrices have dimensions of $4\ _{\mathrm{ch}}\quad 4\ _{\mathrm{ch}}$, with $_{\mathrm{ch}}$ the number of channels. The random matrix theory (RMT) employed in [126] can be applied to account for both mixing of the contributions in different channels and loss of coherence of the waves traveling through the system, in a similar fashion to the average over the phase previously shown. The resulting theory presents a structure similar to the scattering formalism, with $4\quad 4$ spin-dependent transmission and reflection matrices, indicated by a hat. The block matrix describing transport through a conductor takes the form

$$= \begin{pmatrix} & ' \\ & ' \end{pmatrix} \tag{6.21}$$

Each of the four submatrices is defined from the $4\ _{\mathrm{ch}}\quad 4\ _{\mathrm{ch}}$ matrices of the scattering theory, relating different spins and channels, by the following expression:

$$_{\sigma\eta,\sigma'\eta'} = \frac{1}{_{\mathrm{ch}}}\mathrm{Tr}_{N_{\mathrm{ch}}}\left[\ _{\sigma\eta}\ ^{\dagger}_{\sigma'\eta'}\right] \tag{6.22}$$

and indicate the up ( ) or down ( ) spin orientation. Similar expressions hold for the other transmission and reflection matrices. The most important contributions to the obtained matrix are the probabilities $\mathrm{T}_{\sigma\eta} = \ _{\sigma\eta,\sigma\eta}$ and the mixing coefficients $\mathrm{T}_{\mathrm{mx}} = \ _{\sigma\sigma,-\sigma-\sigma}$. The other entries in the matrix have a negligible contribution to the overall transport description and can be disregarded [126]. The final form of the matrix is then given by

$$= \begin{pmatrix} \mathrm{T}_{\uparrow\uparrow} & 0 & 0 & \mathrm{T}_{\uparrow\downarrow} \\ 0 & \mathrm{T}_{\mathrm{mx}} & 0 & 0 \\ 0 & 0 & \mathrm{T}^{*}_{\mathrm{mx}} & 0 \\ \mathrm{T}_{\downarrow\uparrow} & 0 & 0 & \mathrm{T}_{\downarrow\downarrow} \end{pmatrix} \tag{6.23}$$

Similar expressions hold true for the other matrices entering (6.21). The coefficients $\mathrm{T}_{\sigma\eta} = \ _{\sigma\eta,\sigma\eta}$ describe the probability of an electron with spin to be transmitted with spin . The mixing coefficients are related to the precession and loss of coherence of electrons with a spin non-colinear with the magnetization:

$$\mathrm{T}_{\mathrm{mx}} \quad \exp(\quad _{\perp} + \quad _{\mathrm{L}}) \tag{6.24}$$

is the thickness of the ferromagnetic conductor, and $_{\mathrm{L}}$ is the Larmor precession length. The term containing $_{\perp}$ is related to the fact that the amount of precession depends on the direction of incidence of the electron into the ferromagnet. Two electrons with different incidence angles will undergo a dephasing process. This results is

Die approbierte gedruckte Originalversion dieser Dissertation ist an der TU Wien Bibliothek verfügbar.
The approved original version of this doctoral thesis is available in print at TU Wien Bibliothek.
TU WIEN Bibliothek Your knowledge hub

an exponentially decaying spin density orthogonal to the local magnetization which absorbs the transverse components of the spin current. $_{\perp}$ indicates the typical length over which these absorption process occurs.

Most of the quantities described until now can be recast in terms of semi-classical properties. The conductance can now be expressed as

$$= (\mathrm{T}_{\uparrow\uparrow} + \mathrm{T}_{\uparrow\downarrow} + \mathrm{T}_{\downarrow\uparrow} + \mathrm{T}_{\downarrow\downarrow}) \quad _{\mathrm{sh}} \tag{6.25}$$

where $_{\mathrm{sh}} = \quad (\quad _{\mathrm{ch}})$ is the Sharvin resistance. It corresponds to the resistance of a perfectly transparent waveguide, with $_{\mathrm{ch}}$ propagating transversal modes. As shown in [126], the addition laws for transmission and reflection in equation (6.20) are still valid. Moreover, it is shown that the number of degrees of freedom can be reduced from the incoming and outgoing wave function coefficients to vectors of length 4, storing only the charge and spin degrees of freedom. These vectors are noted $^{\pm}_{4,\mathrm{L/R}}$, and the incoming and outgoing vectors are related through the matrix (6.21) as

$$\begin{pmatrix} ^{-}_{4,\mathrm{L}} \\ _{4,\mathrm{R}} \end{pmatrix} = \begin{pmatrix} _{4,\mathrm{L}} \\ ^{-}_{4,\mathrm{R}} \end{pmatrix} \tag{6.26}$$

As shown in [125], one can demonstrate the equivalence of the random matrix description to the spin and charge drift-diffusion formalism. First, transport in a discretized one-dimensional conductor, divided into parts, is considered. The $_4$ vectors of each part can be related through the node equations

$$_{4,\mathrm{L}}[\ +1] = \ _{4,\mathrm{R}}[\ ] \tag{6.27a}$$

$$^{-}_{4,\mathrm{L}}[\ +1] = \ ^{-}_{4,\mathrm{R}}[\ ] \tag{6.27b}$$

where is an index going from 1 to . Through a variable change, the $_4$ vectors can be employed to obtain the four dimensional potential $_4$ and current $_4$ in the system [127]:

$$_4 = \frac{1}{2}(\ _{4,\mathrm{L}} + \ ^{-}_{4,\mathrm{L}}) \tag{6.28a}$$

$$_4 = \frac{1}{2}(\ _{4,\mathrm{L}} \quad ^{-}_{4,\mathrm{L}}) \tag{6.28b}$$

After the change of variables, and by assuming that transmission and reflection properties do not depend on the direction, equations (6.26) and (6.27) can be combined to obtain the following relations:

$$2(\ _4[\ +1] \quad _4[\ ]) = (\quad +1)(\ _4[\ +1] \quad _4[\ ] \quad _4[\ +1] \quad _4[\ ]) \tag{6.29a}$$

$$2(\ _4[\ +1] \quad _4[\ ]) = (\ + \quad 1)(\ _4[\ +1] + \ _4[\ ] \quad _4[\ +1] + \ _4[\ ]) \tag{6.29b}$$

Die approbierte gedruckte Originalversion dieser Dissertation ist an der TU Wien Bibliothek verfügbar.
The approved original version of this doctoral thesis is available in print at TU Wien Bibliothek.
TU WIEN Bibliothek Your knowledge hub

In order to go from the discrete description presented until now to a continuous one which recovers the drift-diffusion formalism, one must go to the limit where the length of each material slice goes to the infinitesimal quantity d . This gives the possibility of describing the thin slices' matrix components with the following parametrization [128]:

$$= 1 \quad {}_{\mathrm{t}}\,\mathrm{d} \tag{6.30a}$$

$$= \quad {}_{\mathrm{r}}\,\mathrm{d} \tag{6.30b}$$

$_{\mathrm{t}}$ and $_{\mathrm{r}}$ are 4 4 matrices. These expressions can be inserted back into equation (6.29), to obtain the following formulation:

$$2(\ {}_4(\ +\mathrm{d} \ ) \quad {}_4(\ )) = \mathrm{d} \ (\ {}_{\mathrm{r}} + \ {}_{\mathrm{t}})(\ {}_4(\ +\mathrm{d} \ ) \quad {}_4(\ ) \quad {}_4(\ +\mathrm{d} \ ) \quad {}_4(\ )) \tag{6.31a}$$

$$2(\ {}_4(\ +\mathrm{d} \ ) \quad {}_4(\ )) = \mathrm{d} \ (\ {}_{\mathrm{r}} \quad {}_{\mathrm{t}})(\ {}_4(\ +\mathrm{d} \ ) + \ {}_4(\ ) \quad {}_4(\ +\mathrm{d} \ ) + \ {}_4(\ )) \tag{6.31b}$$

The equations can then be developed to the first order in d to obtain the continuous differential equations

$$\frac{\quad {}_4}{\quad}(\ ) = 2 \quad {}_4(\ ) \tag{6.32a}$$

$$\frac{\quad {}_4}{\quad}(\ ) = 2 \quad {}_4(\ ) \tag{6.32b}$$

where 2 $=$ $_{\mathrm{t}} +$ $_{\mathrm{r}}$ and 2 $=$ $_{\mathrm{t}}$ $_{\mathrm{r}}$. These matrices, defined so that they fit the Valet-Fert theory, take the form

$$= \begin{pmatrix} \uparrow & 0 & 0 & 0 \\ 0 & \mathrm{mx,eff} & 0 & 0 \\ 0 & 0 & {}^{*}_{\mathrm{mx,eff}} & 0 \\ 0 & 0 & 0 & \downarrow \end{pmatrix} \tag{6.33a}$$

$$= \begin{pmatrix} \mathrm{sf} & 0 & 0 & \mathrm{sf} \\ 0 & \tau & 0 & 0 \\ 0 & 0 & {}^{*}_{\tau} & 0 \\ \mathrm{sf} & 0 & 0 & \mathrm{sf} \end{pmatrix} \tag{6.33b}$$

The coefficients of these two matrices are linked to the characteristic length scales of the material. $_{\uparrow\downarrow} = 1$ $_{\uparrow\downarrow}$ is the mean free path for majority (minority) electrons. It can be rewritten in terms of the mean free path $_{*} = (1 \ {}_{\uparrow} + 1 \ {}_{\downarrow})^{-}$ and spin asymmetry of the material , introduced by Valet-Fert in [121] as $_{\uparrow\downarrow} = (1 \quad) \ (2 \ {}^{*})$. These length scales are connected to the spin-dependent resistivities of the Valet-Fert theory [121] as $_{\uparrow\downarrow} = \ {}_{\mathrm{sh}} \ {}_{\uparrow\downarrow}$ and $_{*} = \ {}_{\mathrm{sh}} \ (4 \ {}_{*})$. $_{\mathrm{mx,eff}} = \ {}_{\mathrm{mx}} \ 2 + (\ {}_{\uparrow} + \ {}_{\downarrow}) \ 2$ is the component describing the behavior of the electrons with spin direction transverse to the local magnetization. $_{\mathrm{mx}} = 1 \ {}_{\perp} \quad {}_{\mathrm{L}}$ is of ballistic origin, and describes the spin-dependent part of the transport, with the Larmor precession length and spin

Die approbierte gedruckte Originalversion dieser Dissertation ist an der TU Wien Bibliothek verfügbar.
The approved original version of this doctoral thesis is available in print at TU Wien Bibliothek.
TU WIEN Bibliothek Your knowledge hub

penetration length introduced in (6.24). The second part is related to the spin-independent part of the transport. $_{\mathrm{sf}} = {}_{*} \; (4 \; {}_{\mathrm{sf}})$ is connected to spin-flip processes, and $_{\mathrm{sf}}$ is referred to as spin diffusion length. Finally, $_{\tau} = \; {}_{\mathrm{mx}} \; 2 + 2 \; {}_{\mathrm{sf}}$ describes the behavior of the non-conserved part of the transverse spins, including the fact that they are also affected by spin-flip processes.

It is then possible to recover charge and spin potentials ($_{\mathrm{c}}$ and $\boldsymbol{\mu}$, respectively) and charge and spin currents ($_{c}$ and , respectively) from the variables $_{4}$ and $_{4}$. The process, described in detail in [125], involves a change of basis based on the set of 4 4 matrices $\mathrm{I}_{\mathrm{ij}} = \; _{\mathrm{i}} \; {}_{\mathrm{j}}^{*}$, where $= 0 \; 1 \; 2 \; 3,$ is the identity matrix and $_{,\,,}$ are the Pauli matrices. The resulting equations can be expressed in the same units employed for the Zhang-Levi-Fert formalism (6.6) through a change of variables. All the potentials and currents described until now are expressed in units of energy. One can express the charge potentials in units of V as $= \; _{\mathrm{c}}$ and convert the spin potential to spin accumulation, expressed in units of A/m, as $= (\; _{\mathrm{B}} \; (\; _{\mathrm{e}})) \; \boldsymbol{\mu}$ [83]. The charge current expressed in the usual units of A/m is $_{\mathrm{C}} = (\; (4 \; _{\mathrm{sh}})) \; _{\mathrm{c}}$, and the spin polarization current density, expressed in units of , is $_{\mathrm{S}} = \; (4 \; _{\mathrm{B}} \; (\; _{\mathrm{sh}}))$ [83, 123]. Furthermore, the relations between the Zhang-Levy-Fert and Valet-Fert theories derived in [83] can be extended to include the length scales coming from the CMRT derivation:

$$ = \frac{1}{_{*}(1 \qquad)} \tag{6.34a}$$

$$_{\mathrm{sf}} = \frac{_{\mathrm{sf}}}{1} \tag{6.34b}$$

$$_{\mathrm{J}} = \frac{_{*} \; _{\mathrm{L}}}{1} \tag{6.34c}$$

$$_{\varphi} = \frac{_{\perp}}{_{\mathrm{L}}} \; _{J} \tag{6.34d}$$

$$ = \frac{_{*}}{1} \tag{6.34e}$$

$_{\varphi}$ is the spin dephasing length introduced in (6.1), $= \overline{\quad} \; _{\mathrm{e}}$ is the momentum relaxation length, and is the time for momentum relaxation [98, 129]. The spin asymmetry parameter of the Valert-Fert model is equivalent to the conductivity polarization $_{\sigma}$ in the Zhang-Levy-Fert approach. Finally, the spin and charge drift-diffusion equations for transport along the x-direction obtained through the for-

Die approbierte gedruckte Originalversion dieser Dissertation ist an der TU Wien Bibliothek verfügbar.
The approved original version of this doctoral thesis is available in print at TU Wien Bibliothek.
TU WIEN Bibliothek Your knowledge hub

malism of [125] are, after the change of variables:

$$_{\mathrm{C}} = \quad + \frac{}{_{\mathrm{B}}} \, _{\mathrm{D}} \quad _{\mathrm{e}}\frac{}{} \tag{6.35a}$$

$$_{\mathrm{S}} \quad \frac{}{J} \qquad _{\mathrm{S}} \quad \frac{}{\varphi} \qquad (\qquad _{\mathrm{S}}) = \frac{_{\mathrm{B}}}{} \, \sigma \qquad _{\mathrm{e}}\frac{}{} \tag{6.35b}$$

$$\frac{_{\mathrm{C}}}{} = 0 \tag{6.35c}$$

$$\frac{_{\mathrm{S}}}{} \qquad _{\mathrm{e}}\frac{}{sf} + \quad _{\mathrm{e}}\frac{}{J} + \quad _{\mathrm{e}}\frac{(\qquad)}{\varphi} = 0 \tag{6.35d}$$

A generalization of these equations to three-dimensions leads to the following expressions [119, 123, 125]:

$$_{\mathrm{C}} = \quad + \frac{}{_{\mathrm{B}}} \, _{\mathrm{D}} \quad _{\mathrm{e}}(\qquad)^{\mathrm{T}} \tag{6.36a}$$

$$_{\mathrm{S}} \quad \frac{}{J}[\quad]_{\times} \; _{\mathrm{S}} \quad \frac{}{\varphi}[\quad]_{\times\times} \; _{\mathrm{S}} = \frac{_{\mathrm{B}}}{} \, \sigma \qquad (\quad) \qquad _{\mathrm{e}} \tag{6.36b}$$

$$_{\mathrm{C}} = 0 \tag{6.36c}$$

$$_{\mathrm{S}} \qquad _{\mathrm{e}}\frac{}{sf} + \quad _{\mathrm{e}}\frac{}{J} + \quad _{\mathrm{e}}\frac{(\qquad)}{\varphi} = 0 \tag{6.36d}$$

$[\quad]_{\times}$ and $[\quad]_{\times\times}$ indicate the matrices associated with the cross-product and double cross-product with   :

$$[\quad]_{\times} = \begin{pmatrix} 0 & _1 & _2 \\ _3 & 0 & _1 \\ _2 & _1 & 0 \end{pmatrix} \quad [\quad]_{\times\times} = \begin{pmatrix} _2 \quad _3 & _1 \; _2 & _1 \; _3 \\ _1 \; _2 & _1 \quad _3 & _2 \; _3 \\ _1 \; _3 & _2 \; _3 & _1 \quad _2 \end{pmatrix} \tag{6.37}$$

The result for the divergence of the spin current in (6.36c) stems from the absence of electric current sources inside the metallic layers, due to the fast redistribution of any charge imbalance [24, 25]. Equation (6.36d) differs from (6.12) by the presence of the spin dephasing term, dependent on $_{\varphi}$, which leads to the torque expression (6.1) presented at the beginning of the chapter. Another important difference of this formulation is the presence of the additional terms on the left side of equation (6.36b), which mix up the orthogonal spin current components depending on the local magnetization orientation. These terms originate from the underlying ballistic origin of the transverse spin precession or dephasing [123], and depend mainly on the ratio between the momentum relaxation length   and the transverse absorption lengths $_{\mathrm{J}}$ and $_{\varphi}$. For transition metal ferromagnets,   and $_{J}$ have the same order of magnitude [98]. The present dissertation, following [25], focuses on a finite element implementation which does not include these additional terms, showing how an appropriate treatment of the tunneling layer and tuning of the system parameters are able to reproduce the most important properties of the torque expected in MTJs, while still retaining the capability of obtaining all torque contributions in several ferromagnetic layers from a

Die approbierte gedruckte Originalversion dieser Dissertation ist an der TU Wien Bibliothek verfügbar.
The approved original version of this doctoral thesis is available in print at TU Wien Bibliothek.
TU WIEN Bibliothek Your knowledge hub

unified expression. Some considerations about the possible influence of the additional spin current terms on the computed spin torque will be presented in Section 8.5 of Chapter 8.

By employing the spin current expression (6.8), the final set of equations defining the spin accumulation and torque is:

$$\mathrm{S} \quad \mathrm{e}\frac{\quad}{sf} \quad \mathrm{S} = 0 \tag{6.38a}$$

$$\mathrm{S} = \frac{B}{\quad} \sigma \left(\mathrm{C} \quad \frac{\quad}{B} D \quad e(\quad)^{\mathrm{T}} \right) \quad e \tag{6.38b}$$

$$\mathrm{S} = \quad \mathrm{e}\frac{\quad}{J} \quad \mathrm{e}\frac{(\quad)}{\varphi} \tag{6.38c}$$

6.2 Finite Element Implementation

The LLG equation, coupled with the spin and charge drift-diffusion formalism for the computation of the torques, allows to describe the magnetization dynamics of structures containing an arbitrary number of different layers. Analytical solutions to these set of partial differential equations (PDEs) are only possible in simplified scenarios, and numerical methods are necessary to resolve the dynamics in a more general sense. In Chapter 4, a FD implementation of the LLG equation was shown. The FD solver is, however, only able to compute the magnetization dynamics of a thin free layer, with an approximate elliptical shape and thickness of one cell. The FE method is naturally able to handle meshes with complex geometries and several material domains [130, 131], and was therefore employed for the implementation of a solver capable of handling charge, spin accumulation and magnetization dynamics. The implementation was carried out by employing the open-source C++ FE library MFEM [132, 133]. The software responsible for the solution of the spin and charge drift-diffusion equations was developed by the author of the present dissertation. The following sections provide a brief overview of the basic principles of the FE method, followed by the weak formulation of both the LLG and spin and charge drift-diffusion equations, necessary in order to obtain a FE solution.

6.2.1 The Finite Element Method

The FE method is a numerical approach for the computation of approximate solutions to partial differential equations. In order to solve a problem, the simulation domain is first divided into an equivalent system of smaller and simpler bodies, referred to as finite elements, interconnected at nodes (points common to two or more elements) and boundary lines or surfaces. This is achieved by the construction of a mesh of the object, containing a finite number of points. The FE formulation of a given problem approximates the solution of differential equations with the solution of a system of algebraic equations. Instead of solving the problem for the entire body in one operation, the equations are first formulated for each element, and are then combined to obtain a solution valid for the whole domain.

Die approbierte gedruckte Originalversion dieser Dissertation ist an der TU Wien Bibliothek verfügbar.
The approved original version of this doctoral thesis is available in print at TU Wien Bibliothek.
TU WIEN Bibliothek Your knowledge hub

Weak Formulation

The first step in the derivation of a FE representation of a given set of PDEs is to write the equations in the so-called weak formulation. To give an example of the derivation of the weak form of a given problem, the following Poisson equation is considered:

$$= \quad \text{in} \tag{6.39}$$

indicates the integration domain, and is the unknown quantity being solved for. The boundary conditions are

$$= \,_{\mathrm{D}} \quad \text{on} \quad _{\mathrm{D}} \tag{6.40a}$$

$$= \quad \text{on} \quad _{\mathrm{N}} \tag{6.40b}$$

where is the external boundary normal, $_{\mathrm{D}}$ is the portion of the external boundary where Dirichlet boundary conditions (6.40a) are applied, and $_{\mathrm{N}}$ is the portion of the external boundary where Neumann conditions (6.40b) are applied. A Dirichlet condition prescribes the value of the solution, while a Neumann condition prescribes the value of the normal derivative of the solution. A boundary condition needs to be specified for each external boundary of the domain. To obtain the weak formulation, both sides of (6.39) are multiplied by smooth functions, referred to as test functions, and integrated over the simulation domain:

$$\int \quad \mathrm{d} \;= \int \quad \mathrm{d} \tag{6.41}$$

indicates a test function. By applying Gauss theorem, stating that $\int \quad \mathrm{d}$ $= \int_{\partial} \quad \mathrm{d}$, to the function $=$, and by considering the product rule of derivation, one obtains the following equivalence:

$$\int \quad = \int \quad \mathrm{d} \quad \int_{\partial} \quad \mathrm{d} \tag{6.42}$$

By putting this expression back into (6.41), and by considering the boundary conditions (6.40), one obtains the following equation:

$$\int \quad \mathrm{d} \quad \int_{\partial \; \mathrm{D}} \quad \mathrm{d} \;= \int \quad \mathrm{d} \;+ \int_{\partial \; \mathrm{N}} \quad \mathrm{d} \tag{6.43}$$

All the terms containing the unknown quantity where put on the left-hand side, while the known terms are on the right-hand side. The Dirichlet conditions are then assigned in a strong sense, imposing $= \,_{\mathrm{D}}$ on $_{\mathrm{D}}$, and the test function is chosen as to satisfy $= 0$ on $_{\mathrm{D}}$. This way, the weak formulation of the Poisson equation takes the form

$$\int \quad \mathrm{d} \;= \int \quad \mathrm{d} \;+ \int_{\partial \; \mathrm{N}} \quad \mathrm{d} \tag{6.44}$$

The test function and the solution are both assumed to belong to Hilbert spaces, and in the so-called Galerkin method, employed for the results presented in this work,

Die approbierte gedruckte Originalversion dieser Dissertation ist an der TU Wien Bibliothek verfügbar.
The approved original version of this doctoral thesis is available in print at TU Wien Bibliothek.
TU WIEN Bibliothek Your knowledge hub

they belong to the same Hilbert space. In particular, a proper choice for such space, referred to as , is the following:

$$:= \left\{ \quad (\ ) \ \middle| \quad [\ (\ )]^{d} \ \& \quad _{\partial} \quad (\ ) \right\} \tag{6.45}$$

is the number of spacial dimensions under consideration, and ( ) is the set of -integrable functions in . The weak form (6.44) is required to hold for all test functions in . This formulation is referred to as "weak" because it only requires equality in an integral sense, while in the original form (6.39) all the terms must be well defined in all points.

From the Weak Formulation to a System of Algebraic Equations

The next step is the derivation of a numerical approximation of the weak form (6.44). For this purpose, the original domain is divided into smaller regular subdomains . The set of all subdomains contained in is labeled $\mathcal{T}$ and referred to as triangulation. Typical choices for the shape of the subdomains are triangles ot squares in two dimensions and tetrahedrons or hexahedrons in three dimensions, but more complex shapes can also be employed. The set of points defining the discretization, referred to as nodes, is indicated as $\mathcal{N} = \quad_{\mathrm{i}}$, where $_{\mathrm{i}}$ is the coordinate vector of node i. By means of the triangulation, a subspace of where to look for the approximate numerical solution $_{\mathrm{h}}$ can be defined as

$$_{\mathrm{h}} := \left\{ \quad (\ ) \ \middle| \ _{T} \text{ is affine} \quad \mathcal{T} \right\} \tag{6.46}$$

$_{\mathrm{h}}$ is referred to as finite element space. Each function $_{\mathrm{h}}$ belonging to $_{\mathrm{h}}$ is uniquely defined by its values at the nodes. The set of nodes can be divided into two subsets, one containing the nodes at the Dirichlet boundary, $\mathcal{N}_{\mathrm{D}}$, and the other containing the remaining (free) nodes, $\mathcal{N}_{\mathrm{f}}$. In order to get a discretized version of (6.44), the functions $_{\mathrm{h}}$ can be represented in terms of the nodal basis $_{\mathrm{i}}$ of $_{\mathrm{h}}$, characterized as

$$_{\mathrm{i}}(\ _{\mathrm{j}}) = \ _{ij} \tag{6.47}$$

The test functions and the finite element solution $_{\mathrm{h}}$ can be represented with respect to this basis:

$$_{\mathrm{h}}(\ ) = \sum_{i}^{N} \ _{\mathrm{i}} \ _{\mathrm{i}}(\ ) \tag{6.48}$$

is the total number of nodes, and $_{\mathrm{i}} = \ _{\mathrm{h}}(\ _{\mathrm{i}})$ are the values assumed by the approximate solution at the nodes. Fig. 6.1 illustrates a possible approximation of the solution through linear basis functions in a one-dimensional scenario. could be taken to represent the electrical potential in a rod with non-uniform charge distribution. The rod is split into eight equal parts (which represent its triangulation), and the basis functions associated with each node have a value of one at their respective node, and 0 at all other nodes. It can be seen how $_{\mathrm{h}}$, as defined by (6.48),

Die approbierte gedruckte Originalversion dieser Dissertation ist an der TU Wien Bibliothek verfügbar.
The approved original version of this doctoral thesis is available in print at TU Wien Bibliothek.
TU Bibliothek WIEN Your knowledge hub

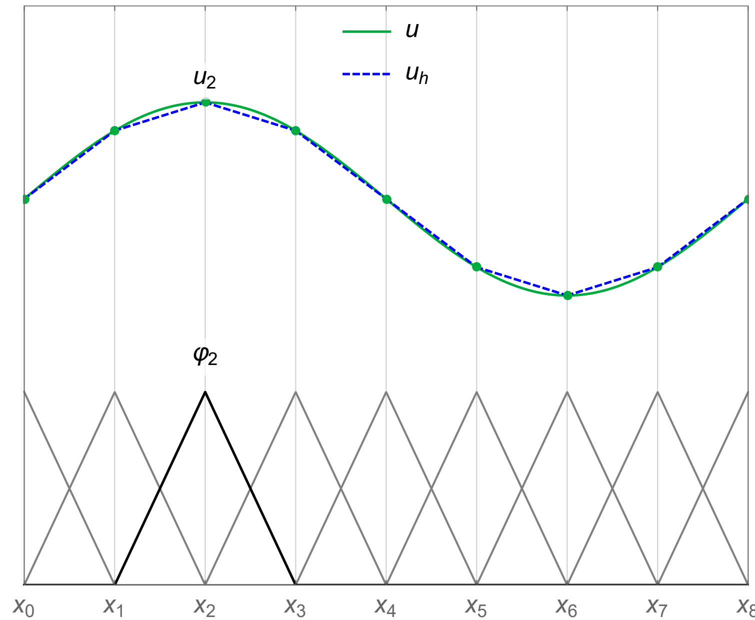

Figure 6.1: Representation of the original solution and the finite element approximation $_h$ in a one-dimensional setting. The basis functions for all the nodes are reported on the bottom of the graph. The basis function and solution value associated with the node are labeled and , respectively.

can be used to approximate the continuous solution . One of the advantages of employing the finite element method is that it offers great freedom in the selection of discretization, both in the choice of elements and basis functions [130]. Moreover, it is possible to locally refine the mesh to obtain a better approximations in the regions where the solution varies quickly.

Determining the coefficients $_i$ gives a unique solution to the problem at hand. The values on $\mathcal{N}_D$ are determined by the Dirichlet boundary conditions:

$$_i = _D(_i) \qquad _i \qquad _D \tag{6.49}$$

All the remaining values can be determined by inserting $_h$ and $_h$ instead of and in (6.44), and then expressing both of them in terms of their nodal values through (6.48). Fulfilling (6.44) for the whole space $_h$ is equivalent to only considering the basis associated with the free nodes $_i$ $_i$ $\mathcal{N}_f$, leading to the following expression:

$$\sum_i \left\{ \int \quad _i \quad _j d \right\} _i = \int \quad _j d \; + \int_{\partial \; _N} \quad _j d \tag{6.50}$$

This equivalence needs to be valid for the whole set of basis functions associated with the free nodes. A matrix $\mathbb{R}^N$ $\mathbb{R}^N$ for the right-hand side of (6.50) and a vector

Die approbierte gedruckte Originalversion dieser Dissertation ist an der TU Wien Bibliothek verfügbar.
The approved original version of this doctoral thesis is available in print at TU Wien Bibliothek.
TU WIEN Bibliothek Your knowledge hub

$\mathbb{R}^N$ for the left-hand side can be defined as

$$_{ji} = \int \quad _{i} \quad _{j}\, d \tag{6.51a}$$

$$_{j} = \int \quad _{j}\, d \quad + \int_{\partial \quad _N} \quad _{j}\, d \tag{6.51b}$$

Both and can be represented in terms of their components acting on the Dirichlet and free nodes:

$$= \begin{pmatrix} _{DD} & _{Df} \\ _{fD} & _{ff} \end{pmatrix} \qquad = \begin{pmatrix} _{D} \\ _{f} \end{pmatrix} \tag{6.52}$$

As only neighboring nodes have overlapping basis functions, is a sparse matrix, with non-zero terms only around the diagonal. By considering the constraint (6.49), and the solution vector $= (\ _i) \ \ \mathbb{R}^N$, $= (\ _D \ \ _f)^{\mathrm{T}}$, (6.50) can be written as the following system of linear equations:

$$\begin{pmatrix} & 0 \\ _{fD} & _{ff} \end{pmatrix} \begin{pmatrix} _{D} \\ _{f} \end{pmatrix} = \begin{pmatrix} _{D} \\ _{f} \end{pmatrix} \tag{6.53}$$

stands for the identity matrix. As the $_D$ values are known, the final symmetric system of $_f$ equations for the determination of the unknown $_f$ values is

$$_{ff} \ _{f} = \ _{f} \quad _{fD} \ _{D} \tag{6.54}$$

6.2.2 Weak Formulation of the Micromagnetic Equations

The implementation of a FE algorithm for the solution of the LLG equation has been of great interest for the solution of micromagnetic problems with meshes of varying complexity. First schemes for a numerical approximation of the weak LLG solution were proposed in [134, 135], by considering only the exchange field contribution to the effective field. In reference [136] the so-called tangent plane integrator scheme, solving for the discrete time derivative, was introduced, and was later generalized to include the full effective field [137, 138]. The unconditional convergence of the tangent plane integrator scheme and of the FE implementation of the spin and charge drift-diffusion equations was proven in [139], and later applied to metallic spin-valves in [23]. Here, the weak formulation of the tangent plane integrator and of the spin and charge transport equations, employed to obtain the results presented in these thesis, is reported. The flow-chart of the simulation process is presented in Fig. 6.2.

LLG Equation

The tangent plane scheme solves the LLG equation for the magnetization derivative $/ \ =$. The weak formulation of the LLG equation comes from the expression

$$\frac{}{} + \quad \frac{}{} = \quad _{\mathrm{eff}} \quad (\quad _{\mathrm{eff}}) \tag{6.55}$$

Die approbierte gedruckte Originalversion dieser Dissertation ist an der TU Wien Bibliothek verfügbar.
The approved original version of this doctoral thesis is available in print at TU Wien Bibliothek.
TU WIEN Bibliothek Your knowledge hub

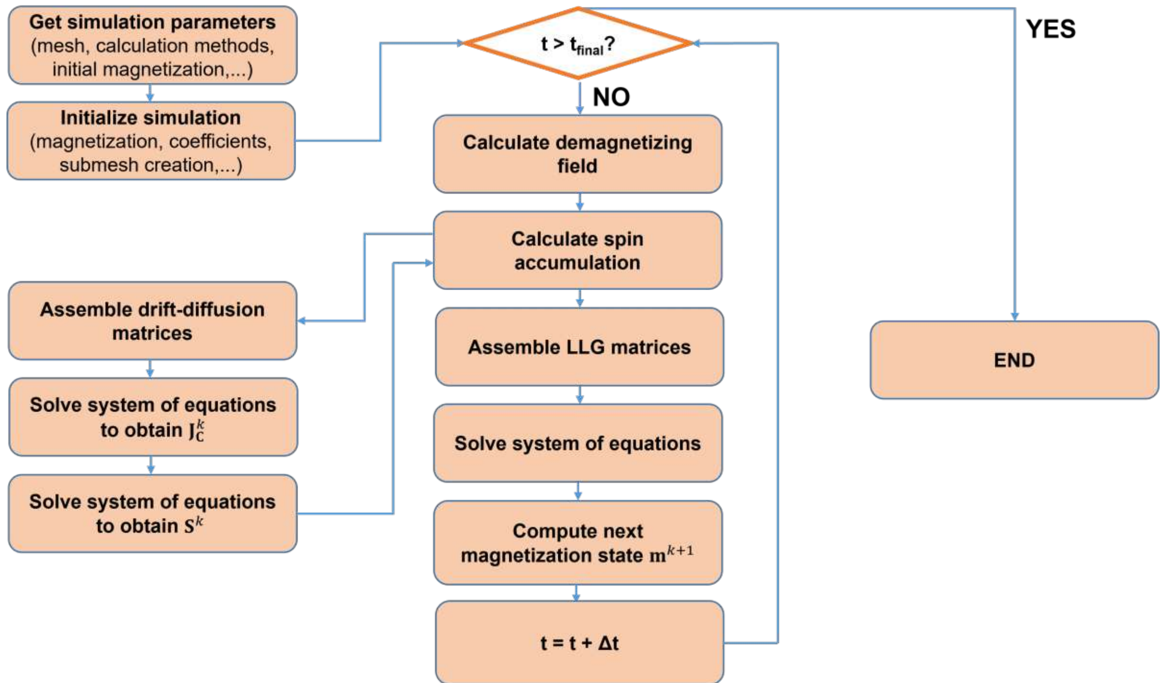

Figure 6.2: Flowchart of the FE solver implementing the weak formulation of both the LLG equation and the spin and charge drift-diffusion equations.

which can be obtained by cross-multiplying (3.9) with , and using the product rule ( ) = ( ) ( ) together with the constraint = 1. For the FE implementation, the magnetization is taken to be a piecewise affine, globally continuous function [83]. Each component belongs to the Sobolev space . It is the space of functions in that additionally admit a weak gradient which also belongs to [138]. The weak gradient is a generalization of the gradient, defined with the help of the test functions and valid in an integral sense, and its existence is needed to be able to evaluate terms containing spatial derivatives in the weak formulation. The notation for the vector space of the magnetization is . Instead of looking for the solution in the same space of the magnetization, the solution space $_T$ is restricted to vectors tangent to the magnetization, so that $_T =$ $\boldsymbol{w}$ $\boldsymbol{w} = 0$. The test functions are also restricted to the same space, so that the weak formulation of (6.55) results in

$$\int_\omega (\quad + \quad) \quad \boldsymbol{w} \, \mathrm{d} \quad = \int_\omega \quad {}_{\mathrm{eff}}(\quad) \quad \boldsymbol{w} \, \mathrm{d} \tag{6.56}$$

where is the subdomain containing only the magnetic parts of the structure under analysis. The last term on the right-hand side of (6.55) is not present, as the test functions are restricted to the tangent space $_T$. The time derivative at a certain time ^{k} is obtained by setting [83]

$$^{k+1} = \quad ^{k} + \tag{6.57}$$

where is the time-step, and is a parameter between 0 and 1, with the value 0 leading to a fully explicit scheme and 1 to a fully implicit one. Each effective

Die approbierte gedruckte Originalversion dieser Dissertation ist an der TU Wien Bibliothek verfügbar.
The approved original version of this doctoral thesis is available in print at TU Wien Bibliothek.
TU Bibliothek WIEN Your knowledge hub

field contribution can be treated with a different value of . In the implementation employed for this work, is different from 0 only for the exchange field contribution (3.17), where the value 1 is employed for stability reasons [140]. The weak formulation employed for the computation of the magnetization dynamics by the FE solver, with the inclusion of the torque terms coming from (6.1), is then

$$\int_\omega (\quad + \quad ^{\mathrm{k}} \quad) \quad \boldsymbol{w}\,\mathrm{d} \quad + \frac{2}{\quad S} \quad \int_\omega \quad : \quad \boldsymbol{w}\,\mathrm{d} \quad =$$

$$\frac{2}{\quad S}\int_\omega \quad ^{\mathrm{k}} : \quad \boldsymbol{w}\,\mathrm{d} \quad + \quad \int_\omega (\quad _{\mathrm{ext}} + \quad _{\mathrm{ani}}(\quad ^{\mathrm{k}}) + \quad _{\mathrm{demag}}(\quad ^{\mathrm{k}})) \quad \boldsymbol{w}\,\mathrm{d} \quad +$$

$$+ \frac{\quad \mathrm{e}}{\quad \mathrm{S}} \int_\omega \left(\frac{\quad ^{\mathrm{k}}}{\quad J} + \frac{\quad ^{\mathrm{k}} \quad ^{\mathrm{k}}}{\quad \varphi} \right) \quad \boldsymbol{w}\,\mathrm{d} \tag{6.58a}$$

$$^{\mathrm{k+1}} = \frac{\quad ^{\mathrm{k}} + \quad}{\quad ^{\mathrm{k}} + \quad} \tag{6.58b}$$

The right-hand side of (6.58b) is evaluated nodewise, indicates the magnetic subdomains, and $\; : \; = \sum_{\mathrm{ij}} (\; _{\mathrm{i}} \; _{\mathrm{j}})(\; _{\mathrm{i}} \; _{\mathrm{j}})$ is the Frobenius inner product of two matrices. The exchange field contribution (3.17), together with (6.57), gives rise to the second term on the left-hand side and to the first term on the right-hand side. The boundary integrals arising from the weak formulation of this contribution are put to zero by the Neumann boundary condition (3.41), applied on the external boundary of the magnetic region . The equations are subject to the initial condition $(0) =$. The system of equations resulting from the FE implementation of this weak formulation includes the tangent plane constraint $\boldsymbol{w} = 0$, and the solution at each time-step is computed through a solver based on the generalized minimal residual (GMRES) method, provided by the library MFEM. The GMRES method is an iterative algorithm for the numerical solution of an indefinite nonsymmetric system of linear equations, as is the case of FE implementation of (6.58a) due to the presence of the cross-product terms. Material parameters that can differ from subdomain to subdomain are treated as piecewise constant functions, unless differently stated. The contribution of the demagnetizing field $_{\mathrm{demag}}$ is evaluated only on the disconnected magnetic domain by using a hybrid approach combining the boundary element method and the FE method [141, 142].

Spin and Charge Drift-Diffusion Equations

The weak formulation for the computation of the spin accumulation is derived from (6.38). The equations are solved for the magnetization $^{\mathrm{k}}$ at each time-step, and the resulting spin accumulation $^{\mathrm{k}}$ is employed in (6.58a).

Die approbierte gedruckte Originalversion dieser Dissertation ist an der TU Wien Bibliothek verfügbar.
The approved original version of this doctoral thesis is available in print at TU Wien Bibliothek.
TU WIEN Bibliothek Your knowledge hub

For the computation of the charge potential and current, a Laplace equation is solved for the whole domain , with the weak formulation

$$\int \qquad \mathrm{d} \quad = 0 \tag{6.59a}$$

$$\int \quad _{\mathrm{C}} \; \boldsymbol{v}\,\mathrm{d} \quad = \int \qquad \boldsymbol{v}\,\mathrm{d} \tag{6.59b}$$

where represents a test function belonging to , while $\boldsymbol{v}$ is a test function in . belongs to , and equation (6.59b) is employed to obtain a projection of $_{\mathrm{C}}$ in the function space [83]. Dirichlet conditions are applied to prescribe the voltage at the contacts. The Neumann condition $= 0$ is assumed on external boundaries not containing an electrode. Special treatment of the conductivity results in an implementation capable of reproducing the charge current dependence on the TMR and relative direction of the magnetization vectors in the FL and RL of an MTJ, as will be shown in Chapter 7. The solution of the system of equations resulting from the FE implementation of (6.59) is computed through a solver based on the conjugate gradient (CG) method, provided by the library MFEM. The CG method is an algorithm for the numerical solution of systems of linear equations whose matrix is positive-definite, as is the case of the FE implementation of (6.59).

The weak formulation of the spin drift-diffusion equations presented in [23] is generalized to apply to (6.38), which includes the additional spin dephasing term, resulting in the following expression:

$$\begin{aligned} & _{\mathrm{e}}\int \Big(\qquad \sigma \;\; \mathrm{D} \qquad \big((\quad)^{\mathrm{T}} \quad \big) \Big) : \quad \boldsymbol{v}\,\mathrm{d} \; + \\ + \; & _{\mathrm{e}}\int \left(\frac{}{sf} + \frac{}{J} + \frac{(\qquad)}{\varphi} \right) \boldsymbol{v}\,\mathrm{d} \; = \\ \frac{B}{} \; _{\sigma} \int_{\omega} (\qquad _{\mathrm{C}}) : \quad \boldsymbol{v}\,\mathrm{d} \quad & \frac{B}{} \; _{\sigma} \int_{\partial \quad \cap \partial\omega} ((\qquad _{\mathrm{C}}) \;\;) \quad \boldsymbol{v}\,\mathrm{d} \end{aligned} \tag{6.60}$$

$\boldsymbol{v}$ represents again a test function belonging to , also belongs to , and indicates the shared external boundary of the whole domain and magnetic subdomain . The boundary integrals arising from the weak formulation are put to zero by the Neumann condition ( ) = , assumed on external boundaries. For contacting regions longer than the spin-flip length, this condition is equivalent to an exponential decay of towards the electrodes [23, 25]. The charge current $_{\mathrm{C}}$ is the one computed from (6.59). The solution of the system of equations resulting from the FE implementation of (6.60) is computed through a solver based on the GMRES method, provided by the library MFEM, as due to the cross product terms the FE implementation of (6.60) results in a nonsymmetric system of linear equations.

Die approbierte gedruckte Originalversion dieser Dissertation ist an der TU Wien Bibliothek verfügbar.
The approved original version of this doctoral thesis is available in print at TU Wien Bibliothek.
TU WIEN Bibliothek Your knowledge hub

Die approbierte gedruckte Originalversion dieser Dissertation ist an der TU Wien Bibliothek verfügbar.
The approved original version of this doctoral thesis is available in print at TU Wien Bibliothek.
TU Wien Bibliothek Your knowledge hub

Chapter 7

Charge Current Redistribution and MTJ Torque Magnitude in the Finite Element Drift-Diffusion Formalism

This chapter focuses first on the development of an approach for reproducing the charge current density dependence on the TMR and on the local angle between magnetization vectors of an MTJ in a FE setting. Then, the dependence of the torque on the various parameters entering the spin and charge drift-diffusion equations is analyzed, and it is shown how such parameters can be tuned to reproduce the torque magnitude expected in MTJs by the Slonczewski expression. The results hereby presented were published by the author in references [143], [144], [145], [146], [147], and [148]. All the reported FE solutions are computed in meshes composed of tetrahedral elements.

7.1 Reproduction of the TMR Effect

MTJs present a strong resistance dependence on the relative magnetization orientation in the FL and the RL, mainly determined by the polarized tunneling process. The dependence of the conductance on the angle between magnetization vectors can be expressed as [16, 64, 65, 99]

$$(\ ) = \quad (1 + \ _{\mathrm{RL}} \ _{\mathrm{FL}} \cos \ ) \tag{7.1}$$

where $\ = (\ _{\mathrm{P}} + \ _{\mathrm{AP}})\ 2$, and is the angle between the unit magnetization vector in the RL $\ _{\mathrm{RL}}$ and in the FL $\ _{\mathrm{FL}}$, $\cos \ = \ _{\mathrm{RL}} \ \ _{\mathrm{FL}}$. This expression is equivalent to (2.4) when taking Julliere's expression (3.51) into account.

In Chapter 4, an analytical solution for the charge current density in an MTJ was reported, which was able to reproduce the voltage drop at the barrier and the current density dependence on the TMR value and on the local angle between the magnetization vectors. This, however, required to solve the Laplace equation separately in the two FM layers. The approach needs to be adapted to a FE implementation,

with the solution computed simultaneously in the whole MTJ structure. In order to reproduce both the TMR effect and the angular dependence of the resistance, the oxide layer is modeled as a poor conductor, whose low conductivity depends on the relative magnetization vectors orientation as

$$(\ \ _{\mathrm{RL}}\ \ \ _{\mathrm{FL}}) = \ \ (1 + \ \ _{\mathrm{FL}}\ \ _{\mathrm{RL}}\ \ _{\mathrm{RL}}\ \ \ _{\mathrm{FL}}) \tag{7.2}$$

where $\ =\ \ _{\mathrm{TB}}$ is the conductivity of the tunnel barrier, with $\ _{\mathrm{TB}}$ and the thickness and surface area of the tunnel barrier, respectively. While the expression for depends linearly on $\ _{\mathrm{TB}}$, the average conductance of the TB decays exponentially with the barrier thickness. $\ _{\mathrm{RL(FL)}}$ is the magnetization of the RL(FL) close to the interface. It is a manifestation of Ohm's law relating the voltage and the charge current through a structure with many transversal modes [123, 127].

A solution for the electric potential and current density in an FE setting can be computed through equation (6.59). The conductivity is described by a piecewise constant coefficient in the metallic layers, and by a coefficient based on equation (7.2) in the tunneling layers. In the scope of the MFEM library [149], only the data associated with a local element can be accessed during the assembly of the system matrices, while the computation of (7.2) in the TB requires knowledge of the magnetization vectors in the neighboring FM layers. In order to get access to the magnetization values, the coefficient describing the TB conductivity is initialized as follows:

- For each point inside the TB where the conductivity needs to be computed, referred to as integration point, the solver loops through the integration points of the RL and FL elements closer to the interfaces
- The RL and FL points near to or at the interface with coordinates closest to the TB point are selected
- The integration point number and element number associated with the nearest RL and FL points are mapped to the coordinates of the TB points

In a transient simulation, the search is carried out only during the initialization of the solver. At every time-step, the data necessary for the computation of (7.2) can be accessed through the generated maps, without the need to repeat the search procedure and waste computational time.

The FE solution obtained from equations (6.59) and (7.2) is first computed in a mesh reproducing the structure schematized in Fig. 4.1. The lateral dimensions are 10 10 nm . The mesh was prepared by modifying one of the built-in MFEM meshes. The magnetization distribution is taken to be parallel in the center of the structure, and anti-parallel on the sides. The potential is fixed with Dirichlet conditions on the left and right boundaries. The values of conductivity, resistance and bias voltage are the same as the ones employed for the analytical solution presented in Chapter 4. The voltage and x-component of the current density computed via the FE method

Die approbierte gedruckte Originalversion dieser Dissertation ist an der TU Wien Bibliothek verfügbar.
The approved original version of this doctoral thesis is available in print at TU Wien Bibliothek.
TU WIEN Bibliothek Your knowledge hub

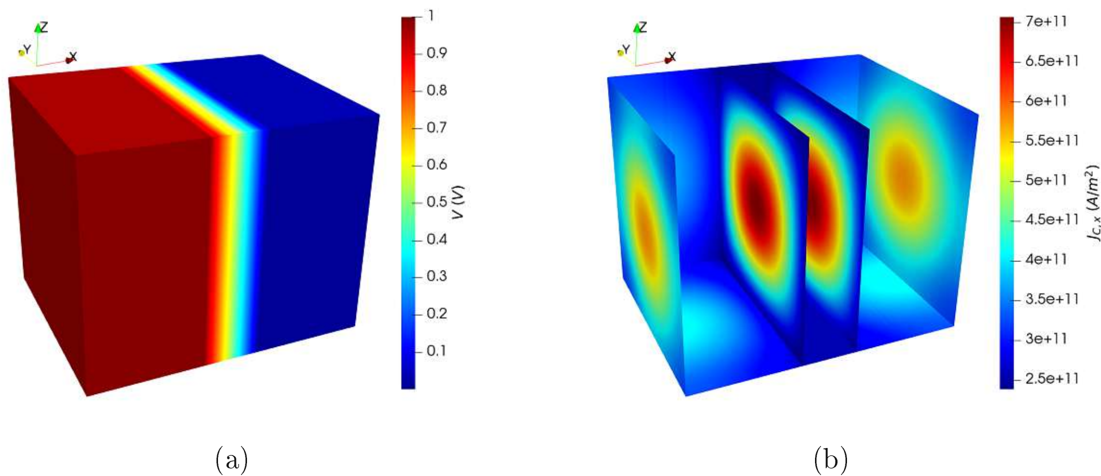

(a) (b)

Figure 7.1: Results obtained through the FE solver fro the charge current. The planes are located at the contacts and TB interfaces. (a) Solution for the electrical potential. The voltage drop localized at the TB is reproduced. (b) Solution for the x-component of the current density. Its distribution is dictated by the magnetization configuration: the structure has better conductance in the center, where the magnetization vectors are parallel.

are reported in Fig. 7.1. The distribution of the latter is evidenced on planes located at the contacts and at the TB interfaces. Both the voltage drop localized at the TB and the TMR dependent redistribution of $_{\mathrm{C}}$ are reproduced, in agreement with the analytical results. The current density flow is higher in the center of the structure, where the parallel magnetization vectors favor the tunneling process and grant a better conductance.

Thanks to the FE implementation, it is then possible to run the solver on meshes representing more realistic MTJ structures. As an example, the current density distribution is computed for the structure reported in Fig. 1.1. This mesh presents a circular cross-section, and includes 50 nm long nonmagnetic contacts. The mesh was prepared by employing the open-source software Netgen, part of the NGSolve package [150]. Dirichlet conditions are employed to apply the bias voltage on the left contact and fix the voltage value on the right one to 0. The cylindrical stack has a diameter of 40 nm, RL and FL of 2 nm thickness, and TB of 1 nm thickness. The conductivity of the nonmagnetic layers is $_{\mathrm{NM}} = 5 \quad 10$ S/m. The values of conductivity in the FM layers, TB average conductance and applied bias voltage are $_{\mathrm{RL}} = \ _{\mathrm{FL}} = 10$ S/m, $= 4\ 76 \quad 10^{-}$ S, and $= 1$ V, respectively, and the magnetization configuration is the same as the one employed for Fig. 7.1. The obtained TMR- and magnetization-dependent current density distribution is reported in Fig. 7.2. Here, all the cross-sections are located inside the nonmagnetic regions. The inner ones are close to the interface between the FM and NM layers, while the outer ones are further inside the nonmagnetic contacts. Fig. 7.2(a) shows how the current density's x-component is non-uniform also inside of the nonmagnetic regions.

Die approbierte gedruckte Originalversion dieser Dissertation ist an der TU Wien Bibliothek verfügbar.
The approved original version of this doctoral thesis is available in print at TU Wien Bibliothek.
TU WIEN Bibliothek Your knowledge hub

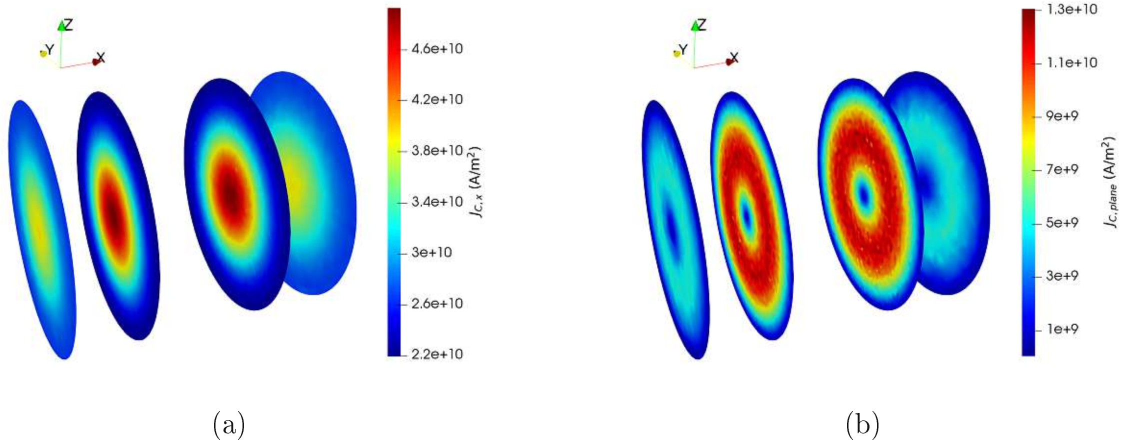

(a) (b)

Figure 7.2: Current density distribution through the cylindrical MTJ stack of Fig. 1.1, with a non-uniform magnetization configuration in the FL. The current density redistribution happens also inside the nonmagnetic contacts, where all the planes are located. (a) Current density's x-component, perpendicular to the structure. (b) Modulus of the y- and z-components, in the plane of the structure.

Due to conservation of the current flow, the current density is redistributed in the yz-plane of the metallic layers. This is evidenced by Fig. 7.2(b), where the modulus of its in-plane components, $_{\mathrm{C,plane}} = \sqrt{_{\mathrm{C,y}} + _{\mathrm{C,z}}}$, is reported.

7.2 Finite Element Solution for the Spin Accumulation

The MFEM implementation of the weak formulation (6.60), which allows to obtain a solution for the spin accumulation in a FE setting, is first tested against known analytical results [98]. The parameters employed for these simulations, taken from [23] and [25], are reported in Table 7.1. The spin accumulation and spin torques are computed for the FL of a metallic spin-valve, magnetized along the z-direction, with a fully spin-polarized current coming from the left boundary, at x=0 nm. Such a current could be generated by a half metallic thick RL [98]. The magnetization in the RL is chosen to point in the negative y-direction. For this simulation, the term containing $_{\varphi}$ is not considered, and a fixed current density flowing in the negative x-direction, with value $_{\mathrm{C,x}} = \ 10 \ \mathrm{A/m}$, is applied. The layer is taken to be 60 nm long. As the magnetization is uniform, the lateral dimensions of the structure do not have any impact on the solution. The layer's mesh was generated by using Netgen. In Fig. 7.3 the analytical result for the spin accumulation is compared to the one computed by employing the MFEM solver, showing an excellent agreement between the two.

The torque acting on the magnetization is related to the spin current via (6.13), where the term describing spin-flip relaxation is subtracted from the divergence of

Die approbierte gedruckte Originalversion dieser Dissertation ist an der TU Wien Bibliothek verfügbar.
The approved original version of this doctoral thesis is available in print at TU Wien Bibliothek.
TU WIEN Bibliothek Your knowledge hub

Table 7.1: Parameters used in the drift-diffusion simulations.

Parameter	Value
Conductivity polarization, $_{\sigma}$	0 9
Diffusion polarization, $_{D}$	0 8
Diffusion coefficient in NM, $_{e,NM}$	10^{-} m /s
Diffusion coefficient in FL and RL, $_{e,FM}$	2 0 10^{-} m /s
Spin flip length, $_{sf}$	10 nm
Spin exchange length, $_{J}$	2 nm
Spin dephasing length, $_{\varphi}$	5 nm

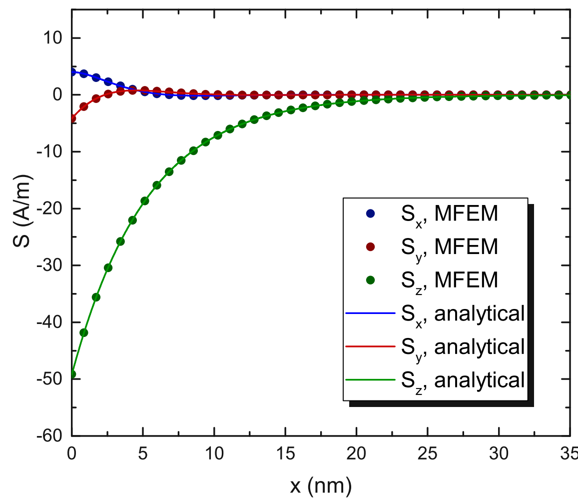

Figure 7.3: Comparison between the spin accumulation computed analytically (dotted lines) and using our FE solver (solid lines). The analytical solution [98] is properly reproduced. The figure was adapted from [146].

the spin current. In case of negligible spin-flip scattering, the relation becomes

$$_{\mathrm{s}} = \qquad _{\mathrm{s}} \tag{7.3}$$

Equations (6.13) and (7.3) should give compatible values for the torque, provided that $_{\mathrm{J}}$ is shorter than $_{\mathrm{sf}}$. This is usually the case for most ferromagnetic materials [98,151]. In order to check the validity of these assumptions, the torque obtained from both expressions is compared. First, the spin current flowing in the x-direction, $_{\mathrm{S,x}}$, is computed from the spin accumulation solution of Fig. 7.3 using (6.6), and is reported in Fig. 7.4(a). It can be noted, that near the interface the spin current is fully polarized along the direction of the magnetization in the RL. The component parallel to the RL magnetization is quickly absorbed. Precession of the spin current around the FL magnetization direction creates a component in the x-direction, perpendicular to the common plane of the magnetization vectors in the RL and the FL. This component is also absorbed on the length scale dictated by $_{J}$. The spin current gets then polarized in the direction of the magnetization in the FL.

Die approbierte gedruckte Originalversion dieser Dissertation ist an der TU Wien Bibliothek verfügbar.
The approved original version of this doctoral thesis is available in print at TU Wien Bibliothek.
TU WIEN Bibliothek Your knowledge hub

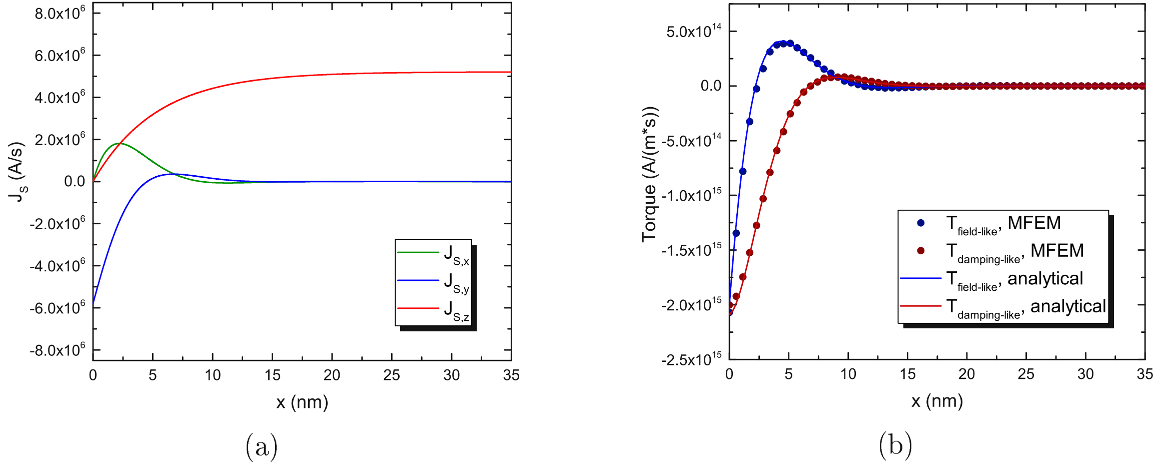

(a) (b)

Figure 7.4: (a) Spin current computed from the spin accumulation in Fig. 7.3. The orthogonal components get absorbed near the interface, and the spin current gets polarized along the magnetization direction. (b) Comparison between the torque computed using (6.13) ( ) and (7.3) ( ). The figures were adapted from [146].

The comparison of the torques computed using (6.13) and (7.3) is reported in Fig. 7.4(b), where the former is labeled as , while the latter is labeled as . The damping-like component of the torque, also called adiabatic component, is the one lying in the plane formed by the magnetization vectors in the RL and the FL, and tends to align them in the parallel or anti-parallel configuration, depending on the sign of the electric current. It acts along the same axis as the Gilbert damping term in the LLG equation. With the unit magnetization vector in the layer where the torque is computed and the one in the polarizing layer, this torque component lies in the direction defined by ( ). In the present simulation, it lies along the y-axis. The field-like component, also referred to as non-adiabatic component, is perpendicular to the plane, and creates a precessing motion, in a manner analogues to an external field. This component lies along the direction defined by . Here, it lies along the x-axis. Both components of the torque computed using the two expressions are in very good agreement, so that the use of (7.3) for computing the torques directly from the spin current is justified if $_J$, $_\varphi$ $_{sf}$.

After verifying the accuracy of the FE implementation in computing the spin accumulation and torques, the formalism can be applied to multi-layered structures, in order to obtain the magnetization dynamics in STT-MRAM cells, composed of multiple magnetic and nonmagnetic layers. To further test the MFEM implementation, the software is employed to compute the spin accumulation in the same scenario as reported by Abert et al. in [23]. The structure under study is a spin valve with 5 nm NM contacts, 2 nm FM layers, and a 3 nm nonmagnetic spacer (NMS). The structure is magnetized in-plane, with the magnetization in the RL pointing towards the y-direction and the one in the FL pointing towards the z-direction. A uniform current density flows through the structure in the x-direction, with value $_{\mathrm{C,x}} = \;\; 10 \;\; \mathrm{A/m}$.

Die approbierte gedruckte Originalversion dieser Dissertation ist an der TU Wien Bibliothek verfügbar.
The approved original version of this doctoral thesis is available in print at TU Wien Bibliothek.
TU WIEN Bibliothek Your knowledge hub

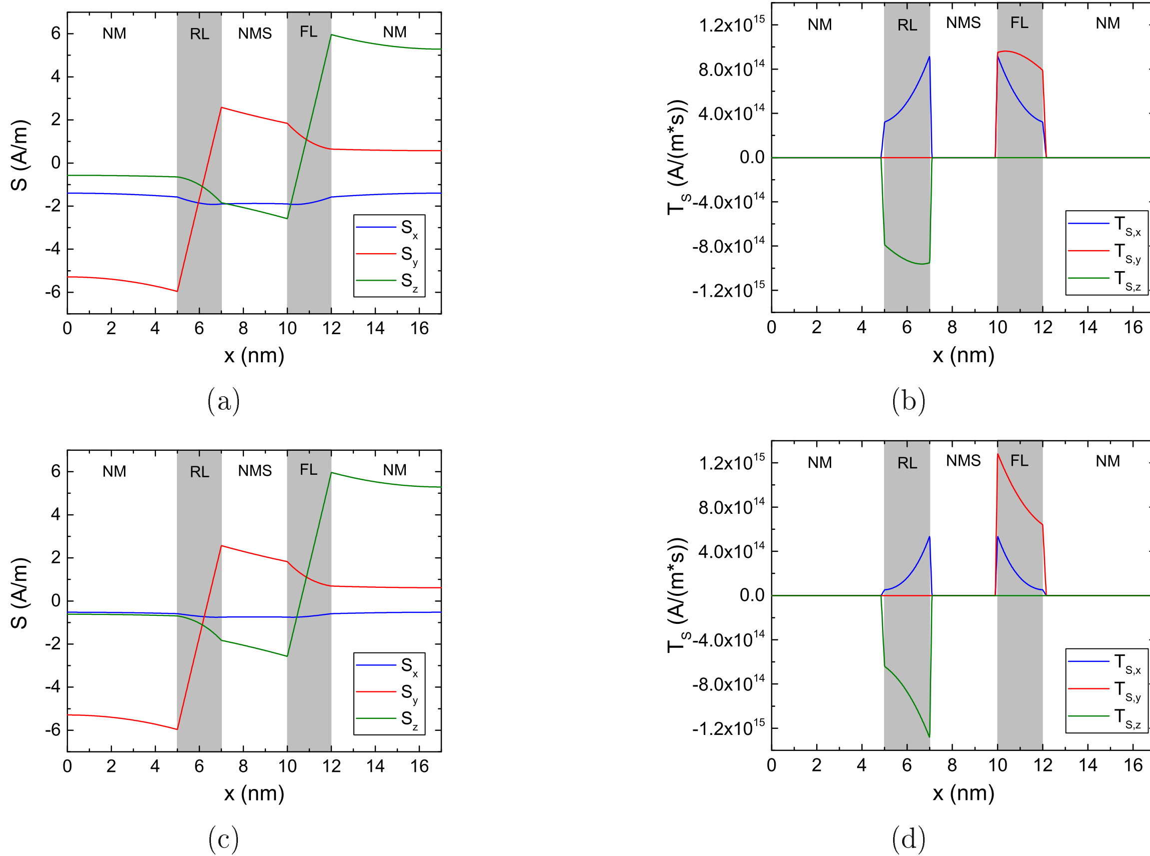

Figure 7.5: Spin accumulation and spin torque solutions in the structure reported in [23], with 2 nm FM layers, 3 nm psacer layer, and 5 nm NM contacts. In (a) and (b) the spin accumulation and torque, respectively, are reported for a torque term not including the spin-dephasing term. In (c) and (d) the spin accumulation and torque, respectively, with the inclusion of the spin-dephasing term and $_{\varphi} = 2$ nm, are reported. The remaining parameters are taken from Table 7.1.

The employed parameters are the ones reported in Table 7.1, without the spin dephasing term. The obtained spin accumulation is reported in Fig. 7.5(a), showing a good agreement with the results by Abert et al..

By looking at (6.38) it can be noted, that the source of the spin accumulation comes from spatial variations of the magnetization. In the present simulation, the magnetization is homogeneous within the FM layers, and the only variation happens at the interfaces with the NM layers, where all the magnetization components go abruptly to zero. The spin accumulation is thus generated at such interfaces, and then diffuses inside the layers. With this set of parameters, the spin accumulation components transverse to the magnetization direction are not completely absorbed inside the FM layers, as they are too thin. This can also be observed in the resulting torque, computed from (6.13) and reported in Fig. 7.5(b). Both a damping-like component (along y in the FL) and a field-like component (along z in the FL) are present, and do not completely decay inside the FM layers.

Die approbierte gedruckte Originalversion dieser Dissertation ist an der TU Wien Bibliothek verfügbar.
The approved original version of this doctoral thesis is available in print at TU Wien Bibliothek.
TU Bibliothek WIEN Your knowledge hub

The shape of both the spin accumulation and torque is modified by the inclusion of the spin-dephasing term, especially when $_{\varphi} \quad _{J}$. The spin accumulation and torque computed by using $_{\varphi} = \ _{J}$, with the torque obtained through (6.1), are reported in Fig. Fig. 7.5(c) and Fig. 7.5(d), respectively. The presence of the spin-dephasing term both enhances the torque absorption and modifies the relative values of the damping-like and field-like components, so that its inclusion can more accurately capture the interaction between magnetization and spin accumulation.

7.3 Torque Evaluation in Spin-Valve Structures

The possibility to compute the spin accumulation in a spin-valve structure gives the opportunity to compare the angular dependence of the damping-like torque obtained from the drift-diffusion implementation with the one obtained from the Slonczewski expression (3.48), which was derived by considering only ballistic transport in a symmetric stack [14]. The simulations are run in the same spin-valve structure described before, with a thinner 1 nm spacer layer to reduce the spin accumulation decay between the FM layers. The spin-flip length in the NM leads, $_{\text{sf}}$, is set to 100 nm, while the remaining parameters are the ones reported in Table 5.1, including the dephasing length $_{\varphi}$. The average torque acting on the FL is computed as

$$_{\text{S,FL}} = \frac{1}{_{\text{FL}}} \int_{x_{\text{FL}}}^{x_{\text{FL}} \quad d_{\text{FL}}} \quad _{\text{S}} \tag{7.4}$$

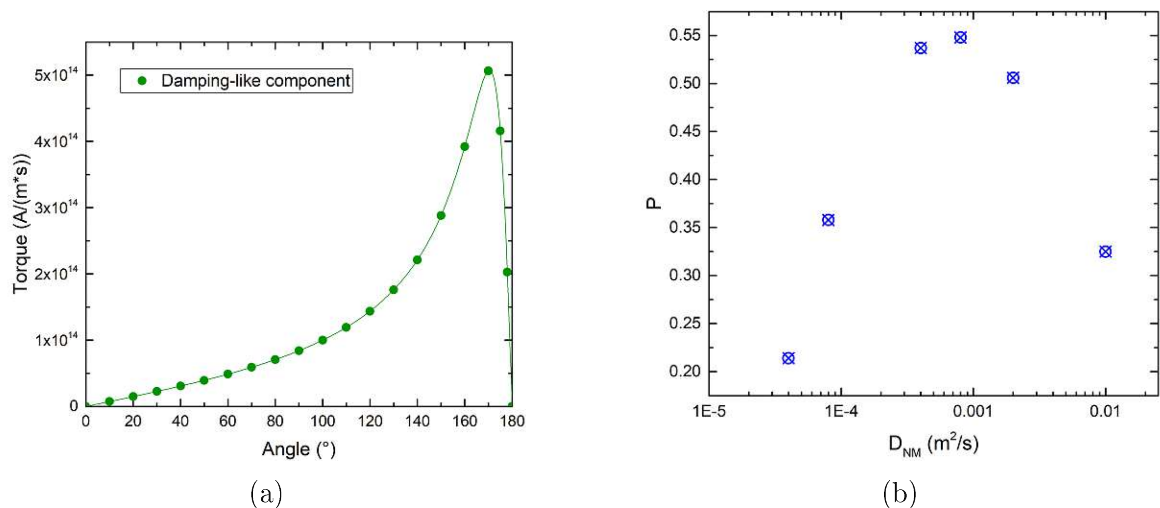

(a) (b)

Figure 7.6: (a) Angular dependence of the torque in a spin-valve for a spin-flip length of 100 nm. The line represents a fit of the data with equation (3.48), describing the angular torque dependence in a symmetric spin valve, a structure with two ferromagnetic layers, RL and FL, separated by a nonmagnetic metal layer. (b) Dependence of the polarization parameter P, extracted from fitting the angular dependence of the torque, on the diffusion coefficient in the non-magnetic layers. The figures were published in [145].

Die approbierte gedruckte Originalversion dieser Dissertation ist an der TU Wien Bibliothek verfügbar.
The approved original version of this doctoral thesis is available in print at TU Wien Bibliothek.
TU WIEN Bibliothek Your knowledge hub

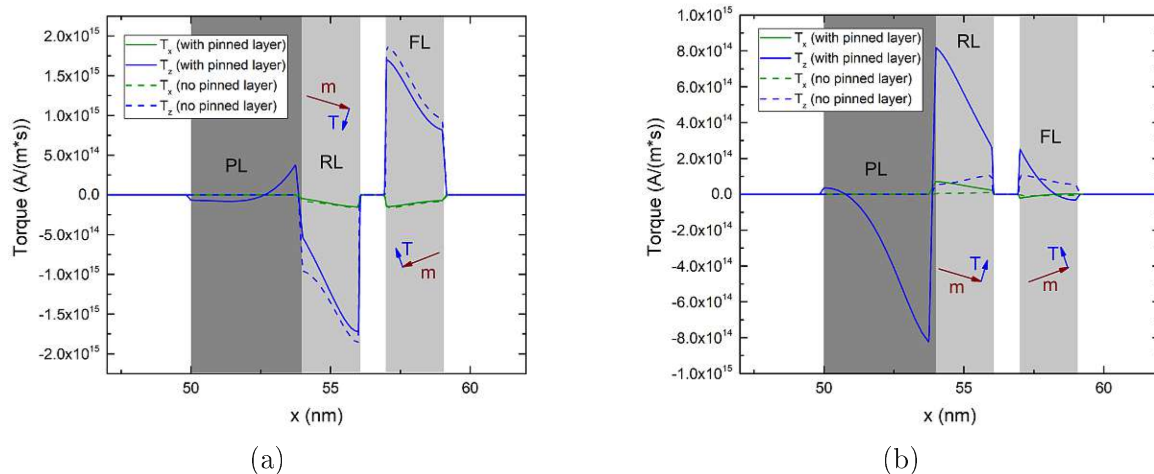

Figure 7.7: Damping-like torque in a multi-layered structure with (a) quasi-parallel and (b) quasi-antiparallel magnetization vectors in the FL and the RL. The solid lines are computed in a structure including the PL, while the dashed lines are computed without the PL inclusion. The figures were published in [145].

where $_{\mathrm{FL}}$ is the x-coordinate of the interface between middle layer and FL, and $_{\mathrm{FL}}$ is the thickness of the FL. The damping-like torque for the angle between the magnetization vectors in the RL and FL going from 0° to 180° is reported in Fig. 7.6(a). The simulated damping-like torque (dots) is fitted with expression (3.48), using the torque amplitude and the polarization as fitting parameters. The Slonczewski expression gives a good fit to the simulated torque and, given that the long spin-flip length reduces diffusive relaxation in the contacts, the fitted polarization parameter of 0 9 matches well the value of $_{\sigma}$ in the drift-diffusion approach.

When the value of $_{sf}$ in the contacts is reduced to 10 nm, however, diffusive effects start playing a bigger role: the extracted value of is reduced to 0 5, so that it does not only represent the conductivity polarization $_{\sigma}$, but also depends on other system parameters. This is confirmed by using the drift-diffusion formalism to study the dependence of the extracted on the diffusion coefficient in the NM layers $_{\mathrm{e,NM}}$, reported in Fig. 7.6(b). It must be noted, that the present results are obtained in a symmetric structure, where RL and FL have the same length. In the presence of asymmetric FM layers, the angular dependence of the torque shows additional features [23], and an updated expression, which takes the diffusive effects into account, must be employed in order reproduce the torque dependence [152].

Even though the expressions for the average torque can be employed to simulate the magnetization dynamics of the FL, one of the main advantages of the drift-diffusion approach is the straightforward possibility to compute the torques acting in all the ferromagnetic layers in a given structure. This is particularly useful when the cell under study contains more layers than just the RL and FL. In [153], the writing failure of an MRAM cell at a high current density was linked to the destabilization of the RL. The torque acting from the FL back on the RL can become strong enough

Die approbierte gedruckte Originalversion dieser Dissertation ist an der TU Wien Bibliothek verfügbar.
The approved original version of this doctoral thesis is available in print at TU Wien Bibliothek.
TU WIEN Bibliothek Your knowledge hub

to cause the reversal of its magnetization, so that an equilibrium state of the cell is never reached. As seen in Chapter 2, the stability of the RL is usually increased by the presence of a pinning layer antiferromagnetically coupled to it. The effect on the torques acting in the structure in the presence of the additional PL is investigated. As the PL is usually a composite of multiple Co/Pd stacks with antiferromagnetic coupling [12], its polarization parameters are taken to be low, ${}_{\sigma} = {}_{\mathrm{D}} = 0\ 1$. The length of the PL is 4 nm, and the spacer layer between RL and FL is 1 nm long. The magnetization is perpendicular to the plane of the structure, pointing along the positive x-direction in the RL and along the negative one in the PL.

The components of the damping-like torque acting at the beginning of a P to AP simulation, with the magnetization of both RL and FL slightly tilted towards the z-axis, are reported in Fig. 7.7(a), compared to the ones acting in a structure without the additional PL. The presence of the pinning layer increases the torque pushing the magnetization to the x-axis, helping the stability of the RL. In Fig. 7.7(b) the torque acting at the end of the switching is reported. While the effect of the PL on the torque is less pronounced, its presence helps to partially reduce the torque destabilizing the RL at the end of the reversal process. These findings suggest that the presence of the PL, while increasing the stability of the RL thanks to the antiferromagnetic coupling, also affects the torque acting in the structure. The drift-diffusion implementation, having the possibility of computing the torque in the whole structure from a unified expression, allows to readily investigate the influence of additional FM and NM layers in modern MRAM cells.

7.4 Parameters Investigation for Reproducing the Torque in MTJs

The spin and charge drift-diffusion formalism was already successfully applied to the computation of the torques acting in a spin-valve structure with a metallic spacer layer [23–25]. However, most modern STT-MRAM cells are based on magnetic tunnel junctions. While the TMR effect on the charge current can be reproduced by employing (7.2), the spin accumulation solution needs also to be able to reproduce the expected magnitude, angular and voltage dependencies peculiar to MTJs [16,99,154]. In this section, the dependence of the spin accumulation on the material parameters entering the drift-diffusion equations is analyzed. It is shown how an effective choice of parameters is able to reproduce the torque magnitude and dependence on the polarization parameters predicted by Slonczewski [16]. The parameters employed for the simulations in this section are the ones reported in Table 7.1, unless differently stated.

TU Bibliothek WIEN Your knowledge hub
Die approbierte gedruckte Originalversion dieser Dissertation ist an der TU Wien Bibliothek verfügbar.
The approved original version of this doctoral thesis is available in print at TU Wien Bibliothek.

In order to treat the middle layer as an ideal barrier with no spin reversal during the tunneling process, the spin-flip length $_{\mathrm{sf}}$ is taken to be infinite inside this layer. The equation for in the middle layer, where $=$, reduces to

$$_{S} \qquad _{\mathrm{S}}\frac{}{_{\mathrm{sf}}} = 0 \tag{7.5}$$

where $_{\mathrm{S}}$ is the diffusion coefficient inside the barrier, and it is treated as a fitting parameter to be chosen properly in order to reproduce the torque behavior in an MTJ. Depending on its value, it can either increase or decrease the slope of the components in the middle layer. The effect of $_{\mathrm{S}}$ on the spin accumulation behavior is reported in Fig. 7.8(a), for a structure with 5 nm long contacts, 2 nm long FM layers, and 1 nm long TB. A fixed current density flowing in the x-direction, perpendicular to the structure, is assumed, with value $_{\mathrm{C,x}} = \quad 10 \quad \mathrm{A/m}$. The structure represents a pMTJ, with magnetization along x in the RL and along z in the FL. When the value of $_{\mathrm{S}}$ is comparable to the one in the FM layers, the spin accumulation decays through the TB (dot-dashed lines), while the choice of a large spin diffusion coefficient reduces the slope in the middle layer to the point that the spin accumulation is practically preserved (solid lines). The solution in the whole structure for the high value of $_{\mathrm{S}}$ is reported in Fig.7.8(b).

The non-magnetic leads are necessary, in a multilayer structure, to ensure decay of the spin accumulation inside the contacts. When they are sufficiently longer than the spin-flip length, all the spin accumulation components are able to fully relax to , as reported in Fig. 7.9(a). The torque obtained from this solution of through (6.1) is reported in Fig. 7.9(b).

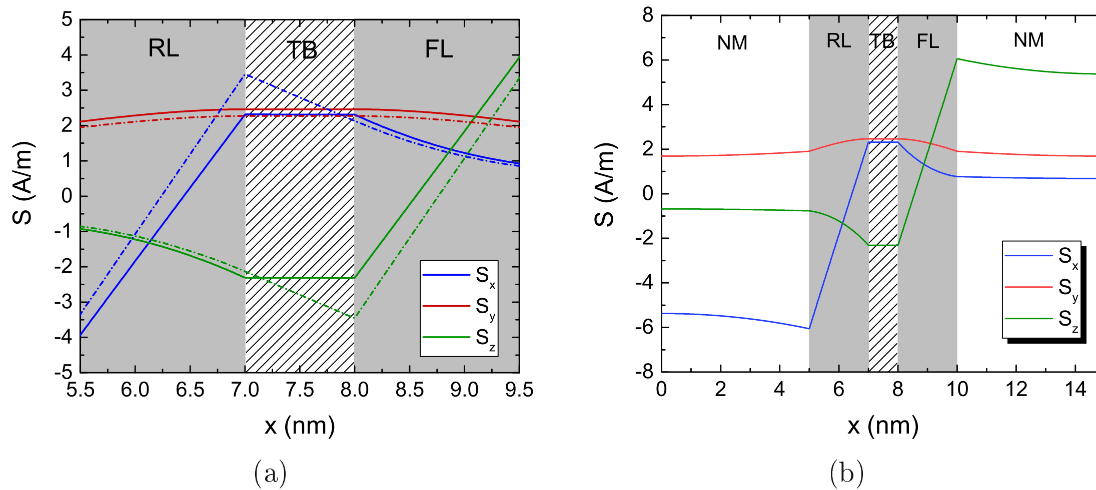

Figure 7.8: Spin accumulation across the tunneling layer. The magnetization lies along x in the FL and along z in the RL. (a) Close-up of the spin accumulation in the tunnel layer. The dashed lines are computed using the same value for $_{S}$ in the TB and $_{e}$ in the FL and the RL, while solid lines use a very high value of $_{S}$, which renders constant across the TB. (b) Spin accumulation solution in the whole structure. The figures were adapted from [143].

Die approbierte gedruckte Originalversion dieser Dissertation ist an der TU Wien Bibliothek verfügbar.
The approved original version of this doctoral thesis is available in print at TU Wien Bibliothek.
TU Bibliothek WIEN Your knowledge hub

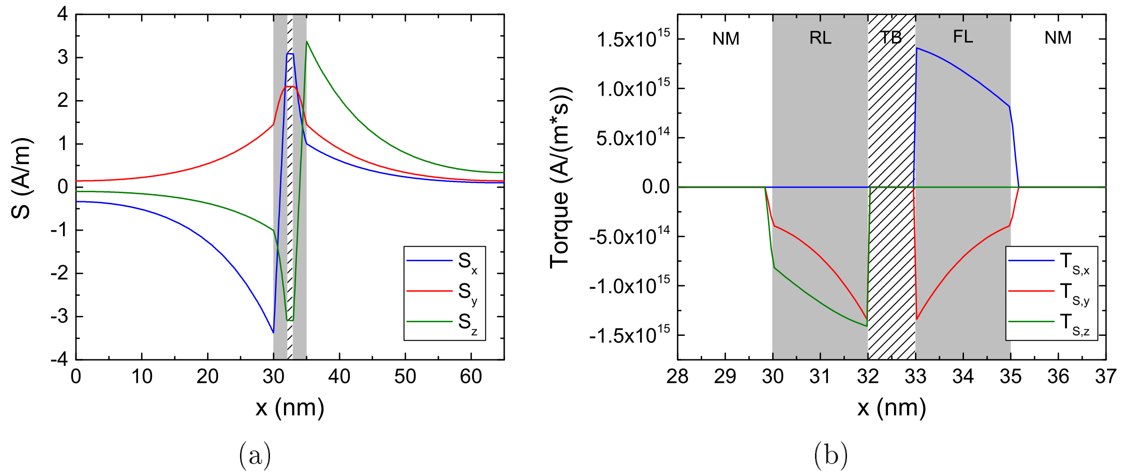

(a) (b)

Figure 7.9: (a) Spin accumulation solution with 30 nm long NM contacts, with the magnetization in the RL pointing in the x-direction and the one in the FL pointing in the z-direction. The solution is able to almost completely relax to . (b) Torque computed from the spin accumulation.

The dependence of the torque on the material parameters entering the spin accumulation equations (6.38) is then evaluated, in order to calibrate the model and to understand, if the choice of effective values for the parameters would be able to reproduce the STT torque predicted by Slonczewski [16]. The magnetization in the RL is set pointing in the x-direction, and the magnetization in the FL pointing in the z-direction. The employed structure has a squared cross-section of 40 40 nm , with ferromagnetic layers of 2 nm thickness and a middle layer of 1 nm thickness. The length of the non-magnetic leads is initially taken to be 5 nm. In Fig. 7.10, the obtained dependencies of both the adiabatic and non-adiabatic torque on several system parameters are reported. For these simulations, the same diffusion coefficient is used for all conducting layers, so that $_{\mathrm{e,NM}} = {}_{\mathrm{e,FM}}$. The remaining non-varying parameters are taken from Table 7.1, unless differently stated.

The dependence on the middle layer diffusion coefficient $_{\mathrm{S}}$ is first analyzed. The results, reported in Fig. 7.10(a), show that the torques increase with the diffusion coefficient. The increase saturates at a value $_S = 2\ 5 \quad 10^{-}$ m /s, which is the one employed to compute the dependence on the other system parameters. This value of $_S$ is also the one preserving the spin accumulation across the middle layer in Fig. 7.8(a). Low values of $_{\mathrm{S}}$, instead, increase the slope of the spin accumulation in the middle layer, and decrease the amount of spin-current transiting from one FM layer to the other, drastically reducing the torque.

The dependence of the torques on the length of the NM contacts is subsequently analyzed. As already pointed out, due to the homogeneous Neumann boundary conditions applied to solve (6.38) with the FE approach, the solution can present a non-physical behavior, if the contacts included in the model are not long enough to allow the spin accumulation to completely decay [24, 25]. Fig. 7.10(b) reports the dependence of the torques on the length of the NM contacts. For the employed value

Die approbierte gedruckte Originalversion dieser Dissertation ist an der TU Wien Bibliothek verfügbar.
The approved original version of this doctoral thesis is available in print at TU Wien Bibliothek.
TU WIEN Bibliothek Your knowledge hub

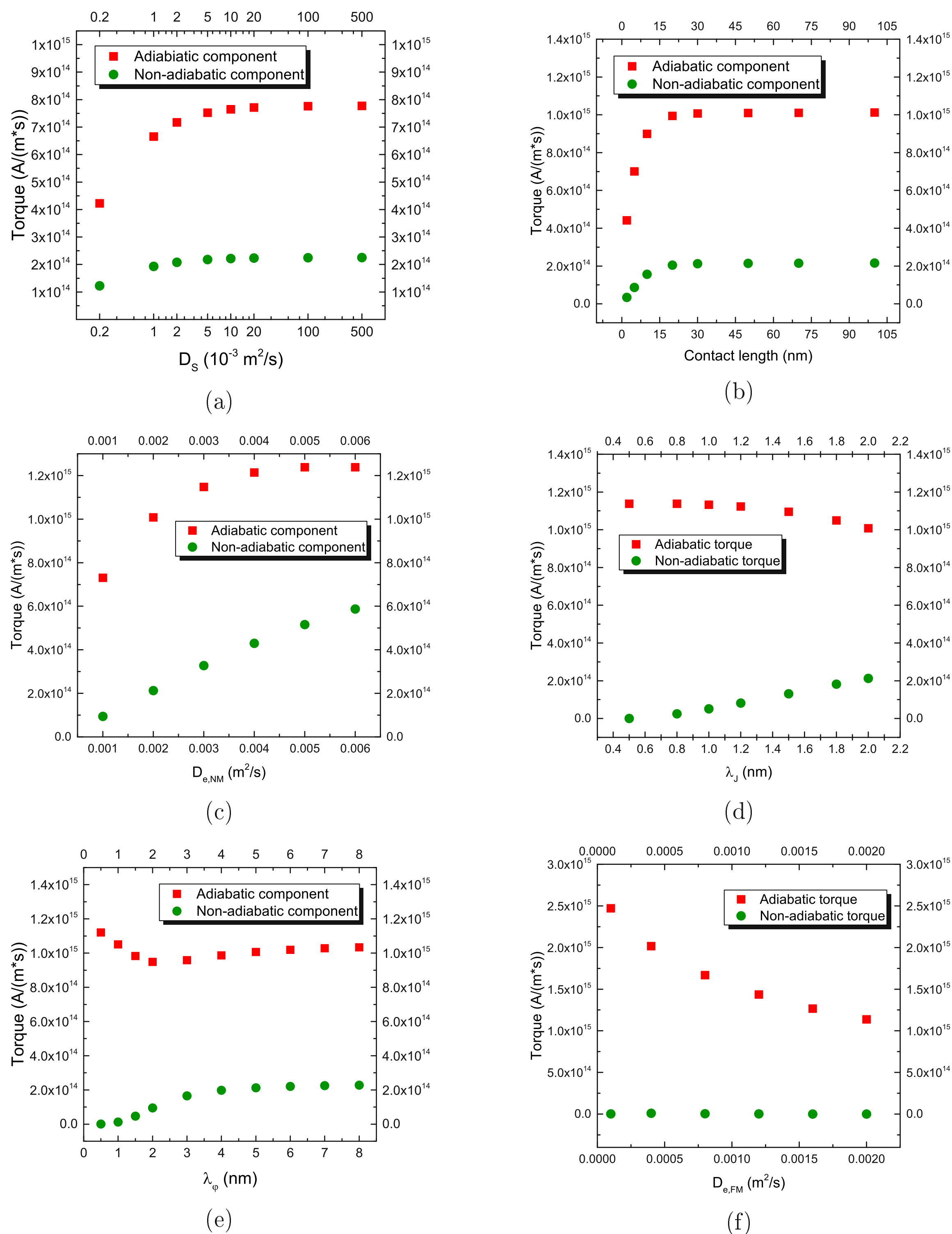

Figure 7.10: Dependence of the average torques acting on the FL on various system parameters. Details are reported in the text. The figures were published in [146].

Die approbierte gedruckte Originalversion dieser Dissertation ist an der TU Wien Bibliothek verfügbar.
The approved original version of this doctoral thesis is available in print at TU Wien Bibliothek.
TU Bibliothek WIEN Your knowledge hub

of $_{\mathrm{sf}}$, a contact thickness of at least 30 nm is required to let relax to and obtain a torque value independent of this parameter. A structure with 50 nm contacts is employed for the remaining analysis.

Fig. 7.10(c) reports the dependence on the magnitude of the diffusion coefficient in the NM contacts, showing that, even if the exchange between the magnetization and the spin accumulation happens in the ferromagnetic layers, this parameter still has an effect on the torque magnitude, due to the continuous nature of the spin accumulation in the presented formalism. When $_{\mathrm{e,NM}}$ $_{\mathrm{e,FM}}$, the balance of diffusion and magnetization change at the FM/NM interface allows for a better polarization of the current, increasing the total amount of torque transferred to the magnetization.

Fig. 7.10(d) then reports the dependence on the value of the exchange length. Lower values of $_{\mathrm{J}}$ imply a stronger exchange coupling, and produce an increased adiabatic torque. They also change the relative importance of the non-adiabatic component coming from the drift-diffusion formalism. A shorter $_{\mathrm{J}}$ implies a faster absorption of the transverse components of , so that values below 1 nm bring these components to almost 0 in the space of the FL.

The influence of the spin dephasing length $_{\varphi}$ on the computation of the torque is also investigated. Results are reported in Fig. 7.10(e). For values of $_{\varphi}$ less than 3 nm, its contribution to the torque is substantial. This suggests that, when the value of $_{\varphi}$ is close to $_{\mathrm{J}}$, the effects of the former have to be taken into consideration for accurately describing the magnetization dynamics.

Finally, Fig. 7.10(f) reports the dependence of the torque on the diffusion coefficient of the FM layers. For this plot, an exchange length $_{\mathrm{J}} = 0\ 5$ nm is employed, which lets the transverse components of be entirely absorbed. The results show that a lower value of $_{\mathrm{e,FM}}$ increases the magnitude of the adiabatic torque, as the first term in equation (6.38), describing the magnetization dependent polarization of the electric current, becomes dominant over diffusive effects, allowing for the spin current to reach the value of $(_{\mathrm{B}}) _{\sigma} \ _{\mathrm{C}}$.

The torque dependencies reported until now considered only one parameter at a time. While this gives an idea of how the torques react to changes in the considered coefficients, possible interdependencies between them could be overlooked. The behavior of the damping-like torque component under changes in several combinations of the involved length and diffusion constants is thus also investigated.

In Fig. 7.11(a) the dependence of the average value of the damping-like torque on the exchange length $_{\mathrm{J}}$ and on $_{\mathrm{S}}$ is reported. As observed before, low values of $_{\mathrm{S}}$ greatly reduce the torque, while high values enhance the torque, for every value of $_{\mathrm{J}}$. Regardless of the value of $_{\mathrm{S}}$, the torque is enhanced by lower values of $_{\mathrm{J}}$, as they allow the transverse components of the spin accumulation to be completely absorbed in the space of the FL.

Fig. 7.11(b) reports the dependence on $_{\mathrm{S}}$ and on the diffusion coefficient of the FM layers $_{\mathrm{e,FM}}$. For high values of $_{\mathrm{S}}$, the torque increases as $_{\mathrm{e,FM}}$ decreases, as observed in the previous analysis, while the lower values of $_{\mathrm{S}}$ reduce the torque to the point that its dependence on $_{\mathrm{e,FM}}$ also becomes less evident.

Fig. 7.11(c) reports the dependence on the diffusion coefficient of the FM layers,

Die approbierte gedruckte Originalversion dieser Dissertation ist an der TU Wien Bibliothek verfügbar.
The approved original version of this doctoral thesis is available in print at TU Wien Bibliothek.
TU WIEN Bibliothek Your knowledge hub

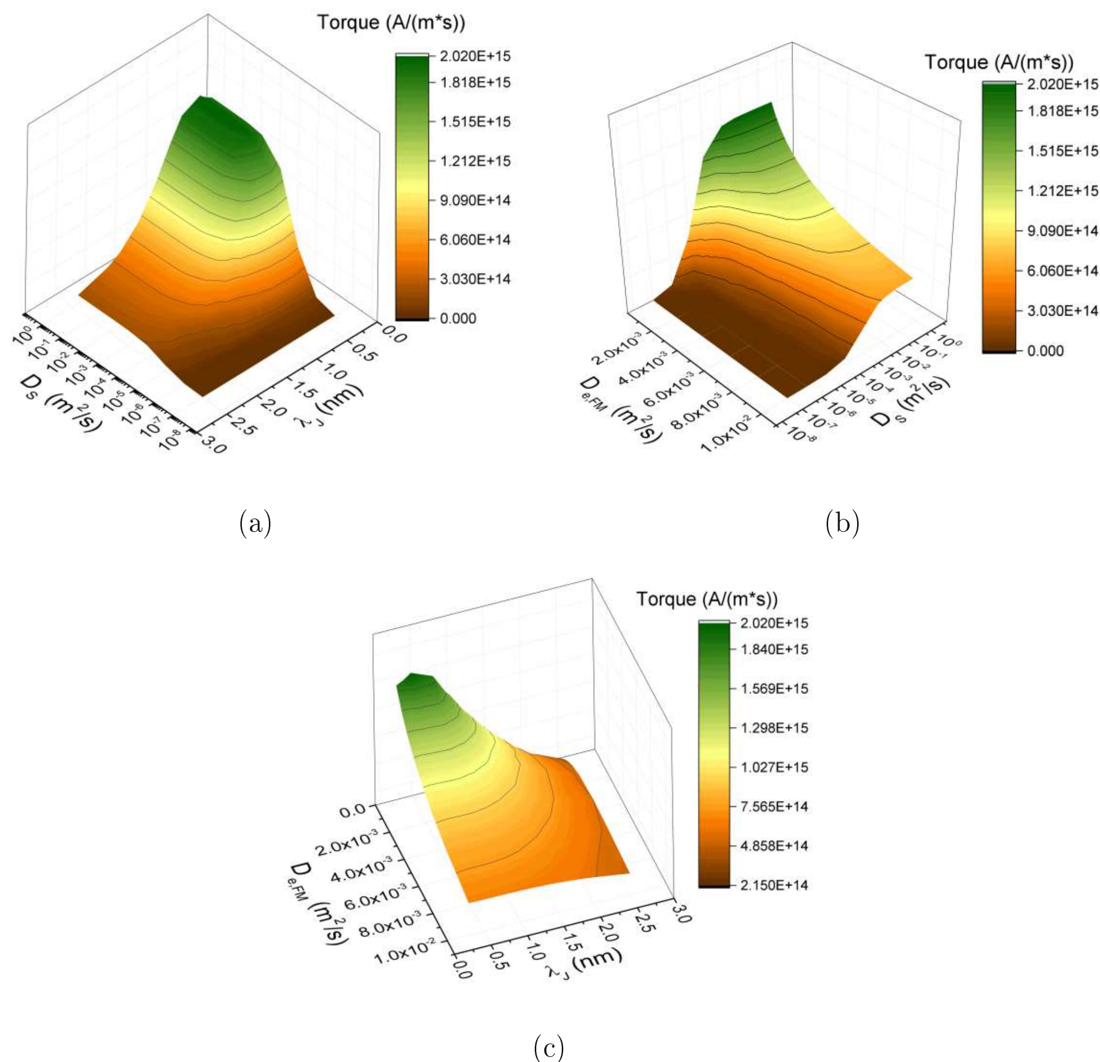

Figure 7.11: Dependence of the average damping-like torques acting on the FL on various combinations of system parameters. Details are reported in the main text. The figures were published in [148].

$_{e,FM}$, and on $_{J}$. As the torque equation (6.1) depends on the ratio of these two parameters, the interplay between them is such that a lower $_{e,FM}$ both enhances the torque, as observed before, and makes it more dependent on the exact value of the exchange length.

The dependence of both the FL and RL adiabatic torque component on the RL conductivity polarization is investigated in Fig. 7.12(a). For this plot, values of $_{e,FM} = 10^{-}$ m /s and $_{J} = 0$ 5 nm are employed. The torque on the FL shows a linear dependence on this parameter, while the torque on the RL is almost independent of it.

Fig. 7.12(b) then shows the dependence of the FL adiabatic torque on the conductivity polarization of both the RL and FL. For any value of $_{\sigma,FL}$, the value of the torque in the FL still shows the same linear dependence on the polarization of

Die approbierte gedruckte Originalversion dieser Dissertation ist an der TU Wien Bibliothek verfügbar.
The approved original version of this doctoral thesis is available in print at TU Wien Bibliothek.
TU Bibliothek WIEN Your knowledge hub

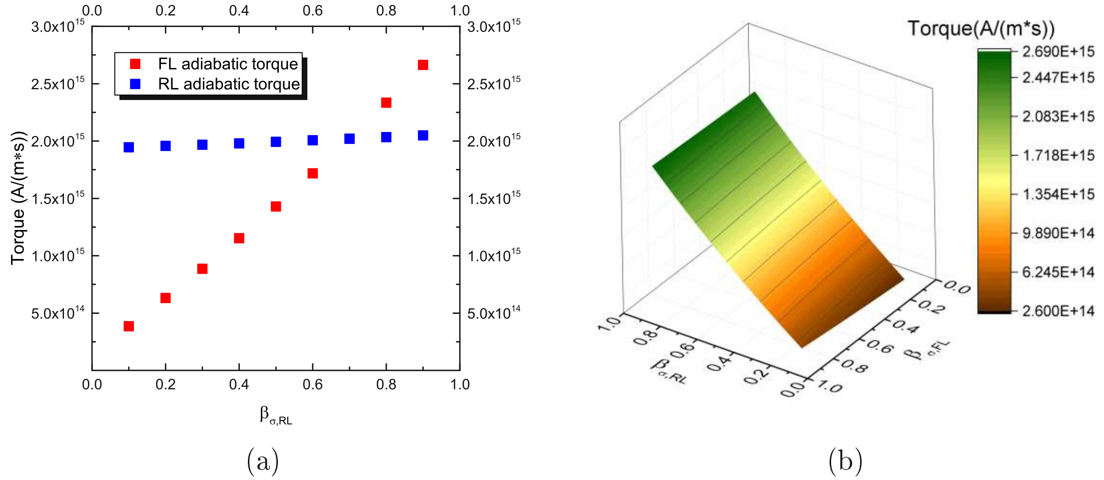

Figure 7.12: (a) Dependence of the average torque acting on the FL and RL on the polarization parameter of the RL, $_{\sigma,RL}$. (b) Dependence of the damping-like torque acting on the FL on the polarization $_{\sigma}$ of both the FL and the RL. (a) was published in [146], (b) was published in [148].

the RL, and it is almost constant with respect to the one of the FL. This behavior is compatible with the dependence on $_{\mathrm{RL}}$ and $_{\mathrm{FL}}$ expected from the adiabatic component of the Slonczewski torque term in (3.47), which, for the FL of the structure under study, takes the form

$$_{\mathrm{S}} = \frac{\ _B \ \ _{\mathrm{C,x}}}{\ _S \ \ _{\mathrm{FL}}} \frac{\ _{\mathrm{RL}}}{2(1 + \ _{\mathrm{RL}} \ \ _{\mathrm{FL}} \cos \ )} \ _{\mathrm{FL}} \ (\ _{\mathrm{FL}} \ \ _{\mathrm{RL}}) \tag{7.6}$$

where is the angle between $_{\mathrm{RL}}$ and $_{\mathrm{FL}}$, so that cos = $_{\mathrm{RL}}$ $_{\mathrm{FL}}$. With = 90° and $_{RL}$ = $_{FL}$ = 0 7 (giving a TMR of 200% from (3.51)), this produces a damping-like (DL) torque in the FL of $_{\mathrm{S,DL}}$ = 2 03 10 A/(m s). The previous analysis can be employed to calibrate the torque produced by the FE drift-diffusion solver and extract a set of effective parameters capable of reproducing the one predicted by the Slonczewski term. In Fig. 7.13(a) the spin accumulation solution for the modified set of parameters reported in Table 7.2 is shown. The lower exchange length allows the transverse components of to be completely absorbed inside the FL, as typically expected for strong ferromagnets [16, 155], while the lower value of the diffusion coefficient in the ferromagnetic layers allows the polarization term in (6.38) to dominate the spin current value. The torque acting on both ferromagnetic layers is reported in Fig. 7.13(b). The solution computed through the solver is compared to one based on analytical expressions for the spin accumulation in the different layers, obtained by including the $_{\varphi}$ term to the results presented in [156] and adapting them to the structure under study. The resulting system of equations is reported in Section A.1 of the Appendix. The two results are in perfect agreement, confirming the accuracy of the FE solver. The average damping-like torque acting on the FL obtained from (7.4) is $_{\mathrm{S,DL}}$ = 2 02 10 A/(m s), which is compatible with the value computed using (7.6). The drift-diffusion approach, thanks to the

Die approbierte gedruckte Originalversion dieser Dissertation ist an der TU Wien Bibliothek verfügbar.
The approved original version of this doctoral thesis is available in print at TU Wien Bibliothek.
TU Bibliothek WIEN Your knowledge hub

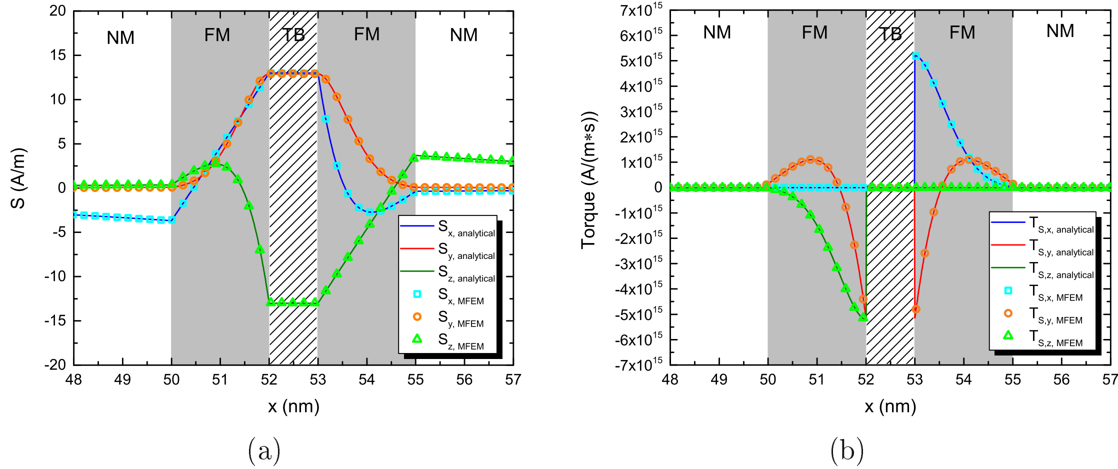

Figure 7.13: Results for both (a) the spin accumulation and (b) the torque computed with the modified parameters reported in Table 7.2. The FE solution is compared to an analytical one, showing very good agreement. The transverse components of the spin accumulation get absorbed inside the FL, and the average value of the adiabatic torque ($_{S,x}$ in the FL) is compatible with that predicted by Slonczewski for an MTJ. The figures were adapted from [147].

Table 7.2: Modified parameters used to reproduce the Slonczewski torque magnitude.

Parameter	**Value**
Charge polarization, $_{\sigma}$	0 7
Electron diffusion coefficient in NM, $_{e,NM}$	1 0 10⁻ m /s
Electron diffusion coefficient in FL and RL, $_{e,FM}$	1 0 10⁻ m /s
Spin exchange length, $_{J}$	0 5 nm

presented effective choice of material parameters, is thus able to reproduce the torque magnitude expected in MTJs.

The advantage of the FE implementation over the presented analytical solution is the possibility to compute   in more articulated structures and with non-uniform magnetization configurations, typical during the switching process. The three components of a three-dimensional solution for the spin accumulation, computed using the parameters in Table 7.2 and the same magnetization configuration, MTJ conductance and TMR employed for the results in Fig. 7.1, is reported in Fig. 7.14. The structure is sandwiched by 50 nm NM contacts. The applied bias voltage is 3 36 V, producing a current density $_{C,x}$ = 10 A/m at = 90°. The spin accumulation is redistributed, in both layers, in response to both the nonuniform magnetization configuration and the current density distribution. This solution, computed using (6.60), (6.59) and (7.2), can be plugged into (6.58a) for computing the torque and evaluating the magnetization dynamics.

Die approbierte gedruckte Originalversion dieser Dissertation ist an der TU Wien Bibliothek verfügbar.
The approved original version of this doctoral thesis is available in print at TU Wien Bibliothek.
TU Bibliothek Your knowledge hub WIEN

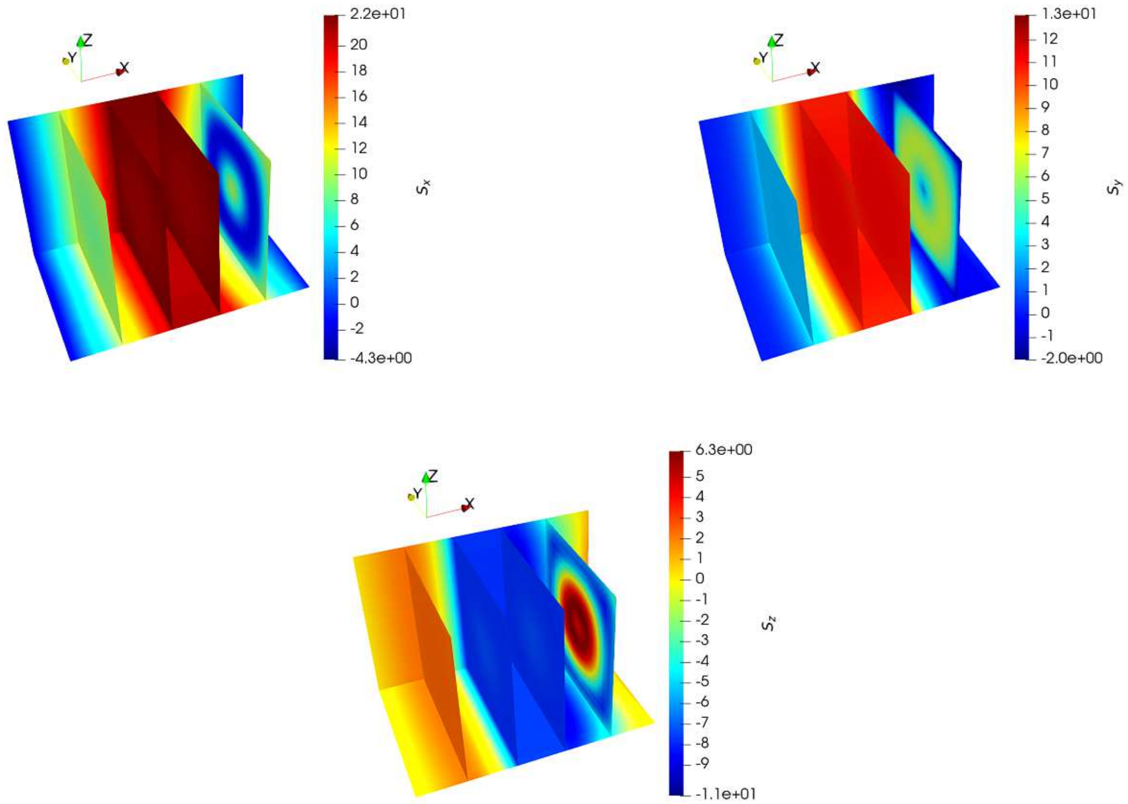

Figure 7.14: Spin accumulation computed with non-uniform magnetization configuration. The top left panel reports the x-component, the top-right panel reports the y-component, and the bottom panel reports the z-component. The values are reported for 4 planes, located in the middle of the RL, at the left interface of the TB, at the right interface of the TB and in the middle of the FL, respectively. The figures were published in [146].

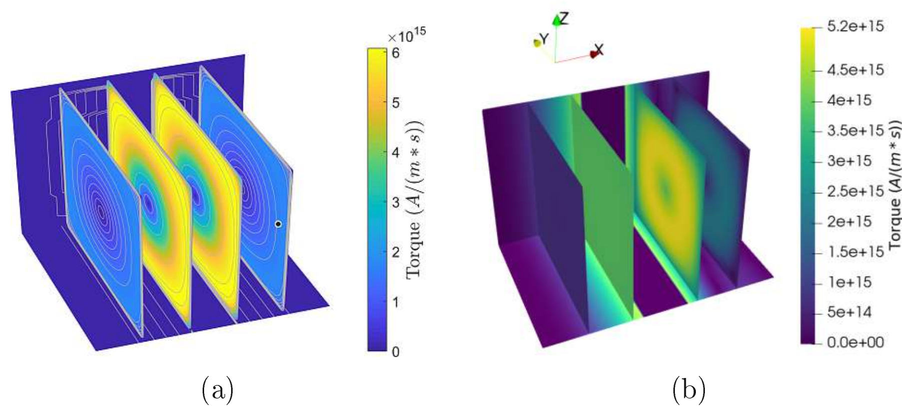

(a) (b)

Figure 7.15: Torque obtained combining multiple analytical solutions (a) compared to the one obtained by the FE solver (b). The former fails to account for the redistribution of due to local gradients in the magnetization. The figures were published in [147] (© 2021 IEEE).

Die approbierte gedruckte Originalversion dieser Dissertation ist an der TU Wien Bibliothek verfügbar.
The approved original version of this doctoral thesis is available in print at TU Wien Bibliothek.
TU WIEN Bibliothek Your knowledge hub

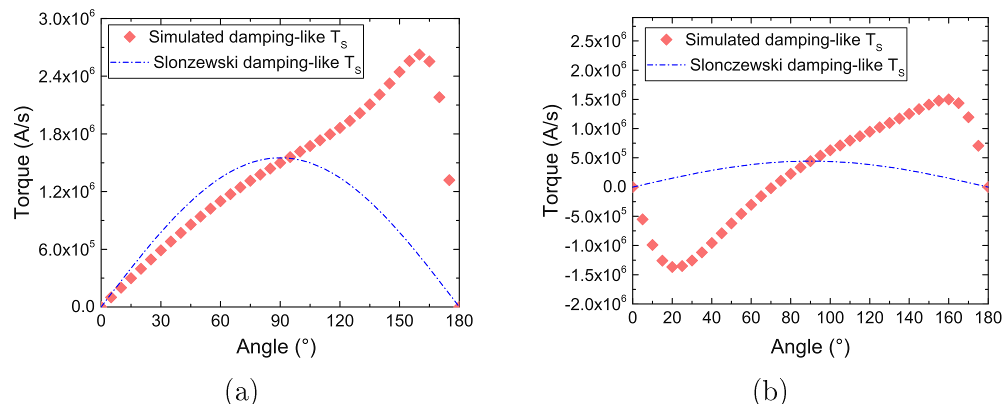

Figure 7.16: Angular dependence of the damping-like torque acting on a semi-infinite FL based on the drift-diffusion approach (dotted line) and on the Slonczewski expression (7.6) (dashed line). (a) Results obtained for the parameters in Table 7.2. (b) Results obtained with $_{\sigma\mathrm{RL}} = 0\ 2$. (a) was adapted from [13].

Moreover, the difference between the torque computed from a combination of analytical solutions at various angles and the fully three-dimensional one is investigated. The solutions for the torque obtained from the analytical expression at several values of were combined into a single image, matching the magnetization distribution showcased in Fig. 4.1. The damping-like component's magnitude for the combined torque is reported in Fig. 7.15(a). The one for the torque obtained from the spin accumulation of Fig. 7.14 is shown in Fig. 7.15(b). It can be seen that the analytical approach fails to account for the redistribution of due to diffusive effects and local gradients in the magnetization, so that the full solution computed by the FE solver can better capture the torque acting on the magnetization.

7.4.1 Limitations of the Effective Parameters' Approach

The results presented in this chapter show that it is possible to employ effective material parameters to obtain a spin accumulation with the right sign and magnitude to reproduce typical values of the STT torque expected in an MTJ. The FE approach to the drift-diffusion formalism gives the possibility of computing the torques in all the ferromagnetic layers of the structure for a variety of three-dimensional meshes. It must be noted, however, that the presented approach is not sufficient to reproduce all the properties of the MTJ torque. The first right hand side term of equation (6.60) poses a strictly linear dependence of the torque on the applied bias voltage, coming from the linear dependence of $_{\mathrm{C}}$ on from equation (6.59). Theoretical calculations [99, 154, 157, 158] and experimental findings [159–162] have shown that, at high bias voltage, the adiabatic component can present a nonlinear behavior, while the non-adiabatic component is symmetric with respect to the applied bias.

Moreover, the angular dependence of the torque obtained by the presented formalism diverges from the sinusoidal one predicted in MTJs under a constant bias voltage [16, 99]. In Fig. 7.16(a), the angular dependence of the damping-like torque

TU Bibliothek Your knowledge hub WIEN
Die approbierte gedruckte Originalversion dieser Dissertation ist an der TU Wien Bibliothek verfügbar.
The approved original version of this doctoral thesis is available in print at TU Wien Bibliothek.

acting on a semi-infinite FL is compared with the Slonczewski expression (7.6). $_{\mathrm{C,x}}$ is extracted from the FE charge current solution for every value of the angle . For these results, semi-infinite FM layers are considered, to exclude any influence of the FL length and of the NM contacts, and a constant bias voltage of $= 1\ 3$ V is applied. Because of the constant bias, the dependence of (7.6) on the angle is given only by sin , in contrast to the dependence at a constant current and current density, where the cos term in the denominator plays a role. The reported values are obtained from the torque integral (7.4) without the division by the FL thickness. While the torques obtained at $= 90°$ are compatible, thanks to the previous calibration, there is a clear deviation of the drift-diffusion results from the expected ones at other values of . A modification in the polarization parameters can also have a huge impact on the angular dependence. In Fig. 7.16(b), results for $_{\sigma,\mathrm{RL}} = 0\ 2$ are reported, compared to the Slonczewski results for $_{\mathrm{RL}} = 0\ 2$. In this case, the discrepancy between the drift-diffusion results and the Slonczewski ones is even greater, with the torque computed by the former changing its sign for 75°. Negative values of the torque indicate that it is favoring the anti-parallel orientation of the layers, rather than the parallel one. This wavy torque behavior has been reported and studied in metallic valves [125], but is not typical of MTJs. In order to employ the approach presented in this chapter to obtain a sinusoidal angular dependence, characteristic to MTJs, several independent sets of angular-dependent parameters are needed for different relative orientations of the magnetization vectors. As this procedure is clearly unacceptable, a more appropriate treatment of the tunneling spin-current is thus required to be able to comprehensively reproduce the properties of the torque acting in MTJs. A suitable approach will be developed in the next Chapter.

TU Bibliothek WIEN Your knowledge hub
Die approbierte gedruckte Originalversion dieser Dissertation ist an der TU Wien Bibliothek verfügbar.
The approved original version of this doctoral thesis is available in print at TU Wien Bibliothek.

Chapter 8

Tunneling Spin Current in the Drift-Diffusion Formalism and Applications to Ultra-Scaled MRAM Switching Simulations

The drift-diffusion approach previously described only accounts for semi-classical transport properties, and needs to be adapted to the description of the tunneling process across an MTJ. While the TMR effect can be reproduced by describing the TB conductivity through (7.2), using effective material parameters for the spin equation is not sufficient to reproduce all the expected torque properties. This chapter shows how the FE solver must be enhanced with appropriate boundary conditions at the TB interfaces to account for the tunneling spin current. It is shown how both the angular and voltage dependencies expected in MTJs are reproduced by the presented approach, which also predicts an interdependence between the torque acting in the presence of magnetization gradients and the tunneling spin current. The solver is then applied to simulate the magnetization dynamics of ultra scaled multi-layered structures with composite ferromagnetic layers. The results hereby presented were published by the author in references [163], [164], and [13].

8.1 Spin Drift-Diffusion Extension to Include MTJ Properties

The drift-diffusion (DD) approach described in the previous chapter needs to be updated to incorporate the effect of the tunneling process on the spin accumulation. In order to do this, an appropriate expression for the tunneling spin current needs to be included in the model. The Nonequilibrium Green Functions (NEGF) formalism has been often employed to compute expressions for the charge and spin current flowing through the TB of an MTJ [118, 157, 165]. Running such calculations at every iteration of the FE solver, however, would be computationally very expensive. Through the circuit-theory approach [154] and by deriving analytical solutions to the

Die approbierte gedruckte Originalversion dieser Dissertation ist an der TU Wien Bibliothek verfügbar.
The approved original version of this doctoral thesis is available in print at TU Wien Bibliothek.
TU Bibliothek WIEN Your knowledge hub

NEGF equations [99], the expressions for tunneling spin and charge currents can be simplified, for practical thick TBs, to include the most prominent characteristics of the transport in a few key parameters:

$$ {}^{\mathrm{TB}}_{\mathrm{C}} = \quad (\;)\;(1 + \;_{\mathrm{RL}}\;\;_{\mathrm{FL}}\cos\;) \tag{8.1a}$$

$$ {}^{\mathrm{TB}}_{\mathrm{S,x}} = \frac{\;_{\mathrm{RL}}\;\;_{\mathrm{RL}} + \;_{\mathrm{FL}}\;\;_{\mathrm{FL}}\cos\;}{1 + \;_{\mathrm{RL}}\;\;_{\mathrm{FL}}\cos\;}\,\frac{\hbar}{2}\;\;{}^{\mathrm{TB}}_{\mathrm{C}} \tag{8.1b}$$

$$ {}^{\mathrm{TB}}_{\mathrm{S,y}} = \frac{1\;\;2\;(\;_{\mathrm{RL}}\;\;^{\eta}_{\mathrm{RL}}\qquad\;_{\mathrm{FL}}\;\;^{\eta}_{\mathrm{FL}})\sin\;}{1 + \;_{\mathrm{RL}}\;\;_{\mathrm{FL}}\cos\;}\,\frac{\hbar}{2}\;\;{}^{\mathrm{TB}}_{\mathrm{C}} \tag{8.1c}$$

$$ {}^{\mathrm{TB}}_{\mathrm{S,z}} = \frac{\;_{\mathrm{FL}}\;\;_{\mathrm{FL}}\sin\;}{1 + \;_{\mathrm{RL}}\;\;_{\mathrm{FL}}\cos\;}\,\frac{\hbar}{2}\;\;{}^{\mathrm{TB}}_{\mathrm{C}} \tag{8.1d}$$

( ) contains the voltage dependent portion of the current density, is the angle between the magnetization vectors in the FL and RL, $_{RL}$ and $_{FL}$ are the in-plane Slonczewski polarization parameters, $^{\eta}_{RL}$ and $^{\eta}_{FL}$ are out-of-plane polarization parameters, and $_{\mathrm{FL}}$ and $_{\mathrm{RL}}$ describe the influence of the interface spin-mixing conductance on the transmitted in-plane spin current. These expressions describe charge and spin currents with the magnetization in the RL pointing in the x-direction and the one in the FL lying in the xz-plane, at an angle from the RL one. The spin current is expressed in the typical units of J/m .

Equation (8.1a), describing the dependence of the charge current on the RL and FL polarization parameters and on the relative angle between their magnetization vectors, traces back to (7.1), and was already included in the model through equation (7.2). As seen by the results of the previous chapter, the spin current part of (8.1) must also be accounted for. The FE approach to the DD equations based on the Galerkin method [23] enforces the continuity of the spin accumulation and current through all the interfaces. Equation (8.1) must thus be included while preserving the continuous nature of both quantities.

When deriving a solution to the spin drift-diffusion equations based on analytical expressions for the spin accumulation, this can be achieved by including (8.1b), (8.1c) and (8.1d) in the continuity equations for the spin current across the TB interfaces, as detailed in Section A.2 of the Appendix. The diffusion coefficient of the TB $_{\mathrm{S}}$ is also taken to be low, proportionally to the conductivity from (7.2), as no diffusive transport happens across the barrier.

In order to obtain the solution through the FE solver, the following boundary terms must be added on the right hand side of the weak formulation (6.60):

$$\int_{\mathrm{RL|TB}} \;{}^{\mathrm{TB}}_{\mathrm{S}}\;\;\boldsymbol{v}\,\mathrm{d}\; + \int_{\mathrm{TB|FL}} \;{}^{\mathrm{TB}}_{\mathrm{S}}\;\;\boldsymbol{v}\,\mathrm{d} \tag{8.2a}$$

$$ {}^{\mathrm{TB}}_{\mathrm{S}} = \;\frac{B}{}\;\frac{\;_{\mathrm{C}}}{1 + \;_{\mathrm{RL}}\;\;_{\mathrm{FL}}\;\;_{\mathrm{RL}}\qquad_{\mathrm{FL}}}\Big[\;_{\mathrm{RL}}\;\;_{\mathrm{RL}}\quad_{\mathrm{RL}} + \;_{\mathrm{FL}}\;\;_{\mathrm{FL}}\quad_{\mathrm{FL}} + $$
$$ + 1\;\;2\;(\;_{\mathrm{RL}}\;\;^{\eta}_{\mathrm{RL}}\qquad_{\mathrm{FL}}\;\;^{\eta}_{\mathrm{FL}})\;\;_{\mathrm{RL}}\qquad_{\mathrm{FL}}\Big] \tag{8.2b}$$

Table 8.1: Parameters used in the DD simulations with the TB boundary terms.

Parameter	Value
Conductivity polarization, $_{\sigma}$	0 7
Diffusion polarization, $_{D}$	0 8
NM diffusion coefficient, $_{e,NM}$	10^{-} m /s
FM diffusion coefficient, $_{e,FM}$	2 0 10^{-} m /s
TB diffusion coefficient, $_{S}$	2 0 10^{-} m /s
NM conductivity $_{NM}$	5 0 10 S/m
FM conductivity $_{FM}$	1 0 10 S/m
TB conductance,	4 76 10^{-} S
Polarization factors $_{RL}=$ $_{FL}$	0 707
In-plane torque reduction $_{\mathrm{RL}}$ = $_{\mathrm{FL}}$	1 0
Out-of-plane polarization $^{\eta}_{RL}=$ $^{\eta}_{FL}$	0 2
Spin flip length, $_{sf}$	10 nm
Spin exchange length, $_{J}$	1 nm
Spin dephasing length, $_{\varphi}$	5 nm

RL|TB and TB|FL are the interfaces between the TB and the RL and FL, respectively, is the interface normal, which for the employed meshes points in the positive x-direction for both interfaces, and $_{\mathrm{RL(FL)}}$ is the unit magnetization vector of the RL(FL) at the interface. By solving (6.60) with the inclusion of (8.2) and the low value of $_{\mathrm{S}}$, the spin current in the TB is fixed to the value prescribed by (8.2b) when $_{\mathrm{C}}$ flows through the MTJ. This is the key to describe the spin currents and the spin accumulations in the RL and FL of an MTJ.

As is the case for (7.2), the inclusion of the additional boundary condition in the MFEM implementation needs special care. The computation of the boundary term associated to (8.2) requires knowledge of the magnetization vector on the opposite interface. In order to get access to these values, the coefficient describing the boundary integral is initialized as follows:

- For each integration point on the RL|TB interface requiring the computation of the tunneling spin current, the solver loops through the integration points of the TB|FL interface
- The TB|FL point with coordinates closest to the RL|TB one is selected
- The integration point number and element number associated with the found TB|FL point are mapped to the coordinates of the RL|TB one
- The mapping procedure is repeated for the TB|FL interface

In a transient simulation, the search is carried out only during the initialization of the solver. At every time-step, the data necessary for the computation of (8.2)

Die approbierte gedruckte Originalversion dieser Dissertation ist an der TU Wien Bibliothek verfügbar.
The approved original version of this doctoral thesis is available in print at TU Wien Bibliothek.
TU WIEN Bibliothek Your knowledge hub

can be accessed through the generated maps, without the need to repeat the search procedure.

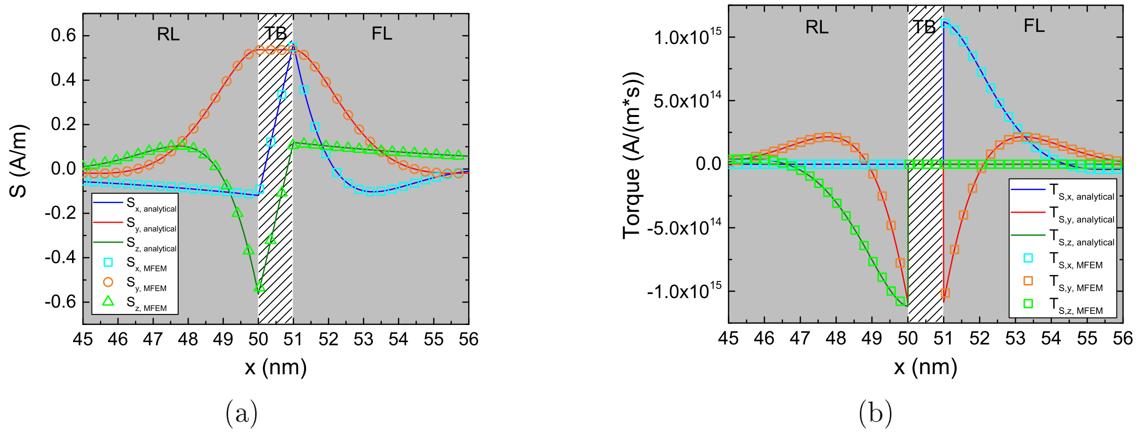

Figure 8.1: Spin accumulation (a) and torque (b) computed with the inclusion of the tunneling spin current, for semi-infinite FM layers. The analytical solution is compared with the FE one, computed with the inclusion of the spin-current boundary condition 8.2, showing perfect agreement. Magnetization is along in the RL, along in the FL.

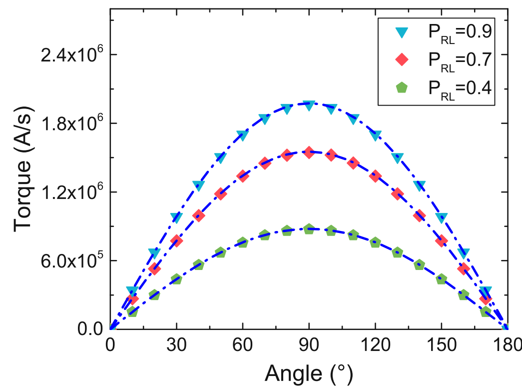

Figure 8.2: Angular dependence of the torque with the spin-current boundary conditions, for semi-infinite FL and RL. The expected sinusoidal angular dependence of an MTJ is reproduced, for several values of the RL spin polarization parameter. The figure was adapted from [13].

8.1.1 Spin Accumulation and Spin Torque Solutions

In Fig. 8.1, the spin accumulation and torque obtained from the parameters of Table 8.1 are reported. The structure employed has semi-infinite ferromagnetic leads and TB of 1 nm thickness. The magnetization of the RL points in the x-direction, while the one of the FL points in the z-direction. The FE solution is compared to the analytical one, showing that the additional boundary terms in the FE implementation

Die approbierte gedruckte Originalversion dieser Dissertation ist an der TU Wien Bibliothek verfügbar.
The approved original version of this doctoral thesis is available in print at TU Wien Bibliothek.
TU Bibliothek WIEN Your knowledge hub

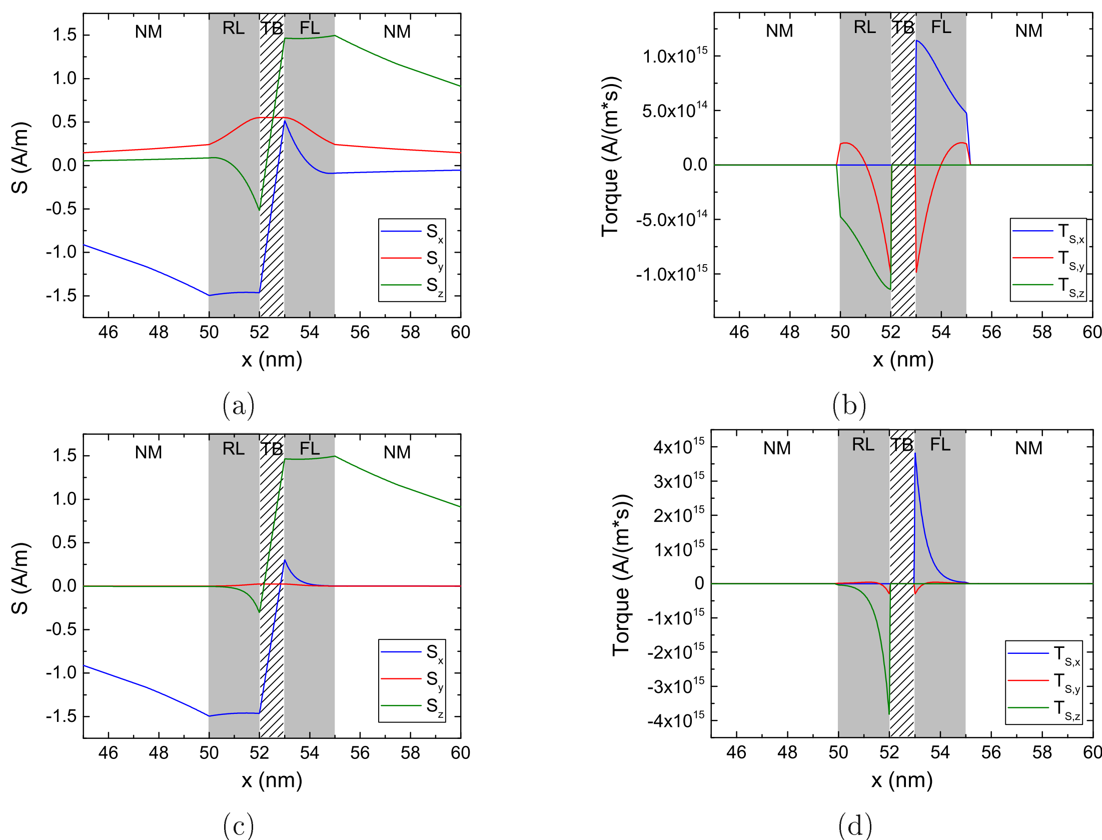

Figure 8.3: Spin accumulation and torque in a symmetric MTJ structure including NM contacts. (a) and (b) present results for $_{\varphi} = 5$ nm. (c) and (d) present results for $_{\varphi} = 0\ 4$ nm. (a) and (c) were adapted from [164].

are able to create perfect agreement between the two. The inclusion of the tunneling spin current terms creates a jump between the values of the spin accumulation components parallel to the magnetization at the left and right interface of the TB. This is the manifestation of the MTJ polarization effects on the spin current [166]. Fig. 8.2 shows the angular dependence of the damping-like torque with the inclusion of the spin current boundary conditions, computed in the same structure through (7.4) without the division by the FL thickness. The typical simple sinusoidal dependence [16, 99, 118] of the torque acting on the FL in an MTJ is now reproduced exactly, for various values of the RL|TB interface spin polarization. The structure is biased by a fixed voltage of $= 1\ 3$ V, so that the torque is independent of the TB|FL polarization, and only depends linearly on the value of the RL|TB one.

While employing (8.2) gives the opportunity to fix the spin current in the TB to the value expected in MTJs, the length parameters entering (6.38) still determine the region over witch the transverse spin accumulation components are absorbed and the behavior of the torque in the bulk of the FM layers. Fig. 8.3(a) and Fig. 8.3(b) show the spin accumulation and torque obtained in a symmetrical MTJ structure including 50 nm thick NM layers, where the FM layers are 2 nm thick and the

Die approbierte gedruckte Originalversion dieser Dissertation ist an der TU Wien Bibliothek verfügbar.
The approved original version of this doctoral thesis is available in print at TU Wien Bibliothek.
TU WIEN Bibliothek Your knowledge hub

TB is 1 nm thick. The material parameters and magnetization orientation are the same as the ones employed for Fig. 8.1. In this case, the torque components are not completely absorbed in the FL, contrary to what is usually expected in strong ferromagnets [16,155], and the spin accumulation components transverse to the local magnetization penetrate inside the NM contacts. By taking an effective dephasing length of $_{\varphi} = 0\ 4$ nm, it is possible to guarantee a faster decay of the transverse spin accumulation components [120], so that the torque acts only in the proximity of the TB interface (cf. Fig. 8.3(c) and Fig. 8.3(d)).

8.1.2 Voltage Dependence of the Spin Torques and TMR

The implementation discussed until now still produces a linear dependence of the torques on the bias voltage, with a vanishing field-like component for $^{\eta}_{RL} = {}^{\eta}_{FL}$. As already mentioned at the end of Chapter 7, fabricated MRAM devices usually exhibit clear non-linearity in the observed voltage dependence of the torques, with the TMR value also depending on the applied bias [159–162]. The presented approach gives the opportunity to account for this non-linearity by having the polarization parameters

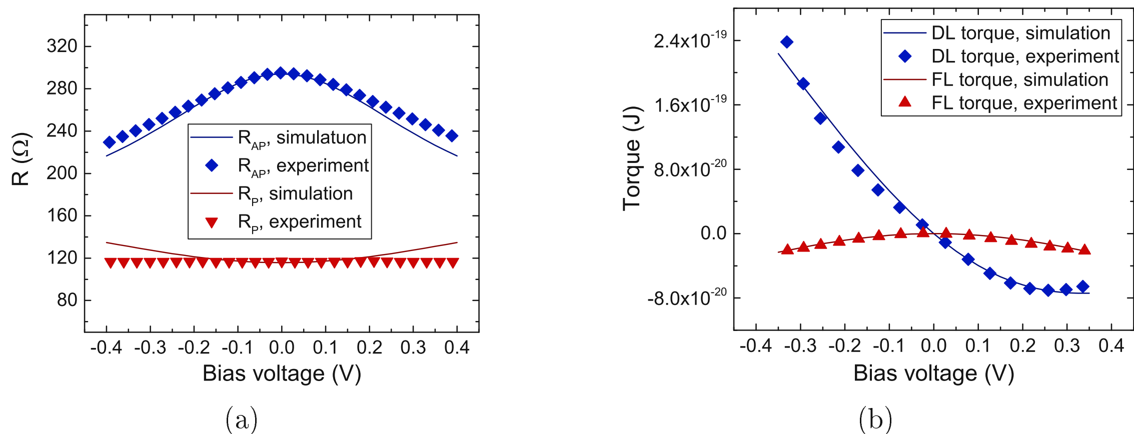

Figure 8.4: Dependence of both resistance (a) and damping-like (DL) and field-like (FL) torques (b) on the applied bias voltage, compared with the experimental results from [159].

Table 8.2: Parameters employed for reproducing the experimental results from [159].

Parameter	Value
Zero bias polarization,	0 66
TB conductance,	6 02 10⁻ S
In-plane torque reduction, $_{RL} = {}_{FL}$	0 36
Out-of-plane polarization, $^{\eta}_{RL} = {}^{\eta}_{FL}$	0 11
Voltage dependence strength,	0.65 V

Die approbierte gedruckte Originalversion dieser Dissertation ist an der TU Wien Bibliothek verfügbar.
The approved original version of this doctoral thesis is available in print at TU Wien Bibliothek.
TU WIEN Bibliothek Your knowledge hub

$_{RL}$ and $_{FL}$ depend on the bias voltage. A phenomenological voltage-dependent expression can be postulated as [167]

$$_{\mathrm{RL}}(\ ) = \frac{1}{1 + \quad \exp(\qquad)} \qquad _{\mathrm{FL}}(\ ) = \ _{RL}(\qquad) \tag{8.3a}$$

$$= \frac{1}{\sqrt{\frac{\mathrm{TMR}_0}{\mathrm{TMR}_0}}} \quad 1 \tag{8.3b}$$

Here, can be extracted from the TMR at zero bias TMR , and from the high bias behavior. A comparison of both TMR and torque results with experimental ones [159] is reported in Fig. 8.4. The values for the torque were obtained by integrating the torque over the whole FL volume, and multiplying the result by $\hbar$ (2 $_{\mathrm{B}}$). The parameters employed to fit the observed TMR and torque dependence on the bias voltage are reported in Table 8.2. was extracted from the anti-parallel resistance $_{AP}$ = 294 and TMR =154% of the experimental structure, possessing a surface area of 70 nm 250 nm. The thicknesses of the RL, FL and TB are 3 nm, 2 nm and 1 nm, respectively. The torque and TMR obtained form the simulations show a good agreement with the experimental ones. A slight deviation of the computed resistance from the experimental one can be observed at higher values of the applied bias. This discrepancy can be attributed to the constant value employed for the conductance [154]. The inclusion of a voltage dependent expression for the tunneling conductance [65] will provide a way to obtain an even better fit to the experimental data.

8.2 GMR Effect in Spin-Valves

The approach detailed in the previous section is able to compute both the TMR and torques in an MTJ. Modern MRAM devices can however include also conductive spacer layers between the FM ones, either as part of the SAF [73], or to include additional RLs and improve the switching performance [168]. In the presence of such a metallic spacer layer, the GMR effect can be of significance. In the drift-diffusion formalism, the resistance dependence on the relative angle between the magnetization vectors in the presence of a metallic spacer can be accounted for by including the second right-hand side term of (6.7a) when computing the electrical potential . By taking $_{\mathrm{C}} = 0$ (in the absence of current sources, see (6.36c)) and expressing the electric field as = in (6.7a), the equation for results in

$$(\qquad) = \quad _{\mathrm{D}} \quad _{\mathrm{e}} \frac{\quad}{B} \quad \left[(\quad)^{\mathrm{T}} \quad \right] \tag{8.4}$$

Die approbierte gedruckte Originalversion dieser Dissertation ist an der TU Wien Bibliothek verfügbar.
The approved original version of this doctoral thesis is available in print at TU Wien Bibliothek.
TU WIEN Bibliothek Your knowledge hub

The weak formulation of (8.4), including the computation of the electric field and charge current density from , becomes then

$$\int \quad \mathrm{d} = \int_{\omega} D \quad e \frac{}{B}\Big[(\quad)^{\mathrm{T}} \quad \Big] \quad \mathrm{d} \tag{8.5a}$$

$$\int \quad \boldsymbol{v}\,\mathrm{d} = \int \quad \boldsymbol{v}\,\mathrm{d} \tag{8.5b}$$

$$\int \; _{\mathrm{C}} \; \boldsymbol{v}\,\mathrm{d} = \int \quad \boldsymbol{v}\,\mathrm{d} + \int_{\omega} D \quad e \frac{}{B}\Big[(\quad)^{\mathrm{T}} \quad \Big] \; \boldsymbol{v}\,\mathrm{d} \tag{8.5c}$$

As the spin-dependent term in (6.7a) is already taken into account in the computation of $_{\mathrm{C}}$, the spin current is described by (6.7b). The weak formulation of the spin accumulation equation (6.38a), with the inclusion of the TB boundary terms, if one is present, can then be expressed as

$$_{\mathrm{e}}\int \quad : \; \boldsymbol{v}\,\mathrm{d} + {}_{\mathrm{e}}\int \left(\frac{}{_{sf}} + \frac{}{_{J}} + \frac{(\quad)}{_{\varphi}} \right) \boldsymbol{v}\,\mathrm{d} =$$

$$\frac{B}{} \; _{\sigma} \int_{\omega} (\quad) : \; \boldsymbol{v}\,\mathrm{d} \quad \frac{B}{} \; _{\sigma} \int_{\partial \; \cap \partial\omega} ((\quad)\;) \; \boldsymbol{v}\,\mathrm{d} \; +$$

$$\int_{\mathrm{RL|TB}} {}^{\mathrm{TB}}_{\mathrm{S}} \; \boldsymbol{v}\,\mathrm{d} + \int_{\mathrm{TB|FL}} {}^{\mathrm{TB}}_{\mathrm{S}} \; \boldsymbol{v}\,\mathrm{d} \tag{8.6}$$

In this formulation, the spin accumulation and the electrical potential depend on each other, creating a coupled system of equations. In order to take the interdependence of and into account, the FE solver is updated to iterate over the solution of (8.5a) and (8.6) until a convergence threshold is reached. This approach can be directly applied to the FE implementation of the two separate equations, and does not require additional care for the inclusion of the boundary condition (8.2) when solving a fully coupled system. The iterative solution is computed as follows:

1. A first estimate for the spin accumulation is obtained by solving (6.59) and (6.60) as before, with the right-hand side term of (6.7a) included in the spin equation
2. is employed to compute a solution to (8.5a)
3. This solution is then used to obtain an updated spin accumulation estimate from (8.6)
4. Steps 2 and 3 are iterated until the solver reaches convergence

$$\frac{\; _{\mathbf{n}} \; _{L} \qquad _{\mathbf{n-1}} \; _{L}}{\; _{\mathbf{n}} \; _{L}} \tag{8.7}$$

In Fig. 8.5(a), the spin accumulation solution in a spin-valve obtained from the iterative approach is compared to the one computed using (6.59) and (6.60). The

Die approbierte gedruckte Originalversion dieser Dissertation ist an der TU Wien Bibliothek verfügbar.
The approved original version of this doctoral thesis is available in print at TU Wien Bibliothek.
TU Bibliothek WIEN Your knowledge hub

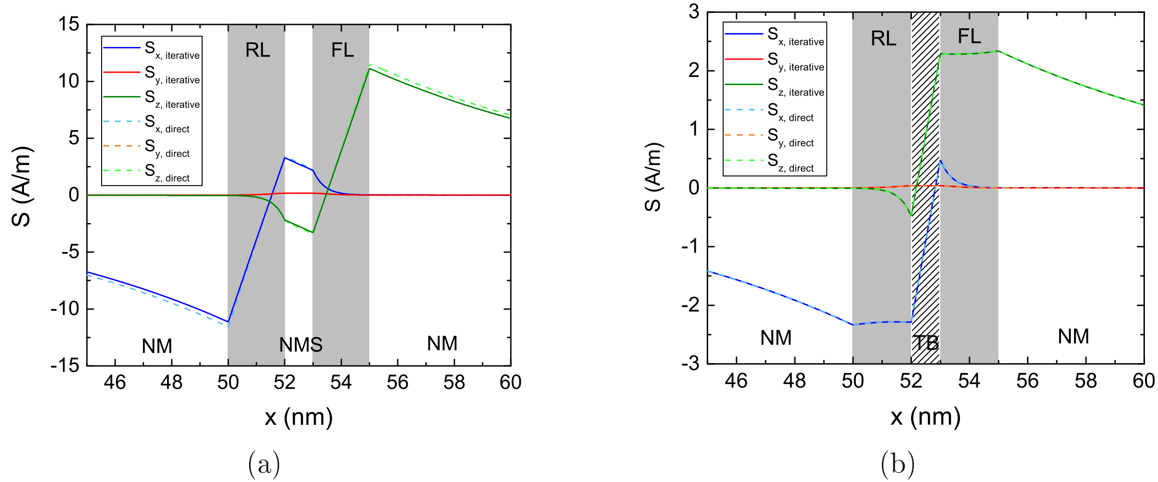

(a) (b)

Figure 8.5: Comparison of the solution of the iterative method described in this section to the one obtained by solving (6.59) and (6.60), for both a spin-valve (a) and an MTJ (b).

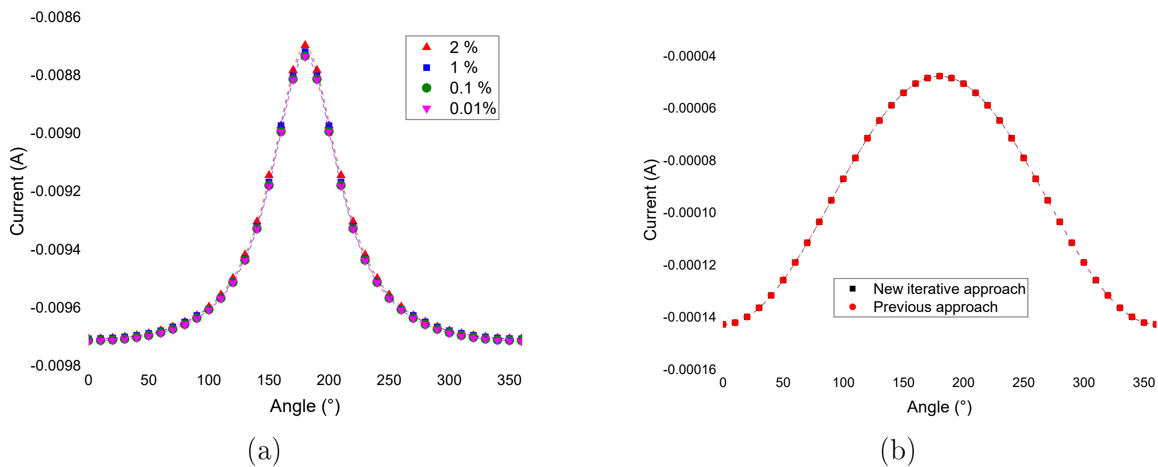

(a) (b)

Figure 8.6: (a) Angular dependence of the total charge current in a spin-valve structure with metallic spacer, computed with the iterative approach for various values of the convergence parameter . (b) Angular dependence of the torque in an MTJ, computed using both the direct and iterative approach. The figures were published in [13].

structure has the same dimensions as the one employed for the results presented in Fig. 8.3, with an NMS in place of the TB. The parameters are the ones of Table 8.1, with $_{\varphi} = 0\ 4$ nm. The two solutions show only a marginal difference between each other, testifying the fact that the iterative approach is useful in case one is interested in the GMR effect, but can be avoided if the main focus is on the computation of the torque and magnetization dynamics. In Fig. 8.5(b), the same comparison is shown for the solution in an MTJ, with a TB separating the two FM layers. In this case, the two solutions show perfect agreement between each other.

Die approbierte gedruckte Originalversion dieser Dissertation ist an der TU Wien Bibliothek verfügbar.
The approved original version of this doctoral thesis is available in print at TU Wien Bibliothek.
TU WIEN Bibliothek Your knowledge hub

Fig. 8.6(a) shows the obtained dependence of the total charge current on the relative angle between the magnetization vectors in the FL and RL, for several values of . The solution is computed in the structure in Fig. 1.1, with the middle layer treated as an NMS, for an applied voltage of 0 2 V. The dashed lines represent a fit carried out using the equation [169]

$$(\ ) = \frac{}{_{\mathrm{P}}} \frac{1 + \quad \cos}{1 + \mathrm{GMR} + (\quad \mathrm{GMR}) \cos} \tag{8.8}$$

where is the applied bias voltage, $_P$ is the resistance in the parallel state, and and GMR are used as fitting parameters. The GMR value is ∽ 11%, with the results obtained using = 1% converging fast (3) and giving a good approximation.

As the voltage drop is localized at the TB in an MTJ, the iterative solution is not necessary for the correct computation of the current. In order to confirm this, the charge current angular dependence with a tunneling middle layer is computed both by using the direct solution of equations (6.59) and (6.60), and by employing the iterative solution described in this section. The obtained results are reported in Fig. 8.6(b). The fitting can be performed by using the angular dependence expression (7.1). As the iterative solver always converges for = 1 and the results are indistinguishable from the direct solution, these findings confirm that the latter can be safely employed for all structures only containing MTJs.

8.3 Torques in Elongated Ultra-Scaled Devices

In the presence of elongated FLs like the ones in Fig. 1.2, the switching of the whole layer at the same time is not guaranteed: a domain wall or magnetization textures can be generated, with their propagation through the FL affecting the switching behavior. In this case, the additional spin torques created by the presence of magnetization gradients in the bulk of the ferromagnetic layers must be taken into account. These torques are modeled by the Zhang and Li (ZL) equation [151]

$$_{\mathrm{ZL}} = \frac{B}{} \frac{\sigma}{1 +} (\quad [\quad (\ _{\mathrm{C}} \quad) \ ] \qquad (\ _{\mathrm{C}} \quad) \ ) \tag{8.9}$$

where $= (\ _{\mathrm{J}} \quad _{\mathrm{sf}})$. This expression can be obtained from (6.12) by taking = and cross-multiplying two times by . This approximation is strictly valid only when the changes in are relatively slow, namely, when they happen over length scales longer than $_{\mathrm{sf}}$. By applying the same procedure to (6.38), (8.9) can be generalized to include $_{\varphi}$, obtaining the following expression:

$$_{\mathrm{ZL}} = \frac{B}{} \frac{\sigma}{1 + (\ + \ ')} ((1 + \ '(\ + \ ')) \quad [\quad (\ _{\mathrm{C}} \quad) \ ] \qquad (\ _{\mathrm{C}} \quad) \ ) \tag{8.10}$$

$' = (\ _J \quad _{\varphi})$ accounts for the additional contributions of the term involving $_{\varphi}$.

In order to test the ZL approximation, the magnetization profile shown in Fig. 8.7(a) is employed to compute both $_{\mathrm{S}}$ and $_{\mathrm{ZL}}$, with the parameters of

Die approbierte gedruckte Originalversion dieser Dissertation ist an der TU Wien Bibliothek verfügbar. The approved original version of this doctoral thesis is available in print at TU Wien Bibliothek.
TU WIEN Bibliothek Your knowledge hub

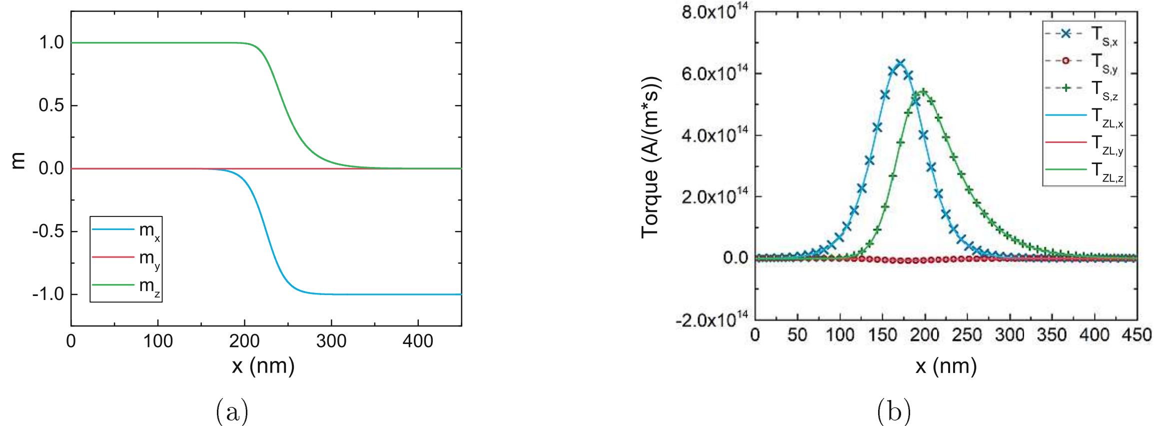

Figure 8.7: (a) Non-uniform magnetization texture with the magnetization orientation changing from z to -x. (b) Comparison of the spin torque $_S$ to the Zhang-Li torque $_{ZL}$ for a 100 nm long magnetization texture, with the parameters of Table 8.1. The two approaches are in good agreement. The figures were adapted from [13].

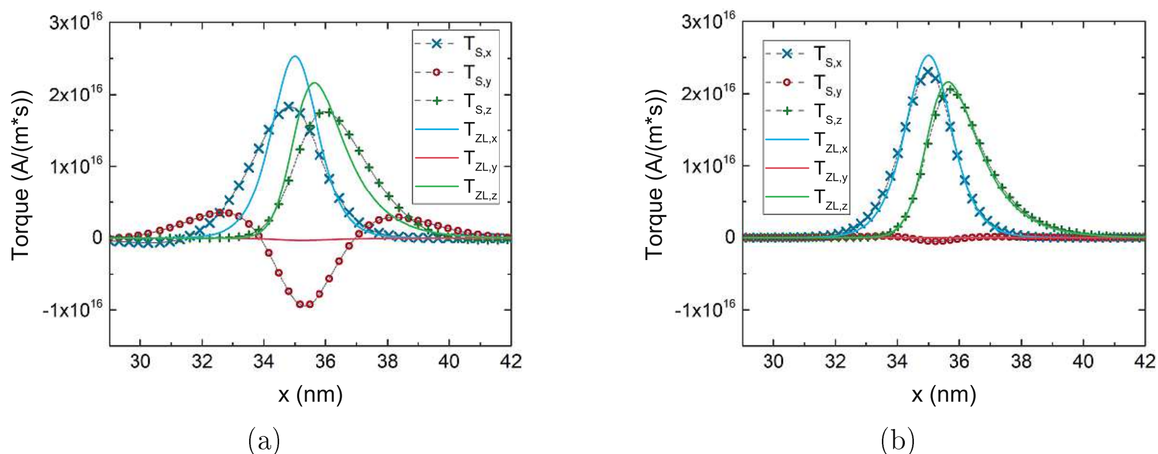

Figure 8.8: Comparison of the spin torque $_S$ to the Zhang-Li torque $_{ZL}$ for a a 3 nm long magnetization texture, for the parameters of Table 8.1 in (a) and $_{\varphi} = 0\ 4$ nm in (b). The shorter dephasing length takes the role of quickly absorbing the transverse spin accumulation components, so that the agreement between the ZL approximation and the drift-diffusion solution is recovered. The figures were adapted from [13].

Table 8.1. The structure used for the simulations is a single ferromagnetic layer of 450 nm. The same constant current density value of $_{C,x}$ = 1 33 10 A/m , flowing in the x-direction, is employed for the two approaches. Fig. 8.7(b) demonstrates that, for the given magnetization profile, with width of 100 nm, $_S$ is well reproduced with (8.9).

Fig. 8.8(a) reports the torques obtained by using the same parameters and a shorter magnetization texture of 3 nm, in a FM layer of 70 nm thickness. In

Die approbierte gedruckte Originalversion dieser Dissertation ist an der TU Wien Bibliothek verfügbar.
The approved original version of this doctoral thesis is available in print at TU Wien Bibliothek.
TU WIEN Bibliothek Your knowledge hub

this case, the spin accumulation gradients neglected in (8.9) affect the result, and a large deviation of $_{\mathrm{S}}$ from $_{\mathrm{ZL}}$ is observed, especially for the field-like torque (y-component). However, when the effective short value of the spin dephasing length $_{\varphi} = 0\ 4$ is employed, it guarantees the fast absorption of the transverse spin accumulation components, and $_{\mathrm{ZL}}$ recovers a good agreement with $_{\mathrm{S}}$, as shown in Fig. 8.8(b).

In MRAM cells with elongated FLs, magnetization textures and domain walls can form along the layer during switching. In this case, the polarized tunneling spin current can interact with such magnetization textures, and create torques that further deviate from the ZL approximation. In order to verify this, the torque is computed in an experimental MTJ structure, reported in [22] and shown in the top of Fig. 1.2. The cell employed for this simulations has a 5 nm RL, 0 9 nm TB (TB), and an elongated FL of 15 nm with a magnetization profile in the FL similar to the one shown in Fig. 8.7(a), with the magnetization vector going from the z-direction to the -x-direction over the length of the layer. The magnetization in the RL is pointing towards the x-direction. The FL is additionally capped by a second 0.9 nm TB (TB), and 50 nm NM contacts are included. The solution is computed with the same parameters as the ones employed for Fig. 8.8(b). The resistance of the overall cell in the parallel state and the polarization parameters used for the two TBs, extracted from the data in [22], are reported in Table 8.3. All parameters pertaining each TB are taken to be equal between its left and right interfaces. As the second TB is only added to grant an additional source of perpendicular anisotropy, thanks to the CoFeB|MgO interface, it can be fabricated to have minimal impact on the total resistance of the structure [21]. For this reason, its conductance is taken to be 5 times greater than the one separating RL and FL. Moreover, as it is directly interfaced with the NM contact, it is also taken to have a lower polarization than the main TB.

The torque $_{\mathrm{S}}$ acting in the FL for this magnetization profile is shown in Fig. 8.9(a), where the magnetization vectors in each part of the FM layers are also reported. Near the first TB, a Slonczewski torque contribution generated by the tunneling spin current can be observed, while the magnetization texture causes the torque contribution in the bulk. In Fig. 8.9(b) a close-up of the bulk portion of $_{\mathrm{S}}$, compared with the result obtained by applying the ZL expression (8.10) to the magnetization configuration of the FL, is reported, for the same value of the current density. The comparison reveals a substantial difference between the torques obtained with the presented model and the ZL approximation, even for the short $_{\varphi}$ value. This implies that the Slonczewski and ZL torque contributions cannot simply be added together, but influence and interact between each other.

Die approbierte gedruckte Originalversion dieser Dissertation ist an der TU Wien Bibliothek verfügbar.
The approved original version of this doctoral thesis is available in print at TU Wien Bibliothek.
TU WIEN Bibliothek Your knowledge hub

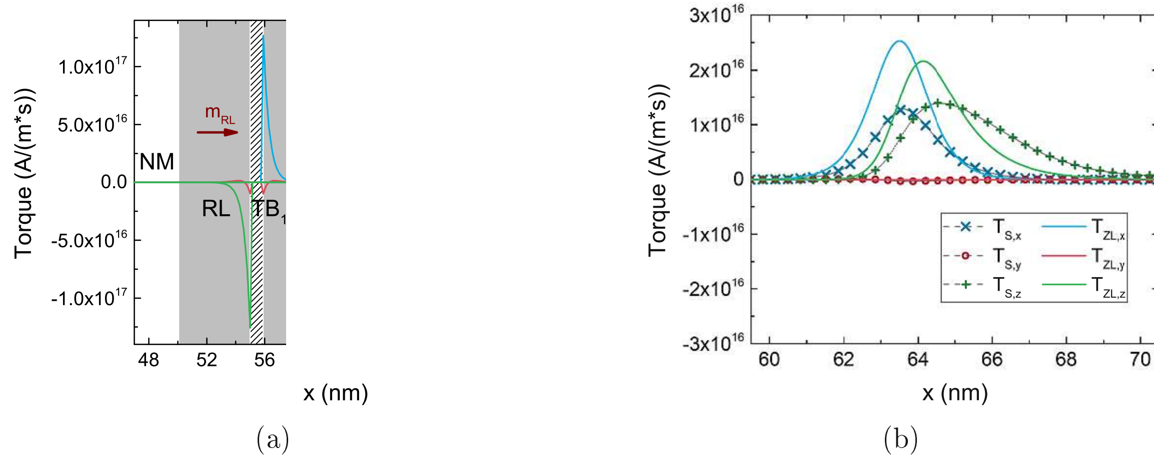

Figure 8.9: (a) Torque computed for an MRAM cell with elongated RL and FL and a magnetization profile in the FL similar to the one of Fig. 8.7(a), with a width of 3 nm. The brown vectors indicate the magnetization direction in the RL and in two parts of the FL. (b) Close-up of the spin torque $_S$ compared to the Zhang-Li torque $_{ZL}$. The presence of the MTJ influences also the bulk portion of the torque, making the unified approach the most suitable for dealing with ultra-scaled MTJs with elongated ferromagnetic layers. The figures were adapted from [13].

Table 8.3: Parameters used for the structure with elongated FL.

Parameter	Value
Parallel resistance, $_P$	4 1 10 k
TB polarization factor, $_{TB_1}$	0 617
TB polarization factor, $_{TB_2}$	0 2

In order to further elaborate on how the presence of the TBs influences the torque generated by the magnetization texture, the drift-diffusion solution is computed and compared to the ZL one with different values of the polarization parameter of the second barrier, $_{TB_2}$. The magnetization texture employed for the following results is a full domain wall, with rotating from +x to -x in the xz-plane. The value of the current density, flowing in the x-direction, is $_{C,x} =$ 10 A/m . First, the purely bulk solution, computed in a single FM layer, is reported in Fig. 8.10(a). The drift-diffusion and the ZL torques are in this case in perfect agreement. The three components of the spin current flowing in the x-direction, obtained from , are reported in Fig. 8.10(b). The spin current follows the magnetization profile, with the x-component assuming the values of $_{S,x} = (\ _B\ )\ _\sigma\ _{C,x}$ and $_{S,x} = (\ _B\ )\ _\sigma\ _{C,x}$ on the left and right of the domain wall, respectively, dictated by the first term of (6.38b).

The effect of the TBs is to modify the spin current flowing in the FM layer. The drift-diffusion solution is computed in the FL of the structure of Fig. 8.9(a), with the

Die approbierte gedruckte Originalversion dieser Dissertation ist an der TU Wien Bibliothek verfügbar.
The approved original version of this doctoral thesis is available in print at TU Wien Bibliothek.
TU Bibliothek WIEN Your knowledge hub

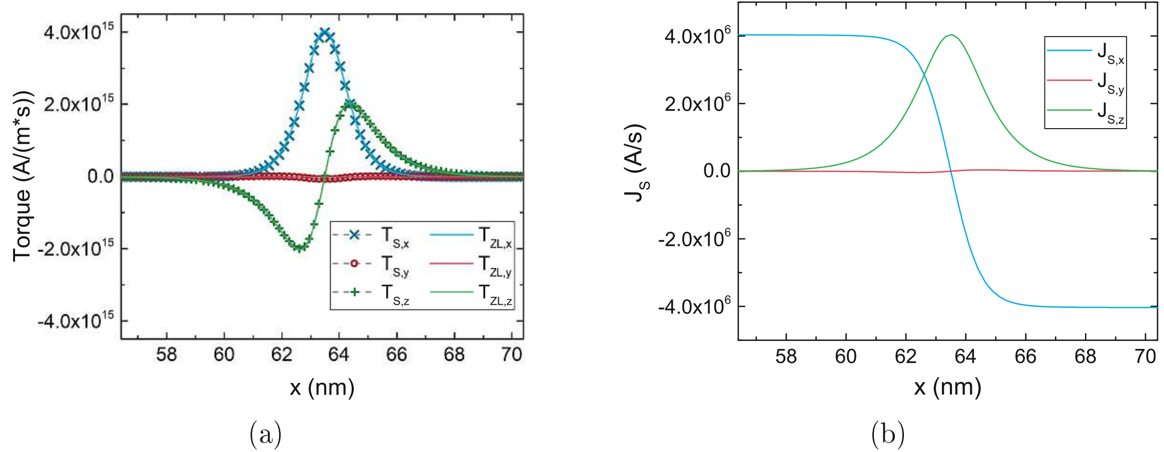

Figure 8.10: (a) Torque computed in a single FM layer with the magnetization going from the x- to the -x-direction over a domain wall of 3 nm. The ZL expression produces a torque in perfect agreement with the drift-diffusion one. (b) Spin current flowing in the x-direction, computed from the drift-diffusion solution. The three components follow the magnetization profile.

complete domain wall from +x to -x in the magnetization, and $_{\mathrm{TB}_2} = 0\ 2$. The spin current obtained in this case is reported in Fig. 8.11(a). At the interfaces of , the RL and FL magnetization vectors are parallel, so that (8.2b) gives the tunneling spin current value in the x-direction of $_{\mathrm{S,x}} = \ (\ _{\mathrm{B}} \ )(2 \ _{\mathrm{TB}_1} \ (1 + \ _{\mathrm{TB}_1})) \ _{\mathrm{C,x}}$. As $2 \ _{\mathrm{TB}_1} \ (1 + \ _{\mathrm{TB}_1}) \ \ _{\sigma}$, this value is greater than the purely bulk one. On the opposite side, at the interface of , as only the FL interface contributes to (8.2b), the tunneling spin current assumes the value of $_{\mathrm{S,x}} = (\ _{\mathrm{B}} \ ) \ _{\mathrm{TB}_2} \ _{\mathrm{C,x}}$, which is lower than the bulk one. The difference between the tunneling and bulk spin currents is reflected in the torques. On the left side of the domain wall, where the spin current is enhanced by the presence of , the drift-diffusion torque is slightly stronger than the ZL one, especially in the z-component. On the right side of it, the spin current is lowered by the presence of , and the drift-diffusion torque is consequently weakened when compared to the ZL expression, valid in the bulk. In Fig. 8.11(c) and Fig. 8.11(d) the spin current and torque for $_{\mathrm{TB}_2} = 0\ 9$ are reported, respectively. In this case, the tunneling spin current at both TBs is greater than the bulk one, so that the torque is enhanced over the whole domain wall.

The same simulations are repeated for a scenario where the magnetization in the FL is inverted, so that it goes from -x to +x over the domain wall. The sign of the current density is also inverted. The RL and FL magnetization vectors at TB are now anti-parallel, so that the tunneling spin current goes to 0. When $_{\mathrm{TB}_2} = 0\ 2$, the spin current at both TBs is lower than the bulk expectation, and the drift-diffusion torque is weaker than the ZL one over the whole layer (see Fig. 8.12(a) and Fig. 8.12(b), respectively). When $_{\mathrm{TB}_2} = 0\ 9$, the spin current tunneling across TB is instead grater than the bulk one, so that $_{\mathrm{S}}$ is slightly grater than $_{\mathrm{ZL}}$ on the right side of the domain wall, while still being weaker on the left side.

Die approbierte gedruckte Originalversion dieser Dissertation ist an der TU Wien Bibliothek verfügbar.
The approved original version of this doctoral thesis is available in print at TU Wien Bibliothek.
TU WIEN Bibliothek Your knowledge hub

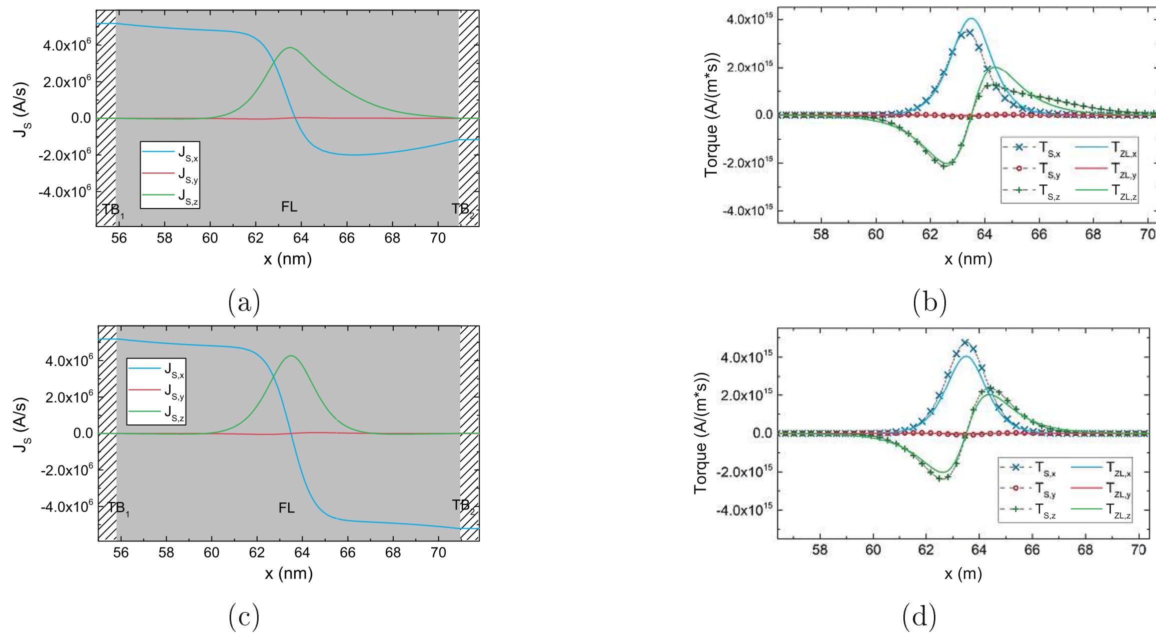

Figure 8.11: Spin currents ((a) and (c)) and torques ((b) and (d)) generated for the magnetization going from the +x- to the -x-direction over a domain wall, in the FL of the structure employed for Fig. 8.9(a). The drift-diffusion torque is compared to the one obtained from the ZL expression. The results in (a) and (b) were computed with $_{\mathrm{TB}_2}$. , the ones in (c) and (d) with $_{\mathrm{TB}_2}$ . .

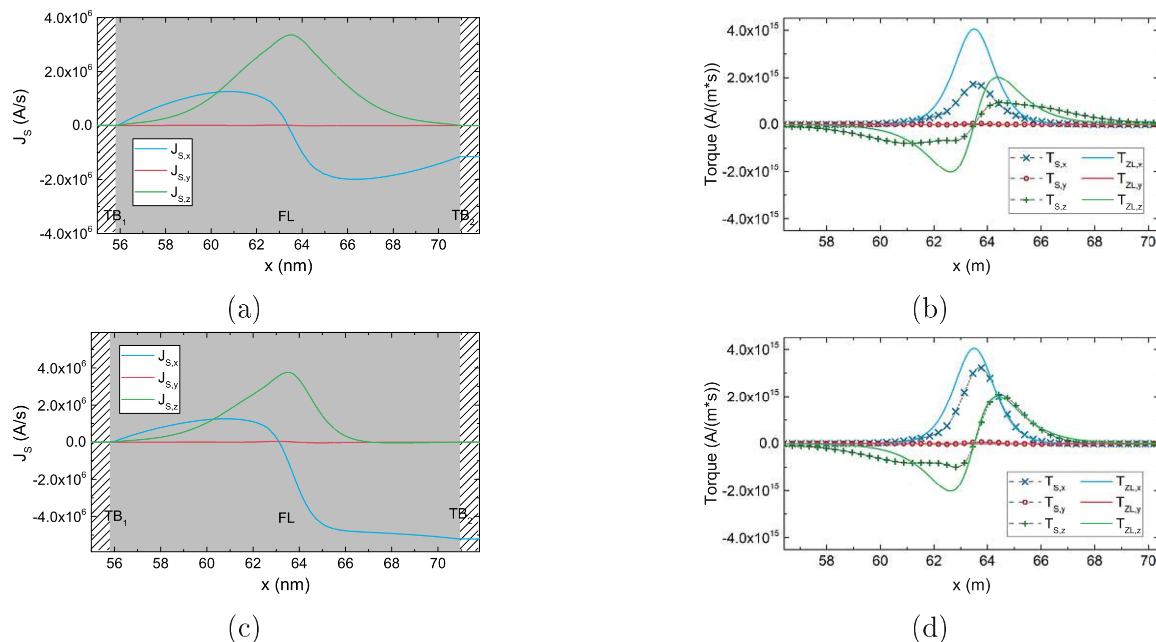

Figure 8.12: Spin currents ((a) and (c)) and torques ((b) and (d)) generated for the magnetization going from the -x- to the +x-direction over a domain wall, in the FL of the structure employed for Fig. 8.9(a). The drift-diffusion torque is compared to the one obtained from the ZL expression. The results in (a) and (b) were computed with $_{\mathrm{TB}_2}$. , the ones in (c) and (d) with $_{\mathrm{TB}_2}$ . .

Die approbierte gedruckte Originalversion dieser Dissertation ist an der TU Wien Bibliothek verfügbar.
The approved original version of this doctoral thesis is available in print at TU Wien Bibliothek.
TU WIEN Bibliothek Your knowledge hub

The extended drift-diffusion approach clearly demonstrates that, in an MTJ with elongated ferromagnetic layers, the contributions to the torque from the tunneling process and from magnetization gradients in the structure are not independent: the presence of the TBs influences the spin currents generated by the magnetization texture, modifying the ZL torque contribution. A unified treatment of the MTJ polarization process and FL magnetization texture is thus required to accurately describe the torque and switching in ultra-scaled MRAM.

8.4 Switching Simulations of Ultra-Scaled MRAM Devices

The proposed approach is applied to evaluate the switching of structures reproducing recently demonstrated Ultra-Scaled MRAM devices [22]. The diameter of all the simulated structures is 2.3 nm, and they all possess NM contacts of 50 nm. As the main interest lies in the switching behavior of the FL, the RL is kept numerically fixed, with the magnetization pointing in the positive x-direction. The magnetization of the FL is tilted 5° away from the perfect P or AP orientation, to emulate the destabilizing effect of a non-zero temperature on the system. The precise value employed for the tilting angle only affects the duration of the incubation period before the start of the switching process, and does not change the overall behavior of the magnetization reversal. The resistance and polarization parameters, employed for all the structures, are the ones reported in Table 8.3. Voltage dependence of the polarization parameters is not considered for these results.

First, switching realizations are carried out in a cell similar to the one employed for the results in the previous section, with an FL of 10 nm. The magnetization trajectories are reported in Fig. 8.13(a). A bias voltage of 1 5 V is applied on the left contact for P to AP or AP to P switching, respectively. The value of the bias voltage, while being sufficient to achieve switching for the AP to P scenario, is not enough to reverse the magnetization from P to AP. The additional stability of the parallel configuration comes from the stray field contribution of the RL, which favors it. Due to the presence of a stronger spin current component parallel to the magnetization at the TB interface in the P state, the interaction of the Slonczewski and Zhang-Li torque contributions quickly generates a texture in the magnetization, whose average x-component slightly deviates from the starting configuration, as evidenced by the dip in the plot during the first nanoseconds of the simulation. Despite this, the overall torque is not strong enough to overcome the perpendicular anisotropy.

Additional simulations with increased bias values of 2 , 3 V and 4 V are carried out, and the resulting magnetization trajectories are reported in Fig. 8.13(b). The increased values of the bias voltage, producing a stronger torque acting on the FL magnetization, are able to achieve switching for both configurations. Moreover, the switching behavior of structures with FL thickness of 5 nm and 7 5 nm is investigated. The results are presented in Fig. 8.13(c). A shorter layer possesses a reduced energy barrier separating the two magnetization configurations [53], so that

Die approbierte gedruckte Originalversion dieser Dissertation ist an der TU Wien Bibliothek verfügbar.
The approved original version of this doctoral thesis is available in print at TU Wien Bibliothek.
TU WIEN Bibliothek Your knowledge hub

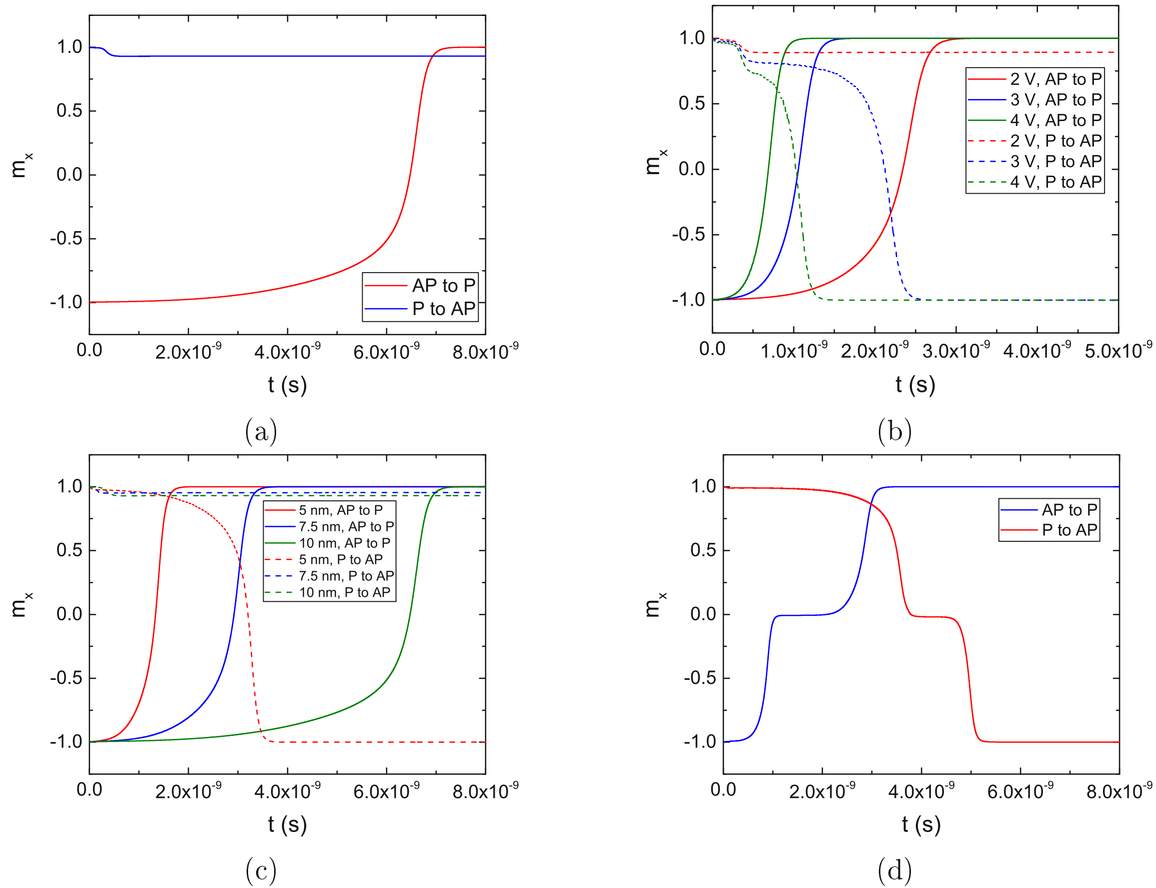

Figure 8.13: (a) Switching results for a structure with an elongated FL, for both the AP to P and P to AP scenarios, under a bias voltage of 1 5 V. (b) Switching results for a structure with an elongated FL under increasing bias voltage values. (c) Switching results for a structure with an elongated FL for several lengths of the FL. (d) Switching results for a structure with composite FL under a bias voltage of 1 5 V. The figures were published in [13].

the speed of AP to P switching is improved, and P to AP reversal is achieved in the case of the 5 nm layer.

The switching performance can be improved by employing a structure where the FL is split into two parts of 5 nm length by an additional MgO layer (TB), presented in the middle of Fig. 1.2. The addition of an MgO layer boosts the overall stability of the cell because of an increased interface anisotropy contribution, while the two parts of the FL have a preferred aligned configuration because of the stray field they exert on one another [22]. The presented approach is employed to carry out switching simulations in such a structure, under a bias voltage of 1 5 V. TB is taken to possess the same conductance of TB , and a polarization parameter $_{\mathrm{TB}_3} = 0\ 57$ [22]. The results are presented in Fig. 8.13(d). The plot evidences how the switching process is overall faster in the composite structure as compared to the one with a

Die approbierte gedruckte Originalversion dieser Dissertation ist an der TU Wien Bibliothek verfügbar.
The approved original version of this doctoral thesis is available in print at TU Wien Bibliothek.
TU Bibliothek Your knowledge hub WIEN

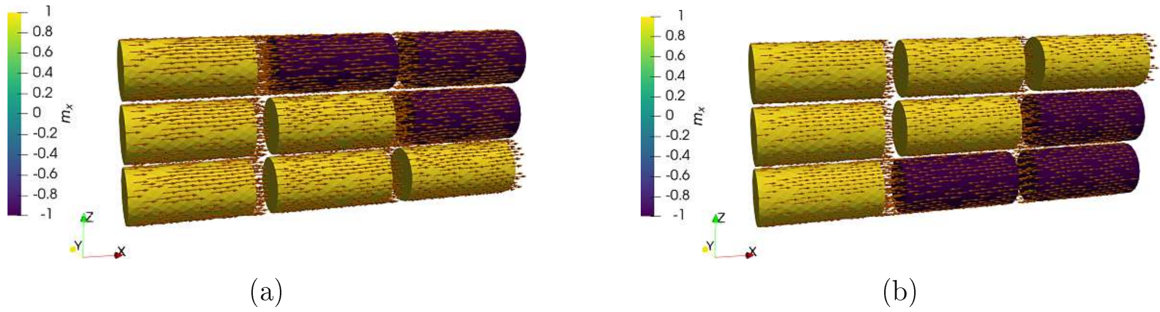

Figure 8.14: Switching stages of an ultra-scaled STT-MRAM cell with composite FL, showcasing how the different parts of the FL switch one at a time. The RL is the first section on the left of the structure, while the second and third sections are the two parts of the FL (from left to right, FL and FL , respectively). AP to P switching is presented in (a), while P to AP switching in (b). The figures were published in [13].

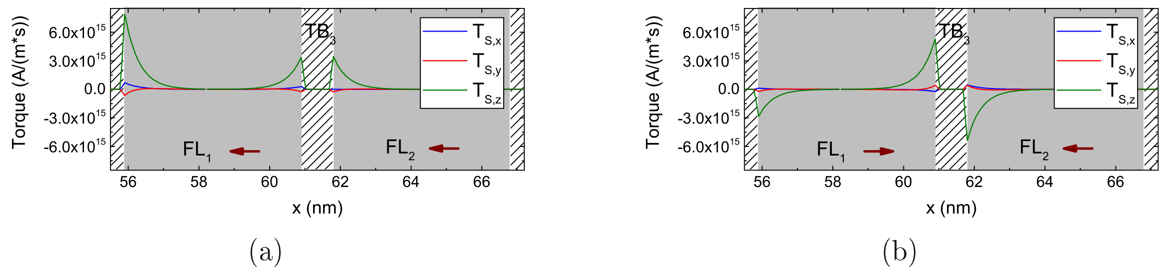

Figure 8.15: (a) Torque configuration near the beginning of the AP to P switching. The torques coming from the RL and FL act together to switch FL . The arrows represent the magnetization vector in the two FL sections. (b) Torque configuration after the first section of the composite FL has almost reached the plateau at $_x = 0$. The torques coming from the RL and FL keep FL stable, while FL is switched by the torque acting on it from FL .

single elongated layer, and that P to AP switching is achieved for lower values of the bias voltage. Both the AP to P and P to AP results present clear steps in the magnetization trajectories.

These steps are best explained by looking at their respective magnetization state, reported in Fig. 8.14. The improved performance of this structure comes from the composite nature of the FL, allowing for its different sections to be switched one at a time. In the AP configuration, the RL exerts a torque on the first part of the FL (FL) to push it in the positive x-direction, parallel to it. At the same time, the second part of the FL (FL) also exerts a torque on FL to push the magnetization to the positive x-direction, so that it is anti-parallel to FL . Both torques' contributions act in the same direction, causing FL to switch first and fast. At the same time, the torque acting from FL towards FL favors the two magnetization vectors to be parallel, keeping FL in its original orientation. However, after the magnetization of FL has switched, the torque acting on FL changes its sign, forcing it to switch as

Die approbierte gedruckte Originalversion dieser Dissertation ist an der TU Wien Bibliothek verfügbar.
The approved original version of this doctoral thesis is available in print at TU Wien Bibliothek.
TU WIEN Bibliothek Your knowledge hub

well. As the torque acts only from FL , the magnitude is smaller than that acting in the first part of the switching process, resulting in a slower reversal of the FL magnetization.

The three stages of AP to P switching are showcased in Fig. 8.14(a). When going from P to AP, the opposite process happens. The torque acting from FL on FL is opposite to that from the RL, while the torque acting from FL on FL is favoring magnetization reversal, so that FL switches first. As only the torque from FL is acting, the switching of FL is relatively slow. After FL has switched, the torque contributions from FL and the RL act on FL in the same direction, completing the switching fast. The three stages of P to AP reversal are shown in Fig. 8.14(b). Fig. 8.15 provides a visual representation of the torques acting at the beginning and during the first step of the AP to P switching. The obtained switching time and the applied bias voltage are in line with the experimentally reported results [22], and show how the presented approach can be applied to investigate the switching behavior of emerging MRAM devices.

In order to further analyze the performance of a composite FL, simulations are performed to investigate the switching behavior of an MRAM cell with three FL segments. These structure has an additional TB (TB) in the FL, with the same properties of TB . The switching realizations are performed in a cell with segments of 3 5 nm thickness, with a similar total length of the FL as the previous two. The structure is reported on the bottom of Fig ,1.2. The results for both AP to P and P to AP switching are reported in Fig. 8.16, for a bias voltage of 1 5 V. The switching process is qualitatively similar to the one of the structure with two FL segments, with the three sections of the FL switching one at a time. In the AP configuration, the torque coming from the RL and FL causes the fast switching of FL to the positive x-direction. At this point, the torque coming from FL and the third part of the FL (FL) causes the magnetization in FL to also switch fast. Finally, as only the torque coming from FL acts on FL , the latter has a slower magnetization reversal which completes the switching process. When going from P to AP, as is the case for the structure with two FL segments, the opposite process happens. The torques acting on FL and FL from the adjacent layers compensate each other, and only the torque acting from FL on FL is able to cause the magnetization reversal of the latter. At this point, the torque acting from FL and FL on FL becomes additive, so that FL switches faster. This is finally followed by the fast switching of FL , as the torque contributions coming from the RL and FL push its magnetization towards the negative x-direction. Fig. 8.16 also shows that the complete switching process is faster in the structure with three FL segments, for both AP to P and P to AP realizations. This is in line with the easier switching of shorter layers observed in Fig. 8.13(c). The simulations show that the increased number of segments provides an advantage in terms of switching time and bias, and the multiple magnetization states reached during the switching process make these structures promising candidates as multi-bit memory cells.

Die approbierte gedruckte Originalversion dieser Dissertation ist an der TU Wien Bibliothek verfügbar.
The approved original version of this doctoral thesis is available in print at TU Wien Bibliothek.
TU Bibliothek WIEN Your knowledge hub

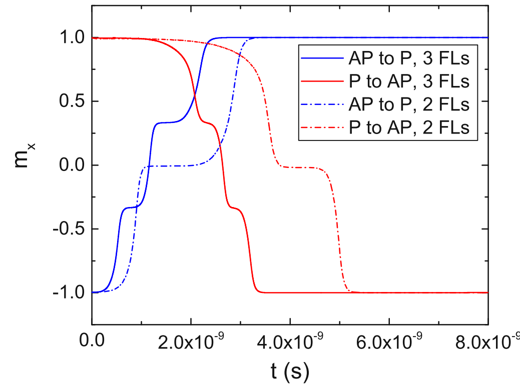

Figure 8.16: Switching results for a structure with three FL segments, for both the AP to P and P to AP scenarios, under a bias voltage of 1.5 V (solid line). The magnetization trajectories are compared to the ones obtained in the structure with two FL segments (dash-dotted lines). The figure was published in [13].

8.5 Ballistic Spin Current Terms

Recent analytical investigations of the behavior of the torque in the ballistic regime based on the NEGF formalism predict a complex absorption pattern for the transverse components, with an oscillatory dependence of the spin torque on the distance from the TB interface [99]. As these complex oscillatory behavior is ballistic in origin, it can only be reproduced by considering the additional spin current terms presented in equation (6.36b). In this case, the spin current expression to be employed in equation (6.38a) becomes

$$_{\mathrm{S,bal}} = {}^{-}(\quad)\ _{\mathrm{S}} \tag{8.11}$$

where $(\quad)$ is a magnetization dependent tensor, with the components

$$(\quad) = \ + \left(\frac{}{_J}\right) \quad (\quad) + \left(\frac{}{_\varphi}\right) \quad (\quad) \tag{8.12a}$$

$$(\quad) = \begin{pmatrix} 0 & _z & _y \\ _z & 0 & _x \\ _y & _x & 0 \end{pmatrix} \tag{8.12b}$$

$$(\quad) = \begin{pmatrix} _y + \ _z & _x\ _y & _x\ _z \\ _x\ _y & _x + \ _z & _y\ _z \\ _x\ _z & _y\ _z & _x + \ _y \end{pmatrix} \tag{8.12c}$$

The system of equations presented in Section A.2 of the Appendix can be adapted to the presence of the additional terms, as detailed in Section A.3. In Fig. 8.17(a) the resulting torque computed using $_J = 1$ nm, $_\varphi = 4\ 3$ nm, and the electron relaxation length $= 5\ 8$ nm in a semi-infinite FL is shown. The RL magnetization points in the x-direction, the one of the FL points in the z-direction. A current density of $_{\mathrm{C,x}} = \ 3 \quad 10 \quad$ A/m is flowing in the x-direction. With these choice of absorption lengths, the oscillating behavior of the torque components is in qualitative agreement with the results reported in [99].

Die approbierte gedruckte Originalversion dieser Dissertation ist an der TU Wien Bibliothek verfügbar.
The approved original version of this doctoral thesis is available in print at TU Wien Bibliothek.
TU Bibliothek WIEN Your knowledge hub

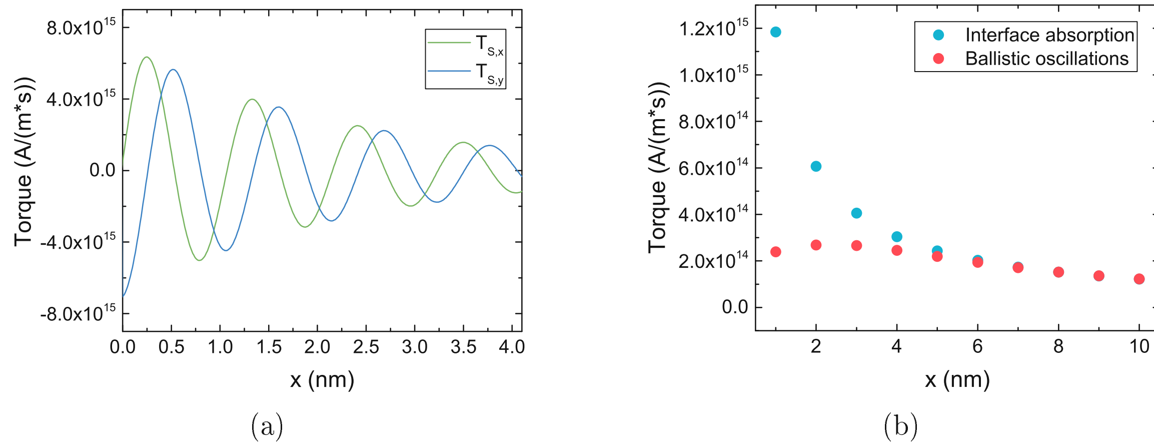

Figure 8.17: (a) Torque computed with the inclusion of ballisitic corrections to the spin current in a semi-infinite FL. Results are in qualitative agreement with [99]. (b) Comparison of the thickness dependence of the total damping-like torque acting on the FL in the presence of fast interface absorption or ballistic and oscillating behavior of the transverse spin accumulation components. The figures were published in [164].

The presence of such a pattern has an effect on the total torque exerted on the FL, obtained from (7.4). In Fig. 8.17(b), a comparison of the dependence of the total damping-like torque computed with the fast absorption of the transverse components, previously presented, and with the oscillating torque of Fig. 8.17(a) is depicted. For long FLs, both approaches show an inverse dependence of the torque on the thickness of the FL. Below 4 nm, however, the transverse components are not completely absorbed in the ballistic approach, so that the dependence of the torque on the FL thickness becomes more complex, and its value is reduced. The observed difference between the total torque acting in short FLs can provide a valid benchmark to establish which of the two approaches is most suitable to accurately describe the switching behavior of STT-MRAM devices.

Die approbierte gedruckte Originalversion dieser Dissertation ist an der TU Wien Bibliothek verfügbar.
The approved original version of this doctoral thesis is available in print at TU Wien Bibliothek.
TU WIEN Bibliothek Your knowledge hub

Die approbierte gedruckte Originalversion dieser Dissertation ist an der TU Wien Bibliothek verfügbar.
The approved original version of this doctoral thesis is available in print at TU Wien Bibliothek.
TU Wien Bibliothek Your knowledge hub

Chapter 9

Summary and Outlook

MRAM devices have gained growing interest due to their nonvolatile nature, high speed, excellent endurance and compatibility with CMOS technology. Spin-transfer torque MRAM shows promise for IoT and automotive applications, and as a replacement for flash memory in embedded DRAM and last level caches.

Development of accurate simulation tools is a valuable help for improving design and performance of emerging STT-MRAM devices. This thesis was thus devoted to the development and study of different approaches to the torque acting in STT-MRAM cells and entering the LLG equation describing the magnetization dynamics.

First, a finite difference implementation of the LLG equation, with the STT torque computed by employing the simplified Slonczewski expression under the assumption of a uniform and constant current density, was described. By deriving an analytical solution for the current density flowing in an MTJ, it was shown that it can be highly nonuniform during switching. The FD solver was thus extended to address this behavior, by including two more realistic approaches that compute the torque term with a fixed voltage and a fixed total current.

The FD solver was employed to compare switching results obtained with the fixed current density, fixed total current and fixed voltage approaches. It was shown that a correction to the value of the fixed current applied in the first two approaches is required to match the switching time distribution of the fixed voltage one. The dependence of the current correction on the TMR, temperature, and structure diameter was investigated, showing how the correction increases with all three parameters. By performing macrospin simulations, it was observed that all the results can be explained by a dependence of the correction on the switching time, with a shorter switching time requiring a larger correction.

Understanding the behavior of the current correction allows for the simple constant current density approach, most commonly employed, to correctly reproduce the switching time distribution. This can lead to the inclusion of the current correction in a compact model, and will allow the development of fast simulation tools for switching realizations in a single free layer.

Die approbierte gedruckte Originalversion dieser Dissertation ist an der TU Wien Bibliothek verfügbar.
The approved original version of this doctoral thesis is available in print at TU Wien Bibliothek.
TU WIEN Bibliothek Your knowledge hub

Recently proposed STT-MRAM devices are often composed of multiple ferromagnetic, nonmagnetic and tunneling layers. Computing the spin accumulation in the whole MRAM stack gives the possibility of deriving all torques contributions from a unified expression. This can be achieved by employing the spin and charge drift-diffusion formalism. The drift-diffusion equations were implemented in an open-source finite element software, and coupled to the LLG equation. The FE method was chosen as it can easily address the more complex structure of modern MRAM devices.

The FE implementation of the drift-diffusion formalism was extended to include the transport properties of MTJs. The TMR effect, and the current density redistribution in the presence of nonuniform magnetization, were successfully reproduced by modeling the tunnel barrier as a poor conductor, with conductivity locally depending on the relative magnetization orientation in the ferromagnetic layers.

The FE solution obtained for the spin accumulation in spin-valves was tested against literature results, showing a very good agreement. The dependence of the torque on several system parameters was investigated, and it was shown that a proper set of effective parameters can be employed to match the spin torque magnitude expected in MTJs. A unique set of parameter, however, does not allow to properly reproduce all the torque properties. The FE implementation was thus further improved with the introduction of appropriate boundary conditions at the tunnel barrier interfaces, to account for the tunneling spin current polarization. It was shown how the solver was then able to reproduce both the angular and voltage dependence observed in MTJs.

The solver was further updated with the possibility of computing an iterative solution of the charge and spin accumulation equations, and it was shown how this procedure allows to account for the GMR effect in a spin-valve, while it is not necessary in structures containing only MTJs.

Furthermore, the presented approach was employed to compute the torque acting in recently proposed ultra-scaled devices, with elongated ferromagnetic layers. It was shown how the torque generated by the MTJ and the one coming from magnetization textures are not independent, so that the computation of the spin accumulation is necessary in order to account for the interplay.

The solver was applied to compute switching simulations of recently proposed ultra-scaled MRAM cells with elongated layers. It was shown how the switching performance is improved by using a free layer composed of two segments, instead of a single one, as the different parts are able to switch one at a time. Investigating the switching of a structure with a free layer composed of three segments revealed an even faster switching process, and suggested the possibility of employing these structures as multi-bit memory cells. Overall, the obtained results validate the use of the proposed approach to help in the design of advanced MRAM devices.

Finally, by deriving a solution for the spin accumulation in the presence of ballistic corrections to the spin current, based on analytical expressions, a more complex oscillatory behavior of the torque, predicted theoretically, was reproduced.

The possibility to apply the developed approach to structures with an arbitrary number of ferromagnetic layers, tunnel barriers or nonmagnetic spacers of different shapes will enable its application in predicting the switching behavior of realistic

Die approbierte gedruckte Originalversion dieser Dissertation ist an der TU Wien Bibliothek verfügbar.
The approved original version of this doctoral thesis is available in print at TU Wien Bibliothek.
TU WIEN Bibliothek Your knowledge hub

MRAM stacks consisting of several layers of different materials. Moreover, the presented solver can be extended with additional terms in the spin current expression to account for spin-orbit coupling effects, opening the possibility of applying it to MRAM cells based on spin-orbit torques.

Die approbierte gedruckte Originalversion dieser Dissertation ist an der TU Wien Bibliothek verfügbar.
The approved original version of this doctoral thesis is available in print at TU Wien Bibliothek.
TU WIEN Bibliothek Your knowledge hub

TU Bibliothek WIEN Your knowledge hub
Die approbierte gedruckte Originalversion dieser Dissertation ist an der TU Wien Bibliothek verfügbar.
The approved original version of this doctoral thesis is available in print at TU Wien Bibliothek.

Appendix A

Analytical Solution

In the presence of uniform current density and magnetization in the ferromagnetic layers, analytical expressions for the spin accumulation entering (6.38) can be derived. The generic form of in NM layers, with the left boundary located at $_{\mathrm{L}}$ and right boundary at $_{\mathrm{R}}$, is given by

$$= {}_{\mathrm{L}} \exp\left(\frac{L}{\mathrm{sf}} \right) + {}_{\mathrm{R}} \exp\left(\frac{R}{\mathrm{sf}} \right) \qquad \text{(A.1)}$$

Here, $_{\mathrm{L}}$ and $_{\mathrm{R}}$ are vectors of real coefficients to be determined. In a ferromagnetic layer with magnetization pointing along x, the expressions for the three components of S are instead

$$_{x} = {}_{\parallel,\mathrm{L}} \exp\left(\frac{\mathrm{L}}{\mathrm{sdl}} \right) + {}_{\parallel,\mathrm{R}} \exp\left(\frac{\mathrm{R}}{\mathrm{sdl}} \right) \qquad \text{(A.2a)}$$

$$_{y} = 2\,\mathrm{Re}\left({}_{\perp,\mathrm{L}} \exp\left(\frac{\mathrm{L}}{+} \right) \right) + 2\,\mathrm{Re}\left({}_{\perp,\mathrm{R}} \exp\left(\frac{\mathrm{R}}{+} \right) \right) \qquad \text{(A.2b)}$$

$$_{z} = 2\,\mathrm{Im}\left({}_{\perp,\mathrm{L}} \exp\left(\frac{\mathrm{L}}{+} \right) \right) + 2\,\mathrm{Im}\left({}_{\perp,\mathrm{R}} \exp\left(\frac{\mathrm{R}}{+} \right) \right) \qquad \text{(A.2c)}$$

Here, $_{\parallel,\mathrm{L}}$ and $_{\parallel,\mathrm{R}}$ are real coefficients, while $_{\perp,\mathrm{L}}$ and $_{\perp,\mathrm{R}}$ are complex coefficients, to be determined, $_{\mathrm{sdl}} = {}_{\mathrm{sf}} \overline{1 \quad {}_{\sigma} \; D}$, and $^{-} = \sqrt{(1 \quad {}_{\mathrm{sf}}) + (1 \quad {}_{\varphi}) \qquad (1 \quad {}_{\mathrm{J}})}$. The expressions can be generalized to a magnetization pointing in a general direction by multiplication with a rotation matrix. In the absence of a left or right boundary (i.e. in the presence of semi-infinite layers), the corresponding terms can be removed from the equations. The coefficients entering both (A.1) and (A.2) must be obtained by imposing boundary conditions at the interfaces between different materials, for both spin accumulation and spin current. Expressions for the spin current can be derived from by using (6.38b). The systems of equations presented here were all solved symbolically by employing Mathematica to produce the analytical results reported in the main text.

Die approbierte gedruckte Originalversion dieser Dissertation ist an der TU Wien Bibliothek verfügbar.
The approved original version of this doctoral thesis is available in print at TU Wien Bibliothek.
TU WIEN Bibliothek Your knowledge hub

A.1 Five Layers N1|F1|C|F2|N2

The following equations describe continuity conditions for both the spin accumulation and current in a five layer structure, where N1 and N2 are nonmagnetic contacts, F1 is the reference layer, F2 is the free layer, and C is the middle layer, separating F1 and F2. The magnetization vector points in the x-direction in F1, while the magnetization in F2 lies in the xz-plane, forming an angle with the one in F1. Spin flipping in the middle layer can be removed by letting $_{\mathrm{sf}}^{C}$. The set of 24 equations can be employed to find the 20 unknown coefficients, 16 real and 4 complex.

A.1.1 Interface N1|F1

Continuity equations for the first interface, located at $= {}_{\mathrm{F1}}$.

Spin accumulation continuity

$$: \quad = \quad + \quad \exp\left(\frac{{}^{\mathrm{F1}} \quad {}^{\mathrm{C}}}{{}^{\mathrm{F1}}_{\mathrm{sdl}}}\right) \tag{A.3}$$

$$: \quad = 2\,\mathrm{Re}\,(\quad) + 2\,\mathrm{Re}\left(\quad \exp\left(\frac{{}^{\mathrm{F1}} \quad {}^{\mathrm{C}}}{{}^{\mathrm{F1}}}\right)\right) \tag{A.4}$$

$$: \quad = 2\,\mathrm{Im}\,(\quad) + 2\,\mathrm{Im}\left(\quad \exp\left(\frac{{}^{\mathrm{F1}} \quad {}^{\mathrm{C}}}{{}^{\mathrm{F1}}}\right)\right) \tag{A.5}$$

Spin current continuity

$$: \quad \frac{{}^{\mathrm{N1}}_{\mathrm{e}}}{{}^{\mathrm{N1}}_{\mathrm{sf}}} = {}^{\mathrm{F1}}_{\sigma} \frac{B}{} {}_{\mathrm{C}} + \frac{2 \; {}^{\mathrm{F1}} (1 \quad {}^{\mathrm{F1}}_{\sigma} \; {}^{\mathrm{F1}}_{D})}{{}^{\mathrm{F1}}_{\mathrm{sdl}}} \left(\quad \exp\left(\frac{{}^{\mathrm{F1}} \quad {}^{\mathrm{C}}}{{}^{\mathrm{F1}}_{\mathrm{sdl}}}\right)\right) \tag{A.6}$$

$$: \quad \frac{{}^{\mathrm{N1}}_{\mathrm{e}}}{{}^{\mathrm{N1}}_{\mathrm{sf}}} = 2 \; {}^{\mathrm{F1}}_{\mathrm{e}} \left(\mathrm{Re}\left(\frac{}{{}_{\mathrm{F1}}}\right) \quad \mathrm{Re}\left(\frac{}{{}_{\mathrm{F1}}} \exp\left(\frac{{}^{\mathrm{F1}} \quad {}^{\mathrm{C}}}{{}^{\mathrm{F1}}}\right)\right)\right) \tag{A.7}$$

$$: \quad \frac{{}^{\mathrm{N1}}_{\mathrm{e}}}{{}^{\mathrm{N1}}_{\mathrm{sf}}} = 2 \; {}^{\mathrm{F1}}_{\mathrm{e}} \left(\mathrm{Im}\left(\frac{}{{}_{\mathrm{F1}}}\right) \quad \mathrm{Im}\left(\frac{}{{}_{\mathrm{F1}}} \exp\left(\frac{{}^{\mathrm{F1}} \quad {}^{\mathrm{C}}}{{}^{\mathrm{F1}}}\right)\right)\right) \tag{A.8}$$

Die approbierte gedruckte Originalversion dieser Dissertation ist an der TU Wien Bibliothek verfügbar.
The approved original version of this doctoral thesis is available in print at TU Wien Bibliothek.
TU WIEN Bibliothek Your knowledge hub

A.1.2 Interface F1|C

Continuity equations for the second interface, located at $\quad = \ _{\mathrm{C}}$.

Spin accumulation continuity

$$: \quad \exp\left(\frac{\ _{\mathrm{C}} \quad \ _{\mathrm{F1}}}{\ _{\mathrm{sdl}}^{\mathrm{F1}}} \right) + \quad = \quad + \quad \exp\left(\frac{\ _{\mathrm{C}}}{\ _{\mathrm{sf}}^{C}} \right) \tag{A.9}$$

$$: \ 2\,\mathrm{Re}\left(\quad \exp\left(\frac{\ _{\mathrm{C}} \quad \ _{\mathrm{F1}}}{\ _{\mathrm{F1}}} \right)\right) + 2\,\mathrm{Re}\,(\quad) = \quad + \quad \exp\left(\frac{\ _{\mathrm{C}}}{\ _{\mathrm{sf}}^{C}} \right) \tag{A.10}$$

$$: \ 2\,\mathrm{Im}\left(\quad \exp\left(\frac{\ _{\mathrm{C}} \quad \ _{\mathrm{F1}}}{\ _{\mathrm{F1}}} \right)\right) + 2\,\mathrm{Im}\,(\quad) = \quad + \quad \exp\left(\frac{\ _{\mathrm{C}}}{\ _{\mathrm{sf}}^{C}} \right) \tag{A.11}$$

Spin current continuity

$$\begin{aligned} : \quad & {}^{\mathrm{F1}}_{\sigma} \frac{\ _B}{\quad} \ _{\mathrm{C}} + \frac{\ _{\mathrm{e}}^{\mathrm{F1}} \left(1 \quad \ _{\sigma}^{\mathrm{F1}} \ _{D}^{\mathrm{F1}}\right)}{\ _{\mathrm{sdl}}^{\mathrm{F1}}} \left(\quad \exp\left(\frac{\ _{\mathrm{C}} \quad \ _{\mathrm{F1}}}{\ _{\mathrm{sdl}}^{\mathrm{F1}}} \right) \quad \right) = \\ & = \frac{\ _{\mathrm{e}}^{C}}{\ _{\mathrm{sf}}^{C}} \left(\quad \exp\left(\frac{\ _{\mathrm{C}}}{\ _{\mathrm{sf}}^{C}} \right)\right) \end{aligned} \tag{A.12}$$

$$\begin{aligned} : \ 2 \ & {}^{\mathrm{F1}}_{\mathrm{e}} \left(\mathrm{Re}\left(\frac{\quad}{\ _{\mathrm{F1}}} \exp\left(\frac{\ _{\mathrm{C}} \quad \ _{\mathrm{F1}}}{\ _{\mathrm{F1}}} \right)\right) \quad \mathrm{Re}\left(\frac{\quad}{\ _{\mathrm{F1}}} \right)\right) = \\ & = \frac{\ _{\mathrm{e}}^{C}}{\ _{\mathrm{sf}}^{C}} \left(\quad \exp\left(\frac{\ _{\mathrm{C}}}{\ _{\mathrm{sf}}^{C}} \right)\right) \end{aligned} \tag{A.13}$$

$$\begin{aligned} : \ 2 \ & {}^{\mathrm{F1}}_{\mathrm{e}} \left(\mathrm{Im}\left(\frac{\quad}{\ _{\mathrm{F1}}} \exp\left(\frac{\ _{\mathrm{C}} \quad \ _{\mathrm{F1}}}{\ _{\mathrm{F1}}} \right)\right) \quad \mathrm{Im}\left(\frac{\quad}{\ _{\mathrm{F1}}} \right)\right) = \\ & = \frac{\ _{\mathrm{e}}^{C}}{\ _{\mathrm{sf}}^{C}} \left(\quad \exp\left(\frac{\ _{\mathrm{C}}}{\ _{\mathrm{sf}}^{C}} \right)\right) \end{aligned} \tag{A.14}$$

Die approbierte gedruckte Originalversion dieser Dissertation ist an der TU Wien Bibliothek verfügbar.
The approved original version of this doctoral thesis is available in print at TU Wien Bibliothek.
TU WIEN Bibliothek Your knowledge hub

A.1.3 Interface C|F2

Continuity equations for the third interface, located at $=$.

Spin accumulation continuity

$$: \quad \exp\left(\frac{\quad^{\mathrm{C}}}{^{C}_{\mathrm{sf}}}\right) + \quad = \left(\quad + \quad \exp\left(\frac{\quad^{\mathrm{F2}}}{^{\mathrm{F2}}_{\mathrm{sdl}}}\right)\right) \cos \; + \left(2\,\mathrm{Im}\,(\quad) + 2\,\mathrm{Im}\left(\quad \exp\left(\frac{\quad^{\mathrm{F2}}}{^{\mathrm{F2}}}\right)\right)\right) \sin \tag{A.15}$$

$$: \quad \exp\left(\frac{\quad^{\mathrm{C}}}{^{C}_{\mathrm{sf}}}\right) + \quad = 2\,\mathrm{Re}\,(\quad) + 2\,\mathrm{Re}\left(\quad \exp\left(\frac{\quad^{\mathrm{F2}}}{^{\mathrm{F2}}}\right)\right) \tag{A.16}$$

$$: \quad \exp\left(\frac{\quad^{\mathrm{C}}}{^{C}_{\mathrm{sf}}}\right) + \quad = \left(2\,\mathrm{Im}\,(\quad) + 2\,\mathrm{Im}\left(\quad \exp\left(\frac{\quad^{\mathrm{F2}}}{^{\mathrm{F2}}}\right)\right)\right) \cos \; + + \left(\quad + \quad \exp\left(\frac{\quad^{\mathrm{F2}}}{^{\mathrm{F2}}_{\mathrm{sdl}}}\right)\right) \sin \tag{A.17}$$

Spin current continuity

$$: \frac{^{C}_{\mathrm{e}}}{^{C}_{\mathrm{sf}}}\left(\quad \exp\left(\frac{\quad^{\mathrm{C}}}{^{C}_{\mathrm{sf}}}\right) \quad\right) = = \left(\quad ^{\mathrm{F2}}_{\sigma}\frac{B}{\quad}\;_{\mathrm{C}} + \frac{^{\mathrm{F2}}_{\mathrm{e}}\left(1 \quad ^{\mathrm{F2}}_{\sigma}\;^{\mathrm{F2}}_{D}\right)}{^{\mathrm{F2}}_{\mathrm{sdl}}}\left(\quad \exp\left(\frac{\quad^{\mathrm{F2}}}{^{\mathrm{F2}}_{\mathrm{sdl}}}\right)\right)\right) \cos \; + 2 \;^{\mathrm{F2}}_{\mathrm{e}}\left(\mathrm{Im}\left(\frac{\quad}{^{\mathrm{F2}}}\right) \quad \mathrm{Im}\left(\frac{\quad}{^{\mathrm{F2}}} \exp\left(\frac{\quad^{\mathrm{F2}}}{^{\mathrm{F2}}}\right)\right)\right) \sin \tag{A.18}$$

$$: \frac{^{C}_{\mathrm{e}}}{^{C}_{\mathrm{sf}}}\left(\quad \exp\left(\frac{\quad^{\mathrm{C}}}{^{C}_{\mathrm{sf}}}\right) \quad\right) = = 2 \;^{\mathrm{F2}}_{\mathrm{e}}\left(\mathrm{Re}\left(\frac{\quad}{^{\mathrm{F2}}}\right) \quad \mathrm{Re}\left(\frac{\quad}{^{\mathrm{F2}}} \exp\left(\frac{\quad^{\mathrm{F2}}}{^{\mathrm{F2}}}\right)\right)\right) \tag{A.19}$$

$$: \frac{^{C}_{\mathrm{e}}}{^{C}_{\mathrm{sf}}}\left(\quad \exp\left(\frac{\quad^{\mathrm{C}}}{^{C}_{\mathrm{sf}}}\right) \quad\right) = = \left(\quad ^{\mathrm{F2}}_{\sigma}\frac{B}{\quad}\;_{\mathrm{C}} + \frac{^{\mathrm{F2}}_{\mathrm{e}}\left(1 \quad ^{\mathrm{F2}}_{\sigma}\;^{\mathrm{F2}}_{D}\right)}{^{\mathrm{F2}}_{\mathrm{sdl}}}\left(\quad \exp\left(\frac{\quad^{\mathrm{F2}}}{^{\mathrm{F2}}_{\mathrm{sdl}}}\right)\right)\right) \sin \; + +2 \;^{\mathrm{F2}}_{\mathrm{e}}\left(\mathrm{Im}\left(\frac{\quad}{^{\mathrm{F2}}}\right) \quad \mathrm{Im}\left(\frac{\quad}{^{\mathrm{F2}}} \exp\left(\frac{\quad^{\mathrm{F2}}}{^{\mathrm{F2}}}\right)\right)\right) \cos \tag{A.20}$$

Die approbierte gedruckte Originalversion dieser Dissertation ist an der TU Wien Bibliothek verfügbar.
The approved original version of this doctoral thesis is available in print at TU Wien Bibliothek.
TU Bibliothek WIEN Your knowledge hub

A.1.4 Interface F2|N2

Continuity equations for the third interface, located at $= {}_{\mathrm{F2}}$.

Spin accumulation continuity

$$:\ \Big(\ \exp\Big(\frac{\mathrm{F2}}{\mathrm{F2}_{\mathrm{sdl}}}\Big) + \ \Big)\cos\ + $$
$$\Big(2\,\mathrm{Im}\Big(\ \exp\Big(\frac{\mathrm{F2}}{\mathrm{F2}}\Big)\Big) + 2\,\mathrm{Im}(\ \ )\Big)\sin\ = \tag{A.21}$$

$$:\ \ 2\,\mathrm{Re}\Big(\ \exp\Big(\frac{\mathrm{F2}}{\mathrm{F2}}\Big)\Big) + 2\,\mathrm{Re}(\ \ ) = \tag{A.22}$$

$$:\ \Big(2\,\mathrm{Im}\Big(\ \exp\Big(\frac{\mathrm{F2}}{\mathrm{F2}}\Big)\Big) + 2\,\mathrm{Im}(\ \ )\Big)\cos\ + $$
$$+\Big(\ \exp\Big(\frac{\mathrm{F2}}{\mathrm{F2}_{\mathrm{sdl}}}\Big) + \ \Big)\sin\ = \tag{A.23}$$

Spin current continuity

$$:\ \Big(\ {}^{\mathrm{F2}}_{\sigma}\frac{B}{}\ {}_{\mathrm{C}} + \frac{{}^{\mathrm{F2}}_{\mathrm{e}}(1\ \ {}^{\mathrm{F2}}_{\sigma}\ {}^{\mathrm{F2}}_{D})}{\mathrm{F2}_{\mathrm{sdl}}}\Big(\ \exp\Big(\frac{\mathrm{F2}}{\mathrm{F2}_{\mathrm{sdl}}}\Big)\ \ \Big)\Big)\cos\ + $$
$$2\ {}^{\mathrm{F2}}_{\mathrm{e}}\Big(\mathrm{Im}\Big(\frac{}{\mathrm{F2}}\exp\Big(\frac{\mathrm{F2}}{\mathrm{F2}}\Big)\Big)\ \ \mathrm{Im}\Big(\frac{}{\mathrm{F2}}\Big)\Big)\sin\ = \frac{{}^{\mathrm{N2}}_{\mathrm{e}}}{\mathrm{N2}_{\mathrm{sf}}} \tag{A.24}$$

$$:\ \ 2\ {}^{\mathrm{F2}}_{\mathrm{e}}\Big(\mathrm{Re}\Big(\frac{}{\mathrm{F2}}\exp\Big(\frac{\mathrm{F2}}{\mathrm{F2}}\Big)\Big)\ \ \mathrm{Re}\Big(\frac{}{\mathrm{F2}}\Big)\Big) = \frac{{}^{\mathrm{N2}}_{\mathrm{e}}}{\mathrm{N2}_{\mathrm{sf}}} \tag{A.25}$$

$$:\ \Big(\ {}^{\mathrm{F2}}_{\sigma}\frac{B}{}\ {}_{\mathrm{C}} + \frac{{}^{\mathrm{F2}}_{\mathrm{e}}(1\ \ {}^{\mathrm{F2}}_{\sigma}\ {}^{\mathrm{F2}}_{D})}{\mathrm{F2}_{\mathrm{sdl}}}\Big(\ \exp\Big(\frac{\mathrm{F2}}{\mathrm{F2}_{\mathrm{sdl}}}\Big)\ \ \Big)\Big)\sin\ + $$
$$+2\ {}^{\mathrm{F2}}_{\mathrm{e}}\Big(\mathrm{Im}\Big(\frac{}{\mathrm{F2}}\exp\Big(\frac{\mathrm{F2}}{\mathrm{F2}}\Big)\Big)\ \ \mathrm{Im}\Big(\frac{}{\mathrm{F2}}\Big)\Big)\cos\ = \frac{{}^{\mathrm{N2}}_{\mathrm{e}}}{\mathrm{N2}_{\mathrm{sf}}} \tag{A.26}$$

A.2 Tunneling Spin Current

In the presence of a tunneling spin current described by (8.2b), the continuity equations for the spin current at the interfaces with the middle layer need to be modified. The new expressions are reported below.

TU Bibliothek WIEN Your knowledge hub
Die approbierte gedruckte Originalversion dieser Dissertation ist an der TU Wien Bibliothek verfügbar.
The approved original version of this doctoral thesis is available in print at TU Wien Bibliothek.

A.2.1 Interface F1|C

Modified spin current continuity

$$
: \quad {}^{\mathrm{F1}}_{\sigma}\frac{B}{} \; {}_{\mathrm{C}} + \frac{{}^{\mathrm{F1}}_{\mathrm{e}}\left(1 \quad {}^{\mathrm{F1}}_{\sigma} \; {}^{\mathrm{F1}}_{D}\right)}{{}^{\mathrm{F1}}_{\mathrm{sdl}}} \left(\quad \exp\left(\frac{{}^{\mathrm{C}} \quad {}^{\mathrm{F1}}}{{}^{\mathrm{F1}}_{\mathrm{sdl}}} \right) \quad \right) =
$$

$$
= \frac{{}_{\mathrm{RL}} \; {}_{\mathrm{RL}} + {}_{\mathrm{FL}} \; {}_{\mathrm{FL}} \cos}{1 + {}_{\mathrm{RL}} \; {}_{\mathrm{FL}} \cos} \frac{\mathrm{B}}{} \; {}_{\mathrm{C}} + \frac{{}^{C}_{\mathrm{e}}}{{}^{C}_{\mathrm{sf}}} \left(\quad \exp\left(\frac{\mathrm{C}}{{}^{C}_{\mathrm{sf}}} \right) \right) \tag{A.27}
$$

$$
: \quad 2 \; {}^{\mathrm{F1}}_{\mathrm{e}} \left(\mathrm{Re}\left(\frac{}{\mathrm{F1}} \exp\left(\frac{{}^{\mathrm{C}} \quad {}^{\mathrm{F1}}}{\mathrm{F1}} \right) \right) \quad \mathrm{Re}\left(\frac{}{\mathrm{F1}} \right) \right) =
$$

$$
= \frac{1 \;\; 2\,({}_{\mathrm{RL}} \; {}^{\eta}_{\mathrm{RL}} \quad {}_{\mathrm{FL}} \; {}^{\eta}_{\mathrm{FL}}) \sin}{1 + {}_{\mathrm{RL}} \; {}_{\mathrm{FL}} \cos} \frac{\mathrm{B}}{} \; {}_{\mathrm{C}} + \frac{{}^{C}_{\mathrm{e}}}{{}^{C}_{\mathrm{sf}}} \left(\quad \exp\left(\frac{\mathrm{C}}{{}^{C}_{\mathrm{sf}}} \right) \right) \tag{A.28}
$$

$$
: \quad 2 \; {}^{\mathrm{F1}}_{\mathrm{e}} \left(\mathrm{Im}\left(\frac{}{\mathrm{F1}} \exp\left(\frac{{}^{\mathrm{C}} \quad {}^{\mathrm{F1}}}{\mathrm{F1}} \right) \right) \quad \mathrm{Im}\left(\frac{}{\mathrm{F1}} \right) \right) =
$$

$$
= \frac{{}_{\mathrm{FL}} \; {}_{\mathrm{FL}} \sin}{1 + {}_{\mathrm{RL}} \; {}_{\mathrm{FL}} \cos} \frac{\mathrm{B}}{} \; {}_{\mathrm{C}} + \frac{{}^{C}_{\mathrm{e}}}{{}^{C}_{\mathrm{sf}}} \left(\quad \exp\left(\frac{\mathrm{C}}{{}^{C}_{\mathrm{sf}}} \right) \right) \tag{A.29}
$$

A.2.2 Interface C|F2

Modified spin current continuity

$$
: \quad \frac{{}_{\mathrm{RL}} \; {}_{\mathrm{RL}} + {}_{\mathrm{FL}} \; {}_{\mathrm{FL}} \cos}{1 + {}_{\mathrm{RL}} \; {}_{\mathrm{FL}} \cos} \frac{\mathrm{B}}{} \; {}_{\mathrm{C}} + \frac{{}^{C}_{\mathrm{e}}}{{}^{C}_{\mathrm{sf}}} \left(\quad \exp\left(\frac{\quad {}^{\mathrm{C}}}{{}^{C}_{\mathrm{sf}}} \right) \quad \right) =
$$

$$
\begin{aligned}
&= \left({}^{\mathrm{F2}}_{\sigma}\frac{B}{} \; {}_{\mathrm{C}} + \frac{{}^{\mathrm{F2}}_{\mathrm{e}}\left(1 \quad {}^{\mathrm{F2}}_{\sigma} \; {}^{\mathrm{F2}}_{D}\right)}{{}^{\mathrm{F2}}_{\mathrm{sdl}}} \left(\quad \exp\left(\frac{\quad {}^{\mathrm{F2}}}{{}^{\mathrm{F2}}_{\mathrm{sdl}}} \right) \right) \right) \cos \; + \\
&\quad 2 \; {}^{\mathrm{F2}}_{\mathrm{e}} \left(\mathrm{Im}\left(\frac{}{\mathrm{F2}} \right) \quad \mathrm{Im}\left(\frac{}{\mathrm{F2}} \exp\left(\frac{\quad {}^{\mathrm{F2}}}{\mathrm{F2}} \right) \right) \right) \sin
\end{aligned} \tag{A.30}
$$

$$
: \quad \frac{1 \;\; 2\,({}_{\mathrm{RL}} \; {}^{\eta}_{\mathrm{RL}} \quad {}_{\mathrm{FL}} \; {}^{\eta}_{\mathrm{FL}}) \sin}{1 + {}_{\mathrm{RL}} \; {}_{\mathrm{FL}} \cos} \frac{\mathrm{B}}{} \; {}_{\mathrm{C}} + \frac{{}^{C}_{\mathrm{e}}}{{}^{C}_{\mathrm{sf}}} \left(\quad \exp\left(\frac{\quad {}^{\mathrm{C}}}{{}^{C}_{\mathrm{sf}}} \right) \quad \right) =
$$

$$
= 2 \; {}^{\mathrm{F2}}_{\mathrm{e}} \left(\mathrm{Re}\left(\frac{}{\mathrm{F2}} \right) \quad \mathrm{Re}\left(\frac{}{\mathrm{F2}} \exp\left(\frac{\quad {}^{\mathrm{F2}}}{\mathrm{F2}} \right) \right) \right) \tag{A.31}
$$

Die approbierte gedruckte Originalversion dieser Dissertation ist an der TU Wien Bibliothek verfügbar.
The approved original version of this doctoral thesis is available in print at TU Wien Bibliothek.
TU WIEN Bibliothek Your knowledge hub

$$: \quad \frac{{}_{\mathrm{FL}} \; {}_{\mathrm{FL}} \sin}{1 + {}_{\mathrm{RL}} \; {}_{\mathrm{FL}} \cos} \frac{}{} {}^{\mathrm{B}} {}_{\mathrm{C}} + \frac{C_{\mathrm{e}}}{C_{\mathrm{sf}}} \left(\exp \left(\frac{{}^{\mathrm{C}}}{C_{\mathrm{sf}}} \right) \right) =$$

$$= \left({}^{\mathrm{F2}}_{\sigma} \frac{B}{} {}_{\mathrm{C}} + \frac{{}^{\mathrm{F2}}_{\mathrm{e}} (1 \; {}^{\mathrm{F2}}_{\sigma} \; {}^{\mathrm{F2}}_{D})}{{}^{\mathrm{F2}}_{\mathrm{sdl}}} \left(\exp \left(\frac{{}^{\mathrm{F2}}}{{}^{\mathrm{F2}}_{\mathrm{sdl}}} \right) \right) \right) \sin +$$

$$+2 \; {}^{\mathrm{F2}}_{\mathrm{e}} \left(\mathrm{Im} \left(\frac{}{{}_{\mathrm{F2}}} \right) \; \mathrm{Im} \left(\frac{}{{}_{\mathrm{F2}}} \exp \left(\frac{{}^{\mathrm{F2}}}{{}_{\mathrm{F2}}} \right) \right) \right) \cos \tag{A.32}$$

A.3 Ballistic Spin Current

When employing (8.11), the continuity equations need to updated to take the additional spin current terms, depending on the momentum relaxation path , into account. The expressions for the spin accumulation remain the same, with the following change of parameters:

$$\bar{} = \sqrt{\frac{{}^{\varphi}}{{}_{\mathrm{d}}} \frac{{}^{\mathrm{J}}}{{}_{\mathrm{J}}} \left(\frac{{}^{\varphi}}{{}_{\mathrm{J}}} + \frac{{}^{\mathrm{J}}}{{}_{\mathrm{d}}} \right)} \tag{A.33a}$$

$${}_{\mathrm{J}} = \left(\frac{}{{}_{\mathrm{J}}} \right) \qquad {}_{\varphi} = 1 + \left(\frac{}{{}_{\varphi}} \right) \qquad \bar{}_{\mathrm{d}} = \sqrt{\frac{1}{{}_{\mathrm{sf}}} + \frac{1}{{}_{\varphi}}} \tag{A.33b}$$

The updated continuity equations for the spin current, which take the tunneling contributions into account, are reported below.

A.3.1 Interface N1|F1

Ballistic spin current continuity

$$: \quad \frac{{}^{\mathrm{N1}}_{\mathrm{e}}}{{}^{\mathrm{N1}}_{\mathrm{sf}}} = {}^{\mathrm{F1}}_{\sigma} \frac{B}{} {}_{\mathrm{C}} + \frac{2 \; {}^{\mathrm{F1}} (1 \; {}^{\mathrm{F1}}_{\sigma} \; {}^{\mathrm{F1}}_{D})}{{}^{\mathrm{F1}}_{\mathrm{sdl}}} \left(\exp \left(\frac{{}^{\mathrm{F1}} \; {}^{\mathrm{C}}}{{}^{\mathrm{F1}}_{\mathrm{sdl}}} \right) \right) \tag{A.34}$$

$$: \quad \frac{{}^{\mathrm{N1}}_{\mathrm{e}}}{{}^{\mathrm{N1}}_{\mathrm{sf}}} = 2 \; {}^{\mathrm{F1}}_{\mathrm{e}} \left(\mathrm{Re} \left(\frac{}{{}_{\mathrm{F1}}} \right) \; \mathrm{Re} \left(\frac{}{{}_{\mathrm{F1}}} \exp \left(\frac{{}^{\mathrm{F1}} \; {}^{\mathrm{C}}}{{}_{\mathrm{F1}}} \right) \right) \right) \frac{{}^{\mathrm{F1}}_{\varphi}}{({}^{\mathrm{F1}}_{\varphi}) + ({}^{\mathrm{F1}}_{\mathrm{J}})} +$$

$$2 \; {}^{\mathrm{F1}}_{\mathrm{e}} \left(\mathrm{Im} \left(\frac{}{{}_{\mathrm{F1}}} \right) \; \mathrm{Im} \left(\frac{}{{}_{\mathrm{F1}}} \exp \left(\frac{{}^{\mathrm{F1}} \; {}^{\mathrm{C}}}{{}_{\mathrm{F1}}} \right) \right) \right) \frac{{}^{\mathrm{F1}}_{\mathrm{J}}}{({}^{\mathrm{F1}}_{\varphi}) + ({}^{\mathrm{F1}}_{\mathrm{J}})} \tag{A.35}$$

$$: \quad \frac{{}^{\mathrm{N1}}_{\mathrm{e}}}{{}^{\mathrm{N1}}_{\mathrm{sf}}} = 2 \; {}^{\mathrm{F1}}_{\mathrm{e}} \left(\mathrm{Re} \left(\frac{}{{}_{\mathrm{F1}}} \right) \; \mathrm{Re} \left(\frac{}{{}_{\mathrm{F1}}} \exp \left(\frac{{}^{\mathrm{F1}} \; {}^{\mathrm{C}}}{{}_{\mathrm{F1}}} \right) \right) \right) \frac{{}^{\mathrm{F1}}_{\mathrm{J}}}{({}^{\mathrm{F1}}_{\varphi}) + ({}^{\mathrm{F1}}_{\mathrm{J}})} +$$

$$+2 \; {}^{\mathrm{F1}}_{\mathrm{e}} \left(\mathrm{Im} \left(\frac{}{{}_{\mathrm{F1}}} \right) \; \mathrm{Im} \left(\frac{}{{}_{\mathrm{F1}}} \exp \left(\frac{{}^{\mathrm{F1}} \; {}^{\mathrm{C}}}{{}_{\mathrm{F1}}} \right) \right) \right) \frac{{}^{\mathrm{F1}}_{\varphi}}{({}^{\mathrm{F1}}_{\varphi}) + ({}^{\mathrm{F1}}_{\mathrm{J}})} \tag{A.36}$$

Die approbierte gedruckte Originalversion dieser Dissertation ist an der TU Wien Bibliothek verfügbar.
The approved original version of this doctoral thesis is available in print at TU Wien Bibliothek.
TU WIEN Bibliothek Your knowledge hub

A.3.2 Interface F1|C

Ballistic spin current continuity

$$: \quad {}^{F1}_{\sigma}\frac{B}{} \; {}_{C} + \frac{{}^{F1}_{e}\left(1 \quad {}^{F1}_{\sigma} \; {}^{F1}_{D}\right)}{{}^{F1}_{sdl}} \left(\quad \exp\left(\frac{{}_{C} \quad {}^{F1}}{{}^{F1}_{sdl}} \right) \quad \right) =$$

$$= \frac{{}_{RL} \; {}_{RL} + {}_{FL} \; {}_{FL} \cos}{1 + \; {}_{RL} \; {}_{FL} \cos} \frac{{}_{B}}{} \; {}_{C} + \frac{C_{e}}{C_{sf}} \left(\quad \exp\left(\frac{{}_{C}}{C_{sf}} \right) \right) \qquad (A.37)$$

$$: \quad 2 \; {}^{F1}_{e} \left(\mathrm{Re}\left(\frac{}{{}_{F1}} \exp\left(\frac{{}_{C} \quad {}^{F1}}{{}_{F1}} \right) \right) \quad \mathrm{Re}\left(\frac{}{{}_{F1}} \right) \right) \frac{{}^{F1}_{\varphi}}{(\; {}^{F1}_{\varphi}) \; + (\; {}^{F1}_{J})}$$

$$+2 \; {}^{F1}_{e} \left(\mathrm{Im}\left(\frac{}{{}_{F1}} \exp\left(\frac{{}_{C} \quad {}^{F1}}{{}_{F1}} \right) \right) \quad \mathrm{Im}\left(\frac{}{{}_{F1}} \right) \right) \frac{{}^{F1}_{J}}{(\; {}^{F1}_{J}) \; + (\; {}^{F1}_{J})} =$$

$$= \frac{1 \;\; 2 \; (\; {}_{RL} \; {}^{\eta}_{RL} \quad {}_{FL} \; {}^{\eta}_{FL}) \sin}{1 + \; {}_{RL} \; {}_{FL} \cos} \frac{{}_{B}}{} \; {}_{C} + \frac{C_{e}}{C_{sf}} \left(\quad \exp\left(\frac{{}_{C}}{C_{sf}} \right) \right) \qquad (A.38)$$

$$: \quad 2 \; {}^{F1}_{e} \left(\mathrm{Re}\left(\frac{}{{}_{F1}} \exp\left(\frac{{}_{C} \quad {}^{F1}}{{}_{F1}} \right) \right) \quad \mathrm{Re}\left(\frac{}{{}_{F1}} \right) \right) \frac{{}^{F1}_{J}}{(\; {}^{F1}_{\varphi}) \; + (\; {}^{F1}_{J})} +$$

$$+2 \; {}^{F1}_{e} \left(\mathrm{Im}\left(\frac{}{{}_{F1}} \exp\left(\frac{{}_{C} \quad {}^{F1}}{{}_{F1}} \right) \right) \quad \mathrm{Im}\left(\frac{}{{}_{F1}} \right) \right) \frac{{}^{F1}_{\varphi}}{(\; {}^{F1}_{J}) \; + (\; {}^{F1}_{J})} =$$

$$= \frac{{}_{FL} \; {}_{FL} \sin}{1 + \; {}_{RL} \; {}_{FL} \cos} \frac{{}_{B}}{} \; {}_{C} + \frac{C_{e}}{C_{sf}} \left(\quad \exp\left(\frac{{}_{C}}{C_{sf}} \right) \right) \qquad (A.39)$$

A.3.3 Interface C|F2

Ballistic spin current continuity

$$: \quad \frac{{}_{RL} \; {}_{RL} + {}_{FL} \; {}_{FL} \cos}{1 + \; {}_{RL} \; {}_{FL} \cos} \frac{{}_{B}}{} \; {}_{C} + \frac{C_{e}}{C_{sf}} \left(\quad \exp\left(\frac{{}_{C}}{C_{sf}} \right) \quad \right) =$$

$$= \left(\; {}^{F2}_{\sigma}\frac{B}{} \; {}_{C} + \frac{{}^{F2}_{e}\left(1 \quad {}^{F2}_{\sigma} \; {}^{F2}_{D}\right)}{{}^{F2}_{sdl}} \left(\quad \exp\left(\frac{{}^{F2}}{{}^{F2}_{sdl}} \right) \right) \right) \cos \; +$$

$$2 \; {}^{F2}_{e} \left(\left(\mathrm{Re}\left(\frac{}{{}_{F2}} \right) \quad \mathrm{Re}\left(\frac{}{{}_{F2}} \exp\left(\frac{{}^{F2}}{{}_{F2}} \right) \right) \right) \right) \frac{{}^{F2}_{J}}{(\; {}^{F2}_{J}) \; + (\; {}^{F2}_{J})} +$$

$$\left(\mathrm{Im}\left(\frac{}{{}_{F2}} \right) \quad \mathrm{Im}\left(\frac{}{{}_{F2}} \exp\left(\frac{{}^{F2}}{{}_{F2}} \right) \right) \right) \right) \frac{{}^{F2}_{J}}{(\; {}^{F2}_{\varphi}) \; + (\; {}^{F2}_{J})} \Bigg) \sin \qquad (A.40)$$

Die approbierte gedruckte Originalversion dieser Dissertation ist an der TU Wien Bibliothek verfügbar.
The approved original version of this doctoral thesis is available in print at TU Wien Bibliothek.
TU WIEN Bibliothek Your knowledge hub

$$: \quad \frac{1 \;\; 2\,(\;\; {}_{\mathrm{RL}} \;\; {}^{\eta}_{\mathrm{RL}} \;\; {}_{\mathrm{FL}} \;\; {}^{\eta}_{\mathrm{FL}})\sin}{1 + \;\; {}_{\mathrm{RL}} \;\; {}_{\mathrm{FL}}\cos} \; \frac{\;\;}{\;\;}{}^{\mathrm{B}} \; {}_{\mathrm{C}} + \frac{C_{\mathrm{e}}}{C_{\mathrm{sf}}}\left(\;\; \exp\left(\frac{\;\; \mathrm{C}}{C_{\mathrm{sf}}}\right) \;\; \right) =$$

$$= 2 \;\; {}^{\mathrm{F2}}_{\mathrm{e}} \left(\mathrm{Re}\left(\frac{\;\;}{\mathrm{F2}}\right) \;\; \mathrm{Re}\left(\frac{\;\;}{\mathrm{F2}}\exp\left(\frac{\;\;\mathrm{F2}}{\mathrm{F2}}\right)\right)\right) \frac{{}^{\mathrm{F2}}_{\varphi}}{(\;{}^{\mathrm{F2}}_{\varphi}) \;\; + (\;{}^{\mathrm{F2}}_{\mathrm{J}})} +$$

$$2 \;\; {}^{\mathrm{F2}}_{\mathrm{e}} \left(\mathrm{Im}\left(\frac{\;\;}{\mathrm{F2}}\right) \;\; \mathrm{Im}\left(\frac{\;\;}{\mathrm{F2}}\exp\left(\frac{\;\;\mathrm{F2}}{\mathrm{F2}}\right)\right)\right) \frac{{}^{\mathrm{F2}}_{\mathrm{J}}}{(\;{}^{\mathrm{F2}}_{\varphi}) \;\; + (\;{}^{\mathrm{F2}}_{\mathrm{J}})}$$

$$: \quad \frac{{}_{\mathrm{FL}} \;\; {}_{\mathrm{FL}}\sin}{1 + \;\; {}_{\mathrm{RL}} \;\; {}_{\mathrm{FL}}\cos} \; \frac{\;\;}{\;\;}{}^{\mathrm{B}} \; {}_{\mathrm{C}} + \frac{C_{\mathrm{e}}}{C_{\mathrm{sf}}}\left(\;\; \exp\left(\frac{\;\; \mathrm{C}}{C_{\mathrm{sf}}}\right) \;\; \right) =$$

$$= \left(\;\; {}^{\mathrm{F2}}_{\sigma}\frac{B}{\;\;} \; {}_{\mathrm{C}} + \frac{{}^{\mathrm{F2}}_{\mathrm{e}}(1 \;\; {}^{\mathrm{F2}}_{\sigma} \; {}^{\mathrm{F2}}_{D})}{{}^{\mathrm{F2}}_{\mathrm{sdl}}} \left(\;\; \exp\left(\frac{\;\;\mathrm{F2}}{{}^{\mathrm{F2}}_{\mathrm{sdl}}}\right)\right)\right)\sin \;\; +$$

$$+2 \;\; {}^{\mathrm{F2}}_{\mathrm{e}} \left(\left(\mathrm{Re}\left(\frac{\;\;}{\mathrm{F2}}\right) \;\; \mathrm{Re}\left(\frac{\;\;}{\mathrm{F2}}\exp\left(\frac{\;\;\mathrm{F2}}{\mathrm{F2}}\right)\right)\right) \frac{{}^{\mathrm{F2}}_{\mathrm{J}}}{(\;{}^{\mathrm{F2}}_{\varphi}) \;\; + (\;{}^{\mathrm{F2}}_{\mathrm{J}})} + \right.$$

$$\left. + \left(\mathrm{Im}\left(\frac{\;\;}{\mathrm{F2}}\right) \;\; \mathrm{Im}\left(\frac{\;\;}{\mathrm{F2}}\exp\left(\frac{\;\;\mathrm{F2}}{\mathrm{F2}}\right)\right)\right) \frac{{}^{\mathrm{F2}}_{\varphi}}{(\;{}^{\mathrm{F2}}_{\varphi}) \;\; + (\;{}^{\mathrm{F2}}_{\mathrm{J}})}\right)\cos \tag{A.41}$$

A.3.4 Interface F2|N2

Ballistic spin current continuity

$$: \quad \left(\;\; {}^{\mathrm{F2}}_{\sigma}\frac{B}{\;\;} \; {}_{\mathrm{C}} + \frac{{}^{\mathrm{F2}}_{\mathrm{e}}(1 \;\; {}^{\mathrm{F2}}_{\sigma} \; {}^{\mathrm{F2}}_{D})}{{}^{\mathrm{F2}}_{\mathrm{sdl}}} \left(\;\; \exp\left(\frac{\mathrm{F2}\;\;}{{}^{\mathrm{F2}}_{\mathrm{sdl}}}\right) \;\; \right)\right)\cos \;\; +$$

$$2 \;\; {}^{\mathrm{F2}}_{\mathrm{e}} \left(\left(\mathrm{Re}\left(\frac{\;\;}{\mathrm{F2}}\exp\left(\frac{\mathrm{F2}\;\;}{\mathrm{F2}}\right)\right) \;\; \mathrm{Re}\left(\frac{\;\;}{\mathrm{F2}}\right)\right) \frac{{}^{\mathrm{F2}}_{\mathrm{J}}}{(\;{}^{\mathrm{F2}}_{\varphi}) \;\; + (\;{}^{\mathrm{F2}}_{\mathrm{J}})} + \right.$$

$$\left. + \left(\mathrm{Im}\left(\frac{\;\;}{\mathrm{F2}}\exp\left(\frac{\mathrm{F2}\;\;}{\mathrm{F2}}\right)\right) \;\; \mathrm{Im}\left(\frac{\;\;}{\mathrm{F2}}\right)\right) \frac{{}^{\mathrm{F2}}_{\varphi}}{(\;{}^{\mathrm{F2}}_{\varphi}) \;\; + (\;{}^{\mathrm{F2}}_{\mathrm{J}})}\right)\sin \;\; = \frac{{}^{\mathrm{N2}}_{\mathrm{e}}}{{}^{\mathrm{N2}}_{\mathrm{sf}}} \tag{A.42}$$

$$: \quad 2 \;\; {}^{\mathrm{F2}}_{\mathrm{e}} \left(\mathrm{Re}\left(\frac{\;\;}{\mathrm{F2}}\exp\left(\frac{\mathrm{F2}\;\;}{\mathrm{F2}}\right)\right) \;\; \mathrm{Re}\left(\frac{\;\;}{\mathrm{F2}}\right)\right) \frac{{}^{\mathrm{F2}}_{\varphi}}{(\;{}^{\mathrm{F2}}_{\varphi}) \;\; + (\;{}^{\mathrm{F2}}_{\mathrm{J}})} +$$

$$2 \;\; {}^{\mathrm{F2}}_{\mathrm{e}} \left(\mathrm{Im}\left(\frac{\;\;}{\mathrm{F2}}\exp\left(\frac{\mathrm{F2}\;\;}{\mathrm{F2}}\right)\right) \;\; \mathrm{Im}\left(\frac{\;\;}{\mathrm{F2}}\right)\right) \frac{{}^{\mathrm{F2}}_{\mathrm{J}}}{(\;{}^{\mathrm{F2}}_{\varphi}) \;\; + (\;{}^{\mathrm{F2}}_{\mathrm{J}})} = \frac{{}^{\mathrm{N2}}_{\mathrm{e}}}{{}^{\mathrm{N2}}_{\mathrm{sf}}} \tag{A.43}$$

Die approbierte gedruckte Originalversion dieser Dissertation ist an der TU Wien Bibliothek verfügbar.
The approved original version of this doctoral thesis is available in print at TU Wien Bibliothek.
TU Bibliothek WIEN Your knowledge hub

$$
\begin{aligned}
:\ \Bigg(\ {}^{\mathrm{F2}}_{\sigma} \frac{B}{\ } \ {}_{\mathrm{C}} + \frac{{}^{\mathrm{F2}}_{\mathrm{e}}\left(1 \quad {}^{\mathrm{F2}}_{\sigma} \ {}^{\mathrm{F2}}_{D}\right)}{{}^{\mathrm{F2}}_{\mathrm{sdl}}} \Bigg(\quad \exp\left(\frac{\mathrm{F2}}{{}^{\mathrm{F2}}_{\mathrm{sdl}}} \right) \quad \Bigg)\Bigg) \sin \ + \\
+2 \ {}^{\mathrm{F2}}_{\mathrm{e}} \Bigg(\Bigg(\mathrm{Re}\left(\frac{\ }{\mathrm{F2}} \exp\left(\ \frac{\mathrm{F2}}{\mathrm{F2}} \right)\right) \quad \mathrm{Re}\left(\frac{\ }{\mathrm{F2}}\right)\Bigg) \frac{{}^{\mathrm{F2}}_{\mathrm{J}}}{\left({}^{\mathrm{F2}}_{\varphi} \right) + \left({}^{\mathrm{F2}}_{\mathrm{J}} \right)} \\
+ \Bigg(\mathrm{Im}\left(\frac{\ }{\mathrm{F2}} \exp\left(\ \frac{\mathrm{F2}}{\mathrm{F2}} \right)\right) \quad \mathrm{Im}\left(\frac{\ }{\mathrm{F2}}\right)\Bigg) \frac{{}^{\mathrm{F2}}_{\varphi}}{\left({}^{\mathrm{F2}}_{\varphi} \right) + \left({}^{\mathrm{F2}}_{\mathrm{J}} \right)} \Bigg) \cos \ = \frac{{}^{\mathrm{N2}}_{\mathrm{e}}}{{}^{\mathrm{N2}}_{\mathrm{sf}}}
\end{aligned}
\tag{A.44}
$$

Die approbierte gedruckte Originalversion dieser Dissertation ist an der TU Wien Bibliothek verfügbar.
The approved original version of this doctoral thesis is available in print at TU Wien Bibliothek.
TU Wien Bibliothek Your knowledge hub

Bibliography

[1] T. Hanyu, T. Endoh, D. Suzuki, H. Koike, Y. Ma, N. Onizawa *et al.*, "Standby-power-free integrated circuits using MTJ-based VLSI computing," *Proc. IEEE*, vol. 104, no. 10, pp. 1844–1863, 2016, doi: 10.1109/JPROC.2016.2574939.

[2] W. J. Gallagher, E. Chien, T. Chiang, J. Huang, M. Shih, C. Y. Wang *et al.*, "22nm STT-MRAM for reflow and automotive uses with high yield, reliability, and magnetic immunity and with performance and shielding options," in *Proc. IEDM Conf.*, 2019, pp. 2.7.1–2.7.4, doi: 10.1109/IEDM19573.2019.8993469.

[3] S. Sakhare, M. Perumkunnil, T. H. Bao, S. Rao, W. Kim, D. Crotti *et al.*, "Enablement of STT-MRAM as last level cache for the high performance computing domain at the 5nm node," in *Proc. IEDM Conf.*, 2018, pp. 18.3.1–18.3.4, doi: 10.1109/IEDM.2018.8614637.

[4] S. Aggarwal, H. Almasi, M. DeHerrera, B. Hughes, S. Ikegawa, J. Janesky *et al.*, "Demonstration of a reliable 1 Gb standalone spin-transfer torque MRAM for industrial applications," in *Proc. IEDM Conf.*, 2019, pp. 2.1.1–2.1.4, doi: 10.1109/IEDM19573.2019.8993516.

[5] K. Lee, J. H. Bak, Y. J. Kim, C. K. Kim, A. Antonyan, D. H. Chang *et al.*, "1Gbit high density embedded STT-MRAM in 28nm FDSOI technology," in *Proc. IEDM Conf.*, 2019, pp. 2.2.1–2.2.4, doi: 10.1109/IEDM19573.2019.8993551.

[6] V. B. Naik, K. Lee, K. Yamane, R. Chao, J. Kwon, N. Thiyagarajah *et al.*, "Manufacturable 22nm FD-SOI embedded MRAM technology for industrial-grade MCU and IOT applications," in *Proc. IEDM Conf.*, 2019, pp. 2.3.1–2.3.4, doi: 10.1109/IEDM19573.2019.8993454.

[7] J. G. Alzate, U. Arslan, P. Bai, J. Brockman, Y. J. Chen, N. Das *et al.*, "2 Mb array-level demonstration of STT-MRAM process and performance towards L4 cache applications," in *Proc. IEDM Conf.*, 2019, pp. 2.4.1–2.4.4, doi: 10.1109/IEDM19573.2019.8993474.

[8] G. Hu, J. J. Nowak, M. G. Gottwald, S. L. Brown, B. Doris, C. P. D'Emic *et al.*, "Spin-transfer torque MRAM with reliable 2 ns writing for last level cache applications," in *Proc. IEDM Conf.*, 2019, pp. 2.6.1–2.6.4, doi: 10.1109/IEDM19573.2019.8993604.

[9] S. H. Han, J. M. Lee, H. M. Shin, J. H. Lee, K. S. Suh, K. T. Nam *et al.*, "28nm 0.08 mm /Mb embedded MRAM for frame buffer memory," in *Proc. IEDM Conf.*, 2020, pp. 11.2.1–11.2.4, doi: 10.1109/IEDM13553.2020.9372040.

TU WIEN Bibliothek Your knowledge hub
Die approbierte gedruckte Originalversion dieser Dissertation ist an der TU Wien Bibliothek verfügbar.
The approved original version of this doctoral thesis is available in print at TU Wien Bibliothek.

[10] Y.-C. Shih, C.-F. Lee, Y.-A. Chang, P.-H. Lee, H.-J. Lin, Y.-L. Chen *et al.*, "A reflow-capable, embedded 8Mb STT-MRAM macro with 9ns read access time in 16nm FinFET logic CMOS process," in *Proc. IEDM Conf.*, 2020, pp. 11.4.1–11.4.4, doi: 10.1109/IEDM13553.2020.9372115.

[11] V. B. Naik, K. Yamane, T. Lee, J. Kwon, R. Chao, J. Lim *et al.*, "JEDEC-qualified highly reliable 22nm FD-SOI embedded MRAM for low-power industrial-grade, and extended performance towards automotive-grade-1 applications," in *Proc. IEDM Conf.*, 2020, pp. 11.3.1–11.3.4, doi: 10.1109/IEDM13553.2020.9371935.

[12] B. Tudu and A. Tiwari, "Recent developments in perpendicular magnetic anisotropy thin films for data storage applications," *Vacuum*, vol. 146, pp. 329–341, 2017, doi: 10.1016/j.vacuum.2017.01.031.

[13] S. Fiorentini, M. Bendra, J. Ender, R. L. de Orio, W. Goes, S. Selberherr *et al.*, "Spin and charge drift-diffusion in ultra-scaled MRAM cells," *Sci. Rep.*, vol. 12, no. 1, p. 20958, Dec. 2022, doi: 10.1038/s41598-022-25586-4.

[14] J. C. Slonczewski, "Current-driven excitation of magnetic multilayers," *J. Magn. Magn. Mater.*, vol. 159, no. 1, pp. L1 – L7, 1996, doi: 10.1016/0304-8853(96)00062-5.

[15] L. Berger, "Emission of spin waves by a magnetic multilayer traversed by a current," *Phys. Rev. B*, vol. 54, pp. 9353–9358, Oct. 1996, doi: 10.1103/PhysRevB.54.9353.

[16] J. C. Slonczewski, "Currents, torques, and polarization factors in magnetic tunnel junctions," *Phys. Rev. B*, vol. 71, p. 024411, 2005, doi: 10.1103/PhysRevB.71.024411.

[17] A. Makarov, "Modeling of emerging resistive switching based memory cells," Ph.D. dissertation, Institute for Microelectronics, TU Wien, 2014. [Online]. Available: https://www.iue.tuwien.ac.at/phd/makarov/

[18] W. Skowroński, M. Czapkiewicz, S. Ziętek, J. Chęciński, M. Frankowski, P. Rzeszut *et al.*, "Understanding stability diagram of perpendicular magnetic tunnel junctions," *Sci. Rep.*, vol. 7, no. 1, p. 10172, 2017, doi: 10.1038/s41598-017-10706-2.

[19] H. Sato, M. Yamanouchi, S. Ikeda, S. Fukami, F. Matsukura, and H. Ohno, "MgO/CoFeB/Ta/CoFeB/MgO recording structure in magnetic tunnel junctions with perpendicular easy axis," *IEEE Trans. Magn.*, vol. 49, no. 7, pp. 4437–4440, 2013, doi: 10.1109/TMAG.2013.2251326.

[20] K. Nishioka, H. Honjo, S. Ikeda, T. Watanabe, S. Miura, H. Inoue *et al.*, "Novel quad interface MTJ technology and its first demonstration with high thermal stability and switching efficiency for STT-MRAM beyond 2Xnm," in *Symp. on VLSI Tech.*, 2019, pp. T120–T121, doi: 10.23919/VLSIT.2019.8776499.

[21] P. Khanal, B. Zhou, M. Andrade, Y. Dang, A. Davydov, A. Habiboglu *et al.*, "Perpendicular magnetic tunnel junctions with multi-interface free layer," *Appl. Phys. Lett.*, vol. 119, no. 24, p. 242404, 2021, doi: 10.1063/5.0066782.

[22] B. Jinnai, J. Igarashi, K. Watanabe, T. Funatsu, H. Sato, S. Fukami *et al.*, "High-performance shape-anisotropy magnetic tunnel junctions down to 2.3 nm," in *Proc. IEDM Conf.*, 2020, pp. 24.6.1–24.6.4, doi: 10.1109/IEDM13553.2020.9371972.

[23] C. Abert, M. Ruggeri, F. Bruckner, C. Vogler, G. Hrkac, D. Praetorius *et al.*, "A three-dimensional spin-diffusion model for micromagnetics," *Sci. Rep.*, vol. 5, no. 1, p. 14855, 2015, doi: 10.1038/srep14855.

Die approbierte gedruckte Originalversion dieser Dissertation ist an der TU Wien Bibliothek verfügbar.
The approved original version of this doctoral thesis is available in print at TU Wien Bibliothek.
TU WIEN Bibliothek Your knowledge hub

[24] C. Abert, M. Ruggeri, F. Bruckner, C. Vogler, A. Manchon, D. Praetorius *et al.*, "A self-consistent spin-diffusion model for micromagnetics," *Sci. Rep.*, vol. 6, no. 1, p. 16, Dec. 2016, doi: 10.1038/s41598-016-0019-y.

[25] S. Lepadatu, "Unified treatment of spin torques using a coupled magnetisation dynamics and three-dimensional spin current solver," *Sci. Rep.*, vol. 7, no. 1, p. 12937, 2017, doi: 10.1038/s41598-017-13181-x.

[26] S. Bhatti, R. Sbiaa, A. Hirohata, H. Ohno, S. Fukami, and S. Piramanayagam, "Spintronics based random access memory: A review," *Mater. Today*, vol. 20, no. 9, pp. 530 – 548, 2017, doi: 10.1016/j.mattod.2017.07.007.

[27] J. G. Zhu and C. Park, "Magnetic tunnel junctions," *Mater. Today*, vol. 9, no. 11, pp. 36 – 45, 2006, doi: 10.1016/S1369-7021(06)71693-5.

[28] D. Apalkov, B. Dieny, and J. M. Slaughter, "Magnetoresistive random access memory," *Proc. IEEE*, vol. 104, no. 10, pp. 1796–1830, 2016, doi: 10.1109/JPROC.2016.2590142.

[29] F. C. Williams and T. Kilburn, "Electronic digital computers," *Nature*, vol. 162, no. 4117, pp. 487–487, Sep. 1948, doi: 10.1038/162487a0.

[30] W. N. Papian, "A coincident-current magnetic memory cell for the storage of digital information," *Proc. IRE*, vol. 40, no. 4, p. 475 – 478, 1952, doi: 10.1109/JRPROC.1952.274045.

[31] R. A. Abbott, W. M. Regitz, and J. A. Karp, "A 4K MOS dynamic random-access memory," *IEEE J. Solid-State Circuits*, vol. 8, no. 5, p. 292 – 298, 1973, doi: 10.1109/JSSC.1973.1050406.

[32] M. N. Baibich, J. M. Broto, A. Fert, F. N. Van Dau, F. Petroff, P. Etienne *et al.*, "Giant magnetoresistance of (001)Fe/(001)Cr magnetic superlattices," *Phys. Rev. Lett.*, vol. 61, pp. 2472–2475, Nov. 1988, doi: 10.1103/PhysRevLett.61.2472.

[33] G. Binasch, P. Grünberg, F. Saurenbach, and W. Zinn, "Enhanced magnetoresistance in layered magnetic structures with antiferromagnetic interlayer exchange," *Phys. Rev. B*, vol. 39, no. 7, p. 4828 – 4830, 1989, doi: 10.1103/PhysRevB.39.4828.

[34] T. Miyazaki, T. Yaoi, and S. Ishio, "Large magnetoresistance effect in 82Ni-Fe/Al-Al2O3/Co magnetic tunneling junction," *J. Magn. Magn. Mater.*, vol. 98, no. 1, pp. L7–L9, 1991, doi: 10.1016/0304-8853(91)90417-9.

[35] T. S. Plaskett, P. P. Freitas, N. P. Barradas, M. F. da Silva, and J. C. Soares, "Magnetoresistance and magnetic properties of NiFe/oxide/Co junctions prepared by magnetron sputtering," *J. Appl. Phys.*, vol. 76, no. 10, pp. 6104–6106, 1994, doi: 10.1063/1.358319.

[36] T. Miyazaki and N. Tezuka, "Giant magnetic tunneling effect in Fe/Al2O3/Fe junction," *J. Magn. Magn. Mater.*, vol. 139, no. 3, pp. L231–L234, 1995, doi: 10.1016/0304-8853(95)90001-2.

[37] J. S. Moodera, L. R. Kinder, T. M. Wong, and R. Meservey, "Large magnetoresistance at room temperature in ferromagnetic thin film tunnel junctions," *Phys. Rev. Lett.*, vol. 74, pp. 3273–3276, Apr. 1995, doi: 10.1103/PhysRevLett.74.3273.

Die approbierte gedruckte Originalversion dieser Dissertation ist an der TU Wien Bibliothek verfügbar.
The approved original version of this doctoral thesis is available in print at TU Wien Bibliothek.
TU WIEN Bibliothek Your knowledge hub

[38] R. C. Sousa, J. J. Sun, V. Soares, P. P. Freitas, A. Kling, M. F. da Silva *et al.*, "Large tunneling magnetoresistance enhancement by thermal anneal," *Appl. Phys. Lett.*, vol. 73, no. 22, pp. 3288–3290, 1998, doi: 10.1063/1.122747.

[39] S. Cardoso, V. Gehanno, R. Ferreira, and P. Freitas, "Ion beam deposition and oxidation of spin-dependent tunnel junctions," *IEEE Trans. Magn.*, vol. 35, no. 5, pp. 2952–2954, 1999, doi: 10.1109/20.801044.

[40] W. H. Butler, X.-G. Zhang, T. C. Schulthess, and J. M. MacLaren, "Spin-dependent tunneling conductance of Fe MgO Fe sandwiches," *Phys. Rev. B*, vol. 63, p. 054416, Jan. 2001, doi: 10.1103/PhysRevB.63.054416.

[41] J. Mathon and A. Umerski, "Theory of tunneling magnetoresistance of an epitaxial Fe/MgO/Fe(001) junction," *Phys. Rev. B*, vol. 63, p. 220403, May 2001, doi: 10.1103/PhysRevB.63.220403.

[42] M. Bowen, V. Cros, F. Petroff, A. Fert, C. Martínez Boubeta, J. L. Costa-Krämer *et al.*, "Large magnetoresistance in Fe/MgO/FeCo(001) epitaxial tunnel junctions on GaAs(001)," *Appl. Phys. Lett.*, vol. 79, no. 11, pp. 1655–1657, 2001, doi: 10.1063/1.1404125.

[43] J. Faure-Vincent, C. Tiusan, E. Jouguelet, F. Canet, M. Sajieddine, C. Bellouard *et al.*, "High tunnel magnetoresistance in epitaxial Fe/MgO/Fe tunnel junctions," *Appl. Phys. Lett.*, vol. 82, no. 25, pp. 4507–4509, 2003, doi: 10.1063/1.1586785.

[44] S. Yuasa, A. Fukushima, T. Nagahama, K. Ando, and Y. Suzuki, "High tunnel magnetoresistance at room temperature in fully epitaxial Fe/MgO/Fe tunnel junctions due to coherent spin-polarized tunneling," *Jpn. J. Appl. Phys.*, vol. 43, no. No. 4B, pp. L588–L590, Apr. 2004, doi: 10.1143/jjap.43.l588.

[45] S. Ikeda, J. Hayakawa, Y. M. Lee, R. Sasaki, T. Meguro, F. Matsukura *et al.*, "Dependence of tunnel magnetoresistance in MgO based magnetic tunnel junctions on Ar pressure during MgO sputtering," *Jpn. J. Appl. Phys.*, vol. 44, no. No. 48, pp. L1442–L1445, Nov. 2005, doi: 10.1143/jjap.44.l1442.

[46] J. A. Katine, F. J. Albert, R. A. Buhrman, E. B. Myers, and D. C. Ralph, "Current-driven magnetization reversal and spin-wave excitations in Co Cu Co pillars," *Phys. Rev. Lett.*, vol. 84, pp. 3149–3152, Apr. 2000, doi: 10.1103/PhysRevLett.84.3149.

[47] W. Kim, J. H. Jeong, Y. Kim, W. C. Lim, J. H. Kim, J. H. Park *et al.*, "Extended scalability of perpendicular STT-MRAM towards sub-20nm MTJ node," in *Proc. IEDM Conf.*, 2011, pp. 24.1.1–24.1.4, doi: 10.1109/IEDM.2011.6131602.

[48] M. Gajek, J. J. Nowak, J. Z. Sun, P. L. Trouilloud, E. J. O'Sullivan, D. W. Abraham *et al.*, "Spin torque switching of 20 nm magnetic tunnel junctions with perpendicular anisotropy," *Appl. Phys. Lett.*, vol. 100, no. 13, p. 132408, 2012, doi: 10.1063/1.3694270.

[49] T. Kawahara, K. Ito, R. Takemura, and H. Ohno, "Spin-transfer torque RAM technology: Review and prospect," *Microelectron. Reliab.*, vol. 52, no. 4, pp. 613–627, 2012, doi: 10.1016/j.microrel.2011.09.028.

Die approbierte gedruckte Originalversion dieser Dissertation ist an der TU Wien Bibliothek verfügbar.
The approved original version of this doctoral thesis is available in print at TU Wien Bibliothek.
TU WIEN Bibliothek Your knowledge hub

[50] A. V. Khvalkovskiy, D. Apalkov, S. Watts, R. Chepulskii, R. S. Beach, A. Ong *et al.*, "Basic principles of STT-MRAM cell operation in memory arrays," *J. Phys. D: Appl. Phys.*, vol. 46, no. 7, p. 074001, Feb. 2013, doi: 10.1088/0022-3727/46/7/074001.

[51] O. Golonzka, J.-G. Alzate, U. Arslan, M. Bohr, P. Bai, J. Brockman *et al.*, "MRAM as embedded non-volatile memory solution for 22FFL FinFET technology," in *Proc. IEDM Conf.*, 2018, pp. 18.1.1–18.1.4, doi: 10.1109/IEDM.2018.8614620.

[52] J. Åkerman, "Toward a universal memory," *Science*, vol. 308, no. 5721, pp. 508–510, 2005, doi: 10.1126/science.1110549.

[53] S. Ikeda, K. Miura, H. Yamamoto, K. Mizunuma, H. D. Gan, M. Endo *et al.*, "A perpendicular-anisotropy CoFeB-MgO magnetic tunnel junction," *Nat. Mater.*, vol. 9, no. 9, pp. 721–724, Sep. 2010, doi: 10.1038/nmat2804.

[54] S. Ikeda, J. Hayakawa, Y. M. Lee, F. Matsukura, Y. Ohno, T. Hanyu *et al.*, "Magnetic tunnel junctions for spintronic memories and beyond," *IEEE Trans. Electron Devices*, vol. 54, no. 5, pp. 991–1002, 2007, doi: 10.1109/TED.2007.894617.

[55] E. Chen, D. Apalkov, Z. Diao, A. Driskill-Smith, D. Druist, D. Lottis *et al.*, "Advances and future prospects of spin--transfer torque random access memory," *IEEE Transactions on Magnetics*, vol. 46, no. 6, pp. 1873–1878, 2010, doi: 10.1109/TMAG.2010.2042041.

[56] W. Thomson, "XIX. On the electro-dynamic qualities of metals:—Effects of magnetization on the electric conductivity of nickel and of iron," *Proc. R. Soc. London*, vol. 8, pp. 546–550, 1857, doi: 10.1098/rspl.1856.0144.

[57] P. P. Freitas, H. Ferreira, R. Ferreira, S. Cardoso, S. van Dijken, and J. Gregg, *Advanced Magnetic Nanostructures*. Springer US, 2006, ch. Nanostructures for Spin Electronics. ISBN 978-0-387-23316-1

[58] M. Getzlaff, *Fundamentals of Magnetism*. Springer Berlin Heidelberg, 2008, ch. Magnetoresistivity. ISBN 978-3-540-31152-2

[59] D. Wang, C. Nordman, J. M. Daughton, Z. Qian, and J. Fink, "70% TMR at room temperature for SDT sandwich junctions with CoFeB as free and reference layers," *IEEE Trans. Magn.*, vol. 40, no. 4, pp. 2269–2271, 2004, doi: 10.1109/TMAG.2004.830219.

[60] S. S. P. Parkin, C. Kaiser, A. Panchula, P. M. Rice, B. Hughes, M. Samant *et al.*, "Giant tunnelling magnetoresistance at room temperature with MgO (100) tunnel barriers," *Nat. Mater.*, vol. 3, no. 12, pp. 862–867, Dec. 2004, doi: 10.1038/nmat1256.

[61] D. D. Djayaprawira, K. Tsunekawa, M. Nagai, H. Maehara, S. Yamagata, N. Watanabe *et al.*, "230% room-temperature magnetoresistance in CoFeB/MgO/CoFeB magnetic tunnel junctions," *Appl. Phys. Lett.*, vol. 86, no. 9, p. 092502, 2005, doi: 10.1063/1.1871344.

[62] J. Hayakawa, S. Ikeda, F. Matsukura, H. Takahashi, and H. Ohno, "Dependence of giant tunnel magnetoresistance of sputtered CoFeB/MgO/CoFeB magnetic tunnel junctions on MgO barrier thickness and annealing temperature," *Jpn. J. Appl. Phys.*, vol. 44, no. No. 19, pp. L587–L589, Apr. 2005, doi: 10.1143/jjap.44.l587.

Die approbierte gedruckte Originalversion dieser Dissertation ist an der TU Wien Bibliothek verfügbar.
The approved original version of this doctoral thesis is available in print at TU Wien Bibliothek.
TU WIEN Bibliothek Your knowledge hub

[63] S. Ikeda, J. Hayakawa, Y. Ashizawa, Y. M. Lee, K. Miura, H. Hasegawa *et al.*, “Tunnel magnetoresistance of 604% at 300 K by suppression of Ta diffusion in CoFeB/MgO/CoFeB pseudo-spin-valves annealed at high temperature,” *Appl. Phys. Lett.*, vol. 93, no. 8, p. 082508, 2008, doi: 10.1063/1.2976435.

[64] H. Jaffrès, D. Lacour, F. Nguyen Van Dau, J. Briatico, F. Petroff, and A. Vaurès, “Angular dependence of the tunnel magnetoresistance in transition-metal-based junctions,” *Phys. Rev. B*, vol. 64, p. 064427, Jul. 2001, doi: 10.1103/PhysRevB.64.064427.

[65] Y. Ji, J. Liu, and C. Yang, “Novel modeling and dynamic simulation of magnetic tunnel junctions for spintronic sensor development,” *J. Phys. D: Appl. Phys.*, vol. 50, no. 2, p. 025005, Dec. 2016, doi: 10.1088/1361-6463/50/2/025005.

[66] R. Sbiaa, H. Meng, and S. N. Piramanayagam, “Materials with perpendicular magnetic anisotropy for magnetic random access memory,” *Phys. Status Solidi RRL*, vol. 5, no. 12, pp. 413–419, 2011, doi: 10.1002/pssr.201105420.

[67] J.-G. Zhu, “Magnetoresistive random access memory: The path to competitiveness and scalability,” *Proc. IEEE*, vol. 96, no. 11, pp. 1786–1798, 2008, doi: 10.1109/JPROC.2008.2004313.

[68] Y. Huai, F. Albert, P. Nguyen, M. Pakala, and T. Valet, “Observation of spin-transfer switching in deep submicron-sized and low-resistance magnetic tunnel junctions,” *Appl. Phys. Lett.*, vol. 84, no. 16, pp. 3118–3120, 2004, doi: 10.1063/1.1707228.

[69] Z. Diao, D. Apalkov, M. Pakala, Y. Ding, A. Panchula, and Y. Huai, “Spin transfer switching and spin polarization in magnetic tunnel junctions with MgO and AlOx barriers,” *Appl. Phys. Lett.*, vol. 87, no. 23, p. 232502, 2005, doi: 10.1063/1.2139849.

[70] H. Kubota, A. Fukushima, Y. Ootani, S. Yuasa, K. Ando, H. Maehara *et al.*, “Evaluation of spin-transfer switching in CoFeB/MgO/CoFeB magnetic tunnel junctions,” *Jpn. J. Appl. Phys.*, vol. 44, no. No. 40, pp. L1237–L1240, Sep. 2005, doi: 10.1143/jjap.44.l1237.

[71] J. Hayakawa, S. Ikeda, Y. M. Lee, R. Sasaki, T. Meguro, F. Matsukura *et al.*, “Current-driven magnetization switching in CoFeB/MgO/CoFeB magnetic tunnel junctions,” *Jpn. J. Appl. Phys.*, vol. 44, no. No. 41, pp. L1267–L1270, Sep. 2005, doi: 10.1143/jjap.44.l1267.

[72] M. J. Carey, R. E. Fontana, and B. A. Gurney, “Magnetic sensors having antiferromagnetically exchange-coupled layers for longitudinal biasing,” Google Patent, 2001. [Online]. Available: https://patents.google.com/patent/US6266218

[73] J. M. Slaughter, R. W. Dave, M. DeHerrera, M. Durlam, B. N. Engel, J. Janesky *et al.*, “Fundamentals of MRAM technology,” *J. Supercond.*, vol. 15, no. 1, pp. 19–25, Feb. 2002, doi: 10.1023/A:1014018925270.

[74] F. J. A. den Broeder, D. Kuiper, A. P. van de Mosselaer, and W. Hoving, “Perpendicular magnetic anisotropy of Co-Au multilayers induced by interface sharpening,” *Phys. Rev. Lett.*, vol. 60, pp. 2769–2772, Jun. 1988, doi: 10.1103/PhysRevLett.60.2769.

Die approbierte gedruckte Originalversion dieser Dissertation ist an der TU Wien Bibliothek verfügbar.
The approved original version of this doctoral thesis is available in print at TU Wien Bibliothek.
TU WIEN Bibliothek Your knowledge hub

[75] W. B. Zeper, F. J. A. M. Greidanus, P. F. Carcia, and C. R. Fincher, "Perpendicular magnetic anisotropy and magneto-optical Kerr effect of vapor-deposited Co/Pt-layered structures," *J. Appl. Phys.*, vol. 65, no. 12, pp. 4971–4975, 1989, doi: 10.1063/1.343189.

[76] B. N. Engel, C. D. England, R. A. Van Leeuwen, M. H. Wiedmann, and C. M. Falco, "Interface magnetic anisotropy in epitaxial superlattices," *Phys. Rev. Lett.*, vol. 67, pp. 1910–1913, Sep. 1991, doi: 10.1103/PhysRevLett.67.1910.

[77] G. H. O. Daalderop, P. J. Kelly, and F. J. A. den Broeder, "Prediction and confirmation of perpendicular magnetic anisotropy in Co/Ni multilayers," *Phys. Rev. Lett.*, vol. 68, pp. 682–685, Feb. 1992, doi: 10.1103/PhysRevLett.68.682.

[78] H. Meng, W. H. Lum, R. Sbiaa, S. Y. H. Lua, and H. K. Tan, "Annealing effects on CoFeB-MgO magnetic tunnel junctions with perpendicular anisotropy," *J. Appl. Phys.*, vol. 110, no. 3, p. 033904, 2011, doi: 10.1063/1.3611426.

[79] H. Sato, S. Ikeda, S. Fukami, H. Honjo, S. Ishikawa, M. Yamanouchi *et al.*, "Co/Pt multilayer based reference layers in magnetic tunnel junctions for nonvolatile spintronics VLSIs," *Jpn. J. Appl. Phys.*, vol. 53, no. 4S, p. 04EM02, Jan. 2014, doi: 10.7567/jjap.53.04em02.

[80] S. Bandiera, R. C. Sousa, Y. Dahmane, C. Ducruet, C. Portemont, V. Baltz *et al.*, "Comparison of synthetic antiferromagnets and hard ferromagnets as reference layer in magnetic tunnel junctions with perpendicular magnetic anisotropy," *IEEE Magn. Lett.*, vol. 1, pp. 3 000 204–3 000 204, 2010, doi: 10.1109/LMAG.2010.2052238.

[81] D. C. Worledge, G. Hu, D. W. Abraham, J. Z. Sun, P. L. Trouilloud, J. Nowak *et al.*, "Spin torque switching of perpendicular Ta|CoFeB|MgO-based magnetic tunnel junctions," *Appl. Phys. Lett.*, vol. 98, no. 2, p. 022501, 2011, doi: 10.1063/1.3536482.

[82] J.-H. Park, Y. Kim, W. C. Lim, J. H. Kim, S. H. Park, J. H. Kim *et al.*, "Enhancement of data retention and write current scaling for sub-20nm STT-MRAM by utilizing dual interfaces for perpendicular magnetic anisotropy," in *Proc. VLSIT Conf.*, 2012, pp. 57–58, doi: 10.1109/VLSIT.2012.6242459.

[83] C. Abert, "Micromagnetics and spintronics: Models and numerical methods," *Eur. Phys. J. B*, vol. 92, no. 6, p. 120, Jun. 2019, doi: 10.1140/epjb/e2019-90599-6.

[84] M. Ruggeri, "Coupling and numerical integration of the Landau-Lifshitz-Gilbert equation," Ph.D. dissertation, TU Wien, 2016. [Online]. Available: https://publik.tuwien.ac.at/files/publik_252806.pdf

[85] H. Kronmüller, *Handbook of Magnetism and Advanced Magnetic Materials.* John Wiley & Sons, Ltd, 2007, vol. Micromagnetism, ch. General Micromagnetic Theory. ISBN 9780470022184

[86] L. D. Landau and E. M. Lifshitz, "On the theory of the dispersion of magnetic permeability in ferromagnetic bodies," *Phys. Z. Sowjetunion*, vol. 8, pp. 153–164, 1935.

[87] T. L. Gilbert, "A phenomenological theory of damping in ferromagnetic materials," *IEEE Trans. Magn.*, vol. 40, no. 6, pp. 3443–3449, 2004, doi: 10.1109/TMAG.2004.836740.

Die approbierte gedruckte Originalversion dieser Dissertation ist an der TU Wien Bibliothek verfügbar.
The approved original version of this doctoral thesis is available in print at TU Wien Bibliothek.
TU WIEN Bibliothek Your knowledge hub

[88] T. L. Gilbert, "Formulation, foundations and applications of the phenomenological theory of ferromagnetism," Ph.D. dissertation, Illinois Institute of Technology Chicago, 1956.

[89] J. E. Miltat and M. J. Donahue, *Handbook of Magnetism and Advanced Magnetic Materials*. John Wiley & Sons, Ltd, 2007, vol. Micromagnetism, ch. Numerical Micromagnetics: Finite Difference Methods. ISBN 9780470022184

[90] M. Labrune and J. Miltat, "Wall structures in ferro/antiferromagnetic exchange-coupled bilayers: A numerical micromagnetic approach," *J. Magn. Magn. Mater.*, vol. 151, no. 1, pp. 231–245, 1995, doi: 10.1016/0304-8853(95)00328-2.

[91] A. Kákay, "Numerical investigations of micromagnetic structures," Ph.D. dissertation, Research Institute for Solid State Physics and Optics, Hungarian Academy of Sciences, 2005. [Online]. Available: https://repozitorium.omikk.bme.hu/bitstream/handle/10890/431/ertekezes.pdf?sequence=1&isAllowed=y

[92] G. Finocchio, M. Carpentieri, B. Azzerboni, L. Torres, E. Martinez, and L. Lopez-Diaz, "Micromagnetic simulations of nanosecond magnetization reversal processes in magnetic nanopillar," *J. Appl. Phys.*, vol. 99, no. 8, p. 08G522, 2006, doi: 10.1063/1.2177049.

[93] G. Finocchio, B. Azzerboni, G. D. Fuchs, R. A. Buhrman, and L. Torres, "Micromagnetic modeling of magnetization switching driven by spin-polarized current in magnetic tunnel junctions," *J. Appl. Phys.*, vol. 101, no. 6, p. 063914, 2007, doi: 10.1063/1.2496202.

[94] J. L. García-Palacios and F. J. Lázaro, "Langevin-dynamics study of the dynamical properties of small magnetic particles," *Phys. Rev. B*, vol. 58, pp. 14 937–14 958, Dec. 1998, doi: 10.1103/PhysRevB.58.14937.

[95] G. T. Rado and J. R. Weertman, "Spin-wave resonance in a ferromagnetic metal," *J. Phys. Chem. Solids*, vol. 11, no. 3, pp. 315–333, 1959, doi: 10.1016/0022-3697(59)90233-1.

[96] J. Xiao, A. Zangwill, and M. D. Stiles, "Macrospin models of spin transfer dynamics," *Phys. Rev. B*, vol. 72, p. 014446, Jul. 2005, doi: 10.1103/PhysRevB.72.014446.

[97] Y. Zhou, "Spin momentum transfer effects for spintronic device applications," Ph.D. dissertation, KTH, 2009. [Online]. Available: http://kth.diva-portal.org/smash/get/diva2:220709/FULLTEXT01.pdf

[98] S. Zhang, P. M. Levy, and A. Fert, "Mechanisms of spin-polarized current-driven magnetization switching," *Phys. Rev. Lett.*, vol. 88, p. 236601, May 2002, doi: 10.1103/PhysRevLett.88.236601.

[99] M. Chshiev, A. Manchon, A. Kalitsov, N. Ryzhanova, A. Vedyayev, N. Strelkov *et al.*, "Analytical description of ballistic spin currents and torques in magnetic tunnel junctions," *Phys. Rev. B*, vol. 92, p. 104422, 2015, doi: 10.1103/PhysRevB.92.104422.

[100] M. Carpentieri, G. Finocchio, B. Azzerboni, L. Torres, L. Lopez-Diaz, and E. Martinez, "Effect of the classical ampere field in micromagnetic computations of spin polarized current-driven magnetization processes," *J. Appl. Phys.*, vol. 97, no. 10, p. 10C713, 2005, doi: 10.1063/1.1853291.

Die approbierte gedruckte Originalversion dieser Dissertation ist an der TU Wien Bibliothek verfügbar.
The approved original version of this doctoral thesis is available in print at TU Wien Bibliothek.
TU WIEN Bibliothek Your knowledge hub

[101] L. Torres, L. Lopez-Diaz, E. Martinez, M. Carpentieri, and G. Finocchio, "Micromagnetic computations of spin polarized current-driven magnetization processes," *J. Magn. Magn. Mater.*, vol. 286, pp. 381–385, 2005, doi: 10.1016/j.jmmm.2004.09.126.

[102] Z. H. Xiao, X. Q. Ma, P. P. Wu, J. X. Zhang, L. Q. Chen, and S. Q. Shi, "Micromagnetic simulations of current-induced magnetization switching in Co/Cu/Co nanopillars," *Journal of Applied Physics*, vol. 102, no. 9, p. 093907, 2007, doi: 10.1063/1.2800999.

[103] M. Carpentieri, G. Finocchio, L. Torres, and B. Azzerboni, "Modeling of fast switching processes in nanoscale spin valves," *J. Appl. Phys.*, vol. 103, no. 7, p. 07B117, 2008, doi: 10.1063/1.2838285.

[104] K. Machida, N. Funabashi, K.-i. Aoshima, Y. Miyamoto, N. Kawamura, K. Kuga *et al.*, "Spin transfer switching of closely arranged multiple pillars with current-perpendicular-to-plane spin valves," *Journal of Applied Physics*, vol. 103, no. 7, p. 07A713, 2008, doi: 10.1063/1.2838473.

[105] M. Julliere, "Tunneling between ferromagnetic films," *Phys. Lett. A*, vol. 54, no. 3, pp. 225–226, 1975, doi: 10.1016/0375-9601(75)90174-7.

[106] P. Bouquin, "The switching paths of spin transfer torque magnetic random access memories," Ph.D. dissertation, Université Paris-Saclay, CNRS, Centre de Nanosciences et de Nanotechnologies, 91120, Palaiseau, France, 2020. [Online]. Available: https://tel.archives-ouvertes.fr/tel-03026404/document

[107] D. V. Berkov and J. Miltat, "Spin-torque driven magnetization dynamics: Micromagnetic modeling," *J. Magn. Magn. Mater.*, vol. 320, no. 7, pp. 1238–1259, 2008, doi: 10.1016/j.jmmm.2007.12.023.

[108] S. U. Jen, Y. D. Yao, Y. T. Chen, J. M. Wu, C. C. Lee, T. L. Tsai *et al.*, "Magnetic and electrical properties of amorphous CoFeB films," *J. Appl. Phys.*, vol. 99, no. 5, p. 053701, 2006, doi: 10.1063/1.2174113.

[109] S. X. Huang, T. Y. Chen, and C. L. Chien, "Spin polarization of amorphous CoFeB determined by point-contact Andreev reflection," *Appl. Phys. Lett.*, vol. 92, no. 24, p. 242509, 2008, doi: 10.1063/1.2949740.

[110] S. Fiorentini, R. L. de Orio, W. Goes, J. Ender, and V. Sverdlov, "Comprehensive comparison of switching models for perpendicular spin-transfer torque MRAM cells," in *Proc. SISPAD Conf.*, 2019, pp. 1–4, doi: 10.1109/SISPAD.2019.8870359. © 2019 IEEE.

[111] D. Aurélio, L. Torres, and G. Finocchio, "Magnetization switching driven by spin-transfer-torque in high-TMR magnetic tunnel junctions," *J. Magn. Magn. Mater.*, vol. 321, no. 23, pp. 3913 – 3920, 2009, doi: 10.1016/j.jmmm.2009.07.050.

[112] D. Tomáš, "Modelling of micromagnetic structures," Ph.D. dissertation, Paris-Sud University, Orsay and Charles University, Prague, 1999.

[113] K. Ito, T. Devolder, C. Chappert, M. J. Carey, and J. A. Katine, "Probabilistic behavior in subnanosecond spin transfer torque switching," *J. Appl. Phys.*, vol. 99, no. 8, p. 08G519, 2006, doi: 10.1063/1.2176869.

Die approbierte gedruckte Originalversion dieser Dissertation ist an der TU Wien Bibliothek verfügbar.
The approved original version of this doctoral thesis is available in print at TU Wien Bibliothek.
TU WIEN Bibliothek Your knowledge hub

[114] S. Fiorentini, R. L. de Orio, S. Selberherr, J. Ender, W. Goes, and V. Sverdlov, "Perpendicular STT-MRAM switching at fixed voltage and at fixed current," in *Proc. EDTM Conf.*, 2020, pp. 1–4, doi: 10.1109/EDTM47692.2020.9117985. © 2020 IEEE.

[115] S. Fiorentini, R. L. de Orio, S. Selberherr, J. Ender, W. Goes, and V. Sverdlov, "Influence of current redistribution in switching models for perpendicular STT-MRAM," *Adv, CMOS-Comp. Semicond. Devices 19*, vol. 97, no. 5, pp. 159–164, Apr. 2020, doi: 10.1149/09705.0159ecst.

[116] S. Fiorentini, R. L. de Orio, S. Selberherr, J. Ender, W. Goes, and V. Sverdlov, "Analysis of switching under fixed voltage and fixed current in perpendicular STT-MRAM," *IEEE J. Electron Devices Soc.*, vol. 8, pp. 1249–1256, 2020, doi: 10.1109/JEDS.2020.3023577.

[117] H. Sato, M. Yamanouchi, K. Miura, S. Ikeda, R. Koizumi, F. Matsukura *et al.*, "CoFeB thickness dependence of thermal stability factor in CoFeB/MgO perpendicular magnetic tunnel junctions," *IEEE Magn. Lett.*, vol. 3, pp. 3 000 204–3 000 204, 2012, doi: 10.1109/LMAG.2012.2190722.

[118] A. Manchon, N. Ryzhanova, N. Strelkov, A. Vedyayev, and B. Dieny, "Modelling spin transfer torque and magnetoresistance in magnetic multilayers," *J. Phys.: Condens. Matter*, vol. 19, no. 16, p. 165212, Apr. 2007, doi: 10.1088/0953-8984/19/16/165212.

[119] P. Graczyk and M. Krawczyk, "Nonresonant amplification of spin waves through interface magnetoelectric effect and spin-transfer torque," *Sci. Rep.*, vol. 11, no. 1, p. 15692, Aug. 2021, doi: 10.1038/s41598-021-95267-1.

[120] P. Haney, H. W. Lee, K. J. Lee, A. Manchon, and M. Stiles, "Current induced torques and interfacial spin-orbit coupling: Semiclassical modeling," *Phys. Rev. B*, vol. 87, Jan. 2013, doi: 10.1103/PhysRevB.87.174411.

[121] T. Valet and A. Fert, "Theory of the perpendicular magnetoresistance in magnetic multilayers," *Phys. Rev. B*, vol. 48, pp. 7099–7113, Sep. 1993, doi: 10.1103/PhysRevB.48.7099.

[122] M. Ruggeri, C. Abert, G. Hrkac, D. Suess, and D. Praetorius, "Coupling of dynamical micromagnetism and a stationary spin drift-diffusion equation: A step towards a fully self-consistent spintronics framework," *Physica B*, vol. 486, pp. 88–91, 2016, doi: 10.1016/j.physb.2015.09.003.

[123] C. Petitjean, D. Luc, and X. Waintal, "Unified drift-diffusion theory for transverse spin currents in spin valves, domain walls, and other textured magnets," *Phys. Rev. Lett.*, vol. 109, p. 117204, Sep. 2012, doi: 10.1103/PhysRevLett.109.117204.

[124] M. D. Stiles and A. Zangwill, "Anatomy of spin-transfer torque," *Phys. Rev. B*, vol. 66, p. 014407, Jun. 2002, doi: 10.1103/PhysRevB.66.014407.

[125] D. Luc, "Théorie unifiée du transport de spin, charge et chaleur," Ph.D. dissertation, Université Grenoble Alpes, 2016, thèse de doctorat dirigée par Waintal, Xavier et Chshiev, Mairbek Nanophysique Université Grenoble Alpes (ComUE) 2016. [Online]. Available: http://www.theses.fr/2016GREAY007

[126] X. Waintal, E. B. Myers, P. W. Brouwer, and D. C. Ralph, "Role of spin-dependent interface scattering in generating current-induced torques in magnetic multilayers," *Phys. Rev. B*, vol. 62, pp. 12 317–12 327, Nov. 2000, doi: 10.1103/PhysRevB.62.12317.

TU Bibliothek WIEN Your knowledge hub
Die approbierte gedruckte Originalversion dieser Dissertation ist an der TU Wien Bibliothek verfügbar.
The approved original version of this doctoral thesis is available in print at TU Wien Bibliothek.

[127] S. Borlenghi, V. Rychkov, C. Petitjean, and X. Waintal, "Multiscale approach to spin transport in magnetic multilayers," *Phys. Rev. B*, vol. 84, p. 035412, Jul. 2011, doi: 10.1103/PhysRevB.84.035412.

[128] V. S. Rychkov, S. Borlenghi, H. Jaffres, A. Fert, and X. Waintal, "Spin torque and waviness in magnetic multilayers: A bridge between Valet-Fert theory and quantum approaches," *Phys. Rev. Lett.*, vol. 103, p. 066602, Aug. 2009, doi: 10.1103/PhysRevLett.103.066602.

[129] J. Chen, C. J. García-Cervera, and X. Yang, "Mean-field dynamics of the spin–magnetization coupling in ferromagnetic materials: Application to current-driven domain wall motions," *IEEE Trans. Magn.*, vol. 51, no. 6, pp. 1–6, 2015, doi: 10.1109/TMAG.2015.2401534.

[130] D. Braess, *Finite Elements: Theory, Fast Solvers, and Applications in Solid Mechanics*, 3rd ed. Cambridge University Press, 2007, ch. Introduction. ISBN 9780511618635

[131] M. G. Larson and F. Bengzon, *The Finite Element Method: Theory, Implementation, and Applications*. Springer Berlin Heidelberg, 2013, ch. Electromagnetics. ISBN 978-3-642-33287-6

[132] R. Anderson, J. Andrej, A. Barker, J. Bramwell, J.-S. Camier, J. C. V. Dobrev *et al.*, "MFEM: A modular finite element library," *Comp. & Math. with Appl.*, 2020, doi: 10.1016/j.camwa.2020.06.009.

[133] "MFEM: Modular finite element methods [Software]," https://mfem.org.

[134] F. Alouges and P. Jaisson, "Convergence of a finite element discretization for the Landau-Lifshitz equations in micromagnetism," *Math. Models Methods Appl. Sci.*, vol. 16, no. 2, p. 299 – 316, 2006, doi: 10.1142/S0218202506001169.

[135] S. Bartels, J. Ko, and A. Prohl, "Numerical analysis of an explicit approximation scheme for the landau-lifshitz-gilbert equation," *Math. Comput.*, vol. 77, no. 262, p. 773 – 788, 2008, doi: 10.1090/S0025-5718-07-02079-0.

[136] F. Alouges, "A new finite element scheme for Landau-Lifchitz equations," *Discrete Contin. Dyn. Syst. S*, vol. 1, no. 2, pp. 187–196, 2008, doi: 10.3934/dcdss.2008.1.187.

[137] F. Alouges, E. Kritsikis, and J.-C. Toussaint, "A convergent finite element approximation for Landau–Lifschitz–Gilbert equation," *Physica B*, vol. 407, no. 9, pp. 1345–1349, 2012, doi: 10.1016/j.physb.2011.11.031.

[138] F. Bruckner, D. Suess, M. Feischl, T. Führer, P. Goldenits, M. Page *et al.*, "Multiscale modeling in micromagnetics: Existence of solutions and numerical integration," *Math. Models Methods Appl. Sci.*, vol. 24, no. 13, pp. 2627–2662, 2014, doi: 10.1142/S0218202514500328.

[139] C. Abert, G. Hrkac, M. Page, D. Praetorius, M. Ruggeri, and D. Suess, "Spin-polarized transport in ferromagnetic multilayers: An unconditionally convergent FEM integrator," *Comp. & Math. with Appl.*, vol. 68, no. 6, pp. 639 – 654, 2014, doi: 10.1016/j.camwa.2014.07.010.

[140] G. Hrkac, C.-M. Pfeiler, D. Praetorius, M. Ruggeri, A. Segatti, and B. Stiftner, "Convergent tangent plane integrators for the simulation of chiral magnetic skyrmion dynamics," *Adv. Comput. Math.*, vol. 45, no. 3, pp. 1329–1368, Jun. 2019, doi: 10.1007/s10444-019-09667-z.

Die approbierte gedruckte Originalversion dieser Dissertation ist an der TU Wien Bibliothek verfügbar.
The approved original version of this doctoral thesis is available in print at TU Wien Bibliothek.
TU WIEN Bibliothek Your knowledge hub

[141] J. Ender, M. Mohamedou, S. Fiorentini, R. L. de Orio, S. Selberherr, W. Goes *et al.*, "Efficient demagnetizing field calculation for disconnected complex geometries in STT-MRAM cells," in *Proc. SISPAD Conf.*, 2020, pp. 213–216, doi: 10.23919/SISPAD49475.2020.9241662.

[142] M. Bendra, J. Ender, S. Fiorentini, T. Hadamek, R. L. de Orio, W. Goes *et al.*, "Finite element method approach to MRAM modeling," in *Proc. MIPRO Conf.*, 2021, pp. 70–73, doi: 10.23919/MIPRO52101.2021.9597194.

[143] S. Fiorentini, J. Ender, S. Selberherr, R. L. de Orio, W. Goes, and V. Sverdlov, "Comprehensive modeling of coupled spin and charge transport through magnetic tunnel junctions," in *Proc. EUROSOI-ULIS Conf.*, 2020, pp. 1–4, doi: 10.1109/EUROSOI-ULIS49407.2020.9365497. © 2020 IEEE.

[144] S. Fiorentini, J. Ender, M. Mohamedou, R. L. de Orio, S. Selberherr, W. Goes *et al.*, "Computation of torques in magnetic tunnel junctions through spin and charge transport modeling," in *Proc. SISPAD Conf.*, 2020, pp. 209–212, doi: 10.23919/SISPAD49475.2020.9241657. © 2020 IEEE.

[145] S. Fiorentini, J. Ender, R. L. de Orio, S. Selberherr, W. Goes, and V. Sverdlov, "Spin drift-diffusion approach for the computation of torques in multi-layered structures," in *Book of Abstracts IWCN Conf.*, 2021, pp. 51–52.

[146] S. Fiorentini, J. Ender, S. Selberherr, R. L. de Orio, W. Goes, and V. Sverdlov, "Coupled spin and charge drift-diffusion approach applied to magnetic tunnel junctions," *Solid State Electron.*, vol. 186, p. 108103, 2021, doi: 10.1016/j.sse.2021.108103.

[147] S. Fiorentini, J. Ender, R. L. de Orio, S. Selberherr, W. Goes, and V. Sverdlov, "Spin and charge drift-diffusion approach to torque computation in magnetic tunnel junctions," in *Proc. SISPAD Conf.*, 2021, pp. 155–158, doi: 10.1109/SISPAD54002.2021.9592559.

[148] S. Fiorentini, J. Ender, S. Selberherr, W. Goes, and V. Sverdlov, "Spin transfer torque evaluation based on coupled spin and charge transport: A finite element method approach," *J. Syst. Cyb. Inf.*, vol. 20, no. 4, pp. 40–44, 2022, doi: 10.54808/JSCI.20.04.40.

[149] "MFEM: Modular finite element methods [Software]," mfem.org.

[150] "Netgen/NGSolve," https://ngsolve.org/.

[151] S. Zhang and Z. Li, "Roles of nonequilibrium conduction electrons on the magnetization dynamics of ferromagnets," *Phys. Rev. Lett.*, vol. 93, p. 127204, Sep. 2004, doi: 10.1103/PhysRevLett.93.127204.

[152] J. Xiao, A. Zangwill, and M. D. Stiles, "Boltzmann test of Slonczewski's theory of spin-transfer torque," *Phys. Rev. B*, vol. 70, p. 172405, Nov. 2004, doi: 10.1103/PhysRevB.70.172405.

[153] C. Abert, H. Sepehri-Amin, F. Bruckner, C. Vogler, M. Hayashi, and D. Suess, "Back-hopping in spin-transfer-torque devices: Possible origin and countermeasures," *Phys. Rev. Appl.*, vol. 9, p. 054010, May 2018, doi: 10.1103/PhysRevApplied.9.054010.

Die approbierte gedruckte Originalversion dieser Dissertation ist an der TU Wien Bibliothek verfügbar.
The approved original version of this doctoral thesis is available in print at TU Wien Bibliothek.
TU WIEN Bibliothek Your knowledge hub

[154] K. Y. Camsari, S. Ganguly, D. Datta, and S. Datta, "Physics-based factorization of magnetic tunnel junctions for modeling and circuit simulation," in *Proc. IEDM Conf.*, 2014, pp. 35.6.1–35.6.4, doi: 10.1109/IEDM.2014.7047177.

[155] A. Brataas, G. E. Bauer, and P. J. Kelly, "Non-collinear magnetoelectronics," *Phys. Rep.*, vol. 427, no. 4, pp. 157–255, 2006, doi: 10.1016/j.physrep.2006.01.001.

[156] A. Shpiro, P. M. Levy, and S. Zhang, "Self-consistent treatment of nonequilibrium spin torques in magnetic multilayers," *Phys. Rev. B*, vol. 67, p. 104430, Mar. 2003, doi: 10.1103/PhysRevB.67.104430.

[157] I. Theodonis, N. Kioussis, A. Kalitsov, M. Chshiev, and W. H. Butler, "Anomalous bias dependence of spin torque in magnetic tunnel junctions," *Phys. Rev. Lett.*, vol. 97, p. 237205, Dec. 2006, doi: 10.1103/PhysRevLett.97.237205.

[158] D. Datta, B. Behin-Aein, S. Datta, and S. Salahuddin, "Voltage asymmetry of spin-transfer torques," *IEEE Trans. Nanotechnol.*, vol. 11, no. 2, pp. 261–272, 2012, doi: 10.1109/TNANO.2011.2163147.

[159] H. Kubota, A. Fukushima, K. Yakushiji, T. Nagahama, S. Yuasa, K. Ando *et al.*, "Quantitative measurement of voltage dependence of spin-transfer torque in MgO-based magnetic tunnel junctions," *Nat. Phys.*, vol. 4, no. 1, pp. 37–41, Jan. 2008, doi: 10.1038/nphys784.

[160] Z. Li, S. Zhang, Z. Diao, Y. Ding, X. Tang, D. M. Apalkov *et al.*, "Perpendicular spin torques in magnetic tunnel junctions," *Phys. Rev. Lett.*, vol. 100, p. 246602, Jun. 2008, doi: 10.1103/PhysRevLett.100.246602.

[161] C. Wang, Y.-T. Cui, J. Z. Sun, J. A. Katine, R. A. Buhrman, and D. C. Ralph, "Bias and angular dependence of spin-transfer torque in magnetic tunnel junctions," *Phys. Rev. B*, vol. 79, p. 224416, Jun. 2009, doi: 10.1103/PhysRevB.79.224416.

[162] D. Tiwari, R. Sharma, O. G. Heinonen, J. Åkerman, and P. K. Muduli, "Influence of MgO barrier quality on spin-transfer torque in magnetic tunnel junctions," *Applied Physics Letters*, vol. 112, no. 2, p. 022406, 2018, doi: 10.1063/1.5005893.

[163] S. Fiorentini, M. Bendra, J. Ender, R. L. de Orio, W. Goes, S. Selberherr *et al.*, "Spin torques in ultra-scaled MRAM devices," in *Proc. ESSDERC Conf.*, 2022, pp. 348–351, doi: 10.1109/ESSDERC55479.2022.9947196. © 2022 IEEE.

[164] S. Fiorentini, J. Ender, S. Selberherr, R. L. de Orio, W. Goes, and V. Sverdlov, "Comprehensive evaluation of torques in ultra-scaled mram devices," *Solid-State Electron.*, vol. 199, p. 108491, 2023, doi: 10.1016/j.sse.2022.108491.

[165] P. Flauger, C. Abert, and D. Suess, "Efficient solution strategy to couple micromagnetic simulations with ballistic transport in magnetic tunnel junctions," *Phys. Rev. B*, vol. 105, p. 134407, Apr. 2022, doi: 10.1103/PhysRevB.105.134407.

[166] J. Fabian, A. Matos-Abiague, C. Ertler, P. Stano, and I. Zutic, "Semiconductor spintronics," *Acta Phys. Slovaca*, vol. 57, Aug. 2007, doi: 10.2478/v10155-010-0086-8.

[167] M. M. Torunbalci, P. Upadhyaya, S. A. Bhave, and K. Y. Camsari, "Modular compact modeling of MTJ devices," *IEEE Trans. Electron Devices*, vol. 65, no. 10, pp. 4628–4634, 2018, doi: 10.1109/TED.2018.2863538.

TU WIEN Bibliothek Your knowledge hub
Die approbierte gedruckte Originalversion dieser Dissertation ist an der TU Wien Bibliothek verfügbar.
The approved original version of this doctoral thesis is available in print at TU Wien Bibliothek.

[168] G. Hu, G. Lauer, J. Z. Sun, P. Hashemi, C. Safranski, S. L. Brown *et al.*, "2X reduction of STT-MRAM switching current using double spin-torque magnetic tunnel junction," in *Proc. IEDM Conf.*, 2021, pp. 2.5.1–2.5.4, doi: 10.1109/IEDM19574.2021.9720691.

[169] J. C. Slonczewski, "Currents and torques in metallic magnetic multilayers," *J. Magn. Magn. Mater.*, vol. 247, no. 3, pp. 324 – 338, 2002, doi: 10.1016/S0304-8853(02)00291-3.

TU Bibliothek, WIEN Your knowledge hub
Die approbierte gedruckte Originalversion dieser Dissertation ist an der TU Wien Bibliothek verfügbar.
The approved original version of this doctoral thesis is available in print at TU Wien Bibliothek.

List of Publications

Journal Articles

- S. Fiorentini, J. Ender, S. Selberherr, R. L. de Orio, W. Goes, and V. Sverdlov, "Comprehensive evaluation of torques in ultra-scaled MRAM devices," *Solid-State Electron.*, vol. 199, p. 108491, 2023, doi: 10.1016/j.sse.2022.108491.
- S. Fiorentini, M. Bendra, J. Ender, R. L. de Orio, W. Goes, S. Selberherr, and V. Sverdlov, "Spin and charge drift-diffusion in ultra-scaled MRAM cells," *Sci. Rep.*, vol. 12, no. 1, p. 20958, Dec. 2022, doi: 10.1038/s41598-022-25586-4.
- S. Fiorentini, J. Ender, S. Selberherr, W. Goes, and V. Sverdlov, "Spin transfer torque evaluation based on coupled spin and charge transport: A finite element method approach," *J. Syst. Cyb. Inf.*, vol. 20, no. 4, pp. 40–44, 2022, doi: 10.54808/JSCI.20.04.40.
- M. Bendra, S. Fiorentini, W. Goes, S. Selberherr, and V. Sverdlov, "Interface Effects in Ultra-Scaled MRAM Cells," *Solid-State Electron.*, vol. 194, p. 108373, 2022, doi: 10.1016/j.sse.2022.108373.
- J. Ender, S. Fiorentini, R. L. de Orio, T. Hadámek, M. Bendra, W. Goes, S. Selberherr, and V. Sverdlov, "Advances in modeling emerging magnetoresistive random access memories: From finite element methods to machine learning approaches," *Proc. SPIE Int. Soc. Opt. Eng.*, vol. 12157, pp. 1215708-1–1215708-14, 2022, doi: 10.1117/12.2624595.
- J. Ender, R. L. de Orio, S. Fiorentini, S. Selberherr, W. Goes, and V. Sverdlov, "Reinforcement learning to reduce failures in SOT-MRAM switching," *Microelectron. Reliab.*, vol. 135, pp. 1–5, 2022, doi: 10.1016/j.microrel.2022.114570.
- T. Hadámek, S. Fiorentini, M. Bendra, J. Ender, R. L. de Orio, W. Goes, S. Selberherr, and V. Sverdlov, "Temperature increase in STT-MRAM at writing: A Fully three-dimensional finite element approach," *Solid-State Electron.*, vol. 193, pp. 108269-1–108269-7, 2022, doi: 10.1016/j.sse.2022.108269.
- N. Jørstad, S. Fiorentini, W. J. Loch, W. Goes, S. Selberherr, and V. Sverdlov, "Finite element modeling of spin-orbit torques," *Solid-State Electron.*, vol. 194, pp. 108323-1–108323-4, 2022, doi: 10.1016/j.sse.2022.108323.

Die approbierte gedruckte Originalversion dieser Dissertation ist an der TU Wien Bibliothek verfügbar.
The approved original version of this doctoral thesis is available in print at TU Wien Bibliothek.
TU WIEN Bibliothek Your knowledge hub

- W. J. Loch, S. Fiorentini, N. Jørstad, W. Goes, S. Selberherr, and V. Sverdlov, "Double reference layer STT-MRAM structures with improved performance," *Solid-State Electron.*, vol. 194, pp. 108335-1–108335-4, 2022, doi: 10.1016/j.sse.2022.108335.
- J. Ender, S. Fiorentini, R. L. de Orio, W. Goes, V. Sverdlov, and S. Selberherr, "Emerging CMOS compatible magnetic memories and logic," *IEEE J. Electron Devices Soc.*, vol. 9, pp. 456–463, 2021, doi: 10.1109/JEDS.2021.3066679.
- J. Ender, R. L. de Orio, S. Fiorentini, S. Selberherr, W. Goes, and V. Sverdlov, "Improving failure rates in pulsed SOT-MRAM switching by reinforcement learning," *Microelectron. Reliab.*, vol. 126, pp. 114231-1–114231-5, 2021, doi: 10.1016/j.microrel.2021.114231.
- J. Ender, R. L. de Orio, S. Fiorentini, S. Selberherr, W. Goes, and V. Sverdlov, "Reinforcement learning approach for deterministic SOT-MRAM switching," *Proc. SPIE Int. Soc. Opt. Eng.*, vol. 11805, pp. 1180519-1–1180519-8, 2021, doi: 10.1117/12.2593937.
- S. Fiorentini, J. Ender, S. Selberherr, R. L. de Orio, W. Goes, and V. Sverdlov, "Coupled spin and charge drift-diffusion approach applied to magnetic tunnel junctions," *Solid-State Electron.*, vol. 186, pp. 108103, 2021, doi: 10.1016/j.sse.2021.108103.
- R. L. de Orio, J. Ender, S. Fiorentini, W. Goes, S. Selberherr, and V. Sverdlov, "Numerical analysis of deterministic switching of a perpendicularly magnetized spin-orbit torque memory cell," *IEEE J. Electron Devices Soc.*, vol. 9, pp. 61–67, 2021, doi: 10.1109/JEDS.2020.3039544.
- R. L. de Orio, J. Ender, S. Fiorentini, W. Goes, S. Selberherr, and V. Sverdlov, "Optimization of a spin-orbit torque switching scheme based on micromagnetic simulations and reinforcement learning," *Micromachines*, vol. 12, pp. 443, 2021, doi: 10.3390/mi12040443.
- R. L. de Orio, J. Ender, S. Fiorentini, W. Goes, S. Selberherr, and V. Sverdlov, "Two-pulse switching scheme and reinforcement learning for energy efficient SOT-MRAM simulations," *Solid-State Electron.*, vol. 185, pp. 108075, 2021, doi: 10.1016/j.sse.2021.108075.
- S. Fiorentini, J. Ender, M. Mohamedou, S. Selberherr, R. Orio, W. Goes, and V. Sverdlov, "Comprehensive modeling of coupled spin-charge transport and magnetization dynamics in STT-MRAM cells," *Proc. SPIE Int. Soc. Opt. Eng.*, vol. 11470, pp. 114701B-1–114701B-7, 2020, doi: 10.1117/12.2567480.
- S. Fiorentini, R. Orio, S. Selberherr, J. Ender, W. Goes, and V. Sverdlov, "Analysis of switching under fixed voltage and fixed current in perpendicular STT-MRAM," *IEEE J. Electron Devices Soc.*, vol. 8, pp. 1249–1256, 2020, doi: 10.1109/JEDS.2020.3023577.

TU WIEN Bibliothek Your knowledge hub
Die approbierte gedruckte Originalversion dieser Dissertation ist an der TU Wien Bibliothek verfügbar.
The approved original version of this doctoral thesis is available in print at TU Wien Bibliothek.

- R. L. de Orio, A. Makarov, W. Goes, J. Ender, S. Fiorentini, and V. Sverdlov, "Two-pulse magnetic field-free switching scheme for perpendicular SOT-MRAM with a symmetric square free layer," *Physica B*, vol. 578, pp. 411743, 2020, doi: 10.1016/j.physb.2019.411743.

- R. L. de Orio, A. Makarov, S. Selberherr, W. Goes, J. Ender, S. Fiorentini, and V. Sverdlov, "Robust magnetic field-free switching of a perpendicularly magnetized free layer for SOT-MRAM," *Solid-State Electron.*, vol. 168, pp. 107730-1–107730-7, 2020, doi: 10.1016/j.sse.2019.107730.

Book Contributions

- T. Hadámek, M. Bendra, S. Fiorentini, J. Ender, R. L. de Orio, W. Goes, S. Selberherr, and V. Sverdlov, "Temperature increase in MRAM at writing: A finite element approach," in *Proc. EUROSOI-ULIS Conf.*, pp. 1–4, 2021, doi: 10.1109/EuroSOI-ULIS53016.2021.9560669.

- S. Fiorentini, J. Ender, S. Selberherr, R. L. de Orio, W. Goes, and V. Sverdlov, "Comprehensive modeling of coupled spin and charge transport through magnetic tunnel junctions," in *Proc. EUROSOI-ULIS Conf.*, pp. 1–4, 2020, doi: 10.1109/EUROSOI-ULIS49407.2020.9365497.

- S. Fiorentini, R. L. de Orio, S. Selberherr, J. Ender, W. Goes, and V. Sverdlov, "Influence of current redistribution in switching models for perpendicular STT-MRAM," in *Adv. CMOS-Comp. Semicond. Devices 19*, vol. 97, no. 5, pp. 159–164, 2020, doi: 10.1149/09705.0159ecst.

- R. L. de Orio, J. Ender, S. Fiorentini, W. Goes, S. Selberherr, and V. Sverdlov, "Reduced current spin-orbit torque switching of a perpendicularly magnetized free layer," in *Proc. EUROSOI-ULIS Conf.*, pp. 1–4, 2020, doi: 10.1109/EUROSOI-ULIS49407.2020.9365497.

- R. L. de Orio, A. Makarov, S. Selberherr, W. Goes, J. Ender, S. Fiorentini, and V. Sverdlov, "Efficient magnetic field-free switching of a symmetric perpendicular magnetic free layer for advanced SOT-MRAM," in *Proc. EUROSOI-ULIS Conf.*, pp. 1–4, 2019, doi: 10.1109/EUROSOI-ULIS45800.2019.9041920.

Conference Contributions (with Proceedings-Entry)

- S. Fiorentini, W. J. Loch, M. Bendra, N. Jørstad, J. Ender, R. L. de Orio, T. Hadámek, W. Goes, V. Sverdlov, and S. Selberherr, "Design analysis of ultra-scaled MRAM cells," in *Proc. ICSICT Conf.*, 2022.

Die approbierte gedruckte Originalversion dieser Dissertation ist an der TU Wien Bibliothek verfügbar.
The approved original version of this doctoral thesis is available in print at TU Wien Bibliothek.
TU WIEN Bibliothek Your knowledge hub

- V. Sverdlov, M. Bendra, S. Fiorentini, J. Ender, R. L. de Orio, T. Hadámek, W.J. Loch, N. Jørstad, W. Goes, and S. Selberherr, "Modeling advanced spintronic based magnetoresistive memory," in *Book of Abstracts IRPhE Conf.*, 2022.
- S. Fiorentini, M. Bendra, J. Ender, R. L. de Orio, W. Goes, S. Selberherr, and V. Sverdlov, "Spin torques in ultra-scaled MRAM devices," in *Proc. ESSDERC Conf.*, 2022, pp. 348–351, doi: 10.1109/ESSDERC55479.2022.9947196.
- S. Fiorentini, J. Ender, R. L. de Orio, S. Selberherr, W. Goes, and V. Sverdlov, "Comprehensive evaluation of torques in ultra scaled MRAM devices," in *Book of Abstracts SISPAD Conf.*, 2022, pp. 11–12.
- S. Fiorentini, J. Ender, R. L. de Orio, S. Selberherr, W. Goes, and V. Sverdlov, "Spin transfer torque evaluation based on coupled spin and charge transport: A finite element method approach," in *Proc. WMSCI Conf.*, 2022, pp. 12–15, doi: 10.54808/WMSCI2022.02.12.
- V. Sverdlov, W. J. Loch, M. Bendra, S. Fiorentini, J. Ender, R. L. de Orio, T. Hadámek, N. Jørstad, W. Goes, and S. Selberherr, "Modeling Approach to Ultra-Scaled MRAM Cells," in *Book of Abstracts ASETMEET Conf.*, 2022, pp. 7–8.
- T. Hadámek, S. Fiorentini, M. Bendra, R. L. de Orio, W. J. Loch, N. Jorstad, S. Selberherr, W. Goes, and V. Sverdlov, "Temperature modeling in STT-MRAM: A fully three-dimensional finite element approach," in *Book of Abstracts NANO Conf.*, 2022.
- N. Jørstad, S. Fiorentini, S. Selberherr, W. Goes, and V. Sverdlov, "Modeling interfacial and bulk spin-orbit torques," in *Book of Abstracts NANO Conf.*, 2022.
- R. L. de Orio, J. Ender, W. Goes, S. Fiorentini, S. Selberherr, and V. Sverdlov, "About the switching energy of a magnetic tunnel junction determined by spin-orbit torque and voltage-controlled magnetic anisotropy," in *Proc. LAEDC Conf.*, 2022, pp. 1–4, doi: 10.1109/LAEDC54796.2022.9908222.
- V. Sverdlov, M. Bendra, S. Fiorentini, J. Ender, R. Orio, T. Hadámek, W. J. Loch, N. Jørstad, W. Goes, and S. Selberherr, "Emerging devices for digital spintronics," in *Proc. GECNN Conf.*, 2022, pp. 32–33.
- M. Bendra, S. Fiorentini, J. Ender, R. Orio, T. Hadámek, W. J. Loch, N. Jørstad, S. Selberherr, W. Goes, and V. Sverdlov, "Spin transfer torques in ultra-scaled MRAM cells," in *Proc. MIPRO Conf.*, 2022, pp. 129–132.
- M. Bendra, S. Fiorentini, J. Ender, R. Orio, T. Hadámek, W. J. Loch, N. Jørstad, W. Goes, and S. Selberherr, "Interface effects in ultra-scaled MRAM cells," in *Book of Abstracts EUROSOI-ULIS Conf.*, 2022.

TU Bibliothek WIEN Your knowledge hub
Die approbierte gedruckte Originalversion dieser Dissertation ist an der TU Wien Bibliothek verfügbar.
The approved original version of this doctoral thesis is available in print at TU Wien Bibliothek.

- V. Sverdlov, M. Bendra, S. Fiorentini, J. Ender, R. Orio, T. Hadámek, W. J. Loch, N. Jørstad, and S. Selberherr, “Modeling advanced magnetoresistive Memory: A journey from finite element methods to machine learning approaches,” in *Proc. Global Webinar on Nanosc. and Nanotec.*, 2022.
- N. Jørstad, S. Fiorentini, W. Goes, V. Sverdlov, “Efficient finite element method approach to model spin orbit torque MRAM,” in *Book of Abstracts MOS-AK Workshop*, 2021, pp. 1.
- S. Fiorentini, M. Bendra, J. Ender, R. L. de Orio, S. Selberherr, W. Goes, and V. Sverdlov, “Design support for ultra-scaled MRAM cells,” in *Proc. IEDM Conf. (Special MRAM Poster Session)*, 2021.
- S. Fiorentini, R. L. de Orio, S. Selberherr, J. Ender, W. Goes, and V. Sverdlov, “Spin and Charge Drift-Diffusion Approach to Torque Computation in Spintronic Devices,” in *Book of Abstracts WINDS Conf.*, 2021.
- J. Ender, S. Fiorentini, R. L. de Orio, T. Hadámek, M. Bendra, W. Goes, S. Selberherr, and V. Sverdlov, “Advanced modeling of emerging MRAM: From finite element methods to machine learning approaches,” in *Proc. ICMNE Conf.*, 2021.
- J. Ender, R. L. de Orio, S. Fiorentini, S. Selberherr, W. Goes, and V. Sverdlov, “Improving failure rates in pulsed SOT-MRAM Switching by reinforcement learning,” in *Proc. ESREF Conf.*, 2021, pp. 1–4, doi: 10.1016/j.microrel.2021.114231.
- M. Bendra, J. Ender, S. Fiorentini, T. Hadámek, R. L. de Orio, W. Goes, S. Selberherr, and V. Sverdlov, “Finite element method approach to MRAM modeling,” in *Proc. MIPRO Conf.*, 2021, pp. 70–73, doi: 10.23919/MIPRO52101.2021.9597194.
- J. Ender, R. L. de Orio, S. Fiorentini, S. Selberherr, W. Goes, and V. Sverdlov, “Reinforcement learning approach for sub-critical current SOT-MRAM switching materials,” in *Proc. SISPAD Conf.*, 2021, pp. 150–154, 10.1109/SISPAD54002.2021.9592561.
- S. Fiorentini, J. Ender, R. L. de Orio, S. Selberherr, W. Goes, and V. Sverdlov, “Spin and charge drift-diffusion approach to torque computation in magnetic tunnel junctions,” in *Proc. SISPAD Conf.*, 2021, pp. 155–158, 10.1109/SISPAD54002.2021.9592561.
- J. Ender, R. L. de Orio, S. Fiorentini, S. Selberherr, W. Goes, and V. Sverdlov, “Reinforcement learning to reduce failures in SOT-MRAM switching,” in *Proc. IPFA Conf.*, 2021, doi: 10.1109/IPFA53173.2021.9617362
- R. L. de Orio, J. Ender, S. Fiorentini, W. Goes, S. Selberherr, and V. Sverdlov, “Deterministic spin-orbit switching scheme for an array of perpendicular MRAM cells suitable for large scale integration,” in *Proc. TMAG Conf.*, 2021.

TU WIEN Bibliothek Your knowledge hub
Die approbierte gedruckte Originalversion dieser Dissertation ist an der TU Wien Bibliothek verfügbar.
The approved original version of this doctoral thesis is available in print at TU Wien Bibliothek.

- T. Hadámek, M. Bendra, S. Fiorentini, J. Ender, R. L. de Orio, W. Goes, S. Selberherr, and V. Sverdlov, "Temperature increase in MRAM at writing: A finite element approach," in *Book of Abstracts EUROSOI-ULIS Conf.*, 2021, pp. 133–134.
- J. Ender, S. Fiorentini, V. Sverdlov, W. Goes, R. L. de Orio, and S. Selberherr, "Reinforcement learning approach for deterministic SOT-MRAM switching," in *Proc. SPIE Conf.*, 2021, pp. 11805-53.
- J. Ender, S. Fiorentini, S. Selberherr, W. Goes, and V. Sverdlov, "Advanced modeling of emerging nonvolatile magnetoresistive devices," in *Book of Abstracts IWCN Conf.*, 2021, pp. 45–46.
- S. Fiorentini, J. Ender, R. L. de Orio, S. Selberherr, W. Goes, and V. Sverdlov, "Spin drift-diffusion approach for the computation of torques in multi-layered structures," in *Book of Abstracts IWCN Conf.*, 2021, pp. 51–52.
- J. Ender, M. Mohamedou, S. Fiorentini, R. L. de Orio, S. Selberherr, W. Goes, and V. Sverdlov, "Efficient demagnetizing field calculation for disconnected complex geometries in STT-MRAM cells," in *Proc. SISPAD Conf.*, 2020, pp. 213–216, doi: 10.23919/SISPAD49475.2020.9241662.
- S. Fiorentini, J. Ender, M. Mohamedou, R. L. de Orio, S. Selberherr, W. Goes, and V. Sverdlov, "Computation of torques in magnetic tunnel junctions through spin and charge transport modeling," in *Proc. SISPAD Conf.*, 2020, pp. 209–212, doi: 10.23919/SISPAD49475.2020.9241657.
- R. L. de Orio, A. Makarov, W. Goes, J. Ender, S. Fiorentini, S. Selberherr, and V. Sverdlov, "Switching of a perpendicularly magnetized free-layer by spin-orbit-torques with reduced currents," in *Proc. WMSCI Conf.*, 2020, pp. 58–61.
- R. L. de Orio, J. Ender, S. Fiorentini, W. Goes, S. Selberherr, and V. Sverdlov, "Reduced current spin-orbit torque switching of a perpendicularly magnetized free layer," in *Book of Abstracts EUROSOI-ULIS Conf.*, 2020, pp. 123–124.
- S. Fiorentini, J. Ender, M. Mohamedou, V. Sverdlov, W. Goes, R. L. de Orio, and S. Selberherr, "Comprehensive modeling of coupled spin-charge transport and magnetization dynamics in STT-MRAM cells," in *Proc. SPIE Conf.*, 2020, pp. 11470–44.
- S. Fiorentini, R. L. de Orio, S. Selberherr, J. Ender, W. Goes, and V. Sverdlov, "Influence of current redistribution in switching models for perpendicular STT-MRAM," in *Book of Abstracts ECS Conf.*, 2020, doi: 10.1149/MA2020-01241389mtgabs
- S. Fiorentini, J. Ender, S. Selberherr, R. L. de Orio, W. Goes, and V. Sverdlov, "Comprehensive modeling of coupled spin and charge transport through magnetic tunnel junctions," in *Book of Abstracts EUROSOI-ULIS Conf.*, 2020, pp. 112–113.

TU WIEN Bibliothek Your knowledge hub
Die approbierte gedruckte Originalversion dieser Dissertation ist an der TU Wien Bibliothek verfügbar.
The approved original version of this doctoral thesis is available in print at TU Wien Bibliothek.

- S. Fiorentini, R. L. de Orio, S. Selberherr, J. Ender, W. Goes, and V. Sverdlov, "Perpendicular STT-MRAM switching at fixed voltage and at fixed current," in *Proc. EDTM Conf.*, 2020, pp. 341–344, doi: 10.1109/EDTM47692.2020.9117985.

- V. Sverdlov, S. Fiorentini, J. Ender, W. Goes, R. L. de Orio, and S. Selberherr, "Emerging CMOS compatible magnetic memories and logic," in *Proc. LAEDC Conf.*, 2020, doi: 10.1109/LAEDC49063.2020.9073332.

- R. L. de Orio, A. Makarov, J. Ender, S. Fiorentini, W. Goes, S. Selberherr, V. Sverdlov, "A dynamical approach to fast and reliable external field free perpendicular magnetization reversal by spin-orbit torques," in *Proc. IEDM Conf. (Special MRAM Poster Session)*, 2019.

- S. Fiorentini, R. Orio, S. Selberherr, J. Ender, W. Goes, V. Sverdlov, "Comprehensive modeling of switching in perpendicular STT-MRAM," in *Proc. WINDS Conf.*, 2019, pp. 107–108.

- R. Orio, S. Selberherr, J. Ender, S. Fiorentini, W. Goes, and V. Sverdlov, "Robustness of the two-pulse switching scheme for SOT-MRAM," in *Book of Abstracts WINDS Conf.*, 2019, pp. 54–55.

- R. L. de Orio, A. Makarov, S. Selberherr, W. Goes, J. Ender, S. Fiorentini, and V. Sverdlov, "Switching speedup of the magnetic free layer of advanced SOT-MRAM," in *Proc. ESSDERC Conf.*, 2019, pp. 146–149, doi: 10.1109/ESSDERC.2019.8901780.

- S. Fiorentini, R. L. de Orio, W. Goes, J. Ender, and V. Sverdlov, "Comprehensive comparison of switching models for perpendicular spin-transfer torque MRAM cells," in *Proc. SISPAD Conf.*, 2019, pp. 57–60, doi: 10.1109/SISPAD.2019.8870359.

- R. L. de Orio, A. Makarov, S. Selberherr, W. Goes, J. Ender, S. Fiorentini, and V. Sverdlov, "Robust magnetic field free switching scheme for perpendicular free layer in advanced spin orbit torque magnetoresistive random access memory," in *Book of Abstracts IWCN Conf.*, 2019, pp. 69–71.

- R. L. de Orio, A. Makarov, W. Goes, J. Ender, S. Fiorentini, and V. Sverdlov, "Two-pulse magnetic field free switching scheme for advanced perpendicular SOT-MRAM," in *Book of Abstracts HMM Conf.*, 2019, p. 34.

- R. L. de Orio, A. Makarov, S. Selberherr, W. Goes, J. Ender, S. Fiorentini, and V. Sverdlov, "Efficient magnetic field free switching of symmetric perpendicular magnetic free layer for advanced SOT-MRAM," in *Book of Abstracts EUROSOI-ULIS Conf.*, 2019, pp. 152–153.

TU Bibliothek WIEN Your knowledge hub
Die approbierte gedruckte Originalversion dieser Dissertation ist an der TU Wien Bibliothek verfügbar.
The approved original version of this doctoral thesis is available in print at TU Wien Bibliothek.

Conference Contributions (no Proceedings-Entry)

- J. Ender, R. Orio, S. Fiorentini, W. Goes, and V. Sverdlov, "Large-scale finite element micromagnetics simulations using open source software," Poster at *EMRS Conf.*, 2019.
- S. Fiorentini, R. L. de Orio, W. Goes, J. Ender, and V. Sverdlov, "Comprehensive comparison of switching models for perpendicular spin-transfer torque MRAM cells," Poster at *EMRS Conf.*, 2019.

Die approbierte gedruckte Originalversion dieser Dissertation ist an der TU Wien Bibliothek verfügbar.
The approved original version of this doctoral thesis is available in print at TU Wien Bibliothek.
TU Bibliothek Your knowledge hub WIEN